


Fall 2013

# Response Of Plasma Facing Components In Tokamaks Due To Intense Energy Deposition Using Particle-In-Cell(pic) Methods

Filippo Genco  
*Purdue University*

Follow this and additional works at: [https://docs.lib.purdue.edu/open\\_access\\_dissertations](https://docs.lib.purdue.edu/open_access_dissertations)

 Part of the [Computer Sciences Commons](#), [Materials Science and Engineering Commons](#), and the [Nuclear Engineering Commons](#)

---

## Recommended Citation

Genco, Filippo, "Response Of Plasma Facing Components In Tokamaks Due To Intense Energy Deposition Using Particle-In-Cell(pic) Methods" (2013). *Open Access Dissertations*. 129.  
[https://docs.lib.purdue.edu/open\\_access\\_dissertations/129](https://docs.lib.purdue.edu/open_access_dissertations/129)

**PURDUE UNIVERSITY**  
**GRADUATE SCHOOL**  
**Thesis/Dissertation Acceptance**

This is to certify that the thesis/dissertation prepared

By Filippo Genco

Entitled

Response of Plasma Facing Components in Tokamaks due to Intense Energy Deposition using Particle-in-Cell (PIC) Methods

For the degree of Doctor of Philosophy

Is approved by the final examining committee:

Ahmed Hassanein, PhD

Chair

Lefteri Tsoukalas, PhD

Valeryi Sizyuk, PhD

Sivanandan S. Harilal, PhD

Yeong Kim, PhD

To the best of my knowledge and as understood by the student in the *Research Integrity and Copyright Disclaimer (Graduate School Form 20)*, this thesis/dissertation adheres to the provisions of Purdue University's "Policy on Integrity in Research" and the use of copyrighted material.

Approved by Major Professor(s): Ahmed Hassanein, PhD

Approved by: Ahmed Hassanein, PhD

Head of the Graduate Program

11/05/2013

Date

RESPONSE OF PLASMA FACING COMPONENTS IN TOKAMAKS DUE TO  
INTENSE ENERGY DEPOSITION USING PARTICLE-IN-CELL(PIC) METHODS

A Dissertation

Submitted to the Faculty

of

Purdue University

by

Filippo Genco

In Partial Fulfillment of the

Requirements for the Degree

of

Doctor of Philosophy

December 2013

Purdue University

West Lafayette, Indiana

A papa' Bartolomeo, perche' da lassu' mi possa guardare e sapere che ho mantenuto la mia promessa. A mamma Rosa, perche' ella possa essere fiera di cio' che ho fatto e sapere che a lei devo tutto. A mio fratello Giacinto che mi ha accompagnato per lunghi tratti di questo cammino, perche' sappia che il mio successo e' anche il suo.

A mia moglie Aksana, perche' e' grazie alla sua dedizione e pazienza che ho potuto completare l'opera. A miei figli Bartolomeo, Viktor e Francesco, luce dei miei occhi, perche' un giorno aprendo queste pagine possano ricordare questi anni e trovare ispirazione sapendo che "Quisque faber est fortunae suae". Dedico questo lavoro anche ai miei nonni paterni Giacinto ed Elisa Genco e materni Filippo e Rosa Calderazzi perche' so che avrebbero gioito con me e perche' eredi di una lunga e straordinaria tradizione avrebbero visto in questo successo, una prosecuzione della storia della famiglia anche lontano dalla sempre amata Altamura.

## ACKNOWLEDGEMENTS

I would like to use this opportunity to thank the many people that along the years helped me to achieve this dream. First and foremost I would like to thank Prof. Ahmed Hassanein without whom all this would have never been possible. His invaluable help and support cannot really be described in words. I can only say that I had the honor and privilege to be his student and learn from him not only about science but also about life. I want to thank him deeply not only for his continuous support but also because he taught me that the importance of conducting high quality research: the experience has been exciting, challenging but memorable. “Only aiming to the excellence, important results can be reached”: this is what I learned from him and will keep with me in my future career wherever this might take me.

Let me also thank the Committee Members Professor Valeryi Sizyuk, Professor Sivanandan S. Harilal, Professor Lefteri Tsoukalas and, last but not the least, Professor Yeong Kim. Their help, encouragement and vivid contribution to my research have been very important as the spirit to acquire a “forma mentis” to contribute in the progress of science.

I would like to thank also Prof. Gennady V. Miloshevsky for the very fruitful discussions and hours spent talking about MPI, FORTRAN codes and particle-in-cell techniques. I want to thank him also for his patience in teaching me aspects of computing I was

unaware of. I would like to thank the US Department of Energy, Office of Fusion Sciences for the continuous support of this research. I would like to thank the ITER Group for allowing the reproduction of some of the ITER schematics in this thesis and the KIT Karlsruhe Institute of Technology for allowing the reproduction of some plots originally published in the Forschungszentrum Karlsruhe GmbH (FZKA) reports.

I would like to thank also my former advisor Dr. Chan K. Choi because his passion for science and teaching lead me to love Fusion and its challenges. I learned a lot from him and I am grateful to have shared with him part of my life at Purdue. I want also to express my deep gratitude for Professor John J. Rusek because through his advices I could always look at things with a different prospective. He has always believed in me and taught me that only thinking to the impossible, dreams can become true. He was a mentor, a friend and a reference to look at and I am truly grateful for having him in my life.

I would like to thank also two people who very important for me and allowed me to arrive at this result: Mr. Rob Miller whose friendship goes far back in time, in a time in which I was a kid, for believing in me and sponsoring my old dream to come to USA with advices and concrete guidance; professor Mihai N. Pascu, who helped me in the darkest year of my life back in 2004 when my father died, believing that I could achieve more and helped me proceed in my career. Thanks and gratitude goes to both of them for being there when I needed the most.

There are many people I would like still to thank for their friendship and love. My life at Purdue was always great thanks to the close friends I am honored to call “part of my life” and who contributed so much in my understanding of life, people and of the world.

Ana Paz Martins and Thomas Dautermann are more than close friends. With them I shared not only great years at Purdue, but also fears, impatience, feelings and love. I am honored to be their friend and will cherish the common memories for many years to come. Kamlesh Nankani whom I consider a brother, has been for long my “alter ego”. In him I see the best qualities of a man and the great passion engineers have for new endeavors. I want to deeply thank you because just your presence made a difference in my life.

Let me also spend few words thanking some of the “educators” I had the fortune to have in my life and that allowed me to arrive to this achievement. It would be too long to name all the Jesuits I have met in my life who helped me to become the man I am today , but special words go to father Michele Caratu’, father Bartolomeo Di Pierro and father Rodolfo Bozzi. A special mention goes also to Saint Thomas Aquinas father Jim Barnett, Dominican as father Dan Davis and father Patrick Baikauskas who have followed me through my years at Purdue.

Finally, I want to dedicate this work and this great achievement to my family and in particular to my mother Rosa and my father Bartolomeo Genco. Many years ago, when the world was all different they understood much before anybody else, that only through a wider and deeper education we could be a meaningful part of the world yet to come. It is impossible to describe fully what they did for me and how much their example, sacrifice, willing to excel has shaped me: they made me the man I am today and of this I will always be grateful. My father taught me almost all I know, made me always wonder about the world and gave me the measure of the highest ethics. My mum gave me the vision, the prospective and I have never known a more loving person than her. She pushed me beyond my limits because she knew I could do more. Thank you because all

this was in the beginning your idea. I want to thank deeply also my wife Aksana. Her patience and loving attitude throughout these last years of study has been outstanding. Her encouragements mixed with wisdom helped me a lot to overcome the difficult moments. I want also to dedicate this achievement to my kids Bartolomeo, Viktor and Francesco because their existence gave me proof of the existence of Paradise.



### The Road Not Taken

Two roads diverged in a yellow wood,  
And sorry I could not travel both  
And be one traveler, long I stood  
And looked down one as far as I could  
To where it bent in the undergrowth;

Then took the other, as just as fair,  
And having perhaps the better claim  
Because it was grassy and wanted wear,  
Though as for that the passing there  
Had worn them really about the same,

And both that morning equally lay  
In leaves no step had trodden black.  
Oh, I marked the first for another day!  
Yet knowing how way leads on to way  
I doubted if I should ever come back.

I shall be telling this with a sigh  
Somewhere ages and ages hence:  
Two roads diverged in a wood, and I,  
I took the one less traveled by,  
And that has made all the difference.

Robert Frost

## SALMO 23

Il Signore è il mio pastore:

non manco di nulla;

su pascoli erbosi mi fa riposare

ad acque tranquille mi conduce.

Mi rinfranca, mi guida per il giusto cammino,

per amore del suo nome.

Se dovessi camminare in una valle oscura,

non temerei alcun male, perché tu sei con me.

Il tuo bastone e il tuo vincastro

mi danno sicurezza.

Davanti a me tu prepari una mensa

sotto gli occhi dei miei nemici;

cospargi di olio il mio capo.

Il mio calice trabocca.

Felicità e grazia mi saranno compagne

tutti i giorni della mia vita,

e abiterò nella casa del Signore

per lunghissimi anni

## TABLE OF CONTENTS

	Page
LIST OF FIGURES .....	xii
ABSTRACT .....	xx
CHAPTER 1. INTRODUCTION .....	1
1.1 Introduction .....	1
1.2 Background: Introduction to Fusion .....	3
1.3 Previous Solutions methods/PIC Methods .....	7
1.4 HEIGHTS-PIC: scope the Code.....	38
References.....	40
CHAPTER 2. MODELING SUMMARY .....	47
2.1 Plasma Material Interaction .....	47
2.2 Plasma Vapor Interactions .....	52
2.3 Radiation Transport and Optical Properties of Plasma .....	58
2.3.1 Continuun Radiation Transport.....	65
2.3.2 Line Radiation Trasport .....	66
References.....	68
CHAPTER 3. HEIGHTS-PIC Code Structure .....	70
3.1 Introduction .....	70
3.2 Main Assumptions.....	73
References.....	77
CHAPTER 4. RESULTS & BENCHMANRCKING.....	78
4.1 Introduction .....	78
4.2 Benchmarking with the MK200 facility experiements .....	80
4.2.1 Erosion &Carbon plate temperature.....	84

	Page
4.2.2	Power Fluxes & Temperature of the plasma vapor cloud.....93
4.2.3	Pressure,Density & Electron Density of the plasma vapor cloud ...104
4.2.4	Benchmarking result with different temporal beam evolutions.....116
4.3	Benchmark with HEIGHTS Computer Package..... 125
4.3.1	Erosion of the target plate & Fluxes .....125
4.3.2	Density & Pressure of the plasma vapor cloud .....134
4.4	Benchmark with Laser Theoretical & experiemental Data..... 138
4.4.1	Theoretical additions to the original HEIGHTS-PIC models .....140
4.4.2	Erosion & Fluxes onto plate.....141
4.4.3	Carbon surface Temperature, Plasma desnity & Temperature .....148
References..... 154	
CHAPTER 5.	DISCUSSION of RESULTS & Limits of the Model..... 159
5.1	Numerical Stability ..... 159
5.2	Accuracy calculation with increasing N ..... 166
5.3	Computational mesh vs numerical stability and computational time ... 171
5.4	Application of different B fields ..... 180
5.5	Limitations of the model ..... 185
References.....188	
CHAPTER 6.	CONCLUSIONS ..... 191
References.....194	
APPENDICES	
Appendix A	Flow Charts of the main subroutines..... 195
A1	Main Program HEIGHTS-PIC .....195
A2	Subroutine MOTION .....199
A3	Subroutine MOVEonXY .....200
A4	Subroutine VAPOR .....205
A5	Subroutine BDIFFUSION .....208
A6	Main Program HEATBEAM .....217
A7	Subroutine HEATCOND .....219

	Page
A8 Subroutine PART .....	226
A9 Subroutine CELL .....	229
A10 Subroutine ORDER .....	233
A11 Subroutine VBOUNDARY .....	235
A12 Subroutine VMASS .....	240
Appendix B Flow Charts of the Radiation Transport .....	245
B1 Subroutine RAYTWO .....	245
B2 Subroutine CHARGE .....	248
B3 Subroutine RADIATION .....	251
VITA .....	258
PUBLICATIONS .....	260

## LIST OF FIGURES

Figure	Page
Figure 1.1 Schematics of a toroidal device and its magnets .....	5
Figure 1.2 Schematics of ITER and its major components .....	6
Figure 1.3 Schematics of ITER DIVERTOR .....	7
Figure 1.4 Configuration of particles in a coarse mesh of cells.....	10
Figure 1.5 Configuration of artificial grid placed around each sample particle .....	15
Figure 1.6 Particle shapes for the NGP and linear weighting in 1D and 2D cases.....	22
Figure 1.7 A grid of quadrilateral zones is illustrated (FLIP zoning).....	30
Figure 2.1 Schematic illustration of various interactions processes with magnetic field during disruptions .....	48
Figure 2.2 Geometry of the 3D Gaussian beam acting on the target surface .....	49
Figure 3.1 Schematic illustration of HEIGHTS – PIC geometry and axes .....	71
Figure 3.2 Schematic illustration of HEIGHTS – PIC geometry, axes and grid distribution .....	71
Figure 3.3 Schematic illustration of HEIGHTS – PIC geometry and axes with angle.....	72
Figure 3.4 Schematic illustration of HEIGHTS – PIC geometry, axes and diffusion across B.....	73
Figure 4.1 Basic scheme of the MK-200UG machine used in Troitsk.....	79
Figure 4.2 Basic geometrical scheme used in HEIGHTS-PIC benchmarking .....	80
Figure 4.3 Evolution along time of the beam power flux over the target plate: beam STEP RISE.....	82
Figure 4.4 Evolution along time of the beam power flux over the target plate: beam rise 5 $\mu$ s.....	83

Figure	Page
Figure 4.5 Evolution along time of the beam power flux over the target plate: beam rise 10 $\mu$ s.....	84
Figure 4.6 Calculated erosion profile (step rise ) in a typical MK-200 experiment simulation with HEIGHTS-PIC (5 sample particles). ....	85
Figure 4.7 Calculated erosion profile (step rise ) in a typical MK-200 experiment simulation with HEIGHTS-PIC (155 sample particles) .....	86
Figure 4.8 Calculated erosion profile (step rise ) in a typical MK-200 experiment simulation with HEIGHTS-PIC (5 vs 155 sample particles).....	87
Figure 4.9 Calculated erosion rate (step rise) in a typical MK-200 experiment simulation with HEIGHTS-PIC (5 vs 155 sample particles).....	88
Figure 4.10 Calculated erosion rate in a typical MK-200 experiment simulation with FOREV-1/FOREV-2.....	90
Figure 4.11 Calculated temperature evolution in a typical MK-200 experiment simulation with HEIGHTS-PIC (5 Particles/Step Rise). ....	91
Figure 4.12 Calculated temperature evolution in a typical MK-200 experiment simulation with HEIGHTS-PIC (155 Particles/Step Rise).....	92
Figure 4.13 Calculated surface temperature evolution at plate center in a typical MK-200 experiment simulation with FOREV-1/FOREV-2.....	93
Figure 4.14 Calculated power fluxes evolution at plate center in a typical MK-200 experiment simulation with HEIGHTS-PIC (N=155) .....	95
Figure 4.15 Calculated power fluxes along the target plate at 45 $\mu$ s in a typical MK-200 experiment simulation with HEIGHTS-PIC (N=155) .....	96
Figure 4.16 Calculated power fluxes along the target plate at 50 $\mu$ s in a typical MK-200 experiment simulation with HEIGHTS-PIC (N=155) .....	97
Figure 4.17 Calculated power fluxes evolution at plate center in a typical MK-200 experiment simulation with HEIGHTS-PIC (N=5) .....	98

Figure	Page
Figure 4.18 Calculated power fluxes evolution at plate center in a typical MK-200 experiment simulation with FOREV-1/FOREV-2.....	99
Figure 4.19 Calculated temperature evolution of the plasma-vapor cloud in a typical MK-200 experiment simulation with HEIGHTS-PIC at 1 $\mu\text{s}$ (step rise) .....	100
Figure 4.20 Calculated temperature evolution of the plasma-vapor cloud in a typical MK-200 experiment simulation with HEIGHTS-PIC at 3.25 $\mu\text{s}$ (step rise) .....	101
Figure 4.21 Calculated temperature evolution of the plasma-vapor cloud in a typical MK-200 experiment simulation with HEIGHTS-PIC at 7.50 $\mu\text{s}$ (step rise) .....	102
Figure 4.22 Calculated temperature evolution of the plasma-vapor cloud in a typical MK-200 experiment simulation with HEIGHTS-PIC at 25.50 $\mu\text{s}$ (step rise) .....	103
Figure 4.23 Calculated temperature evolution of the plasma-vapor cloud in a typical MK-200 experiment simulation with HEIGHTS-PIC at 46 $\mu\text{s}$ (step rise) .....	104
Figure 4.24 Calculated total pressure evolution at the target in a typical MK-200 experiment simulation with HEIGHTS-PIC (step rise) .....	105
Figure 4.25 Calculated pressure evolution at target plate in a typical MK-200 experiment simulation with HEIGHTS-PIC for different times and along the plate (5-20 $\mu\text{s}$ ).....	107
Figure 4.26 Calculated pressure evolution at target plate in a typical MK-200 experiment simulation with HEIGHTS-PIC for different times and along the plate (30-50 $\mu\text{s}$ ).....	108
Figure 4.27 Calculated total pressure evolution at the target in a typical MK-200 experiment simulation with FOREV-1/FOREV-2.....	109
Figure 4.28 Calculated plasma density evolution at the target in a typical MK-200 experiment simulation with HEIGHTS-PIC (at 1.0 $\mu\text{s}$ ).....	110
Figure 4.29 Calculated plasma density evolution at the target in a typical MK-200 experiment simulation with HEIGHTS-PIC (at 3.25 $\mu\text{s}$ ).....	110
Figure 4.30 Calculated plasma density evolution at the target in a typical MK-200 experiment simulation with HEIGHTS-PIC (at 5.25 $\mu\text{s}$ ).....	111
Figure 4.31 Calculated plasma density evolution at the target in a typical MK-200 experiment simulation with HEIGHTS-PIC (at 7.50 $\mu\text{s}$ ).....	111



Figure	Page
Figure 4.32 Calculated plasma density evolution at the target in a typical MK-200 experiment simulation with HEIGHTS-PIC (at 8.25 $\mu$ s).....	112
Figure 4.33 Calculated plasma density evolution at the target in a typical MK-200 experiment simulation with HEIGHTS-PIC (at 17.0 $\mu$ s).....	112
Figure 4.34 Calculated plasma density evolution at the target in a typical MK-200 experiment simulation with HEIGHTS-PIC (at 25.50 $\mu$ s).....	113
Figure 4.35 Calculated plasma density evolution at the target in a typical MK-200 experiment simulation with HEIGHTS-PIC (at 32.50 $\mu$ s).....	113
Figure 4.36 Calculated plasma density evolution at the target in a typical MK-200 experiment simulation with HEIGHTS-PIC (at 40.0 $\mu$ s).....	114
Figure 4.37 Calculated plasma density evolution at the target in a typical MK-200 experiment simulation with HEIGHTS-PIC (at 46.0 $\mu$ s).....	114
Figure 4.38 Calculated plasma density evolution at the target in a typical MK-200 experiment simulation with HEIGHTS-PIC (at 50.0 $\mu$ s).....	115
Figure 4.39 Calculated ELECTRON density of the plasma at the target plate in a typical MK-200 experiment simulation with HEIGHTS-PIC (5-20 $\mu$ s) .....	116
Figure 4.40 Calculated ELECTRON density of the plasma at the target plate in a typical MK-200 experiment simulation with HEIGHTS-PIC (30-50 $\mu$ s) .....	117
Figure 4.41 Calculated erosion profile evolution (10 $\mu$ s LINEAR RISE) in a typical MK-200 experiment simulation with HEIGHTS-PIC (N=155 sample particles). .....	119
Figure 4.42 Calculated erosion profile evolution (5 $\mu$ s LINEAR RISE) in a typical MK-200 experiment simulation with HEIGHTS-PIC (N=155 sample particles) .....	120
Figure 4.43 Calculated erosion profile (5 $\mu$ s rise) in a typical MK-200 experiment simulation with HEIGHTS-PIC (5 vs 155 sample particles).....	121
Figure 4.44 Calculated temperature evolution in a typical MK-200 experiment simulation with HEIGHTS-PIC (N=155 Particles/10 $\mu$ s LINEAR RISE) .....	122
Figure 4.45 Calculated power fluxes evolution at Separatrix in a typical MK-200 experiment simulation with HEIGHTS-PIC (N=155/ 5 $\mu$ s RISE).....	123

Figure	Page
Figure 4.46 Calculated power fluxes evolution at plate center in a typical MK-200 experiment simulation with HEIGHTS-PIC (N=155/ 10 $\mu$ s RISE).....	124
Figure 4.47 Calculated power fluxes along the plate at 45 $\mu$ s in a typical MK-200 experiment simulation with HEIGHTS-PIC (N=155 / 10 $\mu$ s RISE).....	125
Figure 4.48 Calculated evolution of pressure at TARGET PLATE CENTER in a typical MK-200 experiment simulation with HEIGHTS-PIC (N=155 / 5 $\mu$ s RISE).....	126
Figure 4.49 Calculated evolution of pressure at TARGET PLATE CENTER in a typical MK-200 experiment simulation with HEIGHTS-PIC (N=155 / 10 $\mu$ s RISE).....	127
Figure 4.50 HEIGHTS-PIC calculated divertor erosion in carbon plasma during a giant ELM in ITER-like conditions (GRID 10x30 N=95).....	129
Figure 4.51 HEIGHTS-PIC calculated divertor erosion in carbon plasma during a giant ELM in ITER-like conditions (GRID 10x30 N=395).....	130
Figure 4.52 HEIGHTS calculated divertor erosion in carbon plasma during a giant ELM in ITER-like conditions.....	131
Figure 4.53 HEIGHTS-PIC calculated divertor erosion time evolution in carbon plasma during a giant ELM in ITER-like conditions .....	132
Figure 4.54 HEIGHTS-PIC calculated divertor impinging energy fluxes in carbon plasma during a giant ELM in ITER-like conditions (GRID 10x30) .....	133
Figure 4.55 HEIGHTS calculated divertor impinging energy fluxes in carbon plasma during a giant ELM in ITER-like conditions .....	134
Figure 4.56 HEIGHTS-PIC calculated divertor impinging power fluxes into target during a giant ELM in ITER-like conditions .....	135
Figure 4.57 HEIGHTS-PIC calculated density in carbon plasma during a giant ELM in ITER-like conditions (at 1 $\mu$ s) .....	136
Figure 4.58 HEIGHTS-PIC calculated density in carbon plasma during a giant ELM in ITER-like conditions (at 25 $\mu$ s) .....	137
Figure 4.59 HEIGHTS-PIC calculated density in carbon plasma during a giant ELM in ITER-like conditions (at 50 $\mu$ s) .....	137

Figure	Page
Figure 4.60 HEIGHTS-PIC calculated density in carbon plasma during a giant ELM in ITER-like conditions (at 75 $\mu$ s) .....	138
Figure 4.61 HEIGHTS-PIC calculated density in carbon plasma during a giant ELM in ITER-like conditions (at 100 $\mu$ s) .....	138
Figure 4.62 Schematics of the processes involved in ns laser ablation during the first instants of the experiment with approximate timeline of events and addition of the magnetic field B.....	140
Figure 4.63 Temporal and geometrical Laser beam evolution for HEIGHTS-PIC laser experiments .....	141
Figure 4.64 Calculated carbon erosion along the plate at 40 ns and after Laser pulse ...	143
Figure 4.65 Calculated carbon erosion evolution with time during Laser pulse .....	144
Figure 4.66 Calculated carbon erosion evolutions with time during with different reflectivity values.....	146
Figure 4.67 Calculated carbon erosion evolution with time during Laser pulse .....	147
Figure 4.68 Calculated power fluxes up to 40ns.....	148
Figure 4.69 Calculated integrated energy fluxes along time .....	149
Figure 4.70 Evolution of the calculated target temperature along time at different locations .....	150
Figure 4.71 Calculated plasma temperature profiles close to the target at 40 ns and comparison with experimental data .....	151
Figure 4.72 Calculated electron density profiles close to the target at 40 ns and comparison with experimental data .....	152
Figure 5.1 Calculated carbon erosion crater at 50 $\mu$ s in a MK200-like conditions simulation using HEIGHTS-PIC for $\delta t=10^{-5}$ $\mu$ s .....	160
Figure 5.2 Calculated carbon erosion evolution of plate center in a MK200-like conditions simulation using HEIGHTS-PIC (STEP RISE/ $\delta t=10^{-5}$ $\mu$ s).....	161
Figure 5.3 Calculated carbon erosion evolution of plate center in a MK200-like conditions simulation using HEIGHTS-PIC (STEP RISE) with different $\delta t$ .....	162

Figure	Page
Figure 5.4 Calculated carbon erosion evolution of plate center in a MK200-like conditions simulation using HEIGHTS-PIC (STEP RISE/ different $\delta t$ ) .....	163
Figure 5.5 Calculated pressure evolution of plate center in a MK200-like conditions simulation using HEIGHTS-PIC (STEP RISE) with $\delta t=10^{-5}$ $\mu s$ (5-15 $\mu s$ ).....	164
Figure 5.6 Calculated pressure evolution of plate center in a MK200-like conditions simulation using HEIGHTS-PIC (STEP RISE) with $\delta t=10^{-5}$ $\mu s$ (30-50 $\mu s$ ).....	165
Figure 5.7 Calculated carbon erosion along the plate in a MK200-like conditions simulation using HEIGHTS-PIC (5 $\mu$ RISE) with different N .....	166
Figure 5.8 Calculated pressure evolution of plate center in MK200-like conditions simulations using HEIGHTS-PIC (5 $\mu$ RISE) with different N .....	167
Figure 5.9 Calculated carbon erosion along the plate in MK200-like conditions simulations using HEIGHTS-PIC (STEP RISE) with different N .....	168
Figure 5.10 Calculated pressure evolution of plate center in MK200-like conditions simulations using HEIGHTS-PIC (STEP RISE) with different N .....	169
Figure 5.11 Calculated erosion evolution of plate center in MK200-like conditions simulations using HEIGHTS-PIC (10 $\mu s$ RISE with $\delta t=10^{-5}$ $\mu s$ ) with different N.....	170
Figure 5.12 Calculated geometrical erosion evolutions along the plate in MK200-like conditions simulations using HEIGHTS-PIC (with $\delta t=10^{-6}$ $\mu s$ and 18x30 Grids) .....	172
Figure 5.13 Calculated erosion evolutions with time of plate center in MK200-like conditions simulations using HEIGHTS-PIC (with $\delta t=10^{-6}$ $\mu s$ and 18x30 Grids) .....	173
Figure 5.14 Calculated geometrical erosion evolution at plate in MK200-like conditions simulations using HEIGHTS-PIC (with $\delta t=10^{-6}$ $\mu s$ and 18x30 Grid).....	174
Figure 5.15 Calculated power fluxes along the plate in MK200-like conditions simulations using HEIGHTS-PIC (with $\delta t=10^{-6}$ $\mu s$ , 18x30 Grid at 45 $\mu s$ ).....	175
Figure 5.16 Calculated power fluxes at plate center in MK200-like conditions simulations using HEIGHTS-PIC (with $\delta t=10^{-6}$ $\mu s$ , 18x30 Grid ,6x30 Grid and 10 $\mu s$ RISE) .....	176
Figure 5.17 Calculated computational time in MK200-like conditions simulations using HEIGHTS-PIC on the CMUXE Server (different particle loadings for 6x30 Grid). .....	177

Figure	Page
Figure 5.18 Calculated computational time in MK200-like conditions simulations using HEIGHTS-PIC on the CMUXE Server (Comparisons 6x30, 12x30 and 18x30).....	179
Figure 5.19 Calculated erosions along the plate at 50 $\mu$ s in MK200-like conditions simulations using HEIGHTS-PIC for different B fields(N=155).....	181
Figure 5.20 Calculated erosions evolutions along time in MK200-like conditions simulations using HEIGHTS-PIC for different B fields (N=155).....	182
Figure 5.21 Calculated erosions along the plate at 100 $\mu$ s in ITER-like conditions ELM simulations using HEIGHTS-PIC for different B fields (N=95).....	183
Figure 5.22 Calculated erosions along time in ITER-like conditions ELM simulations using HEIGHTS-PIC for different B fields (N=95) .....	184

## ABSTRACT

Genco, Filippo. Ph.D., Purdue University, December 2013. Response of Plasma Facing Components in Tokamaks due to Intense Power Deposition using Particle-In-Cell (PIC) Methods. Major Professor: Ahmed Hassanein.

Damage to plasma-facing components (PFC) due to various plasma instabilities is still a major concern for the successful development of fusion energy and represents a significant research obstacle in the community. It is of great importance to fully understand the behavior and lifetime expectancy of PFC under both low energy cycles during normal events and highly energetic events as disruptions, Edge-Localized Modes (ELM), Vertical Displacement Events (VDE), and Run-away electron (RE). The consequences of these high energetic dumps with energy fluxes ranging from  $10 \text{ MJ/m}^2$  up to  $200 \text{ MJ/m}^2$  applied in very short periods (0.1 to 5 ms) can be catastrophic both for safety and economic reasons. Those phenomena can cause a) large temperature increase in the target material b) consequent melting, evaporation and erosion losses due to the extremely high heat fluxes c) possible structural damage and permanent degradation of the entire bulk material with probable burnout of the coolant tubes; d) plasma contamination, transport of target material into the chamber far from where it was originally picked. The modeling of off-normal events such as Disruptions and ELMs requires the simultaneous solution of three main problems along time: a) the heat transfer in the plasma facing component b) the interaction of the produced vapor from the surface

with the incoming plasma particles c) the transport of the radiation produced in the vapor-plasma cloud. In addition the moving boundaries problem has to be considered and solved at the material surface. Considering the carbon divertor as target, the moving boundaries are two since for the given conditions, carbon doesn't melt: the plasma front and the moving eroded material surface. The current solution methods for this problem use finite differences and moving coordinates system based on the Crank-Nicholson method and Alternating Directions Implicit Method (ADI). Currently Particle-In-Cell (PIC) methods are widely used for solving complex dynamics problems involving distorted plasma hydrodynamic problems and plasma physics. The PIC method solves the hydrodynamic equations solving all field equations tracking at the same time "sample particles" or pseudo-particles (representative of the much more numerous real ones) as they move under the influence of diffusion or magnetic force. The superior behavior of the PIC techniques over the more classical Lagrangian finite difference methods stands in the fact that detailed information about the particles are available at all times as well as mass and momentum transport values are constantly provided. This allows with a relative small number of particles to well describe the behavior of plasma even in presence of highly distorted flows without losing accuracy. The radiation transport equation is solved at each time step calculating for each cell the opacity and emissivity coefficients. Photon radiation continuum and line fluxes are also calculated per the entire domain and provide useful information for the entire energetic calculation of the system which in the end provides the total values of erosion and lifetime of the target material. In this thesis, a new code named HEIGHTS-PIC code has been created and modified using a new approach of the PIC technique to solve the three physics problems involved integrating

each of them as a continuum providing insight on the plasma behavior, evolution along time and physical understanding of the very complex phenomena taking place. The results produced with the models are compared with the well-known and benchmarked HEIGHTS package and also with existing experimental results especially produced in Russia at the TRINITY facility. Comparisons with LASER experiments are also discussed.



## CHAPTER 1. INTRODUCTION

### 1.1 Introduction

Interaction of fusion reactor plasmas with various surrounding materials can produce significant damage to the exposed surfaces due to the great amount of stored magnetic and thermal energies. Investigations of off-normal events due to instabilities are essential for many applications (from space studies to high energy physics) and are extremely important to establish the lifetime of the plasma-facing components (PFC) components as well as their structural behavior during such events. The effect of plasma impacting the PFC materials needs to be well studied and understood in order to mitigate the dramatic effects of melted surfaces, plasma contamination, erosion, surface damage and degradation of performance which ultimately will determine the economical and engineering feasibility of a fusion reactor [1-5]. The amount of energy deposited during major disruptions, edge localized modes (ELM), vertical displacements events (VDE), and runaway electrons (RE) cause significant material erosion with melting and vaporization of the PFC, large temperature changes in the structural material due to the high heat fluxes and ultimately the burnout of the coolant tubes. Primary concern for the safe operation of the fusion reactors is the off normal events where energies up to 200 MJ/m<sup>2</sup> can be deposited in a very short period of time (0.1-3 ms). The plasma surface interaction problem has been studied for several years. Many of the previous studies use

numerical techniques to solve complex models of the plasma surface interactions comparing modeling results with experimental results. This problem is extremely complex requiring the simultaneous solution of multiple dynamics models: the thermal heat transfer in the material with eroding/melting/vaporizing surface (moving boundaries problem); vapor-cloud magnetohydrodynamics (MHD) in the vapor cloud formed above the PFC surface and transport of the radiation created from the interactions of plasma incoming particles and the vapor particles. Several numerical techniques have been used to solve the physical process involved, with the most commonly used being the finite difference method. It's a simple approach proving fairly accurate results both for the thermal problem and the vapor cloud hydrodynamics especially if very small time steps are used. Crank Nicholson and the Alternating Direction Implicit method have been the most used for the thermal problem [6-9]. The Lagrangian finite difference methods instead have been used commonly for solving the hydrodynamic behavior of the plasma-vapor cloud.

With the increasing computational capabilities available for research purposes, more powerful and complete techniques have been developed, and new interest in old techniques like the Particle-In-Cell (PIC) method has increased especially when dealing with highly distorted hydrodynamic flows. Standard Lagrangian techniques in fact, are not very accurate in such cases since detailed mass and momentum transfer transport information are not provided with particle tracking.

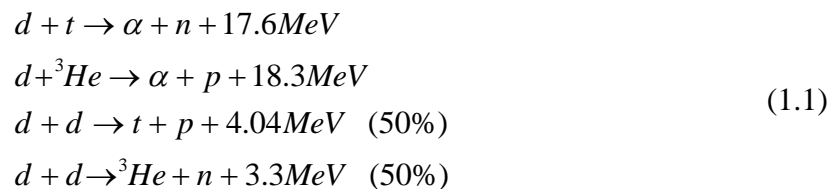
In this thesis the use of a modified and innovative PIC technique will be used in addition to the implicit methods and integrated with the solution of the radiation transport, to model the PFC components behavior during off-normal events and provide clear

snapshots on the dynamical evolution of the plasma-vapor cloud above the target material. In addition, MPI (Message passing interface) libraries are used in order to parallelize the code and provide a tool to integrate the code with future upgrades. The portability of the code (HEIGHTS-PIC) will then be insured and will make the code easy to maintain.

## 1.2 Background: Introduction to Fusion

Fusion reactions do occur very rarely in terrestrial conditions, but happen naturally in stellar media. The fusion process of two nuclei with lower masses than iron is accompanied by the release of a great amount of energy and it is possible in stars thanks to the gravitational force with overcomes the Coulomb repulsion. Achieving sustainable and controllable fusion power on Earth is a very difficult task since we do need to reproduce nature's conditions without having the gravitational force stars have. This amazing goal has been pursued for over five decades now and it is still not at hand due to the tremendous engineering challenges behind the fusion physical process.

In order to get closer to the goal of controllable fusion reaction, it important to understand which fusion reactions are more reachable in engineering terms. There are in fact, several fusion reactions in nature, but the most favorable for energetic requirements typically include deuterium, a heavy isotope of hydrogen, as fuel. They are:



For commercial fusion applications, the most interesting one is the one with the smallest cross section, which can provide energy outputs with plasma energy of 10 keV (roughly  $10^8$  K) while the others require typically temperatures of the order of 100 keV. Fusion can be achieved with two major types of confinement, inertial and magnetic. The inertial confinement scheme is based on the rocket effect principle where powerful laser beams are used to implode very small pellets of fuel in small volumes reaching very fast really high densities and really high temperatures similar to the ones required achieving fusion reactions. Magnetic confinement schemes [10-11] are based instead in containing and shaping the plasma with very powerful magnets and inputting into the system large amount of energy through several devices (resistive heating, compression heating, electromagnetic wave heating, and neutral beam injections). For several decades now, the magnetic confinement community has been focusing on Tokamaks devices. Plasma is shaped by the magnets as a toroid. Toroidal and poloidal magnetic fields associated with the stabilizing fields produced by stabilizing coils confine the plasma allowing it to be managed and heated up. A schematic of the toroidal device is presented in fig.1.1. Currently, the International Thermonuclear Experiment (ITER) is being built in France

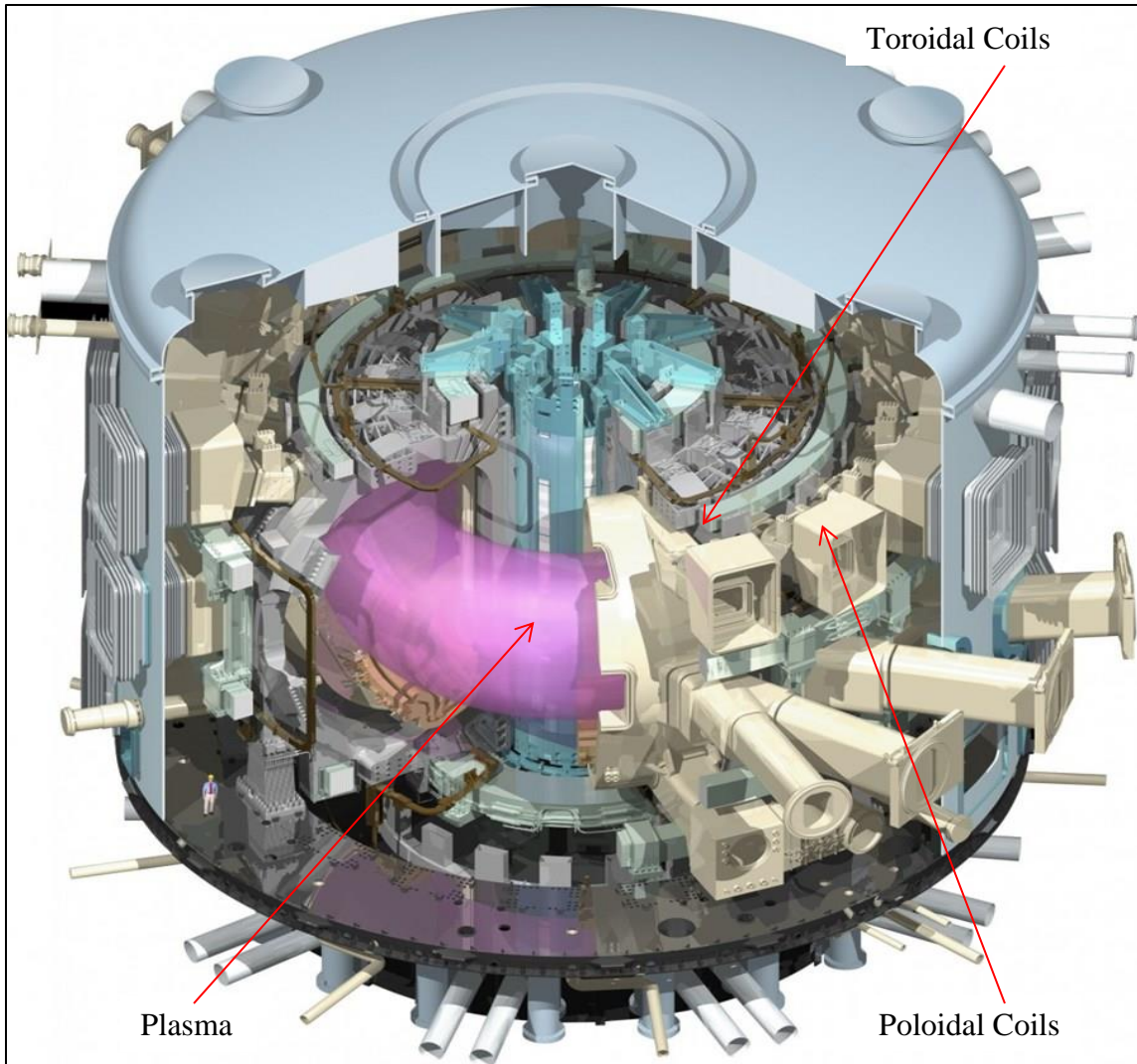


Figure 1.1 Schematics of a toroidal device and its magnets ([13], reproduced thanks to the open permission of ITER Organization)

and among its goals has to reach ignition, produce net energy and prove that commercial fusion power is possible. The task is hard since all the participants have to integrate perfectly and fully in order for the entire machine to work. ITER (fig. 1.2) will be a much larger machine than anything built before and it is a crucial step towards commercial fusion energy as well as for establishing performance characterizations of many

components. The power and energy densities that will be generated by the ITER machine once operational will be of the order of  $MJ / m^3$  in the plasma core and temperatures of the order close to 10 keV.

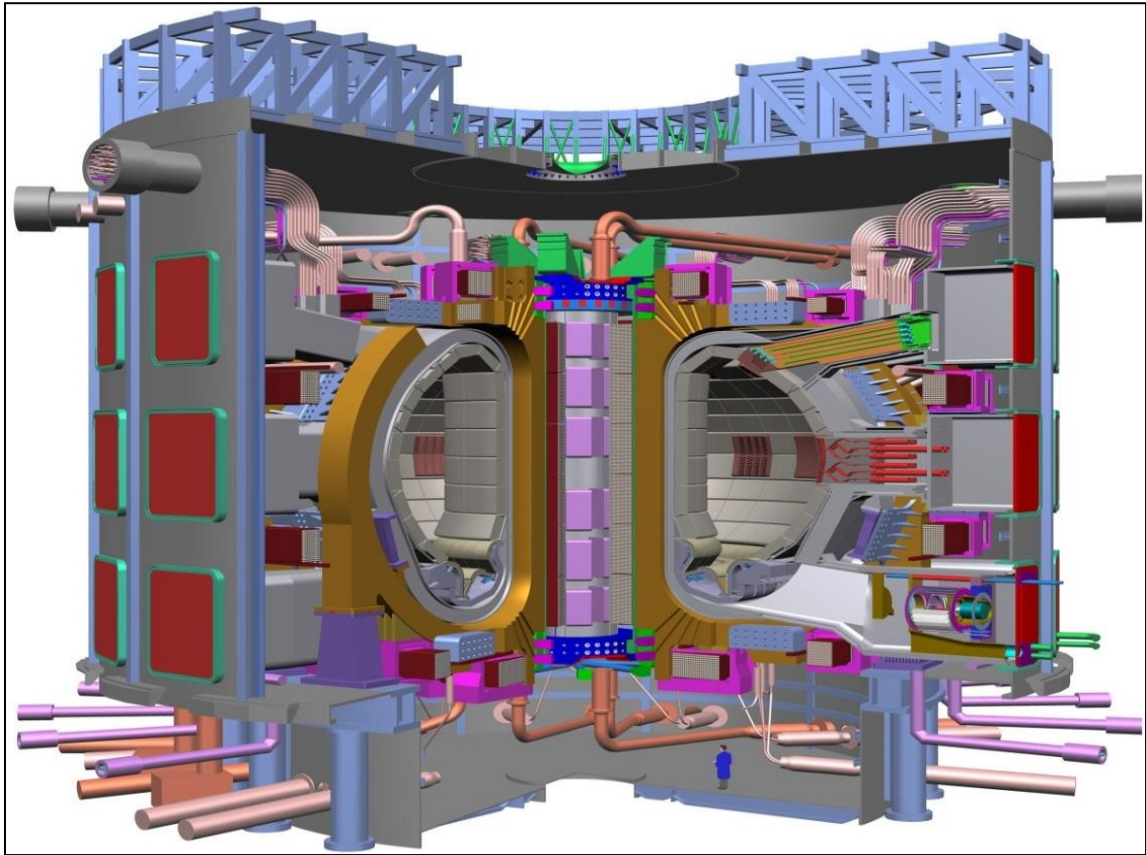


Figure 1.2 Schematics of ITER with all main components ([13], reproduced thanks to the open permission of ITER Organization)

Testing and gathering data of performance during normal and off-normal events will be critical and allow comparing models with real experimental data. Plasma facing components are expected to withstand those energies and conditions [12].

Among the PFC, particularly important is the performance and reliability of the divertor plates (figure 1.3) whose damage might be consistent during off-normal events. ITER

project is also trying to predict and develop damage mitigation strategies based on the numerical evaluation of the evolution of the plasma vapor cloud above the divertor and nearby components. Detailed description of the thermal stresses and possible damage to this key component can be found later in the plasma surface interaction presentation.

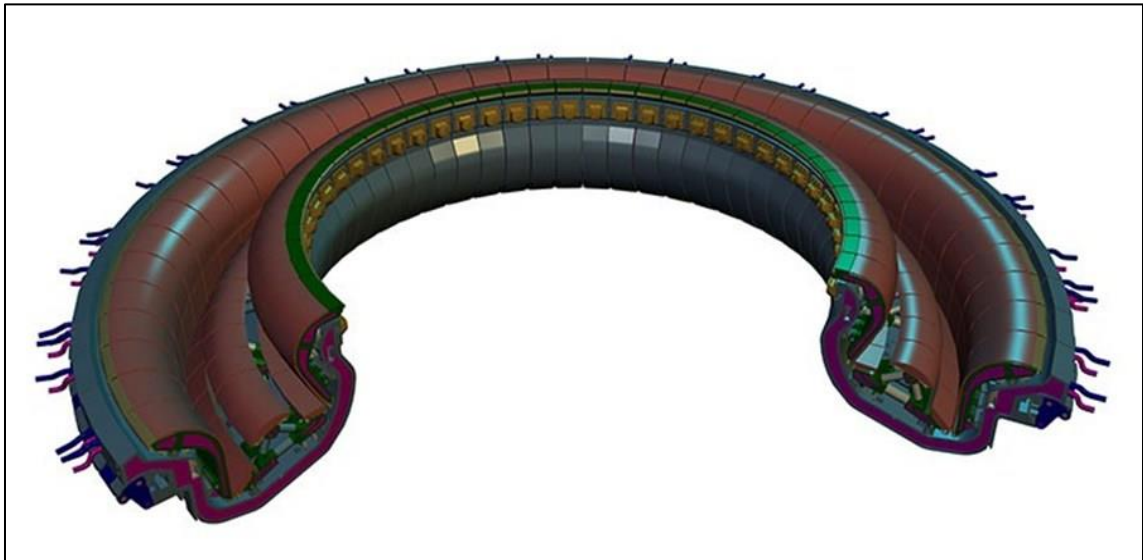


Figure 1.3 Schematics of ITER DIVERTOR ([13], reproduced thanks to the open permission of ITER Organization)

### 1.3 Previous Solutions Methods/PIC Methods

To solve the multidimensional time-varying behavior of a fluid undergoing large distortions, slippage or colliding interfaces is still today a challenge since more and more accuracy is required, faster parallel algorithms as well as capacity to enrich the model with more and more complex situations like the presence of turbulence or phase transitions. Most traditional numerical techniques can be classified as belonging to two main groups: Eulerian or Lagrangian. Both have advantages and disadvantages that are mostly related to the specific application to be implemented.

Eulerian techniques have a fixed coordinates system and are considered quite robust in handling fluid distortions. Unfortunately suffer from numerical diffusion of any discontinuity traveling with the fluid itself. The mesh of cells remains fixed relative the observer while the fluid moves through the mesh with time. Each cell is forced to be homogeneous or considered to be uniform in characteristics: density, pressure, velocity and type of material do not change in the cell. On the contrary, Lagrangian techniques have a coordinate system that follows the fluid in its evolution, permitting very sharp numerical resolution of material interfaces. They have though a weak behavior when dealing with large fluid distortions [14-17] loosing accuracy and suffering from mesh tangling. The values of time dependent values of energy, pressure, and density are defined at the cells centers.

Numerous hybrids have been proposed with time and have been invented to mitigate some of disadvantages of these more traditional techniques. One of these techniques is the Particle-in-Cell method (PIC) developed in 1955 in Los Alamos, specifically thought to address some of these problems and combining a Eulerian mesh of computational cells with a Lagrangian mesh of marker particles. In his original form [14] the PIC method was characterized by: a) Lagrangian marker particles with mass at points; b) Eulerian cells with momentum and energy at cell centers; c) velocity weighting for particle motion ; d) calculation cycle split into phases and e) explicit formulation valid generally for Mach number bigger than 0.3. Sometimes the same technique is referred by plasma physicists as particle-in-cloud method because the size of the model particle is roughly the one of a cell and being many particles in a cell, they look collectively as a cloud in shape. Numerous calculations with the original PIC formulation explored shock interactions



with material interfaces and eventual deformations. Harlow describes the basics of the Particle-in-cell method in several papers and reports [14,16-17, 23-26]. The method is the attempt to combine the best features of both traditional techniques since none of the two is ideal when used separately. Since the initial developments, significant work has been done to improve the method and adapt it to solve plasma related problems [18-22]. This will be presented and discussed later. Even if the combination of the two methods seems a bit complicated, the actual implementation is quite simple. As always in fluid dynamics problems, the region is subdivided into a finite mesh of small zones or cells. The partial equations of motion are then transformed into suitable finite difference for approximating the values. Assuming as in Fig. 1.4 a sample PIC grid with two materials in two space dimensions, the density of the cell is first determined by summing up all the particles in the cell and then knowing the total mass dividing it by the volume of the cell. Each of the two materials has an equation of state, which relates pressure as a function of density and specific internal energy. The box in the example is subdivided into a number of rectangular cells to which the finite difference equations have to be referenced. Each single fluid is represented by “particles” whose individual mass remains the same and are in discrete quantities. Each of the particles is a “sample” particle and represents many more real ones. Some cells might be empty while other filled with both types of materials or only one. The quantities calculated (velocities, pressures, densities and so on) are kept in the memory of the computing machine and are averages of the quantities thought the volume of fluids contained in the cells. Typically the calculation is performed in cycles in which each cycle advances all variables of cell quantities and particle positions to new values slightly different from the preceding cycle, representing a slightly later time. This

time is in cycles can be thought as successive frames of a motion picture. Harlow divided the cycles into three phases [14, 17, 23], described as follows.

Phase 1: new pressures for all cells are calculated from the values of mass, volume and specific internal energy. Tentative values of the velocities are calculated from the gradients of the pressures. These values with the velocities of the preceding cycle and or

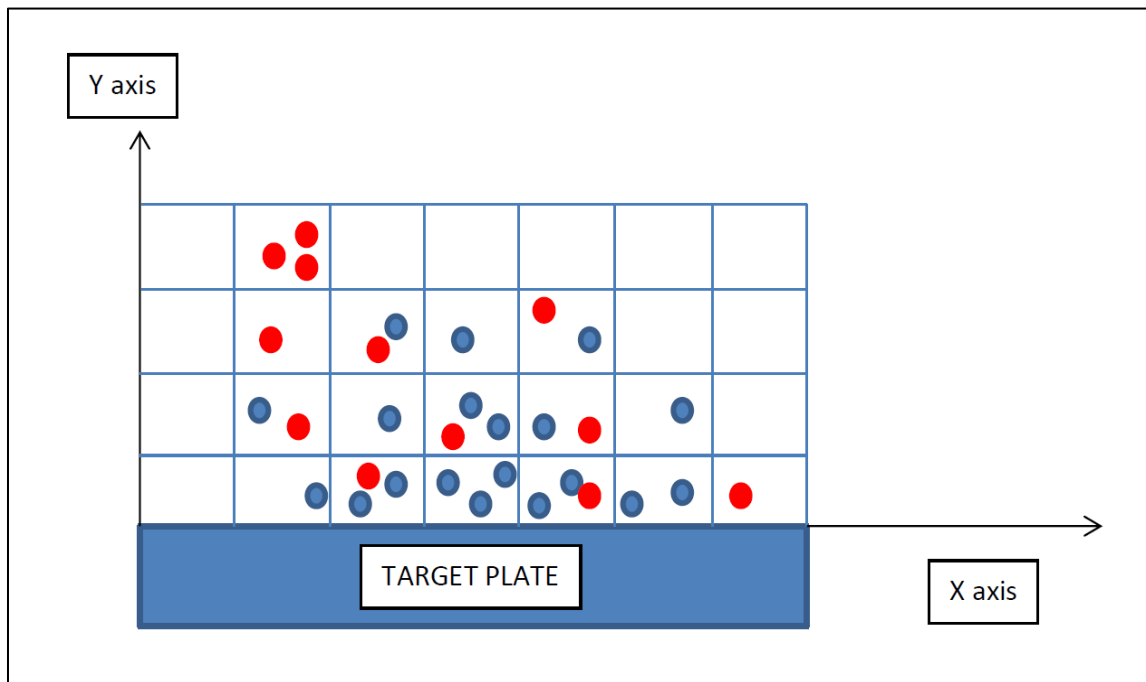


Figure 1.4 Schematics of the configuration of particles in a coarse mesh of cells similar to one proposed by Harlow with two different fluids [14]

from initial conditions, allow the calculation of tentative new values for the specific internal energy for all cells. These values are tentative because the transport term is omitted in this part of the calculation and will be corrected in the following phase. The

finite difference approximation of the fluid differential equations can be written in a two dimensional space as Harlow suggests:

$$\begin{aligned}
\frac{\partial \rho}{\partial t} + u \frac{\partial \rho}{\partial x} + v \frac{\partial \rho}{\partial y} + \rho \left( \frac{\partial u}{\partial x} + \frac{\partial v}{\partial y} \right) &= 0 \\
\rho \frac{\partial u}{\partial t} + \rho u \frac{\partial u}{\partial x} + \rho v \frac{\partial u}{\partial y} + \left( \frac{\partial P}{\partial x} \right) &= 0 \\
\rho \frac{\partial v}{\partial t} + \rho u \frac{\partial v}{\partial x} + \rho v \frac{\partial v}{\partial y} + \left( \frac{\partial P}{\partial y} \right) &= 0 \\
\rho \frac{\partial E_{INT}}{\partial t} + \rho u \frac{\partial E_{INT}}{\partial x} + \rho v \frac{\partial E_{INT}}{\partial y} + P \left( \frac{\partial u}{\partial x} + \frac{\partial v}{\partial y} \right) &= 0
\end{aligned} \tag{1.2}$$

In Harlow's original model explanation, no heat conduction or any other form of energy was taken into account to describe the fluid motion. The first of these equations (mass conservation) is automatically satisfied by the particle model. The momentum equations in this phase are treated using only the contributions to the time derivatives that arise from the terms involving pressure. The transport terms are dropped since no particle motion is considered at this stage. In finite difference form the equations modify according to:

$$\begin{aligned}
\rho_{i,j} \left( \frac{\partial u}{\partial t} \right) &= -\frac{1}{\delta x} \left[ P_{i+1/2,j} - P_{i-1/2,j} \right] \\
\rho_{i,j} \left( \frac{\partial v}{\partial t} \right) &= -\frac{1}{\delta y} \left[ P_{i,j+1/2} - P_{i,j-1/2} \right]
\end{aligned} \tag{1.3}$$

which means that pressures are averaged from adjacent cells. Considering  $P = p + q$

where  $q$  is the artificial viscosity, the energy equation can be treated as follows:

$$\rho \left( \frac{\partial E_{INT}}{\partial t} \right) + P \left( \frac{\partial u}{\partial x} + \frac{\partial v}{\partial y} \right) + \frac{\partial q u}{\partial x} + \frac{\partial q v}{\partial y} - u \frac{\partial q}{\partial x} - v \frac{\partial q}{\partial y} = 0 \tag{1.4}$$

which becomes in finite difference form equal to:

$$\begin{aligned}
\rho_{i,j} \left( \frac{\partial E_{INT}}{\partial t} \right) = & -p_{i,j} \left( \frac{u_{i+1/2,j} - u_{i-1/2,j}}{\delta x} + \frac{v_{i,j+1/2} - v_{i,j-1/2}}{\delta y} \right) - \frac{qu_{i+1/2,j} - qu_{i-1/2,j}}{\delta x} + \\
& - \frac{qv_{i,j+1/2} - qv_{i,j-1/2}}{\delta y} + u_{i,j} \left( \frac{q_{i+1/2,j} - q_{i-1/2,j}}{\delta x} \right) + v_{i,j} \left( \frac{q_{i,j+1/2} - q_{i,j-1/2}}{\delta y} \right)
\end{aligned} \tag{1.5}$$

Cell boundary velocities are in this case averaged from adjacent cells. Harlow explains that the main motivation in distinguishing between p and q when calculating the total pressures for each cell, stands in the fact that p is cell-centered quantity while q is a cell-boundary one. This dichotomy will be particularly important later once the properties of the cell have to be “distributed” according to a prescribed law. The tentative new velocities can be then evaluated using the lowest order term of Taylor expansion:

$$\begin{aligned}
\tilde{u}_{i,j} &= u_{i,j} + \delta t \left( \frac{\partial u_{i,j}}{\partial t} \right) + \dots \quad or \\
\tilde{u}_{i,j} &= u_{i,j} + \frac{\delta y \delta t}{M_{i,j}} \left[ P_{i+1/2,j} - P_{i-1/2,j} \right] \\
\tilde{v}_{i,j} &= v_{i,j} + \delta t \left( \frac{\partial v_{i,j}}{\partial t} \right) + \dots \quad or \\
\tilde{v}_{i,j} &= v_{i,j} + \frac{\delta x \delta t}{M_{i,j}} \left[ P_{i,j+1/2} - P_{i,j-1/2} \right]
\end{aligned} \tag{1.6}$$

A similar treatment of the energy equation cannot be done due to the fact that the Taylor expansion for the energy equation leaves out important parts which might lead to a non-respect of the energy conservation. Also, typically internal energy is not defined for a mixed cell (or cell where more than one constituent is present), so that this very important case needs to be treated separately with some adjustments. To proceed in the calculation, it can be written:

$$\rho \left( \frac{\partial E_{INT}}{\partial t} \right) \rightarrow \frac{1}{\partial x \partial y} \left( \frac{\partial Q_{i,j}}{\partial t} \right) \quad (1.7)$$

where  $Q_{i,j}$  is the total internal energy of the reference cell. The adjustments needed to divide into separate changes the internal energy are done at a later stage of the calculation.

Calculating the new velocities as:

$$\begin{aligned} \bar{u} &\equiv \frac{1}{2}(u + \tilde{u}) \\ \bar{v} &\equiv \frac{1}{2}(v + \tilde{v}) \end{aligned} \quad (1.8)$$

the proper form of the total internal can be then also calculated as:

$$\begin{aligned} \left( \frac{\partial Q_{i,j}}{\partial t} \right) &= -p_{i,j} \left[ \left( \bar{u}_{i+1/2,j} - \bar{u}_{i-1/2,j} \right) \delta y + \left( \bar{v}_{i,j+1/2} - \bar{v}_{i,j-1/2} \right) \delta x \right] \\ &\quad - \delta y \left[ q\bar{u}_{i+1/2,j} - q\bar{u}_{i-1/2,j} - \bar{u}_{i,j} \left( q_{i+1/2,j} - q_{i-1/2,j} \right) \right] \\ &\quad - \delta x \left[ q\bar{v}_{i,j+1/2} - q\bar{v}_{i,j-1/2} - \bar{v}_{i,j} \left( q_{i,j+1/2} - q_{i,j-1/2} \right) \right] \end{aligned} \quad (1.9)$$

So that the total energy in a cell is calculated with:

$$E_{i,j} = Q_{i,j} + \frac{1}{2} M_{i,j} \left[ (u_{i,j})^2 + (v_{i,j})^2 \right] \quad (1.10)$$

the proper form of the total internal can be then also calculated as:

With this equation it is possible to evaluate the change in energy along the entire mesh reducing it to just the boundary fluxes since all internal contributions cancel in pairs. Common boundary conditions are generally calculated into the third phase. From the values of  $\delta Q_{i,j}$  the values of  $E_{INT,i,j}$  for the two species of material under consideration can be determined. For unmixed cell, it can be written:

$$\tilde{E}_{INT\ i,j} = E_{INT\ i,j} + \frac{\delta Q_{i,j}}{M_{i,j}} \quad (1.11)$$

Phase 2 or transport of the material: Each particle is moved according to the scheme involving the tentative new cell velocities and carries its mass, momentum and energy with it. Only after the transport is complete, it is possible to evaluate the final values of specific internal energy and velocity using the new totals of mass, momentum and energy. Generally this phase is subdivided in other 4 steps or sub-phases. The results found into phase 1 are transformed into momenta and energies (step 1):

$$\begin{aligned}
 \tilde{X} &= (M_0 + M_x) \bullet \tilde{u} \\
 \tilde{E}_0 &= M_0 \left[ \tilde{E}_{0\ INT} + \frac{1}{2}(\tilde{u}^2 + \tilde{v}^2) \right] \\
 \tilde{Y} &= (M_0 + M_x) \bullet \tilde{v} \\
 \tilde{E}_x &= M_x \left[ \tilde{E}_{x\ INT} + \frac{1}{2}(\tilde{u}^2 + \tilde{v}^2) \right]
 \end{aligned} \tag{1.12}$$

In step 2, the particles are moved and the coordinates of each particle change according to:

$$\begin{aligned}
 x' &= x + u_{EFF} \delta t \\
 y' &= y + v_{EFF} \delta t
 \end{aligned} \tag{1.13}$$

where the values of the effective velocities can be set to  $\tilde{u}$  or  $\tilde{v}$  as found earlier or applying a velocity weighting process to be more precise and accurate. In this process the effective velocities  $u$  and  $v$  are linearly interpolated from  $\tilde{u}$  and  $\tilde{v}$  of the four neighboring cells (for a 2D approximation) that are overlapped when an artificial cell is drawn centered on the particle itself (Fig. 1.5)

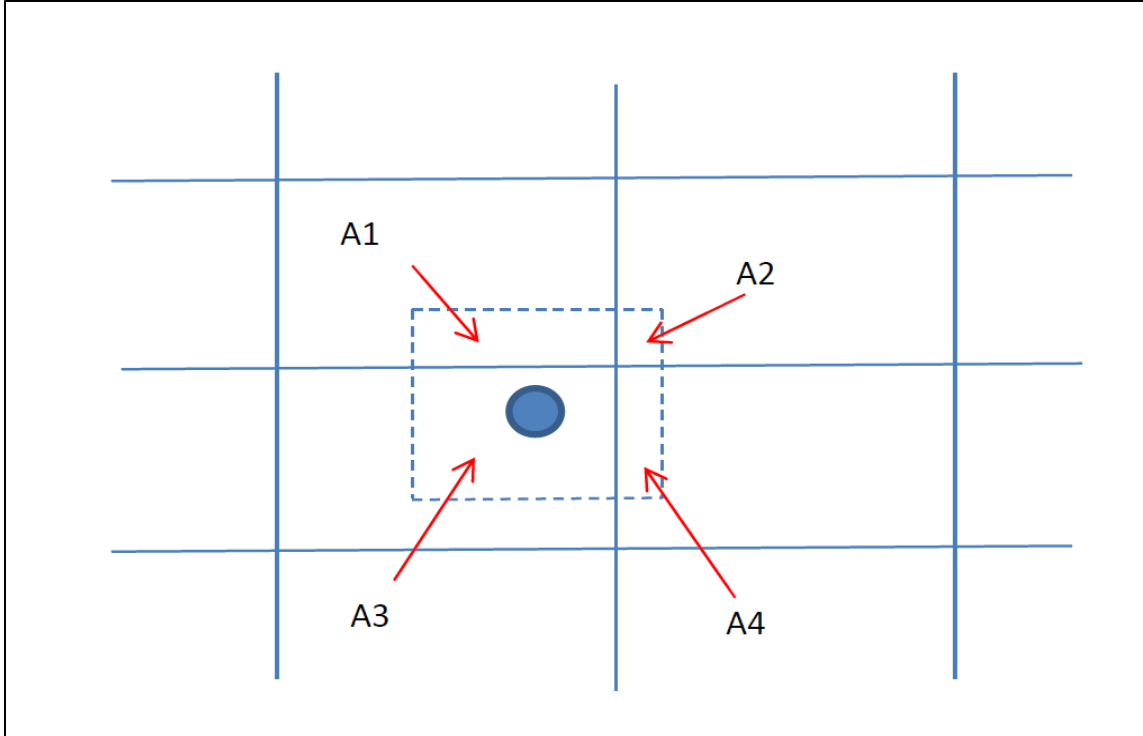


Figure 1.5 Configuration of artificial grid placed around each sample particle

The coefficients for the interpolation come from the ratio of the overlapped cell and the artificial original cell, so that an area weighting process is followed:

$$u_{EFF} = \frac{\sum_1^4 (A_i \tilde{u}_i)}{\sum_1^4 A_i} \quad v_{EFF} = \frac{\sum_1^4 (A_i \tilde{v}_i)}{\sum_1^4 A_i} \quad (1.14)$$

After the particle is moved, it may be found lying still in the same cell from which its motion started. In this case no modification is needed to any of the cell quantities (recall no heat conduction and no external energy source). If instead the particle under study is moved to a new cell, new values have to be calculated and the mass fraction, momentum and energy subtracted from the original cell and added to the new one:

$$\begin{aligned}
\delta M &= m \quad ; \quad \delta \tilde{X} = m \tilde{u}_{i,j} \\
\delta \tilde{Y} &= m \tilde{v}_{i,j} \quad ; \quad \delta \tilde{E} = \frac{m}{M} \tilde{E}
\end{aligned}
\tag{1.15}$$

As step 2 ends, the values of mass momentum and energy sum up to their final values for the cycle. Proceeding to step 3 of this phase, once all particles in the system have been moved, the final velocities for the cycle can be calculated according to Harlow as:

$$u' = \frac{X'}{M'_0 + M'_X} \quad v' = \frac{Y'}{M'_0 + M'_X}
\tag{1.16}$$

with clear meaning of the values of M for the new masses for the cell. In the last step for this phase (step 4), the final specific internal energies for the cycles are computed subtracting the final kinetic energies from the final total ones:

$$\begin{aligned}
E'_{INT\ 0} &= \frac{E'_0}{M'_0} - \frac{1}{2} [(u')^2 + (v')^2] \\
E'_{INT\ X} &= \frac{E'_X}{M'_X} - \frac{1}{2} [(u')^2 + (v')^2]
\end{aligned}
\tag{1.17}$$

Phase 3: In this phase which concludes the calculation for the given time step, the values of total mass and energy of the system are checked using the conservation. Then finally the time step is incremented of the value of dt. In this phase very useful auxiliary calculations need to be performed as comparing the changes calculated with the changes calculated by boundary fluxes. Even though some round-off can be introduced by the significant figures used, the total energy and momentum should still be conserved.

A specific section should be dedicated to the boundary conditions as described by Harlow. First of all the conservative properties of the equations should be addressed and defined. While no problem arises from the conservation of mass as the particle model



insures rigorous conservation, a closer look should be given to the conservation of momentum. Using the finite difference form presented earlier, it can be written:

$$\begin{aligned} M_{i,j}(\tilde{u}_{i,j} - u_{i,j}) &= -\delta y \delta t (P_{i+\frac{1}{2},j} - P_{i-\frac{1}{2},j}) \\ M_{i,j}(\tilde{v}_{i,j} - v_{i,j}) &= -\delta x \delta t (P_{i,j+\frac{1}{2}} - P_{i,j-\frac{1}{2}}) \end{aligned} \quad (1.18)$$

These equations represent phase 1 change in momentum of a cell. Changes occurring in phase 2 are clearly and automatically conservative and need no further consideration while for phase 1 summing up along all the mesh we are left with only the values at the boundary or the surface. In fact the internal values cancel each other in pair. Pressure also needs at the boundary between an empty cell and a cell with material. To show the consistency of the method also with the energy equation, some more calculations are needed. Adding the change in kinetic energy resulting from the momentum equations to the change of internal energy from the energy equation, the terms similarly to the pressure cancel in pairs along the entire system. Across the boundary the remaining flux of energy is given then by:

$$Flux_{i+\frac{1}{2},j} = \frac{1}{2} (P_{i+1,j} \bar{u}_{i,j} - P_{i,j} \bar{u}_{i+1}) + (q\bar{u})_{i+\frac{1}{2},j} \quad (1.19)$$

According to the type of situation (rigid wall, external applied pressure) conditions might change. The material equation of state is specified quite independently from the rest of the procedure.

This original model explained and presented by Harlow and his colleagues in several papers [14-17, 23-26], has been with time modified and applied to several other fields. The first plasma related PIC simulations have been probably made by Buneman and Dawson [18-19, 27] who simulated the motion of a small number of particles (50 to 1000)

including the possible interactions among them. The main reason for using the PIC technique in plasma science stands in the fact that the number of assumptions to be done in physical model is generally reduced to a minimum allowing high-dimensional simulations and plasma-surface interactions. The technique simulates the motion of plasma particles calculating all macro quantities (like density, energy, pressure as for the pure fluid case) from the position and velocity the particles possess. The particles are “simulation particles” and all equations of motion solved are evaluated for the N particles of the system. It has to be noticed that the velocity of a classical fluid is a single-valued function of position and in PIC considered a cell quantity. By contrast, in collisionless plasma there is more correctly a “distribution” of particle velocities and so a slightly different approach is necessary to get correct physical results. Since velocity can be interpreted as a sample particle quantity, so are electric charge, mass and position. The cell quantities are then the electromagnetic fields and the summed particle densities and currents from which they are computed. In simulating collisionless plasmas [20] it is important to evaluate the Debye length ( $\lambda_D \propto \left(\frac{\text{temperature}}{\text{density}}\right)^{1/2}$ ) and recall that our interest is in the collective behavior of the plasma at wavelength longer than the Debye length ( $\lambda > \lambda_D$ ). Considering the contribution of the electric field E at a generic point p of the space, this value will be given by the sum of a local field ( $E_1$ ) and the average field of the apparent continuum of charges outside the Debye sphere ( $E_2$ ) so that the total electric field is  $E = E_1 + E_2$ . In gas-like assembly, if the total number of charged particles into the Debye sphere is large, the local field may be considered equal to zero. So to describe the plasma model with sufficient completeness, we need also that the mesh step

$\Delta$  must be smaller than the Debye length (this would provide reasonable values for the average field). In order for the system to be stable and avoid excessive fluctuations, the typical number of particles in a cell must be large:  $n\Delta^3 \gg 1$ . An assembly of  $N$  particles is then described by the positions and velocities of each particle:

$$\begin{aligned}\frac{d\vec{X}_i}{dt} &= \vec{V}_i \\ \frac{d\vec{V}_i}{dt} &= \vec{F}_i(t, \vec{X}_i, \vec{V}_i, \mathcal{Q})\end{aligned}\tag{1.20}$$

where the force  $F_i$  for  $i = 1, \dots, N$  is the general force acting upon the generic super particle  $i$ , while  $X_i$  and  $V_i$  are the multidimensional coordinate and velocity.  $\mathcal{Q}$  is function of the field quantities associated with the particles. Using Lorentz's force for the force equation we can write the Maxwell's equations as follows:

$$\begin{aligned}\frac{d\vec{X}_i}{dt} &= \vec{V}_i \\ \frac{d\vec{V}_i}{dt} &= \frac{e_i}{m_i} (\vec{E}(\vec{X}_i) + \vec{V}_i \times \vec{B}(\vec{X}_i))\end{aligned}\tag{1.21}$$

and for  $i = 1, \dots, N$  write:

$$\begin{aligned}\nabla \vec{D} &= \rho(\vec{r}, t) & \frac{\partial \vec{B}}{\partial t} &= -\nabla \times \vec{E} & \vec{D} &= \epsilon \vec{E} \\ \nabla \vec{B} &= 0 & \frac{\partial \vec{D}}{\partial t} &= -\nabla \times \vec{H} - \vec{J}(\vec{r}, t) & \vec{B} &= \mu \vec{H}\end{aligned}\tag{1.22}$$

These equations associated with the general formulation describing the charge and current density

$$\begin{aligned}\rho &= \rho(X_1, V_1, \dots, X_N, V_N) \\ \vec{J} &= \vec{J}(X_1, V_1, \dots, X_N, V_N)\end{aligned}\tag{1.23}$$

provide a full set of equations to be solved into the PIC code;  $\varepsilon$  and  $\mu$  are the permittivity and permeability of the medium. If the system has electromagnetic forces as in tokamaks environments, then the Maxwell's equations set needs to be solved, otherwise if only the electrostatic force is present, the Poisson's equation is invoked to provide the particle-field description (the potential is then used to find the electric field):

$$\begin{aligned} \frac{d\vec{V}_i}{dt} &= \frac{e_i}{m_i} \frac{\partial \Phi}{\partial X_i} \\ \Phi(X_i) &= \sum_i \Phi_i \\ \nabla^2 \Phi &= -4\pi\rho \end{aligned} \tag{1.24}$$

In order to solve the Poisson's equation, the most appropriate integration scheme for the equations of motion of the particles is the leapfrog scheme: alternate time levels (n, n-1 or n+1) are used to produce the positions of the particles (n) or the velocity associated (n-1). So the solution of the electric field across the general cell (i,j) occupied by the general particle becomes:

$$\begin{aligned} E_{X\ i,j}^{n-1} &= -(\Phi_{i+1,j}^{n-1} - \Phi_{i-1,j}^{n-1})/2\Delta_{MESH\ STEP} \\ E_{Y\ i,j}^{n-1} &= -(\Phi_{i,j+1}^{n-1} - \Phi_{i,j-1}^{n-1})/2\Delta_{MESH\ STEP} \end{aligned} \tag{1.25}$$

These values of the electric field are used to update the coordinates of the general particle:

$$\begin{aligned} V_M^n &= V_M^{n-2} + \frac{e_M}{M} 2\Delta t E_{i,j}^{n-1} \\ X_M^{n+1} &= X_M^{n-1} + V_M^n 2\Delta t \end{aligned} \tag{1.26}$$

where  $\Delta t$  is the time step. It is important to notice that as new coordinates are determined, a new charge density (at n+1 time step) is defined on the space mesh by the updated distribution of particles. This is a key point since there are several methodologies to “distribute” the particle's charge and the method chosen influence greatly the accuracy

and stability of the final results. In fact in general all macro quantities associated with particles (n, J...) need “particle weighting”. The plasma parameters are known at grid points while we need to associate them with the particles present inside the cells through the choice of the shape function S(x). This function needs to satisfy several conditions. Charge conservation and space isotropy are typically the first two conditions to be respected:

$$\begin{aligned} \sum_i S(\bar{x}_i - \bar{X}) &= 1 \\ S(x) &= S(-x) \end{aligned} \quad (1.27)$$

Both conditions are very important and are necessary. The following conditions instead are generally dictated by the increasing level of desired accuracy of the weighting scheme. Using the Green function for a simple 1D case as suggested by Tskhakaya [28], let's for example evaluate the potential generated at the point x by a unit charge located at the point X:

$$\Phi(x) = e \sum_{i=1}^{N_{points}} S(x_i - X) G(x - x_i) \quad (1.28)$$

Expanding the Green function close to the neighborhood of X point (=x - X) we get:

$$\begin{aligned} \Phi(x) &= e \sum_{i=1}^{N_{points}} S(x_i - X) G(x - x_i) + \sum_{i=1}^{N_{points}} S(x_i - X) \sum_{n=1}^{\infty} \frac{(X - x_i)^n}{n!} \frac{d^n G(x - X)}{dx^n} = \\ &= eG(x - X) + \delta\phi(x) \end{aligned} \quad (1.29)$$

The value of  $\delta\Phi$  is unphysical and introduced by the weighting process. This term needs to be the smallest possible to reduce the error creating the condition of:

$$\sum_{i=1}^{N_{points}} S(x_i - X) (x - x_i)^n = 0 \quad (1.30)$$

The shape functions can be constructed mathematically directly from those conditions and be very different from each other. The simplest shape function that can be used is the nearest grid point (NGP) with  $N_{\text{points}}=1$  which satisfies well the first two conditions. This weighting is called zero order and it is easy to implement but also computationally noisy. Much more important is the first order (Fig. 1.6) weighting scheme which assigns density to the two nearest grid points ( $N_{\text{points}} = 2$ ) and is often called Cloud-in-Cell (CIC) scheme [21-22,28-29].

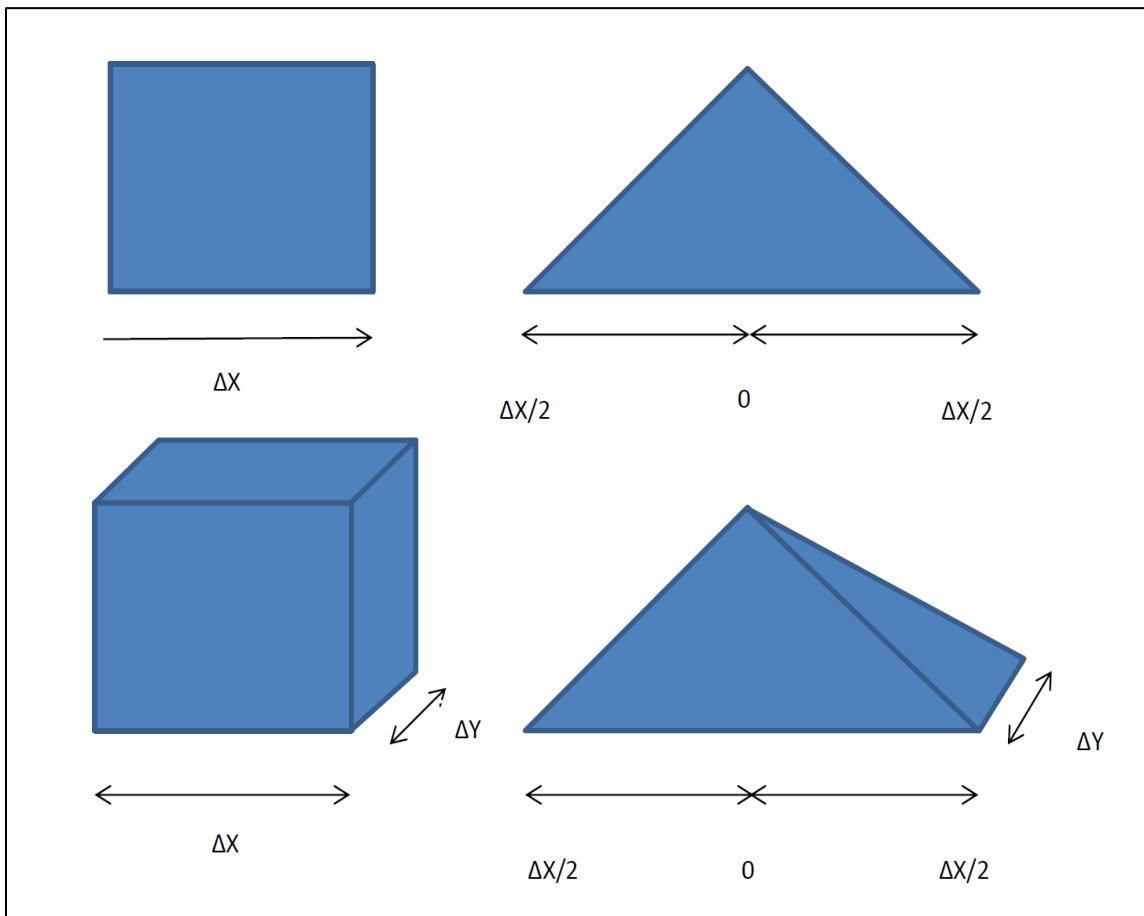


Figure 1.6 Particle shapes for the NGP (left) and linear (right) weighting in 1D (a) and 2D (b) cases similar to [28]

It is much more accurate than the NGP and very commonly used nowadays. Clearly higher order schemes can be used extensively but they also require much higher computational time to increase the accuracy of the simulation.

Once the weighting scheme has been decided, the system can proceed into the field weighting which is very important to establish the macro quantities at the particle level instead of the grid level. In fact the solution of the Maxwell's equation for example, produces the values of the fields at the grid points and needs to be transported at the particles into the cells:

$$\vec{E}(\vec{x}) = \sum_{i=1}^{N_{points}} \vec{E}_i S(x_i - x) \quad (1.31)$$

Similarly for the momentum equation, it can be written:

$$\begin{aligned} \frac{d\vec{P}}{dt} = \vec{F} &= \sum_{i=1}^N e_p \left( \vec{E}(\vec{x}_p) + \vec{V}_p \times \vec{B}(\vec{x}_p) \right) \\ &= \sum_{i=1}^N e_p \sum_i \vec{E}_i S(x_i - x_p) + e_p \vec{V}_p \times \sum_i \vec{B}_i S(x_i - x_p) \end{aligned} \quad (1.32)$$

with the subscript p stands for particle P. Also it is important to notice that this momentum-conserving scheme, not necessarily preserves energy.

Most of Birdsall research papers [20-22] deal with plasma charged-particle simulations using electromagnetic field solutions. The particles are placed on grid as in the original Harlow's work, and through the weighting process they allow to evaluate the macro quantities for the cells as seen above. These plasma particle simulations are useful in solving non-collisional plasmas. In tokamaks though where the plasma vapor cloud developed after the disruption develops as highly collisional, Birdsall's technique cannot solve adequately the problem. In fact the momentum and energy of such gas like plasma

particles are not retained and more correctly shared with the surrounding particles. Expressed in terms of statistical mechanics, the molecule of plasma gas within some very small region establish a sort of thermal equilibrium over a very short time scale and can be represented in velocity space with for example a Boltzmann Maxwell type of distribution. Using this fundamental idea, already used for the description of motion of galaxies, a more hydrodynamic fluid behavior of the PIC technique can be used as approach.

Motion of particles must be linked with the time dependent equations of a continuous fluid in order to develop the collision dominated particle-in-cell model. The fundamental equations then are for conservation of mass and momentum:

$$\begin{aligned}\frac{\partial \rho}{\partial t} + \nabla \cdot (\rho \vec{V}) &= 0 \\ \frac{\partial \rho \vec{V}}{\partial t} + \nabla \cdot (\rho \vec{V} \vec{V}) &= -\nabla p\end{aligned}\tag{1.33}$$

with  $p$  the pressure of the fluid. Density, velocity and pressure are fluid variables defined over the generic point  $(\vec{x}, t)$  in space and time. Using the expression:

$$\frac{d}{dt} = \frac{\partial}{\partial t} + \vec{V} \cdot \nabla\tag{1.34}$$

It is possible to write in Lagrangian form the momentum equation:

$$\frac{\partial \rho}{\partial t} \vec{V} + \rho \frac{\partial \vec{V}}{\partial t} + (\nabla \cdot \rho \vec{V}) \vec{V} + \nabla \cdot (\rho \vec{V} \cdot \nabla) \vec{V} = -\nabla p\tag{1.35}$$

and canceling the first and third terms using the conservation of mass, with the time derivative we can rewrite:

$$\rho \frac{d\vec{V}}{dt} = -\nabla p\tag{1.36}$$



The local acceleration of the fluid is then due only to the change in pressure of the fluid itself. In the end, to close the set of equations, there is need for the state equations which for an ideal polytropic fluid becomes:

$$\frac{P}{\rho^\gamma} = const \quad (1.37)$$

with  $\gamma$  ration of the specific heats. In Lagrangian form this becomes:

$$\frac{d}{dt} \left( \frac{P}{\rho^\gamma} \right) = 0 \quad (1.38)$$

and is valid only for ideal gases with no production of entropy. All these equations are particularly simple to apply especially because simulations particles due to the molecular motion will transport mass, momentum and energy. Using  $n$  as number density of particles at any point of the grid, the equations for an ideal gas type can be rewritten as:

$$\begin{aligned} \frac{\partial(nm)}{\partial t} + \nabla \cdot (nm\vec{V}) &= 0 \\ \frac{\partial(nm\vec{V})}{\partial t} + \nabla \cdot (nm\vec{V}\vec{V}) &= -\nabla p \\ \frac{\partial}{\partial t} \left( n \frac{P}{\rho^\gamma} \right) + \nabla \cdot \left( n \frac{P}{\rho^\gamma} \vec{V} \right) &= 0 \end{aligned} \quad (1.39)$$

At each time step  $(t)^n$  at least six variables will be associated with each particle:

$$P_{particle} = f(x^n, y^n, m, mv_x^n, mv_y^n, e^n) \quad (1.40)$$

As seen before, the Eulerian part of the calculation can be carried out calculating the effect of the pressure gradient in the acceleration equation to determine temporary (before Lagrangian motion) values of the velocities associated with the cells. So it is possible to write:

$$\begin{aligned}
\tilde{v}_X^{n+1}{}_{i,j} &= v_X^n{}_{i,j} + \frac{\Delta t}{2\Delta\rho_{i,j}^n} [p_{i+1,j} - p_{i-1,j}] \\
\tilde{v}_Y^{n+1}{}_{i,j} &= v_Y^n{}_{i,j} + \frac{\Delta t}{2\Delta\rho_{i,j}^n} [p_{i,j+1} - p_{i,j-1}]
\end{aligned} \tag{1.41}$$

In calculating these values, it is important to make sure that the Courant-Friedrichs-Lewy condition [60] typically imposed on the dimension  $\Delta t$  is respected:

$$\Delta t \leq \frac{\Delta}{|V|} \tag{1.42}$$

where  $V$  is the fastest propagation velocity anywhere in the space mesh and  $\Delta$  is the mesh dimension. If this condition for the solution of the explicit method is not respected, a new  $\Delta t$  or  $\Delta$  needs to be considered and the velocity recalculated.

The important point in this procedure is that the new momenta and energy of the particles are obtained from the cell variables and not from the previous particle values using the assumption that the time is just enough to let the particles inside a cell equilibrate. So the characteristics of the particles are:

$$P_{particle} = f(x^n, y^n, m, mv_X^{n+1}{}_{i,j}, mv_Y^{n+1}{}_{i,j}, \tilde{e}_{i,j}^{n+1}) \tag{1.43}$$

At this point similarly to what shown before, the particles can be moved to the new coordinates according to:

$$\begin{aligned}
\frac{dx}{dt} &= \bar{V}_X \\
\frac{dy}{dt} &= \bar{V}_Y
\end{aligned} \tag{1.44}$$

Note that it is important to interpolate from the velocities of the four nearest cells velocities in order to get:

$$\begin{aligned}\bar{V}_{i,j} &= \frac{1}{2}(\tilde{V}_{i,j}^{n+1} + V_{i,j}^n) \\ \bar{V}_{AVERAGE} &= \frac{1}{\Delta^2}(a_{i+1,j}\bar{V}_{i+1,j} + a_{i+1,j+1}\bar{V}_{i+1,j+1} + a_{i,j+1}\bar{V}_{i,j+1} + a_{i,j}\bar{V}_{i,j})\end{aligned}\quad (1.45)$$

where the values of the four areas “a” are clearly representing the overlap of a particle over the bordering cells (area weighting). Finally the new particle positions can be calculated as:

$$\begin{aligned}x^{n+1} &= x^n + \Delta t \frac{1}{2}\bar{V}_x \\ y^{n+1} &= y^n + \Delta t \frac{1}{2}\bar{V}_y\end{aligned}\quad (1.46)$$

The time step is completed once all particle variables are updated. If a particle crosses a cell boundary, the mass, momentum and energy of the new cell are incremented preserving the conservation on the entire mesh.

The collision-dominated particle-in-cell method is simple and very flexible, but requires a lot of memory storage. Also, being not centered in time, stability is acquired through diffusion arising from the intermediate velocities. Consequently, momentum and energy tend to be diffused with a diffusion coefficient that can be evaluated with:

$$D \approx \left\langle v^2 + \frac{\mathcal{P}}{\rho} \right\rangle \Delta t \quad (1.47)$$

There has been a considerable amount of work to improve the original PIC methods as described so far by the Harlow papers and Birdsall papers. In increasing the accuracy of PIC, researchers have followed two approaches. In the first one, Nishiguchi and Yabe [30-31] have developed more accurate momentum convection schemes for the general PIC technique. They still have the momentum transfer from the grid to the particles and vice versa. However, restricting the transfers from the grid to the particles and back to

changes in momentum due to particle displacements, the diffusion varies according to the particles displacements rather than number of cycles in the calculation. The second approach has been suggested by the use of PIC technique in plasma simulation [19, 27].

Since each numerical particle represents a large number of real and physical particles and has assigned many important pieces of information as mass, charge, position and velocity, there is no reason for why more information cannot be loaded or attached to a sample particle being the grid a pure computational “help” in organizing data. No permanent information is carried by the grid itself but by the particles, which can help in achieving more accuracy. Mc Croy and later LeBoeuf [32-33] use full particle models in which momentum and internal energy are assigned to each particle achieving almost no diffusion but also increasing the numerical noise and multistreaming problems. So, in order to overcome these difficulties, Brackbill [34-36] has proposed to solve the large computational diffusion with the use of adaptively zoned grids. The idea was to reduce as much as possible the computational problems allowing the particles to carry information more effectively and avoiding the passage from the grid to the particles and back from the particles to grid points. The adaptive grid method is called FLIP (fluid implicit particle) and was developed at LANL. The great advantage of this methodology stands in assigning momentum to the particles eliminating the major source of computational diffusion. Besides the method allows for a difference between the velocity with which a particle moves through the mesh and the momentum it carries introducing the effect of collisions. Multistreaming is also solved with such procedure without introducing dissipation. The information that the particle carries is enough to characterize the fluid flow reducing the grid as in plasma simulation to a convenient mathematical tool.

In FLIP, the fluid is constituted by Lagrangian fluid particles moving through the grid. The information transferred in each time step by the particles to the grid by projections permits the solution of the equations on a relatively small number of points. In FLIP typically a grid with quadrilateral zones is established as shown in fig. 1.7 with reference point  $x_v$ . Natural coordinates  $(\xi, \eta)$  are defined for convenience by mapping each quadrilateral onto a unit square. At each vertex natural coordinates  $(i, j)$  are assumed while elsewhere the mapping between the physical coordinates and natural one is provided by the bilinear interpolation:

$$\bar{x} = \sum_v x_v s(\xi - i, \eta - j) \quad (1.48)$$

where  $s$  is a positive and continuous function with values ranging from 0 to 1. The function can be normalized with:

$$\iint_D d\xi d\eta s = 1 \quad ; \quad \sum_{i,j} s(\xi - i, \eta - j) = 1 \quad (1.49)$$

Once the grid is in place and the particles distributed across the grid, Brackbill suggests that particle data can be projected by using the bilinear interpolation function:

$$\begin{aligned} \rho_c &= \sum_p m_p s_{pc} / V_c \\ M_v &= \sum_p m_p s_{pv} \\ U_v &= \sum_p m_p \bar{u}_p s_{pv} / M_v \\ I_c &= \sum_p e_p s_{pc} / \rho_c V_c \end{aligned} \quad (1.50)$$

where  $\rho$ ,  $M$ ,  $U$  and  $I$  are the fluid's density, mass, velocity and internal energy respectively. The subscript  $c$  stands for cell so that  $V_c$  that is the volume of the cell, while  $p$  stands for particle and  $v$  for vertex of the quadrilateral grid. So  $m$ ,  $u$  and  $e$  are the

mass, velocity and energy of the particle. At each time step, the solution is advanced in two steps. In the Lagrangian phase, the grid moves with the local fluid velocity allowing no relative movement between the grid and the particles. Since the grid points are much less in number than the particles, this becomes a very efficient substitution. In the second phase or convective transport step, the particles are relocated onto the moving grid and the fluid information provided by the particle data.

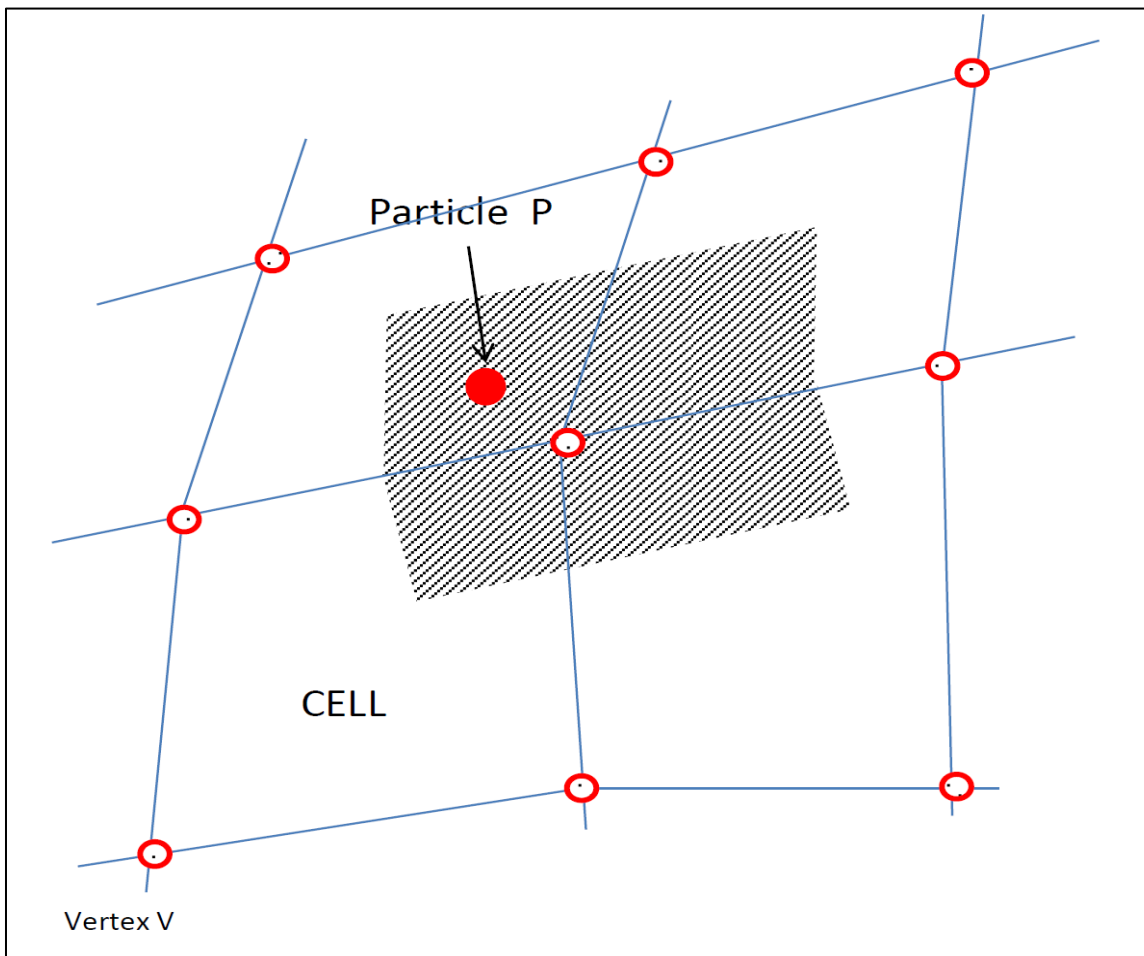


Figure 1.7 A grid of quadrilateral zones similar to the one proposed in [35] is illustrated.

Vertices, cell centers and particles are labeled  $v$ ,  $c$  and  $P$  while the shaded area generalizes the area weighting

Once the particles information has been projected onto the grid, the Lagrangian part can be solved using the equations of motion:

$$\begin{aligned}
\frac{d\rho}{dt} + \rho(\nabla \cdot U) &= 0 \\
\rho \frac{dU}{dt} + \nabla P - \nabla(\lambda + 2\mu)(\nabla \cdot U) + \nabla \times \mu(\nabla \times U) &= 0 \\
\rho \frac{dI}{dt} + P(\nabla \cdot U) - (\lambda + 2\mu)(\nabla \cdot U)^2 - \mu(\nabla \times U)^2 &= 0
\end{aligned} \tag{1.51}$$

If  $\lambda$  and  $\mu$  are considered constants, the viscous terms reduce the momentum equation to the standard form. Differentiating the density with respect to time and using the fact that  $ds_p / dt = 0$  then:

$$\frac{d\rho}{dt} = \sum_p m_p s_p d(J^{-1}) / dt = -\rho(\nabla \cdot U) \tag{1.52}$$

and using the definitions:

$$\begin{aligned}
\nabla \cdot U &= \sum_v U_v \cdot \nabla S_v \\
\nabla \times U &= \sum_v \nabla S_v \times U_v \\
\text{with } S_v &= S(\vec{x} - \vec{x}_v)
\end{aligned} \tag{1.53}$$

the internal energy equation can be re-written according to Brackbill as:

$$\begin{aligned}
\rho \frac{dI}{dt} &= -\{(P + Q)\nabla S_v \cdot U_v - (\psi) \cdot (\nabla S_v \times U_v)\} \\
Q &\equiv -(\lambda + \mu) \sum_v \nabla S_v \cdot U_v = \text{viscous pressure} \\
\psi &\equiv \mu \sum_v \nabla S_v \times U_v = \text{viscous shearing stress}
\end{aligned} \tag{1.54}$$

Solving the momentum equation with some simplifying assumptions as assuming that the pressure is constant within each cell,  $J(\vec{x}_c) = V_c$  and using a geometric coefficient ( $d_{vc}$ )

that allows the simple replacement of  $\nabla S_v$  using  $d_{vc} = \int dV \nabla S_v / V_c$ :

$$\begin{aligned}
(\nabla \cdot U)_c &= \sum_v d_{vc} \cdot U_v \\
(\nabla \times U)_c &= \sum_v d_{vc} \times U_v
\end{aligned} \tag{1.55}$$

the results can be written as:

$$0 = M_v (dU_v / dt) - \left[ \sum_c \{P_c + Q_c\} d_{vc} + d_{vc} \times \psi_c \right] V_c \tag{1.56}$$

Solving in a finite difference form for the intermediate fluid velocity  $U_v^g$  using the superscript as the previous step:

$$0 = M_v^0 (U_v^g - U_v^0) - \left[ \sum_c \{\tilde{P}_c + Q_c\} d_{vc} + d_{vc} \times \psi_c^0 \right] V_c g \Delta t \tag{1.57}$$

The intermediate fluid velocity  $U_v^g$  is calculated at some intermediate time  $t + \theta \Delta t$  ( $0.5 < \theta < 1$ ). Using the fluid intermediate velocities, the new densities for each cell can be found with:

$$0 = \rho_c^1 \left[ 1 + \sum_c d_{vc} \cdot U_v^g \Delta t \right] - \rho_c^0 \tag{1.58}$$

and solved implicitly for the new density. Finally the final new velocity can be calculated as:

$$U_v^1 = (U_v^g - (1 - g)U_v^0) / \theta \tag{1.59}$$

The internal energy of the grid is calculated using the particle energy information provided before and as a result there is no need to solve the energy conservation simplifying the process and shortening the computational time. Brackbill suggests that solving the particle equations of motion allows velocity, position, energy ( $u_p^1, x_p^1$  and  $e_p^1$ ) to be known at all times. As the particle information are all known, the



grid is regenerated and new particle coordinates are found to be ready for next time-step. Brackbill proposes also some considerations about the number of particle per cells with the minimum number set at 9 and Lapenta [37] reviews the necessity to control the number of particles in each zone in order to improve the accuracy results.

It is worth recalling that most the improvements proposed along time and modifications implemented for the PIC techniques are well summarized in very important monographs [22, 28-29, 38-39]. Some observations needs to be done also about collision dominated PIC methods which are all essentially based on assuming that particle distribution is near to Maxwellian and so averaging the force acting on particles due to collisions [29, 38]. Inter particles forces inside grid cells are generally underestimated due to the fact that field solvers are generally excluding self-forces. Then, typically to compensate such effect a Coulomb collision operator is introduced. The very first models were simulating the exact interaction between each pair. Lately Monte Carlo methods have been implemented to provide a more effective and statistical treatment of the subject. Since most of the interesting plasmas have particle distributions far from Maxwellian, non-linear models have also been considered [40]. Unfortunately, very large number of particles is required to get an accurate velocity distribution able to provide though the function the exact collision force.

Most of the non-linear Coulomb collision operators are based on the binary collisions model introduced by Takizuka and Abe [41]. The typical size of a PIC cell is in order of the Debye length ( $\lambda_D$ ) so that the interaction between particles in different cells can be neglected. The collision operator preserves energy and momentum in a very accurate way. The solution proceeds in three steps: a) all particles are grouped according to the cells

where they belong; b) The particles are paired randomly and statistically collided ; c) the after collision velocities are expressed respecting conservation of momentum and energy using the pre-collision values:

$$\vec{V}'_1 = \vec{V}_1 + \frac{m_2}{m_1 + m_2} \Delta \vec{V} \quad ; \quad \vec{V}'_2 = \vec{V}_2 + \frac{m_1}{m_1 + m_2} \Delta \vec{V} \quad (1.60)$$

where accordingly  $\Delta \vec{V} = \vec{V}' - \vec{V}$  ,  $\vec{V} = \vec{V}_2 - \vec{V}_1$  ,  $\vec{V}' = \vec{V}'_2 - \vec{V}'_1$  and  $(\vec{V}')^2 = V'^2$  . The relative velocity of the scattering process is then very important and can be solved using:

$$\Delta \vec{V} = (\hat{O}(\chi, \psi) - 1) \vec{V} \quad (1.61)$$

with  $\hat{O}(\chi, \psi)$  the matrix corresponding to the rotation on scattering angle  $\chi$  and azimuthal angle  $\psi$  [41]. The scattering angle is evaluated from the corresponding statistical distribution.

Coulomb interaction is a long range interaction. However the main contributor to collisionality is the cumulative and global effect of many small scattering collisions. The time step for the Coulomb collisions  $\Delta t_c$  should be then very small so that  $v \Delta t_c \ll 1$  being  $v$  the characteristic relaxation time. Even though usually  $\Delta t_c \gg \Delta t$  , the binary collision operator still absorbs a lot of computational time. Several efforts have been done in order to improve this situation [42].

In realistic conditions, plasma contains several neutral particles that can collide with plasma particles. Two schemes treat this type of collisions into PIC: Direct Monte Carlo Methods and Null Collisions methods. The main difference between the two methodologies stands essentially in how the collided particle is chosen.

The null collision method [39, 43-44] requires generally a small amount of particles to be sampled. Since in each time step only a small fraction of particles effectively undergo collision with neutrals, there is no need for analyzing all particles. In order to calculate the maximum collision probability during the chosen time, a null collision constraint is used:

$$P_{\max} = 1 - e^{(-v_{\max} \Delta t)} \quad (1.62)$$

So the maximum number of particles that can effectively collide is given by:

$N_{\text{NEUTRAL to PLASMA COLLISIONS PARTICLES}} = N_{NC} = P_{\max} N \ll N$  . This saves a lot of the computational time allowing also the  $N_{NC}$  to be randomly chosen. The random sampling procedure includes the calculation of the probability of sampled particle:  $R \leq P_1 / P_{\max} \approx v_1 / v_{\max}$  . If no collision takes place, R (random number between typically 0 and 1) will be bigger than the ratio of the collision frequencies  $v$ . The difference between nonlinear and linear null collision operators stands in the way the collided neutral particles are treated. In the linear model typically the neutral velocity is evaluated from the distribution (for given temperature and density frequently it is Maxwellian). On the contrary for the nonlinear case, the motion of neutrals is solved in the simulation using randomization for the collided ones.

The direct Monte Carlo model is a common MC scheme where all particles carry information about their collisional probability [45] and frequently used in low temperature plasmas. Again the collisional probability is defined as:

$$P(t) = 1 - e^{(-v t)} \quad (1.63)$$

where  $\nu$  is the sum of all possible collision frequencies. The frequencies depend on local conditions of plasma, energy and cross sections. The average time between collisions can be found as:  $t_c = -\ln R / \nu$  where  $R$  is again a random number from 0 to 1. During the simulation  $t_c$  is calculated for each particle. When the collision takes place, the random number is compared to the corresponding collision probabilities so that:

$$R \leq \frac{P_1(t_c)}{P(t_c)} = \frac{1 - e^{-\nu_1 t_c}}{P(t_c)} \approx \frac{\nu_1}{\nu} \quad (1.64)$$

If more collisions take place, the expression is modified as:  $R \leq (P_1(t_c) + P_2(t_c)) / P(t_c) \approx (\nu_1 + \nu_2) / \nu$  and so on. It is important to note that, as it is the method cannot be used directly for plasma applications since particles can accelerate during the collisionless motion drastically changing then the collision frequency. A modification to this method has been introduced by Skullerud [46]: the collision frequency used is the maximum possible, reducing the time of time intervals and the accuracy of the operator. The direct MC methods require all particles to be analyzed for a collision probability increasing the computational time and the memory requirement with respect of the null methods. A small review of collision models including collision of particles with different weight can be found in [47].

Another recent and interesting application of PIC techniques is the dusty plasmas. Dust particles are generally much heavier than plasma ions (much more than 1000 times) and this feature makes this type of simulation very difficult to implement. An interesting exception though has been reported by Matyash and Scheneider [48] who used an artificial reduced mass ratio  $M_{DUST} / M_i = 640$ . The dust particles in this PIC simulation

are assumed to be immobile and the plasma interaction is modeled through electrostatic interaction of charged particles. Other models [49] use a PIC-MC particle collision model to describe the ion/electron absorption at the dust.

Several studies have been conducted recently in order to improve to capabilities of PIC methodologies and make them fully parallel [50-53]. Several approaches can be followed but essentially any parallelization of the code has to be tailored to the problem itself. Depending of the underlying physics, each specific application might need a different algorithm in order to be solved in parallel form and be balanced. Essentially two different parallelization strategies have been proposed in the literature. The first one assigns the computational particles to processors independently from their position into the computational domain. The advantage of this strategy stands in the balanced workload for both the field solver and the particle mover, though creating a non-local management problem for the “send and receive” operations. In fact a particle belonging to a cell for which its executing processor doesn’t hold the field degrees of freedom, needs the data to be sent and received by a remote (master) processor thus increasing the communications costs [54, 61]. The second parallelization scheme is based on the partitioning of the computational domain among the available nodes or processors. Each node is responsible for the computational tasks regarding a “specific “geometrical area so that no excessive communication operations need to take place. However this scheme, especially if the particle distribution changes dynamically with time, will unbalance the workload leading eventually even to deterioration of the performance or failure if one node runs out of memory. Also particle leaving one subdomain for a bordering one might lead to increase in the intercommunication process. In some cases this additional costs

even compensate the benefit of a better-balanced workload. Further insight can be found in [55].

Another interesting and recent application of PIC techniques is the multiphase particle-in-cell method. Even though not relevant for plasma applications, it is very interesting since it overcomes the problems relative to mapping from the solid particles to the grid with interpolating functions and treating the solid particles as a continuum. The methodology given its efficiency and stability is ideal for industrial scale chemical processes involving particle fluid flows. The multiphase particle-in-cell (MP-PIC) method was originally developed for a one-dimensional case in the mid-1990s by P.J. O'Rourke [56] from Los Alamos National Lab, who also invented the term MP-PIC. The extension of the method to two-dimensions was performed later by D.M. Snider and O'Rourke [57] and in 2001 D.M. Snider had extended the MP-PIC method to full three-dimensions [58].

#### 1.4 HEIGHTS-PIC: scope of the code

HEIGHTS-PIC code [59] has been created, based on previous HEIGHTS work, to provide a new approach using the Particle-in-cell technique to extremely complex problems as instabilities developing in tokamaks during their operations. The code as described in the second chapter is extremely complex and large. The code is formed by more than 40 subroutines all well integrated and connected. The physical processes studied and developed into HEIGHTS-PIC can be summarized as follows:

1. Heat Conduction inside the solid target
2. Target melting and vaporization

3. Solid target heating by incoming hot SOL plasma, by radiation and by incoming particles heat conduction
4. Formation of the plasma shield and its MHD movement
5. Magnetic field diffusion
6. Heating and momentum transfer to the target by incoming hot plasma
7. Radiation transport
8. Energy distribution between ions and, electrons with internal excitations of ions.

The importance of this new approach can be viewed in different ways. The aim of this work stands in creating a not only a new mathematical/ numerical model for simulating plasma evolution during ELM or disruptions, but rather to provide a new tool to be used in several fields and applications. Modern PIC methods generally find the bottleneck of their calculations in attempt to provide an accurate solution of the Poisson's equation. In our approach, we rather re-evaluate under a different light the fluid approach of particles in cell techniques acquiring the aimed accuracy directly solving the radiation transport equation. Potentially the technique can be used in all problems involving plasma and plasma material interactions ranging from lasers applications (chapter 4 analyzes directly laser numerical experiments run with HEIGHTS-PIC) to the study of plasma thrusters for satellites and plasma propulsive systems.

## References

1. A., HASSANEIN, T., SIZYUK, "Comprehensive simulation of vertical plasma instability events and their serious damage to ITER plasma facing components", Journal of Nuclear Fusion, 48, 115008, 2008.
2. A. HASSANEIN et al., "Impact of various plasma instabilities on reliability and performance of Tokamak fusion devices", Fusion Eng. Des., 85:1331-1335, 2010.
3. A.S., KUKUSHKIN, H.D., PACHER et al., "Divertor issues on ITER and extrapolation to reactors." Fusion Engineering and Design 65(3): 355-366, 2003.
4. A., HASSANEIN, T., SIZYUK et al., "Integrated simulation of plasma surface interaction during edge localized modes and disruptions: Self-consistent approach." Journal of Nuclear Materials, 390-91: 777-780, 2009.
5. A. HASSANEIN, "Modeling and key issues of plasma/surface interactions in future tokamaks", Fusion Engineering and Design 69, 781-787. 60, PII S0920-3796(02)00006, 2002
6. J. CRANK, "A practical method for numerical evaluation of solution of partial differential equations of the heat-conduction type", Proc. Camb. Phil. Soc. 43, 50-67., 1947
7. J. DOUGLAS and H.H. RACHFORD, "On the Numerical Solution of Heat Conduction Problems in two and three space variables", Trans. Amer. Math. Soc. 82, 421-439 1956.
8. J. CRANK, "Free and moving boundary problems", Clarendon Press, Oxford, 1984.



9. J.M. DSUSINBERRE, "A Note on Latent Heat in Digital Computer Calculations", ASME-AIChE Joint Heat Transfer Conference, Evanston, 1958.
10. J.WESSON, "TOKAMAKS", 2<sup>nd</sup> Edition, Clarendon Press, Oxford, 1997.
11. ENEA, Italian National Agency for New Technologies energy and Sustainable Economic Development, at <http://www.fusione.enea.it/FTU/powers.html.en>
12. A.S. KUKUSHKIN, H.D. PACHER et al. , "Divertor issues on ITER and extrapolation to reactors." Fusion Eng. and Des. 65(3): 355-366, 2003.
13. ITER Director, "Summary of ITER Final Design Report", ITER, 2001.
14. F.H. HARLOW, "Machine calculation method for hydrodynamics problems", Los Alamos Scientific Laboratory Report LAMS-1956, 1955.
15. A.A. AMSDEN, "The Particle-in-Cell Method for the calculation of Dynamics of Compressible Fluids". Los Alamos Scientific Laboratory Report LA-3466, 1966.
16. M.W. EVANS and F.H. HARLOW, "The Particle-in-Cell Method for hydrodynamic calculations." Los Alamos Scientific Lab., LA-2139, 1957.
17. F.H. HARLOW, "The Particle-in-cell method for numerical solution of problems in fluid dynamics", in Proceedings of Symposia in Applied mathematics, 15, p. 269-288,1963.
18. O.BUNEMAN, Physics Review, vol. 115(3), 503, 1959.
19. J. DAWSON, Physics of Fluids, 5, 445, 1965.
20. C.K. BIRDSALL and D. FUSS , "Clouds-in-clouds, clouds-in-cell physics for many-body plasma simulations", J. Comp. Phys., 3, 494,1969.
21. C.K. BIRDSALL, A.B., LANGDON and H. OKUDU, "Finite-size particle physics applied to plasma simulation", Meth. Comp. Phys., 9, 242, 1970.

22. C.K. BIRDSALL, A.B., LANGDON, "Plasma Physics via Computer Simulation", McGraw-Hill, New York, 1985.
23. F.H. HARLOW, "The Particle-in-cell computing method for fluid dynamics", Methods of Computational Physics, 3, 319-343, 1964.
24. F.H. HARLOW and AA. AMSDEN, "Fluid Dynamics", Los Alamos Scientific Report, LA-4700, 1971.
25. F.H. HARLOW, and J.E. WELCH, "Numerical Calculation of time-dependent viscous incompressible flow of fluid with a free surface", Physics of Fluids, 8, 2182-2189, 1965.
26. F.H. HARLOW, "PIC and its progeny", Computer Physics Communications, 48, 1-11, 1988.
27. J.M. DAWSON, "Particle simulation of plasmas", Reviews of Modern Physics, 55, 403-447, 1983.
28. D. TSKHAKAYA, "The Particle-in-Cell Method, chapter 6, Computational Many Particle Physics", Springer, New York, 2007.
29. D. POTTER, "Computational Physics", John Wiley & Sons, London 1973.
30. A. NISHIGUCHI, and T. YABE, "Finite-sized fluid particle in a non-uniform moving grid", Journal of Computational Physics, 47, 297-302, 1982.
31. A. NISHIGUCHI, and T. YABE, "Second-Order Fluid Particle Scheme", Journal of Computational Physics 52, 390-413, 1983.
32. J.N. LEBOEUF, T. TAJIMA and J.M. DAWSON, "A magnetohydrodynamic particle code for fluid simulation of plasma", Journal of Computational Physics, 31, 379-408, 1979.

33. R.L. MCCROY, R.L. MORSE and K.A. TAGGART, "Growth and Saturation of instability of spherical implosions driven by laser or charged particle beams", Nuclear Science and Engineering, 64,163-176, 1977.
34. J.U. BRACKBILL and W.E. PRACHT, "An Implicit Almost-Lagrangian Algorithm for Magnetohydrodynamics", J. Comput. Phys. 13:455, 1973.
35. J.U. BRACKBILL and H.M. RUPPEL, "FLIP - A method for adaptively zoned, Particle-in-Cell calculation of fluid-flows in 2 dimensions." Journal of Computational Physics 65(2): 314-343, 1986.
36. J.U. BRACKBILL, D. B., KOTHE et al., "FLIP-A low-dissipation, Particle-in-Cell method for fluid-flow." Computer Physics Commun. 48(1):25-38, 1988
37. G. LAPENTA, "Particle Rezoning for Multidimensional Kinetic Particle-In-Cell Simulations", Journal of Computational Physics, 181, 317–337, 2002.
38. R. W., HOCKNEY and J. W. EASTWOOD , "Computer Simulations using Particles", CRC Press,1988.
39. J P VERBONCOEUR, "Particle simulation of plasmas: review and advances" , Plasma Physics and Controlled Fusion , 47 ,A231-A260, 2005
40. O.V. BATISHCHEV et al. , "Kinetic effects on particle and heat fluxes in detached plasmas", Physics of Plasmas,3,issue 9,3386,1996.
41. T. TAKIZUKA and H. ABE, "A binary collision model for plasma simulation with a particle code," Journal Computational Physics, 25, 205, 1977.
42. A.V. BOBYLEV, K. NANBU, "Theory of collision algorithms for gases and plasmas based on the Boltzmann equation and the Landau-Fokker-Planck equation", Physics Review E, issue 4, 4576-4586, 2000.

43. C. BIRDSALL, "Particle-in-cell charged-particle simulations, plus Monte Carlo collisions with neutral atoms, PIC-MCC", IEEE Transactions on Plasma Science , In Plasma Science,19, issue 2,65-85,1991.
44. V. VAHEDI, M. SURENDRA,"A Monte Carlo collision model for the particle-in-cell method: applications to argon and oxygen discharges", Computer Physics Communications, 87, 179-198, 1995.
45. V.V. SERIKOV, S. KAWAMOTO, and K. NANBU , "Particle-in-Cell Plus Direct Simulation Monte Carlo (PIC-DSMC) Approach for Self-Consistent Plasma-Gas Simulations", IEEE Transactions on plasma science, 27, issue 5,1999.
46. H.R. SKULLERUD," The stochastic computer simulation of ion motion in a gas subjected to a constant electric field ", Journal of Physics D: Applied Physics, 1, 1567-1569, 1968.
47. K. NANBU, "Probability theory of electron-molecule, ion-molecule, molecule-molecule, and Coulomb collisions for particle modeling of materials processing plasmas and cases", IEEE Transactions on Plasma Science, 28 , issue 3, 971-990, 2000.
48. K. MATYASH, R. SCHNEIDER, "Kinetic modeling of dusty plasmas", Contributions to Plasma Physics, 44, issues 1-3, 157-161, 2004.
49. YU.I. CHUTOV et al., "Dusty Sheaths in Magnetized Plasmas", Contributions to Plasma Physics, 44, issues 1-3, 138-143, 2004.
50. V.K. DECYK, "Skeleton PIC Codes for Parallel Computers", Computer Physics Communications, 87, issue 1-2, 87-94, 1995.
51. V.K. DECYK," UCLA parallel PIC framework", Computer Physics Communications, 164, issue 1-3, 80-85, 2004.

52. S. BASTRAKOV et al., "Particle-in-cell plasma simulation on heterogeneous cluster systems", *Journal of Computational Science*, 474-479, 2012.
53. B. DI MARTINO, S. BRIGUGLIO, G. VLAD. and P. SGUAZZERO, "Parallel PIC plasma simulation through particle decomposition techniques", *Parallel Computing*, 27, 295–314., 2001
54. E. A. CARMONA, L.J. CHANDLER," On parallel PIC versatility and the structure of parallel PIC approaches", *Concurrency: Practice and Experience*,9, issue 12,1377-1405,1997.
55. F. WOLFHEIMER et al., "A parallel 3D particle-in-cell code with dynamic load balancing", in *Nuclear Instruments and Methods in Physics Research Section A*, 202-204,2006.
56. M.J. ANDREWS and P.J., O'ROURKE, "The Multiphase Particle-in-Cell (MP-PIC) Method for Dense Particle Flows", *International Journal of Multiphase Flow*, 22, 2: 379–402, 1996.
57. D.M. SNIDER, P.J., O'ROURKE, P.J., and M.J., ANDREWS, "An Incompressible Two-Dimensional Multiphase Particle-In-Cell Model for Dense Particle Flows", NM, LA-17280-MS (Los Alamos National Laboratories, Los Alamos, NM), 1997.
58. D.M. SNIDER, "An Incompressible Three-Dimensional Multiphase Particle-in-Cell Model for Dense Particle Flows", *Journal of Computational Physics*, 170:523–549, 2001

59. F. GENCO, A. HASSANEIN, "Modeling of Damage and Lifetime Analysis of Plasma Facing Components during Plasma Instabilities in Tokamaks", *Fusion Science and Technology*, 60,339-343, 2011
60. G. FEDERICI, A. LOARTE, et al., "Assessment of erosion of the ITER divertor targets during type I ELMs". *Plasma Physics and Controlled Fusion* , 45(9):1523-1547, 2003
61. R. COURANT, K. FRIEDRICHS, H. LEWY, "Über die partiellen Differenzgleichungen der mathematischen Physik", *Mathematische Annalen* (in German) 100 (1): 32–74 , 1928.
62. C. S. LIN, A.L. THRING, J. KOGA, "A parallel particle-in-cell model for the massively parallel processor", *Proceedings, The 2nd Symposium on the Frontiers of Massively Parallel Computation* (Cat. No.88CH2649-2), IEEE, 1988.

## CHAPTER 2. MODELING SUMMARY

### 2.1 Plasma Material Interaction

The thermal response of the plasma facing components is solved using the time dependent heat conduction equation in one or two dimensions:

$$\rho c_p \frac{\partial T}{\partial t} = \nabla \cdot (K \nabla T) + \dot{q}(z, t) \quad (2.1)$$

where T is the temperature,  $c_p$  is the specific heat,  $\rho$  is the density, K is the thermal conductivity and  $\dot{q}$  is the volumetric energy deposition rate of the energetic electrons and ions into the plasma. All material related properties are assumed to be temperature dependent and calculated accordingly. Surface temperature is calculated using the boundary conditions and the dynamics of the evaporation process. At the beginning of the disruption, as all energy is being deposited onto the material, the surface temperature starts rising diffusing deeper and deeper (fig.2.1, [1]).

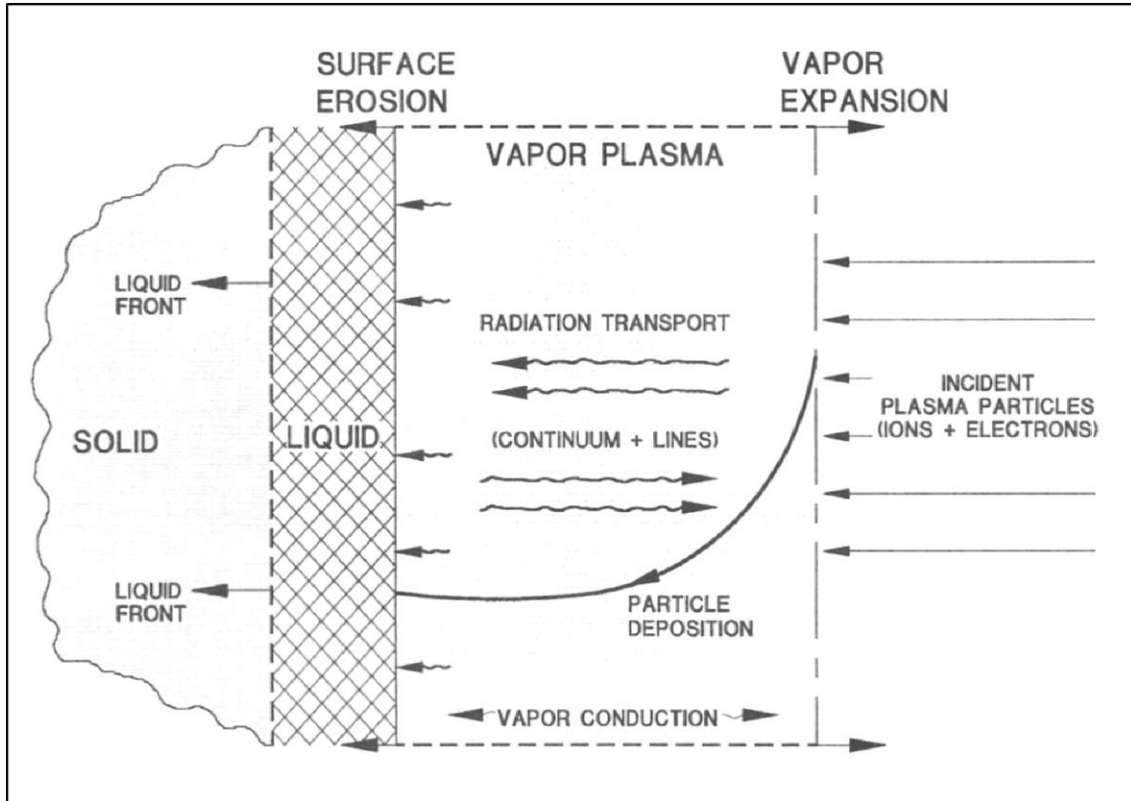


Figure 2.1 Schematic illustration of various interactions processes with magnetic field during disruptions [1]

Once the material surface is high enough to vaporize (carbon doesn't melt for the given condition of pressure), a vapor cloud starts forming above the divertor. Photon radiation due to the interaction of plasma particles and vapor particles is born becoming more and more important (fig. 2.1). The heat conduction equation is typically solved in cylindrical coordinates with  $z$  being the perpendicular direction to the material surface (fig. 2.2, [2-3]). In the PIC HEIGHTS models, different shapes of the incoming plasma have also been implemented with particular considerations to the Gaussian, exponential and the uniform shape.



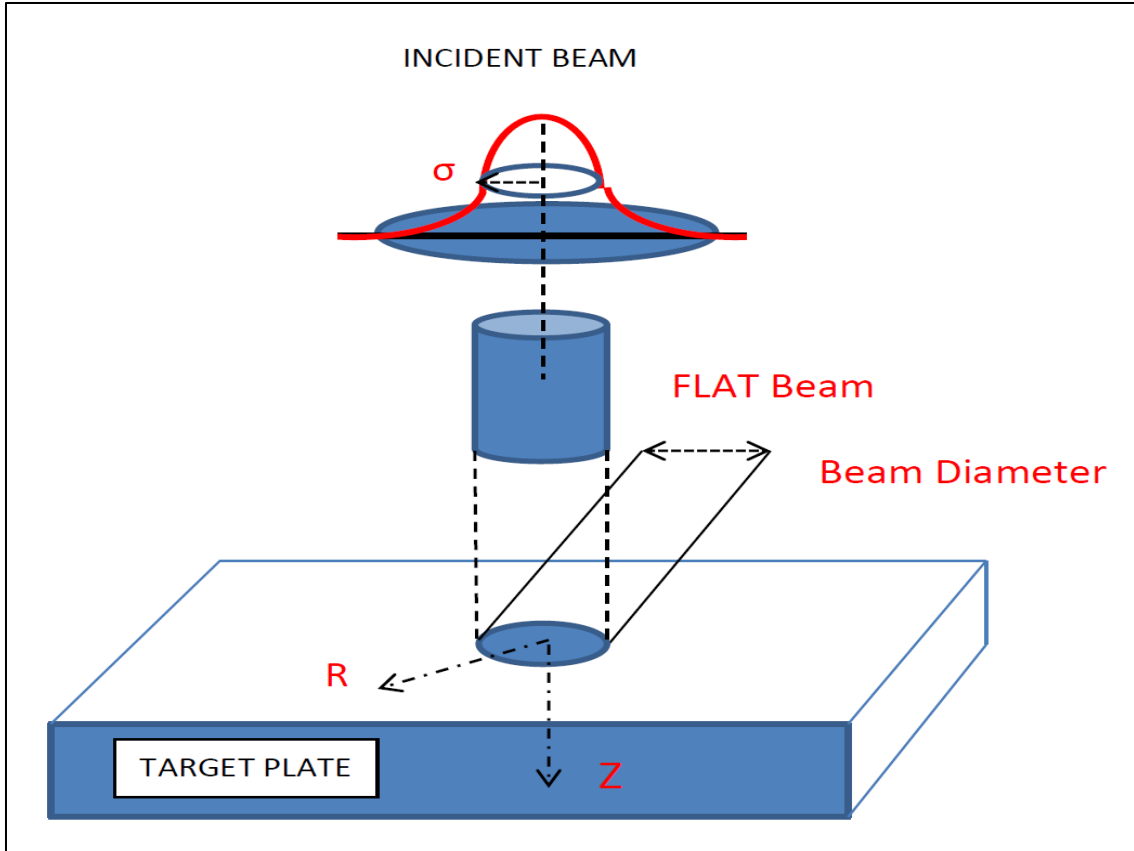


Figure 2.2 Schematics of geometry of the 3D Gaussian beam acting on the target surface similar to [3, 11]

The surface temperature calculation requires the evaluation of the single portions of incident energy that go into conduction, melting, evaporation, and radiation. The kinetics of the evaporation provides the physical and mathematical connection between the outgoing net particle flux from the surface and the surface temperature. The boundary condition is expressed by:

$$F(r,t) = -K(T_v) \frac{\partial T}{\partial z} + \rho(T_v) L_v(T_v) V(T_v) + \sigma \epsilon (T_v^4 - T_0^4) \quad (2.2)$$

where  $F(r,t)$  is the radial heat flux coming from the plasma,  $L_v$  is the heat of vaporization,

$V(T_v)$  is the velocity of the receding surface and  $T_v = T(r, z = 0, t)$ . The velocity of the receding surface is typically function of the instantaneous surface temperature and other materials parameters. The last term of the equation is the radiative heat transfer term. It contains  $T_0$  which is the temperature of the surroundings,  $\sigma$  as the Stefan-Boltzmann constant and  $\varepsilon$  material emissivity.

As the vapor starts building up and becomes thicker and thicker above the PFC surface, the vapor shielding becomes more and more efficient changing the boundary condition into:

$$-K \frac{\partial T}{\partial z}(0, t) = q_{GAS} + q_{RAD} - q_{EVAP} \quad (2.3)$$

where  $q_{GAS}$  is the net heat flux from the near-wall vapor cloud,  $q_{RAD}$  is the radiation heat flux absorbed at the material surface and  $q_{EVAP}$  is the evaporation heat flux calculated from the enthalpy of evaporation for the material under investigation (carbon in our case).

The evaporation flux is calculated using the well-known Hertz-Knudsen-Langmuir theory of evaporation and condensation under non-equilibrium conditions providing [3]:

$$J(t) = J_E^{EQ}(T_v(t)) \left[ 0.8 + 0.2e^{-(t-t_v)/10\tau_c} \right] \quad (2.4)$$

where  $J(t)$  is the net evaporation flux,  $t_v$  is the preheat time in order for the vapor to form,  $\tau_c$  is the collision time while  $T_v$  is the surface temperature. Note that  $\tau_c$  represents the time scale for the recombination effects and can be evaluated as:

$$1/\tau_c = 16\sqrt{\pi} n a_0^2 (kT_v / m)^{1/2} \quad (2.5)$$

with  $\pi a_0^2$  being the scattering elastic cross section for the vapor atoms and  $n$  the vapor density in front of the surface.

The maximum vacuum evaporation rate  $J_E^{EQ}$  can be calculated using the Maxwell-Boltzmann relationship and using the average velocity to provide:

$$J_E^{EQ} = n(kT_v / 2\pi m)^{1/2} \quad (2.6)$$

where  $m$  is the mass per atom and  $k$  is the Boltzmann constant.

The net heat flux  $q_{GAS}$  due to the particle transport from the near surface vapor to the target can be described by the expression:

$$q_{GAS} = \alpha \frac{1}{4} n_i v_i \frac{3}{2} k (T_i - T_s) \quad (2.7)$$

where  $v_i$  is the thermal ion velocity,  $T_i$  is the ion temperature,  $T_s$  is the target surface temperature and  $\alpha$  is a collisional factor (roughly equal to 0.2) of the free-streaming energy transport. It is important to notice that the free streaming term is more important for high  $Z$  materials than for low ones. In fact, close to the target where the vapor is denser, the vaporized atoms do not move really fast making this term more important. Also, no electron free streaming term is considered since the surface has a positive potential.

The volumetric energy deposition function is calculated in the solid target material using very detailed models that include also the slowing down physics of ions into solids. The change of phase for the surface materials considered (carbon) is also included. The heat conduction equation is solved in two dimensions. This requires the use of a coordinate frame which moves with the receding surface using the instantaneous surface position

$$z(r, t) = z_0 - \int_0^t v(r, t) dt \quad (2.8)$$

where  $z_0$  is the original position of the surface at the beginning of the calculation (i.e. disruption or off-normal event) and  $v(r,t)$  is the surface velocity. Using the fact that in our problem, symmetry exists so that we can consider  $\partial T/\partial r = 0$  the equation transforms into:

$$\rho c_p \frac{\partial T}{\partial t} = \rho(T) c_p(T) V(r,t) \frac{\partial T}{\partial z} + \dot{q}(r, z, t) \quad (2.9)$$

that includes a convective term before not present. The boundary condition seen before applies for  $z = 0$ . Typically the temperature at the boundary inside the material is given for two dimensions but it's fixed and equal to the ambient temperature  $T_b$ . The surface velocity needed to evaluate the boundary condition can be calculated from [3]:

$$V(r,t) = 5.8 \cdot 10^{-2} \frac{\alpha \sqrt{A} P_v(T_v)}{\rho(T_v) \sqrt{T_v}} \left[ 0.8 + 0.2 e^{\frac{-t}{10\tau_c}} \right] \quad (2.10)$$

where  $\alpha$  is the sticking probability,  $A$  is the atomic mass of the target material,  $P_v$  is the vapor pressure and  $\tau_c$  is the collision time.

## 2.2 Plasma Vapor Interactions

Once the incoming plasma starts impinging onto the target surface heating up the entire system, the temperature into the bulk of the material and on the surface continues to rise. Once the surface temperature has reached and overcome the evaporation one, significant ablation and vapor forming takes place. The produced vapor will accumulate, expand and start interacting with the incoming plasma particles. As the vapor heats up more and more due to the incoming plasma energy, vapor ionization will also start taking place. The ionized vapor particles will interact with the strong magnetic field limiting

their free expansion and keeping the vapor cloud compact and well over the target surface. This behavior enhances the vapor shielding effect eventually leading to a condition where all the plasma particles will be stopped into the vapor cloud. Further heating of the material is then provoked only by vapor produced photon radiation and vapor conduction.

Vapor expansion into vacuum with the presence of a strong magnetic field is determined by solving at the same time the magneto-hydrodynamics equations for conservation of mass, momentum and energy given by [1, 11]:

$$\begin{aligned}
 \frac{\partial \rho}{\partial t} + \nabla \cdot (\rho \vec{V}) &= 0 \\
 \rho \frac{\partial \vec{V}}{\partial t} + \nabla(P) &= 0 \\
 \frac{\partial E}{\partial t} + \nabla(E \cdot \vec{V}) + P \nabla \cdot (\vec{V}) &= \nabla \cdot (K \nabla T) + \nabla \cdot Q_r + \nabla \cdot Q_b
 \end{aligned} \tag{2.11}$$

where  $\rho$  is the density,  $\vec{V}$  is the vapor velocity,  $P$  the pressure,  $E$  the energy,  $K$  the vapor conductivity,  $Q_b$  is the incident particle flux from the incoming plasma and  $Q_r$  is the radiation flux. All quantities of these equations are both time-dependent and space-dependent.

The ionized vapor particles move freely following the magnetic field lines and their motion can be described by the equation [1]:

$$\rho \frac{\partial \vec{V}}{\partial t} = -\nabla P + \vec{J} \times \vec{B} \tag{2.12}$$

The magnetic force  $\vec{J} \times \vec{B}$  acts as a retarding force for the expanding vapor with important consequences towards the final and total erosion of the plate the incident particle flux from the incoming plasma. The force acts mainly perpendicularly to the magnetic force. The equation of vapor motion needs to be solved in two directions, along

and perpendicular to the divertor plate. The radiation transport equations are not influenced by the magnetic field and are solved in two dimensions. The magnetic force is composed of two parts: the pressure force  $F_m$  and the friction force  $F_C$  which is due to the curvature of the magnetic field  $B$ . They can be calculated as:

$$F_m = \frac{1}{\mu_0} \nabla \vec{B}^2 \quad F_C = \frac{1}{\mu_0} \frac{\vec{B}^2}{R_C} \quad (2.13)$$

where  $\mu_0$  is the magnetic permeability and  $R_C$  is the radius of curvature of the magnetic field lines. The current density  $\vec{J}$  is provided by:

$$\vec{J} = \frac{1}{\mu_0} \nabla \times \vec{B} \quad (2.14)$$

The magnetic diffusion in the vapor cloud needs to be considered in the solution of the MHD equation. The variation along time of the magnetic field can be calculated with:

$$\frac{\partial \vec{B}}{\partial t} = -\frac{1}{\mu_0} \nabla \times (\varepsilon + \vec{V} \times \vec{B}) \quad (2.15)$$

where  $\varepsilon$  is the induced electric field and can be calculated as:

$$\varepsilon = -\frac{\vec{J}}{\sigma} \quad (2.16)$$

The vapor conductivity  $\sigma$  for weakly-ionized plasmas is directly proportional to the vapor plasma collision time  $\tau$  and the electron density  $n_e$  and can be calculated by:

$$\sigma = \frac{4\pi n_e e^2}{m_e} \tau \quad (2.17)$$

The vapor equations are solved in 2D coordinates system along and across the magnetic field lines. Then they are transformed back to the xy axis reference

(perpendicular to the divertor and parallel to the divertor). Joule heating of the vapor cloud is also considered and evaluated in this phase of the calculation. In order to evaluate the eroded mass due to the disruption on the reference target surface, the following relationship is used:

$$\Delta m = \int_{t=0}^{t=\infty} \int_{r=0}^R 2\pi r \rho V(r, t) dt \quad (2.18)$$

The entire system of magneto-hydro-dynamics equations can be summarized as [1, 11]:

$$\begin{aligned} \frac{\partial \rho}{\partial t} + \vec{\nabla} \cdot \rho \vec{V} &= 0 \\ \frac{\partial \rho \vec{V}_x}{\partial t} + \vec{\nabla} \cdot \rho V_x \vec{V} + \frac{\partial}{\partial x} \left( P + \frac{B^2}{2\mu_0} \right) - \frac{1}{\mu_0} \left( \vec{B} \cdot \vec{\nabla} \right) B_x &= F_x \\ \frac{\partial \rho \vec{V}_y}{\partial t} + \vec{\nabla} \cdot \rho V_y \vec{V} + \frac{\partial}{\partial x} \left( P + \frac{B^2}{2\mu_0} \right) - \frac{1}{\mu_0} \left( \vec{B} \cdot \vec{\nabla} \right) B_y &= F_y = 0 \\ \frac{\partial \rho \vec{V}_z}{\partial t} + \vec{\nabla} \cdot \rho V_z \vec{V} + \frac{1}{\mu_0} \left( \vec{B} \cdot \vec{\nabla} \right) B_z &= 0 \\ \frac{\partial}{\partial t} \left\{ \rho e_i + \frac{\rho V^2}{2} + \frac{B^2}{2\mu_0} \right\} + \vec{\nabla} \cdot \left\{ \vec{V} \left( \rho e_i + \frac{\rho V^2}{2} \right) + \vec{P} \cdot \vec{V} - K \vec{\nabla} T_e + S_{Rad} + \frac{\vec{E} \times \vec{B}}{\mu_0} \right\} &= \\ = Q_{Beam} \\ \frac{\partial \vec{B}}{\partial t} &= -\vec{\nabla} \times \vec{E} \\ \frac{1}{\mu_0} \vec{\nabla} \times \vec{B} &= \vec{j} \\ \vec{\nabla} \cdot \vec{B} &= 0 \\ \vec{\nabla} \cdot \vec{E} &= \rho_e \\ \vec{E} + \vec{V} \times \vec{B} &= \frac{1}{\sigma} \vec{j} \end{aligned} \quad (2.19)$$

where  $T_e$  is the target plasma electron temperature,  $\sigma$  is the plasma conductivity and  $\vec{j}$

the electric current density. Also,  $\vec{B}$  is the magnetic field inductance,  $\rho, \vec{V}, e_i, P$  are the

plasma density, the velocity, thermal energy and the pressure while  $S_{rad}$  is the radiation heat flux. No viscosity term is considered given the high heating due to the incoming hot plasma.  $Q$  is the power density deposited to the target plasma and the target by the incoming hot SOL plasma by collisional stopping.

If the Poynting vector term  $\vec{\nabla} \frac{\vec{E} \times \vec{B}}{\mu_0}$  and the equation of the magnetic field are rewritten using Ohm's law and Maxwell's equation, the system of equations can be transformed into:

$$\begin{aligned}
\frac{\partial \rho}{\partial t} &= -\vec{\nabla} \cdot \rho \vec{V} = 0 \\
\frac{\partial \rho \vec{V}_x}{\partial t} &= -\vec{\nabla} \cdot \rho V_x \vec{V} - \frac{\partial}{\partial x} \left( P + \frac{B^2}{2\mu_0} \right) + \frac{1}{\mu_0} \left( \vec{B} \vec{\nabla} \right) B_x + F_x \\
\frac{\partial \rho \vec{V}_y}{\partial t} &= -\vec{\nabla} \cdot \rho V_y \vec{V} - \frac{\partial}{\partial x} \left( P + \frac{B^2}{2\mu_0} \right) + \frac{1}{\mu_0} \left( \vec{B} \vec{\nabla} \right) B_y \\
\frac{\partial \rho \vec{V}_z}{\partial t} &= -\vec{\nabla} \cdot \rho V_z \vec{V} + \frac{1}{\mu_0} \left( \vec{B} \vec{\nabla} \right) B_z \\
\frac{\partial}{\partial t} \left\{ \rho e_i + \frac{\rho V^2}{2} + \frac{B^2}{2\mu_0} \right\} + \vec{\nabla} \cdot \left\{ \vec{V} \left( \rho e_i + \frac{\rho V^2}{2} + \frac{B^2}{2\mu_0} \right) + \left( P + \frac{B^2}{2\mu_0} \right) \cdot \vec{V} - \frac{\vec{B}}{\mu_0} \left( \vec{V} \vec{B} \right) \right\} - \vec{\nabla} \cdot \left( \hat{k} \vec{\nabla} T_e \right) + \\
+ \vec{\nabla} \cdot \vec{S}_{Rad} + \frac{\left( \vec{\nabla} \times \vec{B} \right)^2}{\sigma \mu_0^2} + \vec{B} \vec{\nabla} \times \left( \frac{\vec{\nabla} \times \vec{B}}{\sigma \mu_0^2} \right) &= Q
\end{aligned} \tag{2.20}$$

$$\frac{\partial \vec{B}}{\partial t} = \vec{\nabla} \cdot \left( \frac{1}{\sigma \mu_0^2} \vec{\nabla} \vec{B} \right) + \left( \vec{\nabla} \vec{B} \right) \vec{V} - \vec{B} \left( \vec{\nabla} \vec{V} \right) - \left( \vec{V} \vec{\nabla} \right) \vec{B}$$

In the last equation, it is clear that the first term on the right side describes the diffusion while the second describes the convection of the magnetic field. Along the three main axes, the last equation can be written as:



$$\begin{aligned}
\frac{\partial B_x}{\partial t} &= \frac{\partial}{\partial x} \left( \frac{1}{\sigma \mu_0} \frac{\partial B_x}{\partial t} \right) + \frac{\partial}{\partial y} \left( \frac{1}{\sigma \mu_0} \frac{\partial B_x}{\partial t} \right) + \frac{\partial}{\partial y} (B_y V_x - B_x V_y) \\
\frac{\partial B_y}{\partial t} &= \frac{\partial}{\partial x} \left( \frac{1}{\sigma \mu_0} \frac{\partial B_y}{\partial t} \right) + \frac{\partial}{\partial y} \left( \frac{1}{\sigma \mu_0} \frac{\partial B_y}{\partial t} \right) + \frac{\partial}{\partial x} (B_x V_y - B_y V_x) \\
\frac{\partial B_z}{\partial t} &= \frac{\partial}{\partial x} \left( \frac{1}{\sigma \mu_0} \frac{\partial B_z}{\partial t} \right) + \left( \frac{1}{\sigma \mu_0} \frac{\partial B_y}{\partial t} \right) + \frac{\partial}{\partial x} (B_x V_z - B_z V_x) + \frac{\partial}{\partial y} (B_y V_z - B_z V_y)
\end{aligned} \tag{2.21}$$

In the solution of the systems of equations, very important are the boundary conditions imposed to the computational domain. In particular, they need to be imposed on all the four sides of the domain with special consideration to the treatment of the heat transport inside the solid target. It is assumed that the target is a bulk material so that a reflective boundary condition is imposed with the addition of a source due to vaporization. For the “side walls “(still considered as computational domain since the only effective and real wall is the target itself) reflective boundary conditions are chosen.

This means that the plasma expansion is stopped at rigid walls or at the boundary. The artificial mesh created around the computational domain to impose the boundary condition can then be determined assigning to those cells precise values. The momentum perpendicular to the boundary cells has generally opposite sign with respect to the neighboring meshes. All the other values (as temperature, pressure, density or mass associated to the cell) are kept identical to the first mesh while energy is imposed equal to zero.

The value of  $B_x$  is not assumed to be frozen at the graphite target and posed equals to the one in the first computational cell: this is done to consider possible diamagnetic effects.

### 2.3 Radiation Transport and optical properties of plasma

It is the solution to the radiation transport that finally determines the net energy flux arriving onto the target material and consequently the net erosion as well as the final lifetime of the PFC [1, 11]. As vapor becomes thicker and thicker above the target surface, the plasma particles start slowing down more and more up to a point in which they are totally stopped into the vapor cloud. Their energy is then deposited into the cloud causing continuous vapor heating and vapor photon emission. The plasma energy is then indirectly transmitted to the surface through photon radiation. Radiation transport then plays a fundamental role in determining the final parameters for the target and its ability to withstand degrading conditions. The solution of the radiation transport equation and the optical properties of the plasma were implemented from the previous HEIGHTS work [1]. A summary of that work is given below.

For quasi-stationary conditions the transport equation for the radiation has the form [1]:

$$\bar{\Omega}\nabla I_\nu = \eta_\nu - \alpha_\nu I_\nu \quad (2.22)$$

where  $I_\nu$  is the radiation intensity,  $\nu$  is the frequency,  $\eta_\nu$  is the vapor emissivity,  $\bar{\Omega}$  is the solid angle and  $\alpha_\nu$  is the absorption coefficient. Given the highly dynamical development of the disruption/instability process, the radiation process cannot be considered stationary so that the radiation transport equation should be written as:

$$\left[ \frac{1}{c} \frac{\partial}{\partial t} + \vec{n} \cdot \nabla \right] I_\nu = \eta_\nu - \alpha_\nu I_\nu \quad (2.23)$$

Based on the carbon available atomic data, the collisional-radiation (CRE) equilibrium model is used into HEIGHTS-PIC to calculate the ion population balance of the plasma, thermodynamic functions and above all the absorption and emission

coefficient at each time step [1, 11]. Collisional processes include collisional excitation and re-excitation, collisional ionization and three-body recombination. The populations of atomic levels are determined from detailed analysis of collisional and radiative atomic processes. The latter ones can include discrete spontaneous transitions, photo recombination and dielectric recombination. In a collisional process, free electrons transfer energy to bound electrons (excitation and ionization) while in pure radiative processes; photons transfer all their energy to electrons via inverse Bremsstrahlung radiation, photo-excitation and photoionization. Collisional de-excitation, recombination, radiative de-excitation, spontaneous and induced emission, bremsstrahlung and dielectric recombination are all inverse processes.

Using the output results for the level populations just described, the emission and absorption coefficient are calculated evaluating the transition probabilities between the various energetic states. Transitions taken into account are the free-free, bound free and bound-bound type. This last transition produces an emission or absorption of line radiation. Bound-free transitions instead result in continuum recombination radiation and are due to the transitions of electrons from the bound state to the free state.

Typically for values of plasma densities above  $10^{18} \text{ cm}^3$  and relative low temperatures (less than 10 eV for example) plasma can be considered in local thermodynamic equilibrium (LTE). In such conditions, plasma is dominated by recombination and de-excitation processes: Saha equation is used for the calculation of ions concentration, while both emission and absorption coefficient are considered identical. The level populations are calculated using Boltzmann distribution.

For values of plasma densities below  $10^{17} \text{ cm}^3$  instead and temperatures bigger than 10 eV, the LTE approximation cannot be considered valid or applied since recombination, dielectric recombination and radiative de-excitation become much more important and cannot be considered negligible anymore. Non-LTE plasmas exhibit typically a lower ionization degree as well as a population of excited levels. For such reasons the emission coefficients of non-LTE plasmas are smaller.

In optically thin plasmas, the transition frequencies of all atomic processes are dependent solely on density and temperature. For this reason, radiative excitation and ionization processes have a negligible influence. In optically thick plasmas, reabsorption of radiation is occurring. Radiative excitation and ionization have to be calculated as well as their transition probabilities. Both these quantities depend on the local radiation flux, which is typically obtained from the transport calculations: in this case calculations are performed for plasma with constant density and temperature.

Hydrodynamic equations are generally written in form of pressure and internal energy while the equations of radiation transport are generally written in function of the density and temperature. The two processes are solved self-consistently while the equation of state for carbon represents the link between these two processes. The radiation transport equation system also uses additional information regarding the ionic and electronic concentration in the plasma which depend on the populations of atomic levels and charge distribution in each examined cell of the mesh. To solve the radiation transport along each time step, the absorption and emission coefficients are calculated per each cell. They depend on temperature, density and are also function of the frequency of absorbed and emitted elements. The calculation is quite complex since for each computational cell and

for each time step, the populations levels and cross-sections of the atomic processes have to be evaluated. For getting highly accurate results, the populations of atomic levels and ion structure of the plasma need to be calculated. Several assumptions can be made and accounting or not all different atomic processes will influence the degree of confidence of the results. The use of the tabulated values for the energy levels, oscillator strength and other atomic parameters for carbon allows the calculation of photoionization cross-sections and in this way the evaluation of the radiation broadening of spectral lines.

The ionization structure of the plasma and populations of atomic levels can be found using the non-steady kinetic equation typically written as [1, 11]:

$$\frac{dN_i}{dt} = -N_i \sum_{j \neq i} K_{i,j} + \sum_{i \neq j} N_j K_{j,i} \quad (2.24)$$

where  $N_i$  is the population of atomic levels  $i$  produced by the transitions from this level to other level  $j$  (with transition rate equal to  $K_{i,j}$ ) and the transitions from other level  $j$  to the level  $i$  (with transition rate equal to  $K_{j,i}$  this time). If the ground level is  $i$ , then this is the ion concentration in the plasma. To be complete, one equation for each atomic level needs to be written creating a system of equations. If atomic transitions are much faster than the typical thermodynamic processes of the plasma, then the atomic system can be considered in equilibrium for each hydrodynamic step so that the previous equation becomes homogeneous:

$$0 = -N_i \sum_{j \neq i} K_{i,j} + \sum_{i \neq j} N_j K_{j,i} \quad (2.25)$$

so that: 
$$\frac{dN_i}{dt} = 0 \quad (2.26)$$

Since the kinetic rates of radiation and photoionization strictly depend on radiation flux, the equations just seen need to be integrated with frequency-dependent equations of radiation transport which are defined by the radiation process in the whole plasma domain. The problem is then spatially non-local and requires more attention. The CRE approximation in general accounts for collisional processes, photo de-excitation and photo-recombination while it neglects the processes of photo-excitation and photo-ionization. This means that locally the approximation well describes the characteristics of optically thin plasma in a wide range of temperature and density. The model can be further simplified leading to important specific applications as the coronal model. In this approximation excited states are connected only with the ground state so that only collisional excitation and radiation de-excitation are considered. These effects are typical of very hot, optically thick plasmas. The collisional-radiative (CRE) model has been developed to fill the gap of several orders of magnitude in electron density where neither LTE nor corona equilibrium is valid and used in HEIGHTS-PIC because suits the need of the calculation. Collisional transitions as well as radiative decay from higher bound levels are considered united with three-body recombination and radiative recombination. This methodology is complicated and computationally very intensive but also quite accurate.

Transition rates  $K_{i,j}$  are defined by the interplay of radiative and collisional processes. Different transitions are described by different processes: the transition to continuum spectrum is defined by the electronic collisional ionization while the discrete transitions from lower level to higher levels are described by the electronic collisional excitation. The rate of transitions to the lower level can be obtained from the radiative spontaneous transitions and electronic collisional de-excitation. The recombination rate is calculated

taking into account dielectronic recombination, three-body recombination and photo-recombination. The first one in particular, is determined by the ion capture of an electron and concurrent excitation of the associated electron: this leads to a spontaneous transition to the ground state. Also in the calculation for the ionization and excitation rates the radiative processes of photo-excitation and photoionization need to be considered. This complicates the sets of equation since the processes are generally defined by non-local plasma properties (inserted as inputs) making the solution of the algorithm quite complex.

For calculating the opacities of the plasma acting on the entire computational mesh, it is important to evaluate all three main contributions coming from the Bremsstrahlung radiation, the photo-ionization from the ground, excited and inner cells, and finally the discrete transitions. Each effect is described by the corresponding cross section which needs to be evaluated. The profiles of spectral lines need special attention since all broadening mechanisms (Doppler, Stark and radiation) might be important according to the conditions of the plasma. So in the CRE approximation, the total absorption coefficient  $K_{TOT}$  depends on local values of density  $\rho$ , the temperature  $T$  the ionization  $Z$  of the plasma. The total value is calculated summing up the contribution from each free-free transition, bound-free and bound-bound transitions and can be written typically as:

$$k_{tot}(\rho, T, h\nu) = k_{free\ free}(\rho, T, h\nu) + k_{bound\ free}(\rho, T, h\nu) + k_{bound\ bound}(\rho, T, h\nu) \quad (2.27)$$

$$k_{free\ free}(\rho, T, h\nu) = N_e(T, \rho) \times \sum_i \sigma_i^{ff}(T, h\nu) (1 - e^{-h\nu/kT}) \times N_i(T, \rho)$$

$$k_{bound\ free}(\rho, T, h\nu) = \sum_i \sum_j \sigma_{i,j}^{bf}(h\nu) \times N_{i,j}(T, \rho) \quad (2.28)$$

$$k_{bound\ bound}(\rho, T, h\nu) = \sum_i \sum_j \sigma_{i,j}^{bb}(h\nu) \times N_{i,j}(T, \rho)$$

with  $i$  and  $j$  the energy states :  $j$  is the excitation level while  $i$  is the ionization state.

Special attention should be put in calculating the line profile due to broadenings mechanisms. Atomic and ionic spectral lines originate from specified electronic transitions between very well defined energy levels of atoms and ions. The lines though are not sharp because of several broadening mechanics so that the effective line has a finite width. The mechanisms that contribute to the finite width of the line profile are four: natural broadening, Doppler broadening, Stark broadening, and interaction with neighboring particles. Natural broadening arises from the finite lifetime of an ion in some given state which leads to the corresponding energy spectrum. Radiation damping always exist even though often is not a very effective broadening mechanism. Doppler broadening is due to the thermal motion of the emitting or absorbing atoms. It results in shifting the wavelength of moving radiating particles. Stark broadening appears due to the presence of an external static electric field, which acts on electrons of an atom in any moment. Fast changes of the field result in a splitting effect. The broadening of the Stark effect can be significant with respect to the natural one. It is also important to notice that collisional broadening is negligible at temperature below 1 eV because plasma is essentially composed by neutral atoms at that stage and electronic density is also very low (low temperature plasma). Doppler broadening in such plasma is more important but still quite small at low temperatures. In highly ionized and moderately dense plasmas (as in tokamaks) Stark broadening is definitely the dominant effect and becomes more and more effective as temperature and density rise. In fact the energy levels within a single atom may be modified due to the electric field of nearby atoms or ions.

The CRE model well describes the optically thin steady state plasma. However, in



in presence of optically thick plasma or external energy applied, the CRE model needs modifications so that the model becomes self-consistent and non-local. Additional effects are added in HEIGHTS-PIC case and they generally depend on the initial state of the problem. In particular, the photoionization process is particularly important in the description of plasmas with high temperature gradients and only if an outer plasma source is present since plasma cannot generate radiation that is energetically higher than the ionization potential of its major ion.

For both continuum radiation and line radiation, the set of self-consistent equations are given in the following paragraphs and can be checked using references [4-9].

### 2.3.1 Continuum radiation transport

The system of equations describing energy transport by the continuum radiation is based on the followings [1]:

$$\frac{1}{c} \frac{\partial I_\nu}{\partial t} + \vec{\Omega} \cdot \nabla I_\nu = -(\alpha_\nu I_\nu - \eta_\nu) = -\alpha_\nu (I_\nu - S_\nu) \quad (2.29)$$

associated with the material energy equation :

$$\frac{\partial E}{\partial t} = 4\pi \int \alpha_\nu (J_\nu - S_\nu) d\nu + Q \quad (2.30)$$

where as before,  $I_\nu$  is the radiation intensity,  $\nu$  is the frequency ,  $\eta_\nu$  is the vapor emissivity,  $\vec{\Omega}$  is the solid angle and  $\alpha_\nu$  is the absorption coefficient, Q represents other energy sources and  $J_\nu$  is the angle-averaged radiation intensity:

$$J_\nu = \frac{1}{4\pi} \int I_\nu d\Omega \quad (2.31)$$

and  $S_\nu = \eta_\nu / \alpha_\nu$  is the source function. In LTE, the source function is the Plank function  $B_\nu$  and depends only on temperature.

Discretizing in time and linearizing about the actual temperature  $T_0$  the material energy equation:

$$c_T(T - T_0) = \Delta t \int \alpha_\nu (J_\nu - S_\nu^0) d\nu + Q \Delta t \quad (2.32)$$

where  $c_T$  is the specific heat for the total system of matter and radiation. Combining this equation with linearized version of the transport, it follows:

$$\begin{aligned} \frac{1}{c} \frac{I_\nu - I_\nu^0}{\Delta t} + \vec{\Omega} \cdot \nabla I_\nu &= -\alpha_\nu (I_\nu - S_\nu^0) + \alpha_\nu \frac{\partial S_\nu}{\partial T} (T - T^0) = \\ &= -\alpha_\nu (I_\nu - S_\nu^0) + \frac{\Delta t}{c_T} \alpha_\nu \frac{\partial S_\nu}{\partial T} \int \alpha_\nu (J_\nu - S_\nu^0) d\nu + Q \frac{\Delta t}{c_T} \alpha_\nu \frac{\partial S_\nu}{\partial T} \end{aligned} \quad (2.33)$$

In this equation the integral term couple together intensities for all frequencies and for all angles. In our case, the entire space is divided into 8 fundamental directions or rays and the equation solved for each single one accounting for a portion of the real diffusion and movement of the radiation field.

### 2.3.2 Line Radiation Transport

In this case, the fundamental equation for radiation transport is combined with the atomics kinetics rate equation [1, 10]:

$$\begin{aligned} \frac{1}{c} \frac{\partial I_\nu}{\partial t} + \vec{\Omega} \cdot \nabla I_\nu &= -(\alpha_\nu I_\nu - \eta_\nu) = -\alpha_\nu (I_\nu - S_\nu) \\ \frac{dY}{dt} &= AY \end{aligned} \quad (2.34)$$

where  $Y$  is the vector representing the population densities of the atomic levels and  $A$  is the rate matrix. The total rate  $A_{ij}$  connecting two generic atomic levels  $i$  and  $j$ , includes all collisional and radiative transitions both discrete (bound – bound) and continuous (free-bound). The different populations respond to radiation through the effects on the transition rates. Both absorption and emission coefficients are calculated similarly to the procedure explained in [10]. The entire system of equations of HEIGHTS-PIC is well explained and summarized in [11].

## References

1. A. HASSANEIN and I. KONKASHBAEV, "Modeling Plasma Material Interactions during a Tokamak Disruption", ANL/FPP/TM-271,1994
2. A.M. HASSANEIN, "On the numerical solution with applications to two moving boundary heat conduction problems", Proceedings of ASME/JSME Thermal Engineering J. C., 1991.
3. A. HASSANEIN, "Simulation of Plasma Disruption induced Melting and Vaporization by ion or electron beam", Journal of Nuclear Materials, 122 & 123, 1453, 1984.
4. D. MIHALAS, "Stellar atmospheres", San Francisco, W.H. Freeman & Co., 1978.
5. MIHALAS & MIHALAS, "Foundations of Radiation Hydrodynamics", New York, Oxford University Press, 1984.
6. JOHN CASTOR, "Radiation Hydrodynamics", Cambridge University Press, 2004.
7. SOBELMAN, I.I., "Atomic Spectra and Radiative Transitions", Springer-Verlag, Berlin, 1979.
8. JACQUELINE, LENOBLE, "Radiative Transfer in Scattering and Absorbing Atmospheres: Standard Computational procedures", A. Deepak Publishing, 1985.
9. G.C. POMRANING, "The Equations of Radiation Hydrodynamics", Pergamon Press, 1973.
10. V. MOROZOV, V. TOLKACH and A. HASSANEIN, "Calculation of Tin atomic data and plasma properties", Argonne National Lab Report, ANL-ET-04/24 Argonne, Illinois, 2004.

11. F. GENCO and A. HASSANEIN, "Particle-in-Cell (PIC) Methods in predicting materials behavior during high power deposition". Submitted to *Laser and Particle Beams*, Cambridge University Press, Accepted for Publications, November 2013.

## CHAPTER 3. HEIGHTS-PIC CODE STRUCTURE

### 3.1 Introduction

HEIGHTS-PIC is a FORTRAN code composed of 1 main program and 44 subroutines solving the entire problem of highly energetic tokamaks plasma impinging on a carbon divertor plate, eroding the material and then interacting with the vapor cloud formed and expanding as a consequence. In this section the entire code will be explained and motivated showing the entire logical and mathematical structure.

Before starting explaining the logical flow chart of the code (see Appendix A), it is important to review some of the fundamental assumptions made to develop HEIGHTS-PIC. First of all the geometry used is based on a natural distribution of the three axis (X, Y and Z). The first one (X-axis, fig. 3.1 and 3.2) is perpendicular to the divertor plate and it will provide a spatial measure of the evolution of the plasma above the target. The Y-axis is the radial direction of the toroid and is also the “poloidal direction” for the B field. The Z-axis instead represents the toroidal direction for the B field. The computational grid (fig. 3.2) where the mesh will be placed is so perpendicular to the plate and provides a spatial projection of the plasma movement along time.

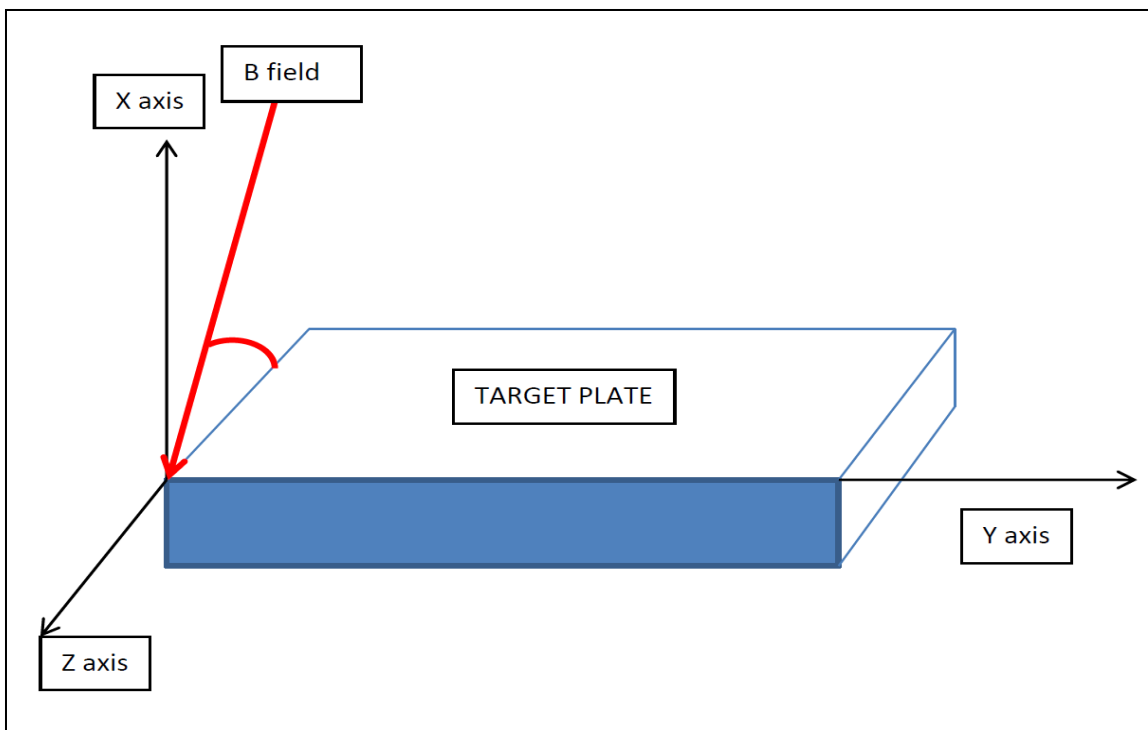


Figure 3.1 Schematic illustration of HEIGHTS – PIC geometry and axes [7]

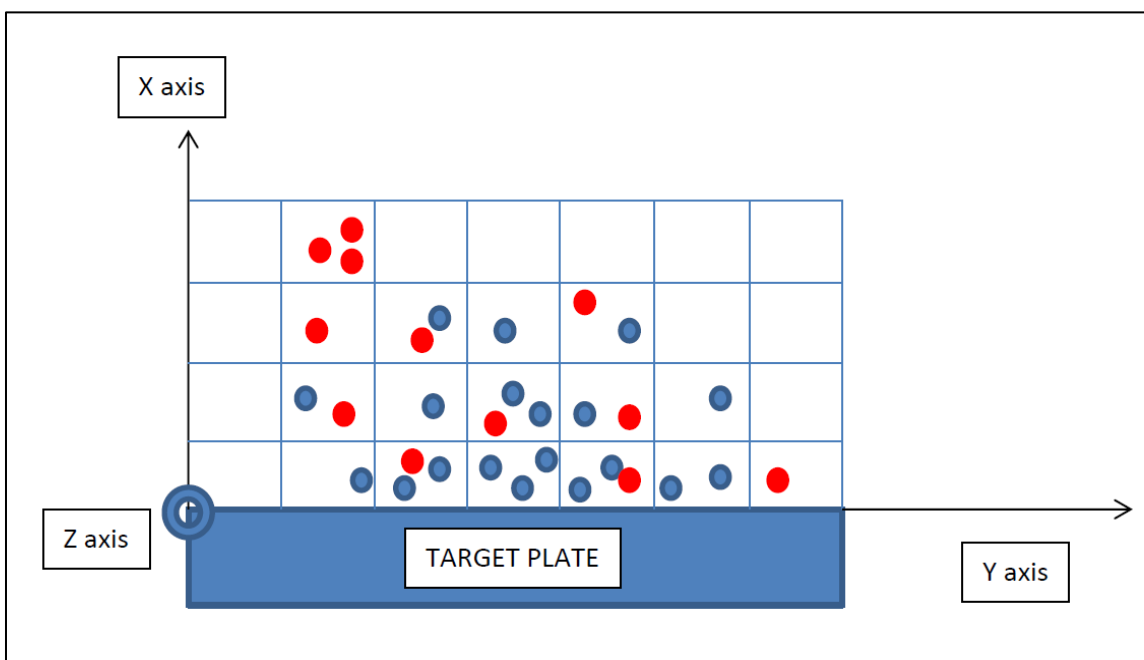


Figure 3.2 Schematic illustration of HEIGHTS – PIC geometry, axes, and grid distribution.

The mesh is formed by rectangular cells having X and Y components. The number of cells along X and Y can be chosen arbitrarily, as the inclination of the divertor plate with respect to the natural axis  $X_{nat}$  and  $Y_{nat}$  (fig. 3.3).

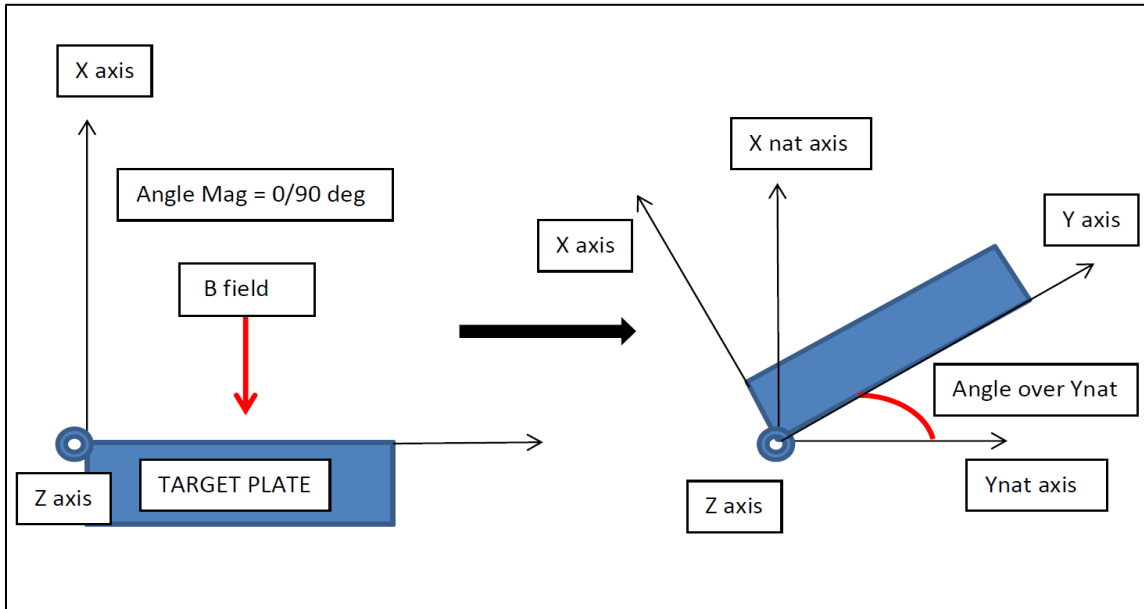


Figure 3.3 Schematic illustration of HEIGHTS – PIC geometry and axes with angle [7].

The toroidal angle (or magnetic angle) can also be chosen and it is the angle between the B field and the divertor plate.

The initial state of the computational mesh is defined having some cells (the ones directly facing the divertor or target plate) filled with neutral vapor with a specified initial density. Some important assumptions regard the absence of motion along the Y-axis as the fact that the beam energy is deposited and absorbed according to the range of ions.



### 3.2 Main assumptions

The plasma disruption is then numerically “interpreted” as a beam of energy with specified characteristics as the shape, flux, and maximum intensity. In particular HEIGHTS-PIC supports so far three fundamental beam shape as the uniform one, the Gaussian one and the exponential one with peak close to the striking point on the divertor. The plasma beam acts similarly to a “thermal imprint” onto the target surface. Given those assumptions, the particle motion will be onto the X-Y plane with diffusion across the B field along the X direction. In this particular case, using the Braginskii equations [1], it is easy to verify that for the given ITER operating conditions, heat conduction across the B field can be considered negligible leading to the fact that only  $K_{\parallel}$  is significant (fig. 3.4).

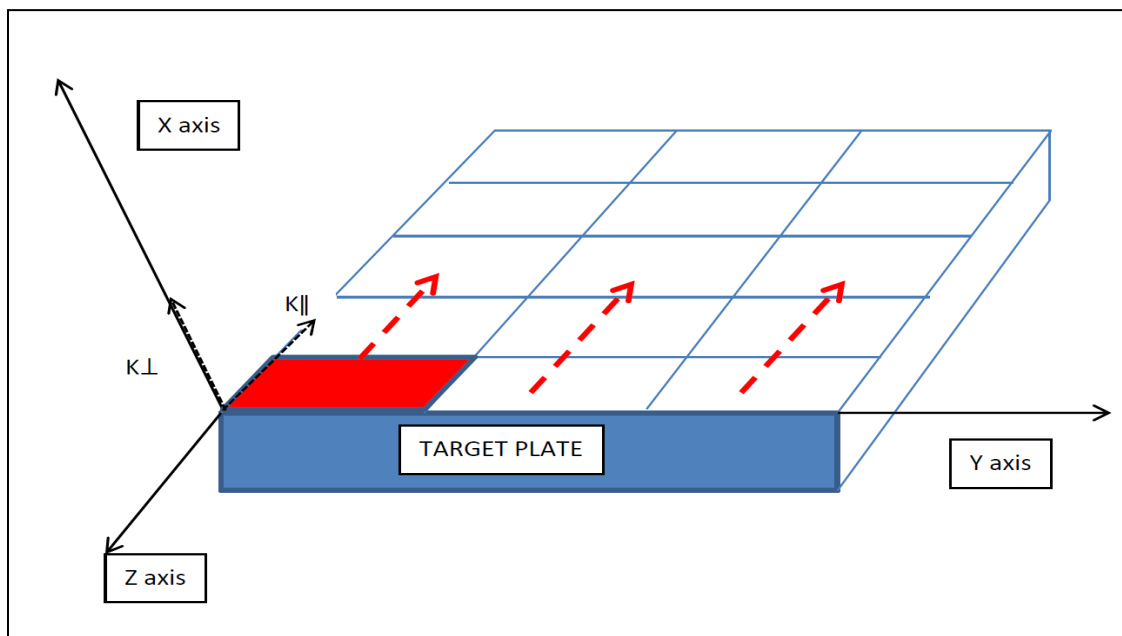


Figure 3.4 Schematic illustration of HEIGHTS – PIC geometry, axes, and diffusion across B magnetic field

Sample particles or super particles are assumed to have a finite size dimension (1D) which is generally provided by the dimension of the cell (along Y) divided by the number of initially loaded particles. It is useful to remember that the code is developed in such way that particles are arranged in a “layered” way respecting always this configuration during their evolution and eventually piling up in layers along the other direction, which is X. For this reason the values of the “layers” along the X direction change per each cell of the mesh dynamically along time and due both for the motion and the eventual new production of new particles. Whenever the mass of vapor exceeds a pre-established value a new super particle is produced. This pre-established value of mass can be changed defying the results more accurately according to how much mass a single super particle effectively represents.

The particles methodology used in HEIGHTS–PIC is similar to the one identified by Belotserkovskii and Davidov [2-3] called “coarse particle method”. In fact, the original differential equations describing the physics of the phenomena are split according to the physical processes they represent. The method has been widely used in the past to solve gas-dynamic flows, diffraction problems and transonic flows. The classical Particle–in-cell sub steps are present: Eulerian, Lagrangian, and a final one. In the first one, the internal variation of a sub- system is evaluated. Davydov calls this subsystem “large particle” [2]. At this stage, the fluid is considered constrained and only quantities of the cell are modified allowing the cancellation of the convective terms (as the divergence of density, velocity, etc.). Translational effects are then absent in this stage and the density can be considered “frozen” [2, 4]. The motion of the subsystem is analyzed into the Lagrangian and final phase leaving the interior state unchanged. The mass flow through

the boundaries is assumed to be moving only with component perpendicular to the boundary itself in such way that:

$$\Delta M_{i+1/2,j}^n = \langle \rho_{i+1/2,j}^n \rangle \langle u_{i+1/2,j}^n \rangle \Delta y \Delta t \quad (4.1)$$

It is important to notice that  $\rho$  and  $u$  are quantities at the cell boundaries. According to Davydov the choice of these parameters is extremely important for the stability of the system and the accuracy of the general computation. Various schemes exist and various approximations can be used also for momentum and energy flows.

The final step the fields Eulerian parameters for the flow are found at the time  $t^{n+1} = t^n + \Delta t$ . The conservation of mass, momentum and energy are applied. The conservation is insured by the total energy  $E$ . This methodology can be considered as a different application of the splitting method [2]. A similar application had been developed by Anuchina [5], still using the splitting method as development of the Harlow's particle in cell original one for solving gasdynamical problems involving large deformations. In that case, though sample particles were effectively considered having a geometrical dimension: both one-dimensional and two-dimensional particles are examined in order to reduce the fluctuations especially in the Eulerian step of the methodology. In our case, HEIGHTS-PIC uses one-dimensional particles which are arranged in "layers" along the cell which is subdivided along the Y-axis  $n$  times. Each particle occupies one segment and when more are produced or transported they are simply allocated one on top of the other but without a physical dimension along the X-axis. The particles are not cylindrical (as in [5] nor spherical or quadrangular as in [6]). Also the system is "constantly fed" through the melting and evaporating boundary at the

target plate while particles reaching the left or right side of the computational domain might be “lost” by the system. Also, in the computational solution, for the upper boundary, only cells effectively “filled” in with particles are calculated.

## References

1. S.L. BRAGINSKJI, Transport phenomena in plasmas. In: "The problems of plasma theory" edited by M.A. Leontovitch, 'Atomizdat', Vol. 1, p. 183. (in Russian), 1963.
2. O.M. BELOZERKOVSKY, YU.M., DAVIDOV, "Non-stationary 'COARSE PARTICLE' Method for Gas Dynamical Computations, Moscow, 1970.
3. O.M. BELOZERKOVSKY, YU.M. DAVIDOV, "The method of large particles in gas dynamics", M. Nauka, (in Russian), 1982.
4. H. WURZ et al., "Hot Plasma Target Interaction and Quantification of Erosion of the ITER Slot Divertor during Disruptions and ELM", FZKA 6198, Karlsruhe, Germany, 1999.
5. N.N. ANUCHINA, V.E., PRETENKO et al., "On numerical methods of solving Gas dynamical problems with large deformations", Fluid Dynamics Transactions, 5, p. 9-32, 1969.
6. E.V. VOROZHTSOV, "On the Influence of shape and dimensions of particles on the properties of the modified particle-in-cell Method", Computers and Fluids, 9, p. 313-326, 1981.
7. F. GENCO and A. HASSANEIN, "Particle-in-Cell (PIC) Methods in predicting materials behavior during high power deposition". Submitted to Laser and Particle Beams, Cambridge University Press, Accepted for Publications, November 2013.

## CHAPTER 4. RESULTS AND BENCHMARKING

### 4.1 Introduction

Several experiments have been performed with magnetized plasma streams in order to reproduce similar conditions to the ones presents during an ELM and/or Tokamak disruptions. In particular, at TRINITI in Troitsk, Russian Federation and at the QSPA facility in Kharkov, Ukraine several experiments have been done aiming to study experimentally the behavior and performance of high temperature magnetized plasma with different target materials [1-3]. Even though, those facilities can reproduce similar heat loads on plasma facing components effectively present in tokamaks, some of the other conditions as strength of the magnetic field, pulse duration and energy density can differ significantly leading to very different results in target erosion. Results need then to be carefully and critically interpreted with respect to tokamak relevant conditions.

Pulsed plasma gun MK-200UG generates plasma with ion energy  $E_i \geq 1keV$  and density  $n = 1 - 5 \times 10^{15} \text{ cm}^{-3}$ . The magnetic field provided in the machine is, in proximity of the target, equal to 2 T. The pulse is typically relatively short in duration (40 – 50  $\mu s$ ). The basic scheme of the MK-200 is shown in Fig.4.1 [1].

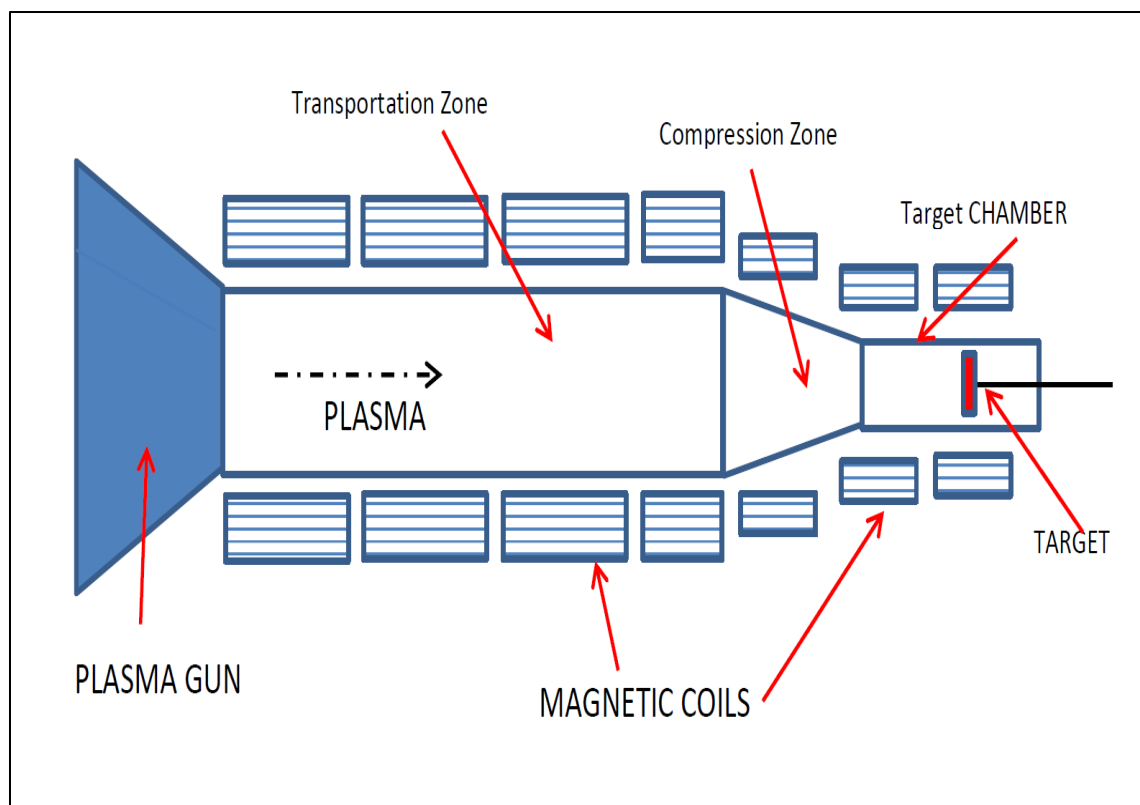


Figure 4.1 Basic scheme of the MK-200UG machine used in Troitsk, Russia [1]

The facility consists of a pulsed plasma gun, a long drift tube and a target chamber. Hydrogen plasma is typically injected into the drift tube where the plasma is compressed and magnetized. The scheme of the MK-200 CUSP is similar even though the drift tube is much smaller making some of the plasma parameters at target different. The ion energy is maximum equal to 1 keV while the pulse duration is much shorter (7-12  $\mu\text{s}$ ).

The energy densities of the two plasma guns are comparable (1400  $\text{J}/\text{cm}^2$  vs. 1500  $\text{J}/\text{cm}^2$ ) while the peak magnetic field at the target can be higher in the MK-200 CUSP (3.3 T vs. 2.0 T for the MK-200 UG) [1].

In the QSPA the typical values of the magnetic field are around 0.55 T while the pulse duration can be much longer (from 200-300  $\mu\text{s}$  up 600  $\mu\text{s}$ ). Energy density is typically equal to 700 J/cm<sup>2</sup> [3].

The results available in the literature from the MK-200 UG have been used to do a first benchmarking of HEIGHTS-PIC code.

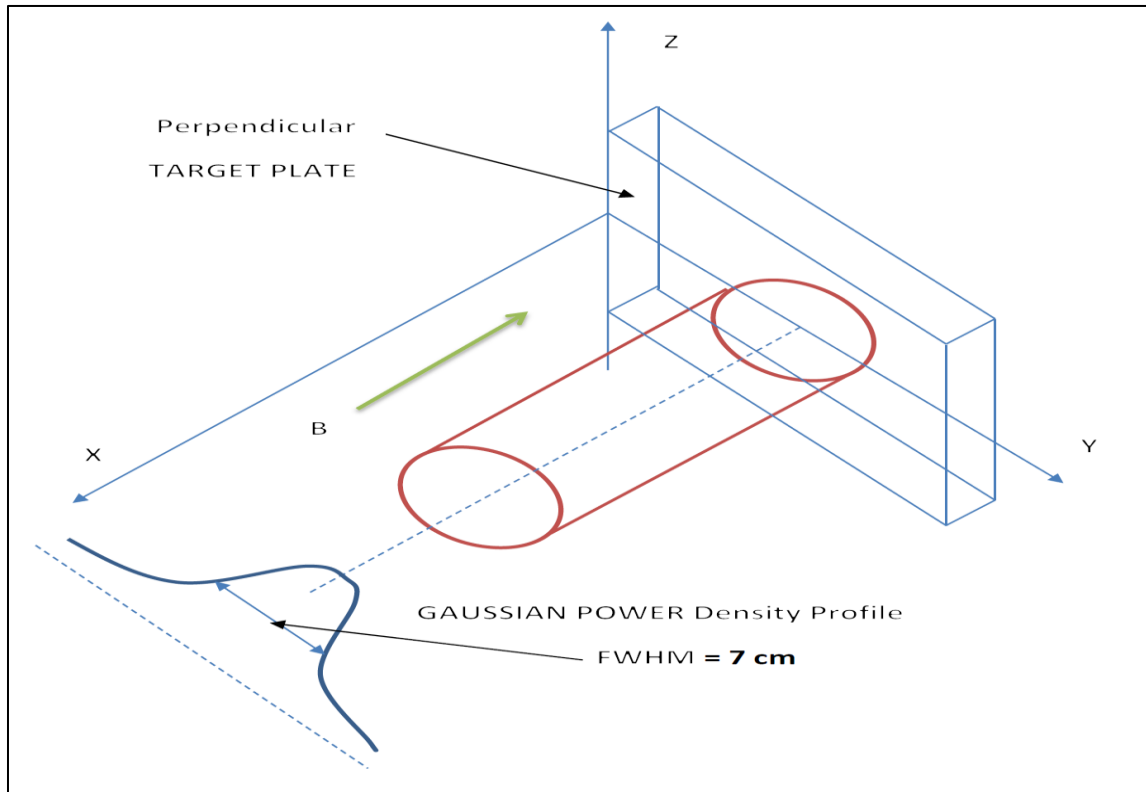


Figure 4.2 Basic geometrical scheme used in HEIGHTS-PIC benchmarking [41]

The results also available from other similar computer packages as FOREV-1/FOREV-2 [5-6] and have been used to compare the behavior of HEIGHTS-PIC computer package for off-normal conditions relevant to tokamaks. In the following sections, comparisons with experiments are critically evaluated and discussed. A geometrical configuration as close as possible to the MK-200UG plasma gun experiments is used in



HEIGHTS-PIC (fig.4.2) which is also similar compared to the one used into FOREV-1/FOREV-2 [5-6].

Then an entire section is dedicated to the comparisons with HEIGHTS computer package [9] results produced for an ELM event with respect to ITER relevant conditions.

HEIGHTS-PIC was then modified to perform laser numerical experiments to provide more comparisons for benchmarking. The last section of this chapter is dedicated to Laser comparisons done using several data published in the literature for laser experiments [23-25, 27, 32] and also using some in-house experiments performed using a ND:YAG laser of the CMUXE laboratory at Purdue University .

#### 4.2 Benchmark with the MK200-UG facility Experiments

In evaluating the conditions present in the MK-200 UG facility, particular attention has been given to interpret numerically both the beam shape and its progress along time. It assumed for the simulations run with HEIGHTS-PIC that the beam has a Gaussian shape power density profile with full width half maximum of 7.0 cm. The peak of the power density is equal to  $35 \text{ MW/cm}^2$  and the total working time for the plasma gun is 50  $\mu\text{s}$ . In the MK200 plasma gun, the time evolution of the power density provided has been interpreted for our calculations in three different ways. In fact, it is highly probable that the gun does not reach immediately full power (case with a quadratic beam shape along time or case 1 figure 4.3) but more rather achieves the peak with a slow but liner increase [12].

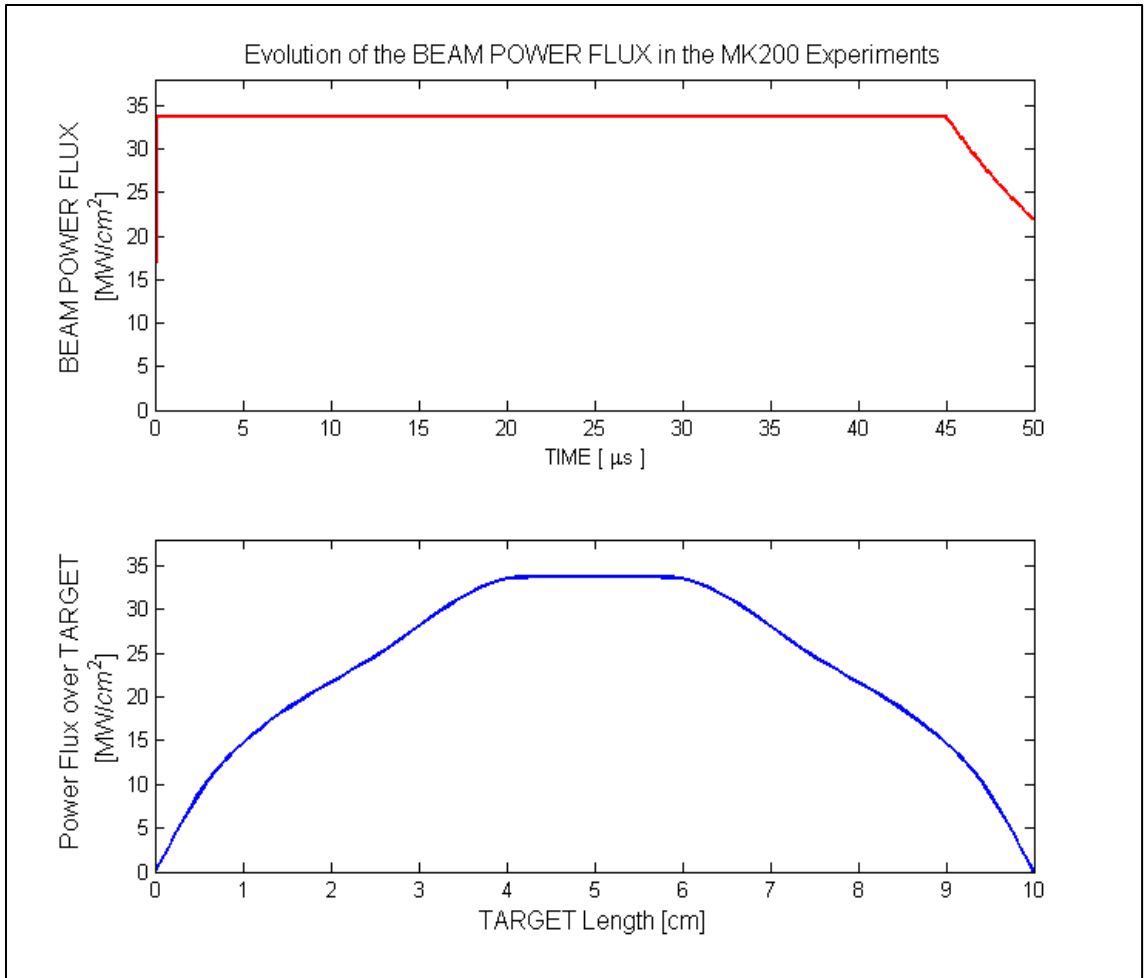


Figure 4.3 Evolution along time of the beam power flux over the target plate: step beam rise with only 6 cells along the target plate (step rise)

For this reason two different linear rises were chosen for the beam: 5 μs and 10 μs as shown in figure (4.4 and 4.5). It is also probable that the beam is not kept at the peak for most of the time but rather starts “fading” just before the end of the experiment. For this reason an exponential fading profile has been chosen for the last part of the beam evolution starting at 45 μs. For both linear rises cases the beam remains at its maximum power for 15 μs.

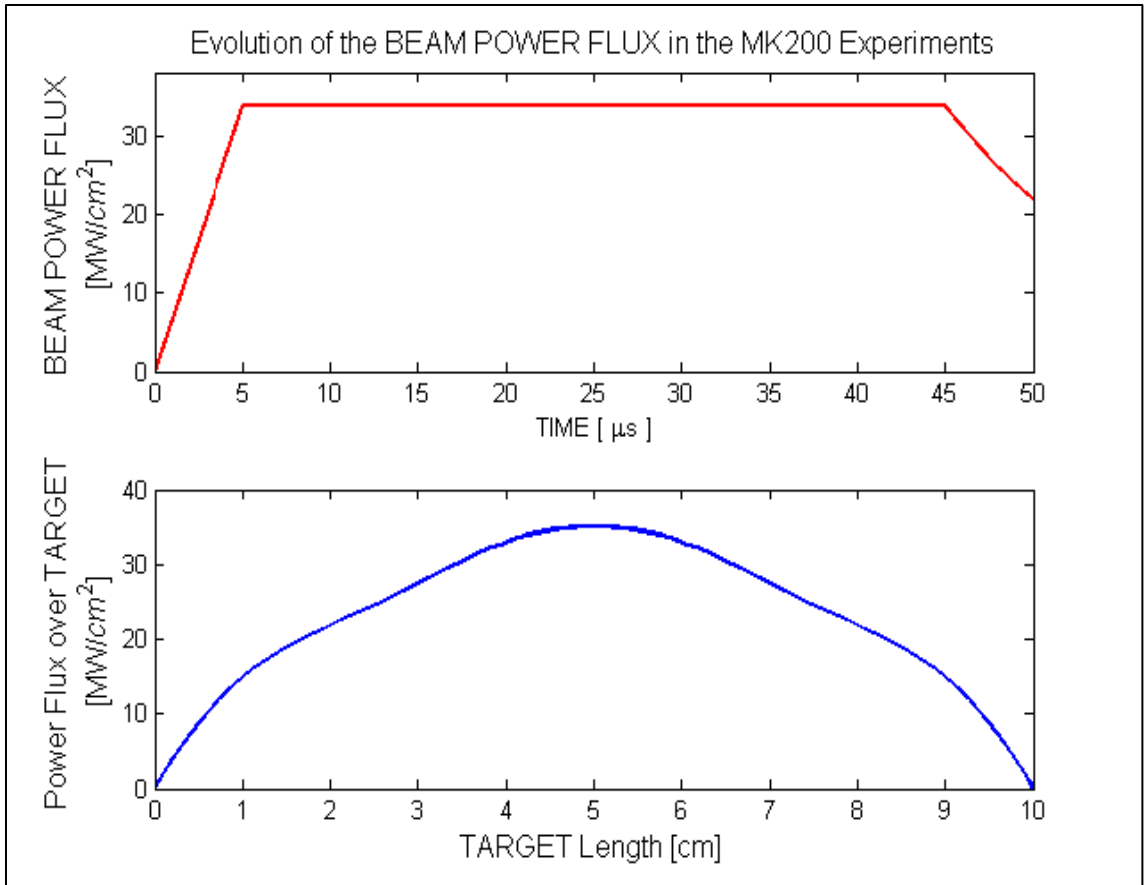


Figure 4.4 Evolution along time of the beam power flux over the target plate: beam rise 5  $\mu\text{s}$  (with 18 cells along the target plate)

The beam time evolution is an important factor for calculating the final erosion as well as the total hydrodynamics evolution of the plasma-vapor system. Besides the computational mesh used for mapping the space over the target plate (in terms of number of cells) is critical for both accuracy and computational time. In the simulations here presented while along the X (perpendicular) axis the number of cells was the same, it was varied along Y axis. The incoming beam was then more and more close to reality and the simulations smoother and smoother.

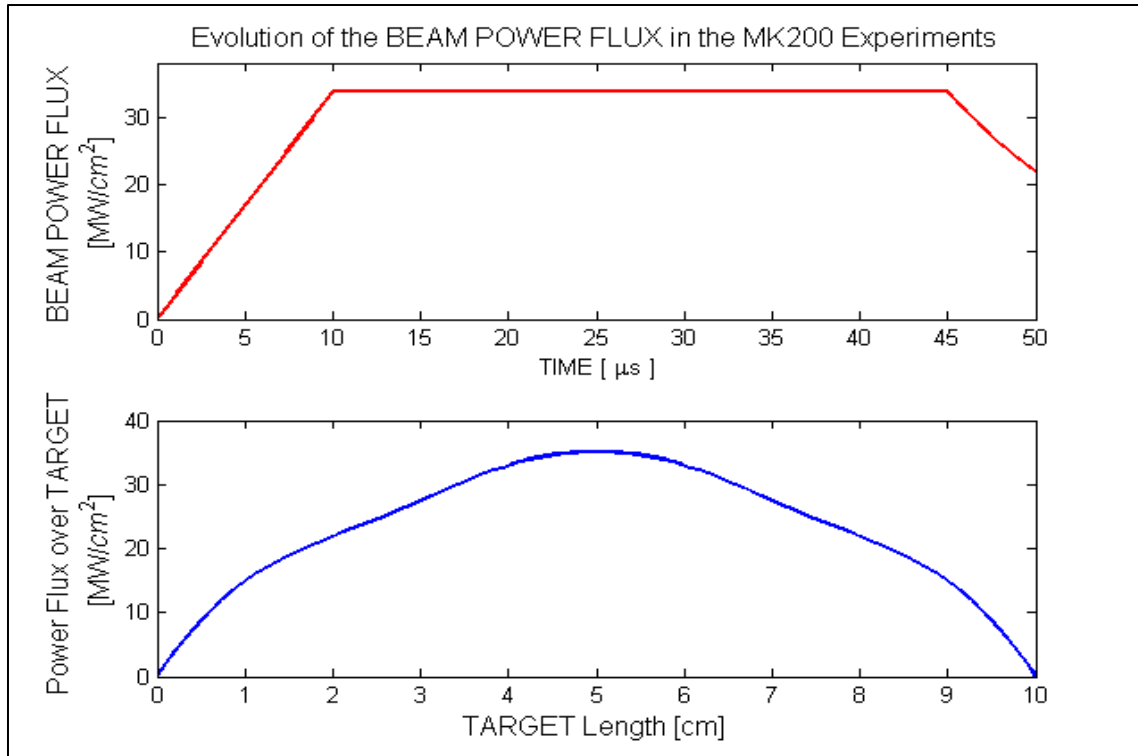


Figure 4.5 Evolution along time of the beam power flux over the target plate: beam rise  
10  $\mu\text{s}$  (with 18 cells along the target plate)

The total energy provided in the three temporal profiles differs for a number close to 7%. This fact though does not make results very different from each other as it will be shown later. The guiding magnetic field for all cases is 2 T at the target position and as used in the experiments. The target dimensions were 10 cm by 10 cm. Also, in order to verify some of the characteristics of the new PIC technique used into HEIGHTS-PIC, several simulations have been run using different initial particle loadings. In all simulations results here presented, the computational grid was formed by 30 cells perpendicular to the plate and 10 or 20 along the target itself making the dimension of single cell of 1.0 cm x 0.5 cm or 0.5 cm in each direction. Also several adjustments have

been done in order to find the ideal dt which stabilizes the calculations into the loops providing at the same time the level of accuracy required.

4.2.1 Erosion and Carbon Surface Temperature

The evolution of the erosion of the carbon target plane can be seen in the following figures (fig. 4.6, 4.7, and 4.8). As plasma energy reaches the plate, the temperature of the

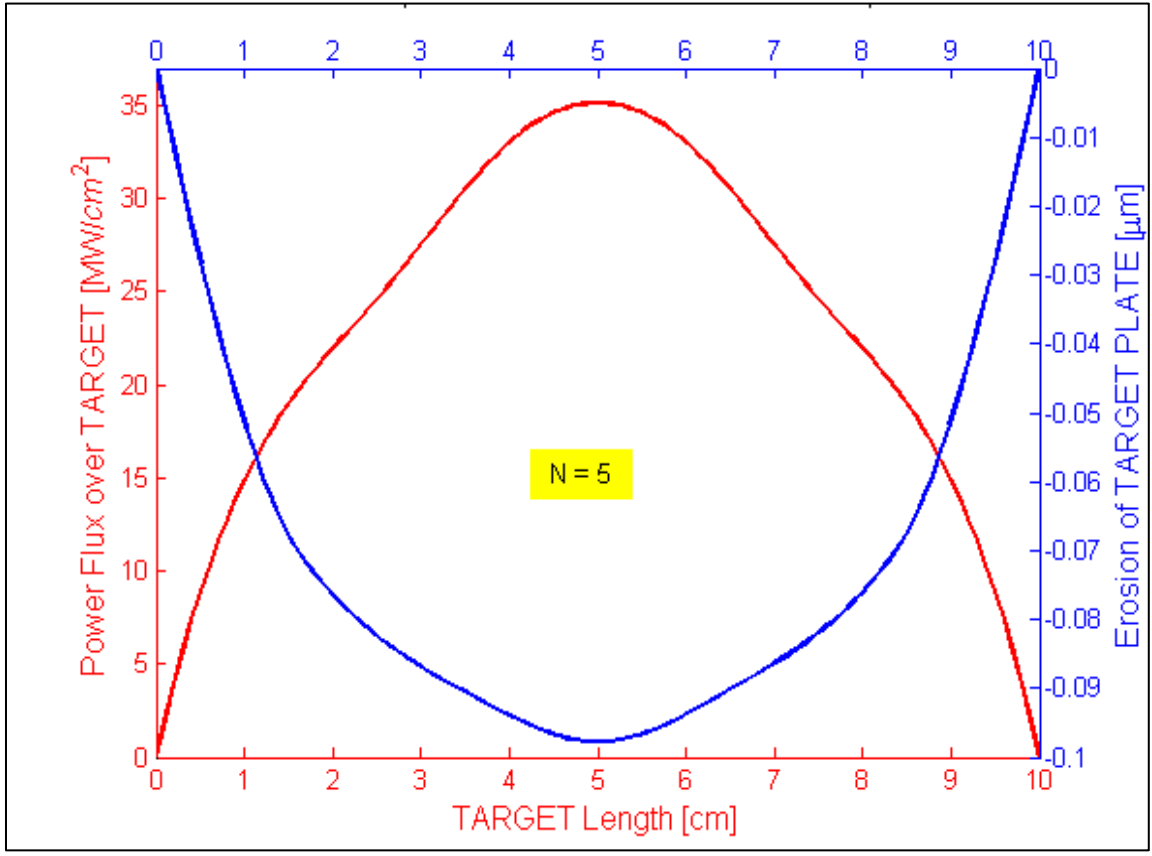


Figure 4.6 Calculated erosion profile (step rise) in a typical MK-200 experiment simulation with HEIGHTS- PIC (5 sample particles initial loading).

solid carbon increases reaching fast the sublimation point (for carbon in these conditions there is no melting phase) after which carbon particles are emitted from the surface.

Close to the target density increases and vapor-plasma interaction also starts. As we can see from the figure number 4.8, even though the final erosion profiles look all similar in shape, they provide final erosion values according to the number of initial neutral vapor

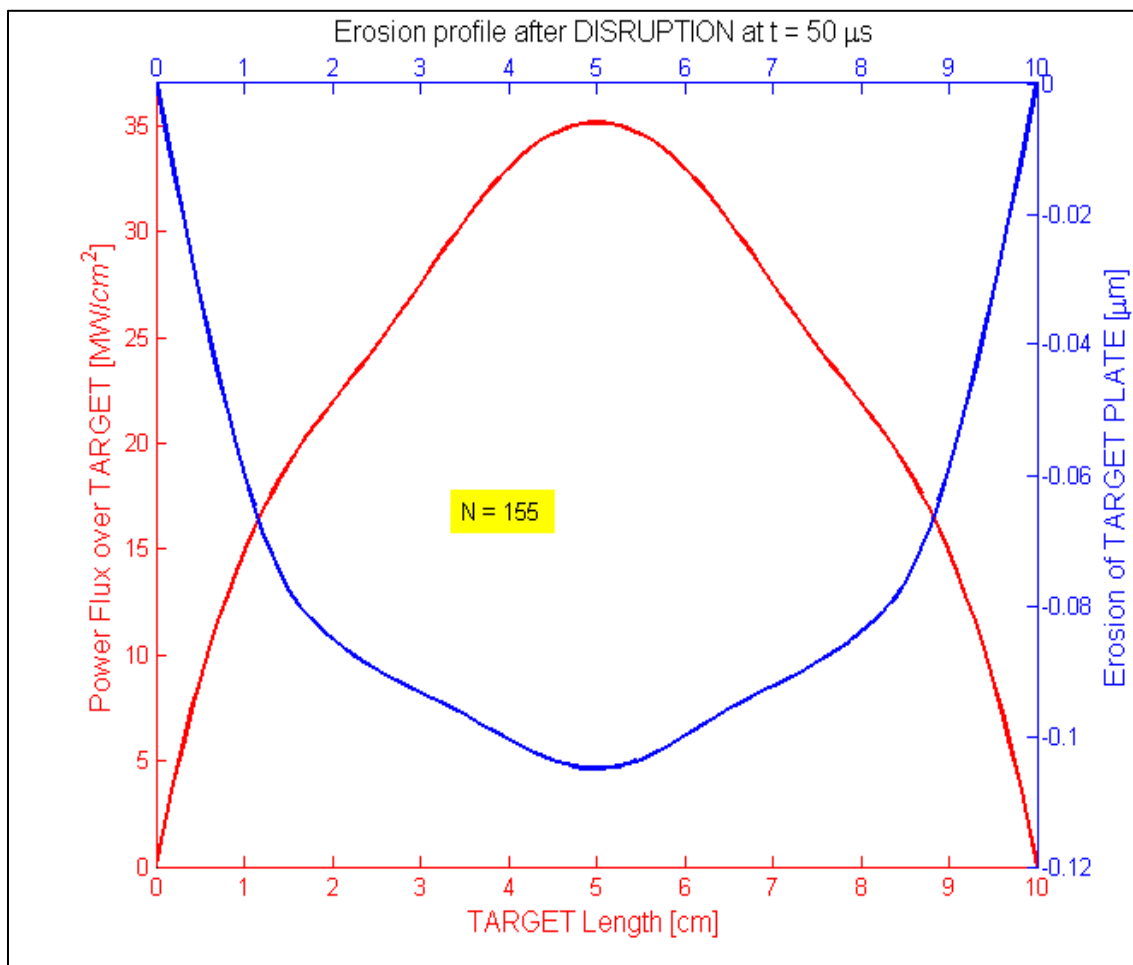


Figure 4.7 Calculated erosion profile (step rise) in a typical MK-200 experiment simulation with HEIGHTS-PIC (155 sample particles initial loading).

particle loading per cell. If not enough sample or big particles are provided, the results are not so accurate. As the number of particles increases (in this case from 5 to 155 sample ones), results become more accurate ( $= 0.114 \mu\text{m}$ ) and closer to the measured

value of 0.10  $\mu\text{m}$  for pure carbon [1, 3, 7]. The same calculation though seems to provide an erosion value much lower of the one reported for the MPG8, which a doped Russian tokamak graphite reported at 0.40  $\mu\text{m}$  for the same conditions.

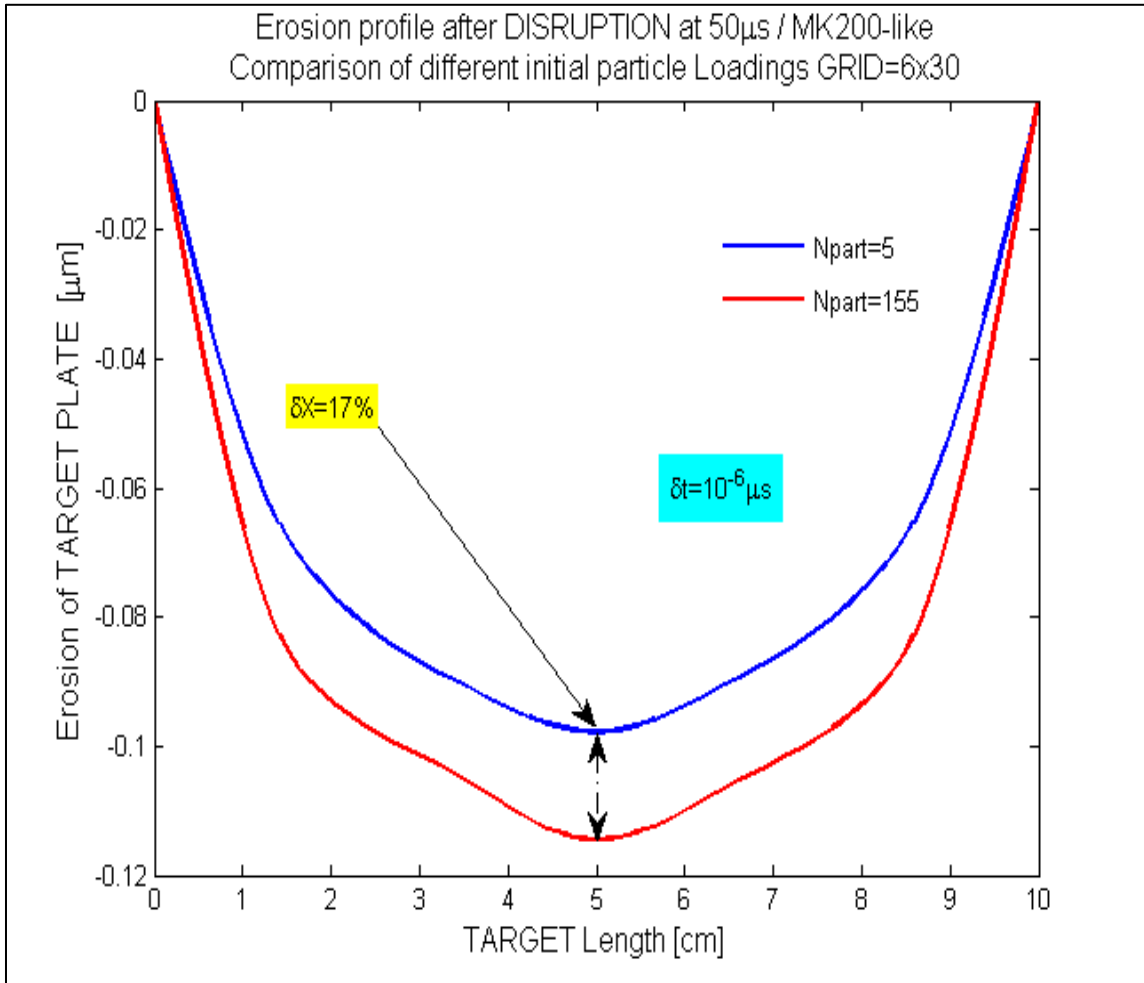


Figure 4.8 Calculated erosion profile (step rise) in a typical MK-200 experiment simulation with HEIGHTS- PIC (5 vs. 155 sample particles initial loading).

Looking at the evolution of the erosion along time, it is immediately evident that even if the trend for both simulations (N=5 particles vs. N=155 particles) is the same, the latter

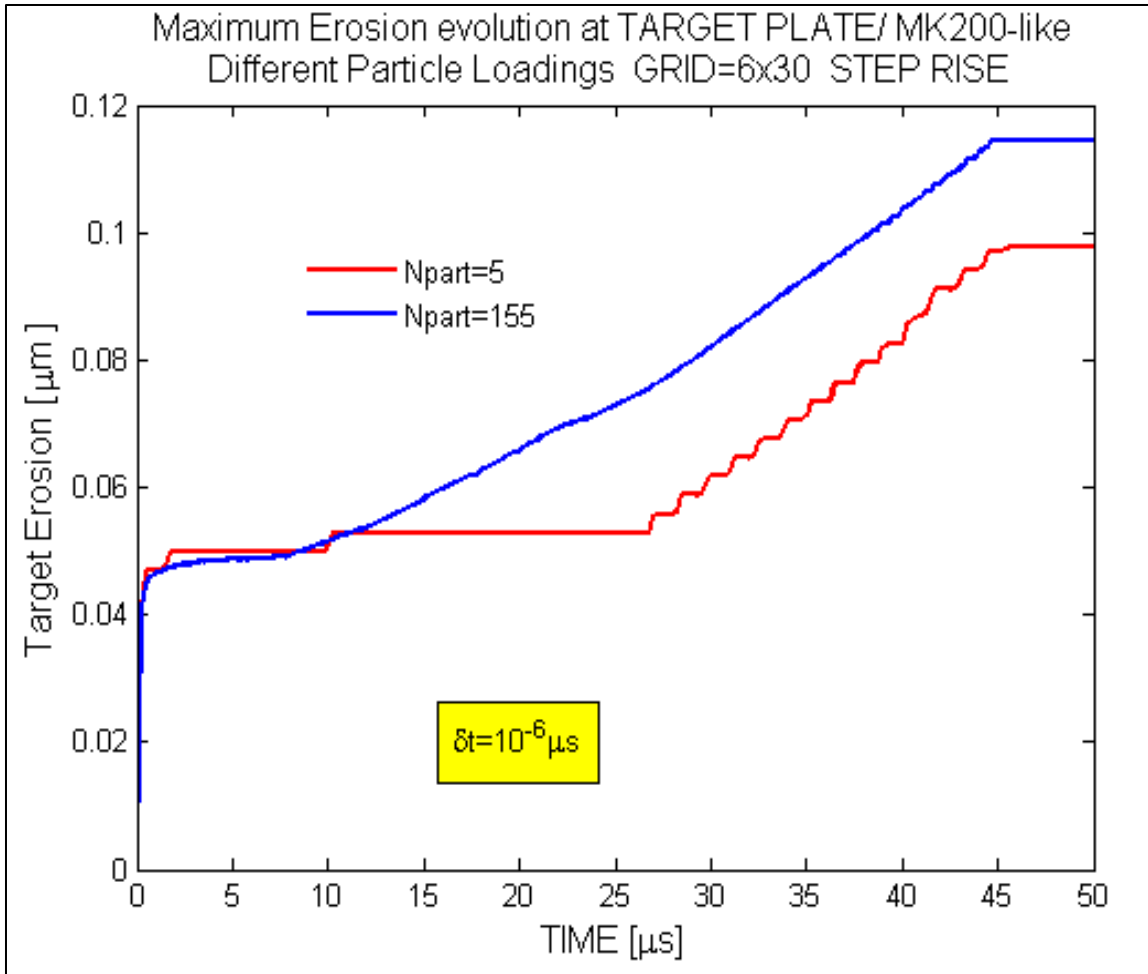


Figure 4.9 Calculated erosion profile evolution (step rise) in a typical MK-200 experiment simulation with HEIGHTS- PIC (5 vs. 155 sample particles initial loading).

one is much more smoother and numerically stable as expected. The effect of the number of super particles representing the plasma is critical for the precision of the calculated values but will be discussed further in another section.

Also the trend towards the saturation value (due to full efficiency of the screening effect) appears to be different since in the first case ( $N=5$ ) the increase in erosion is essentially stopped after the first few  $\mu\text{s}$ ; and increases only when the plasma vapor cloud starts



finally its expansion phase. In the other case instead (N=155) it appears to proceed smoothly starting the plasma vapor expansion around roughly 8  $\mu\text{s}$ . In both cases erosion stops increasing just before the exponential fading part start at 45  $\mu\text{s}$ . The computational grid used was 6x30 for both cases. This result shows as expected that increasing the number of sample particles in the initial loading, produces much more accurate results due to higher representativeness of the effective atoms and molecules present in the plasma-vapor cloud.

It is useful to compare these results with the one produced by FOREV-1/FOREV-2 (Fig. 4.10). Even though, this computer package is essentially a hydrodynamics one, the results proposed are relatively close to the ones published in the literature and produced by the experiments but considering graphite MPG8 and ranging from 0.32  $\mu\text{m}$  to 0.48  $\mu\text{m}$  according to different vales of the energy transport to the target(i.e. coefficient  $\alpha$ ). In this case the value for the magnetic field diffusion coefficient used was equal to  $D_0 = \chi_m = 15 \times 10^5 \text{ cm}^2/\text{s}$ . It has to be said that as noticed in the experiments conducted at the MK200 facility [8], different carbon based materials reacts differently [38]. In fact when the thermal stress value of the intergranular bond of graphite granules exceeds the failure value, the bond brakes and brittle destruction occurs. When brittle destruction occurs, the erosion value greatly increases since major size particles are ejected into the plasma [38]. A fraction is vaporized while superficial cracks keep developing. HEIGHTS-PIC does not have any brittle destruction calculation.

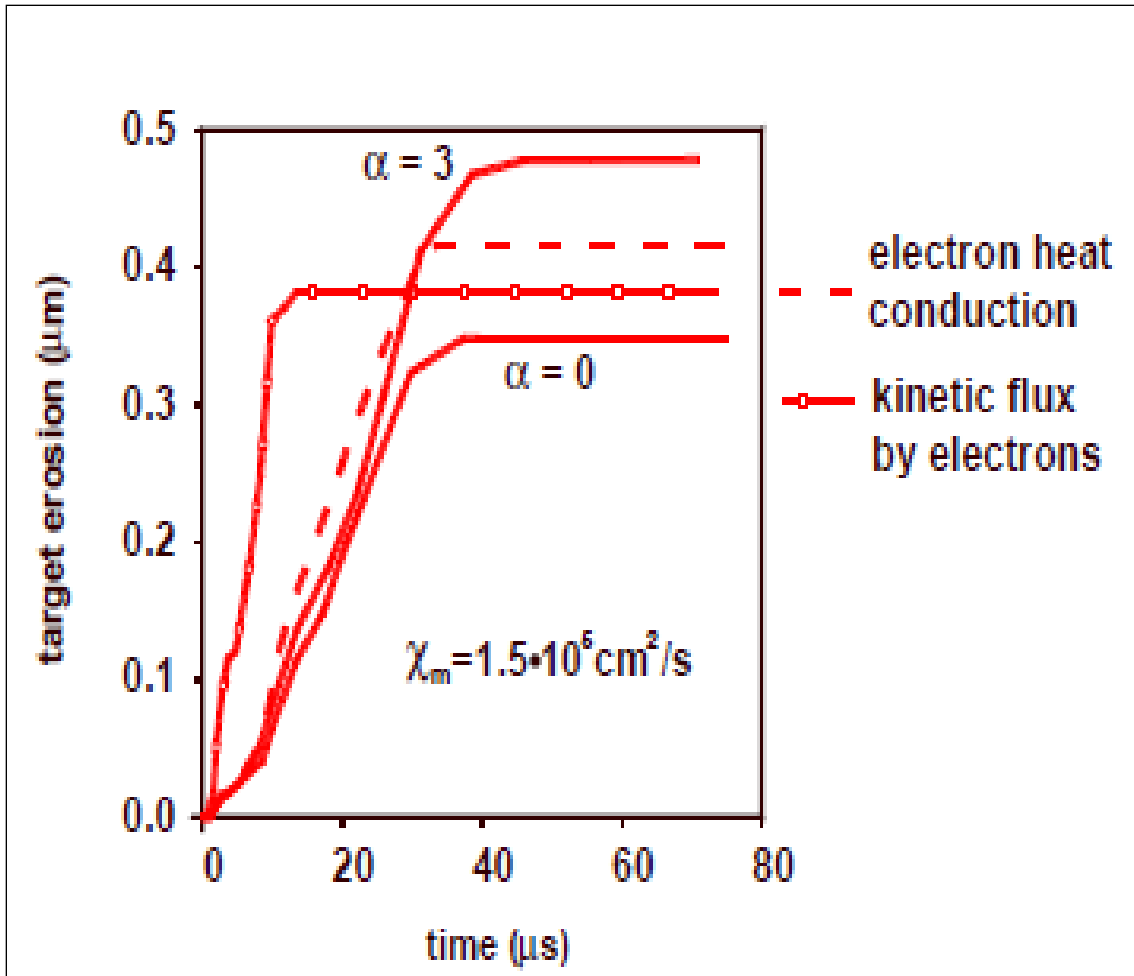


Figure 4.10 Calculated erosion rate in a typical MK-200 experiment simulation with FOREV-1/FOREV-2 [6] (reproduced with permission)

In this case four different values of erosion are reported. For more exhaustive explanation, check appendix A2 of the relative reference. In general though it can be noticed that the calculated values by FOREV-1/FOREV-2 are much bigger than HEIGHTS-PIC using the experimental reference value  $\alpha = 3$  but still with a different material.

It is also very important to examine the plasma shield dynamics along the time while the eroded surface develops as well as the behavior of the carbon plate itself. Analyzing the variation of the surface temperature at the Separatrix (peak point for the Gaussian beam and center of the plate), it is evident for both cases here presented that it increases very rapidly in the first 2 to 3  $\mu\text{s}$ . As shown in figures 4.11 and 4.12, the peak is reached with values close to 5350 K (5334 K for  $N=5$  and 5342 K for  $N=155$ ).

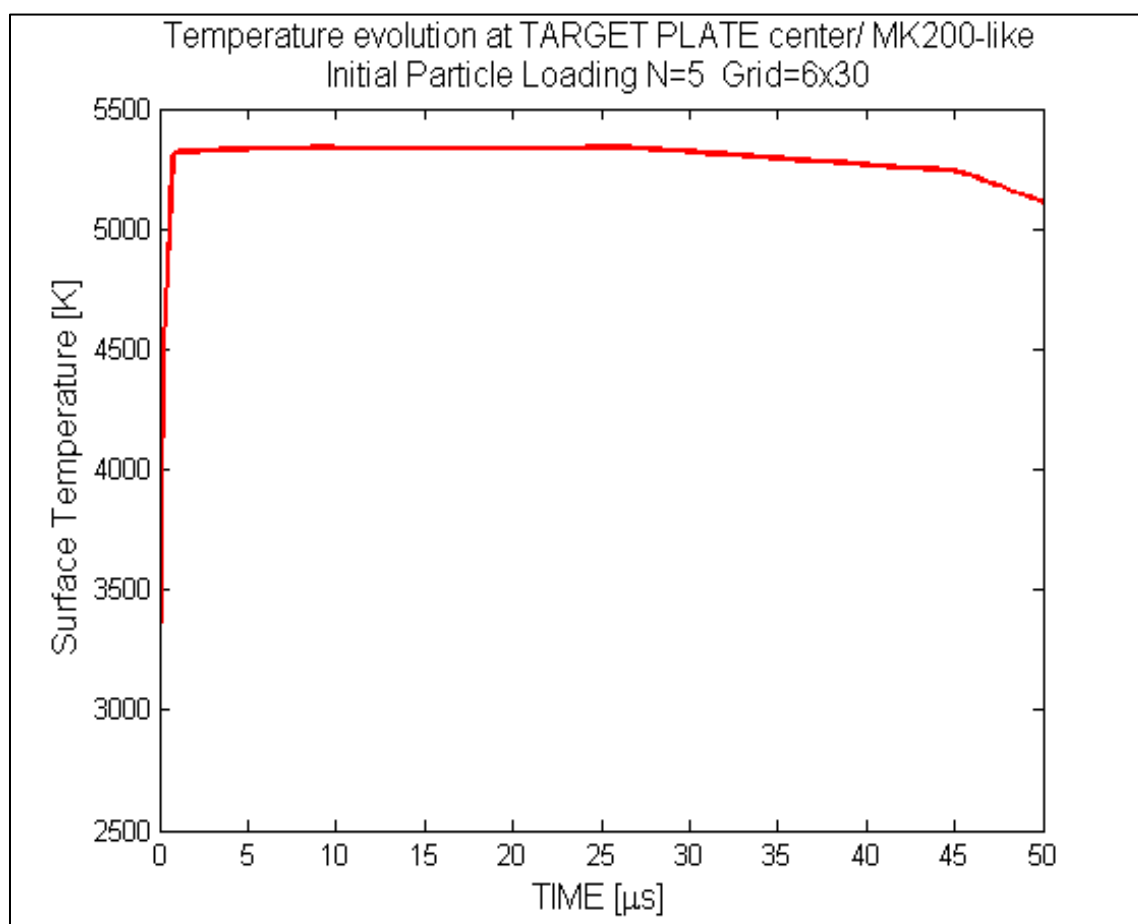


Figure 4.11 Calculated temperature evolution in a typical MK-200 experiment simulation with HEIGHTS-PIC ( $N=5$  Particles)

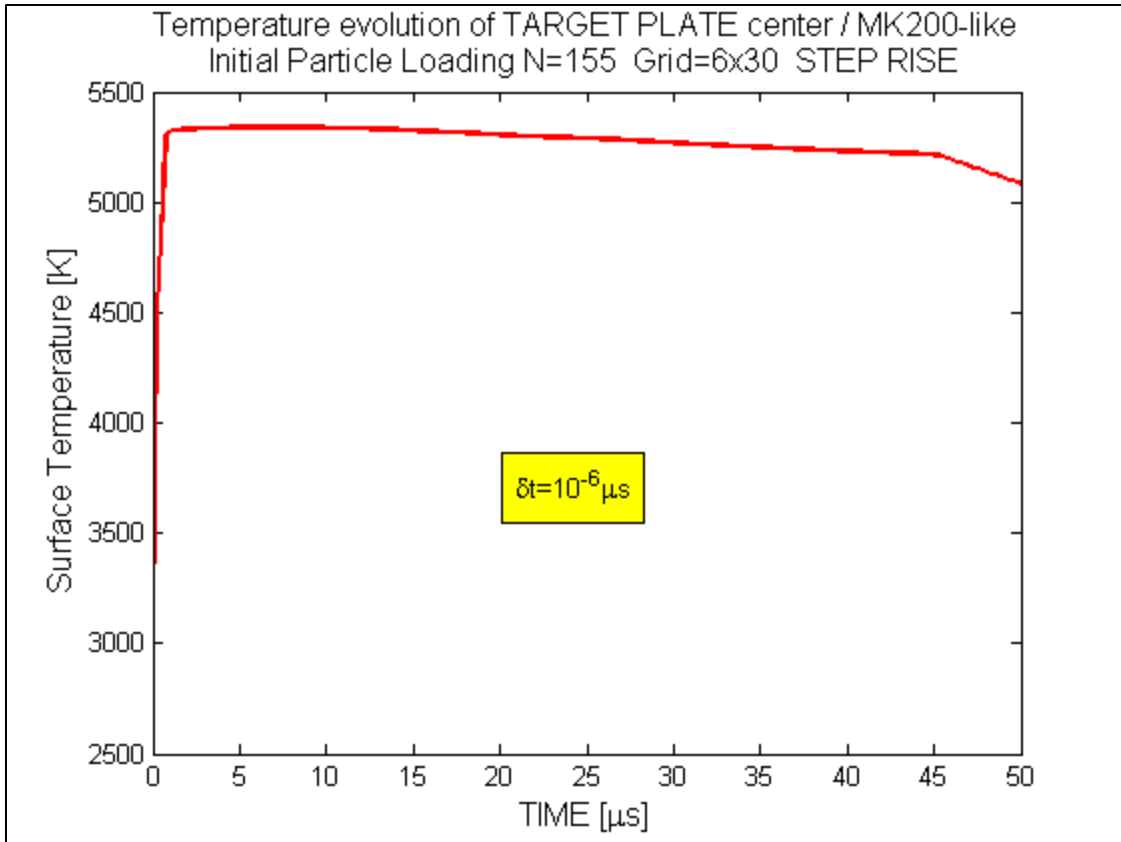


Figure 4.12 Calculated temperature evolution in a typical MK-200 experiment simulation with HEIGHTS-PIC (155 Particles)

The trends of the surface temperature are similar and not much difference exists in the stability of the solution for different initial particle loading. It is worth recalling that in the simulations here presented the plate was preheated starting at a value close to 2970 K). It is important to notice that the temperature of the surface remains relatively constant for most of the period in which the power beam flux is at its maximum ( $S_{\text{beam}}=35 \text{ MW/cm}^2$ ) starting to decrease around 12-13  $\mu\text{s}$ . The decrease in surface temperature is more pronounced as soon as the beam power starts fading into the exponential decaying phase. Given the short time of operation (from 15 to 50  $\mu\text{s}$ ) no effective cooling can be expected

of the surface due to heat diffusion into the solid target. Comparing these trends with the equivalent calculated into FOREV-1/FOREV-2 (figure 4.13), it is noticeable that even though the general trend looks similar, the decrease of the surface temperature corresponding to the exponential reduction of the power beam flux is very pronounced going from 1.3 of the carbon sublimation temperature into vacuum (equals to 4211 K) to 0.8-0.75 of the same value. So the maximum value calculated here is roughly 5475 K.

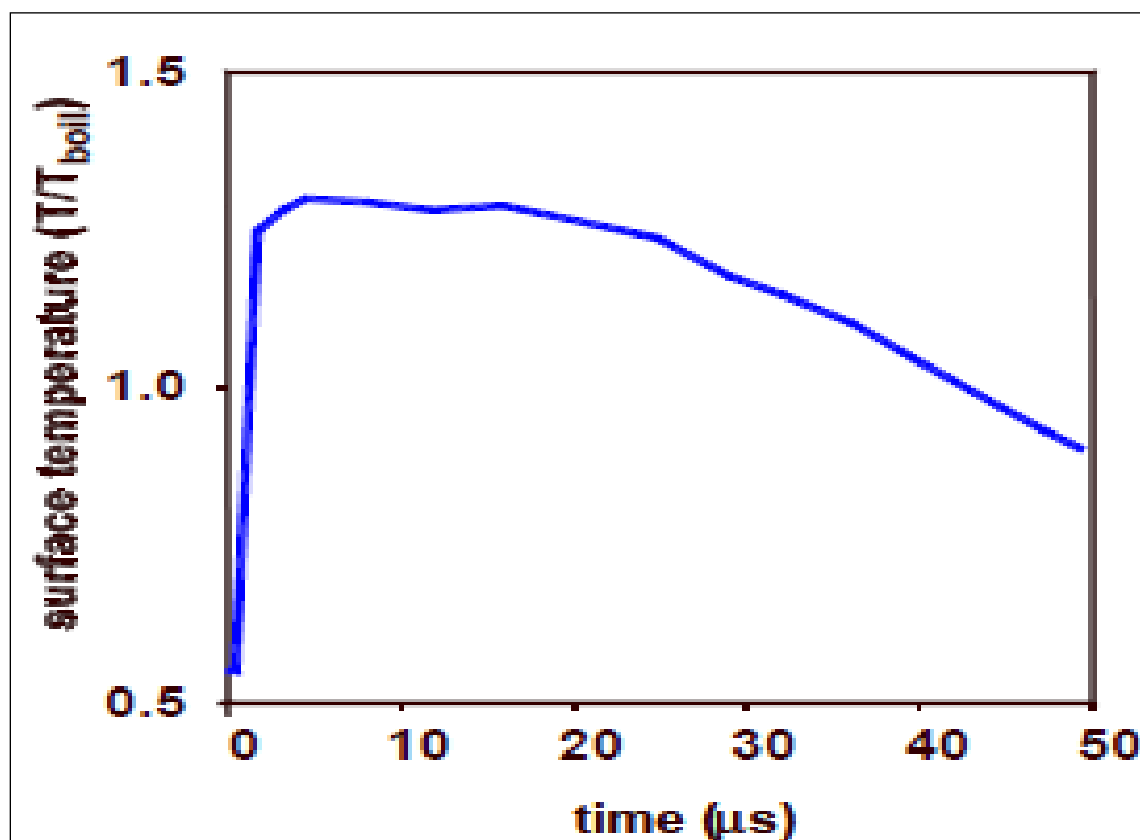


Figure 4.13 Calculated surface temperature evolution at plate center in a typical MK-200 experiment simulation with FOREV-1/FOREV-2 [6] (reproduced with permission)

This can be only explained with extremely high heat diffusion into the carbon, which though seems not really reproducing the typical material behavior. No real data exist

regarding at least the MK200-UG experiments about the evolution of the surface temperature due to the very difficult conditions to perform onto the plate or close to the surface reliable and accurate measurements. Using instead values produced into the calculations by HEIGHTS, we see that the evolution of T surface at the center of the plate is very close to the one calculated with HEIGHTS-PIC.

#### 4.2.2 Power Fluxes & Temperature of the plasma vapor cloud

Calculated heat target fluxes are shown in figure 4.14 for the central cells of the plate into a 6x30 configuration. During the entire disruption time, the radiation dominates the target heat load as well as the entire plasma-vapor grid. Direct energy deposition absorbed effectively into the target peaks roughly at 1  $\mu$ s being later on almost entirely stopped by the interaction of the plasma particles and carbon vapor cloud. After the first few instants and as soon as the power beam flux reaches its maximum (black line), the radiation power rate to target also assumes the same profile of the full beam. The hot plasma stream at this point is clearly all stopped leaving the surface of the carbon material subjected only to radiation. The profile though follows well the exponential decay after 45  $\mu$ s. Two important considerations need to be done here. The first one is that the total calculated beam power flux (cyan line) is less than the one effectively provided with the beam (black line). This is due to the approximation performed using only 6 cells along the target and so 6x6 cells to solve completely the radiation transport equation. The method in this case even though well responds to the general methodology is produces a coarse results.

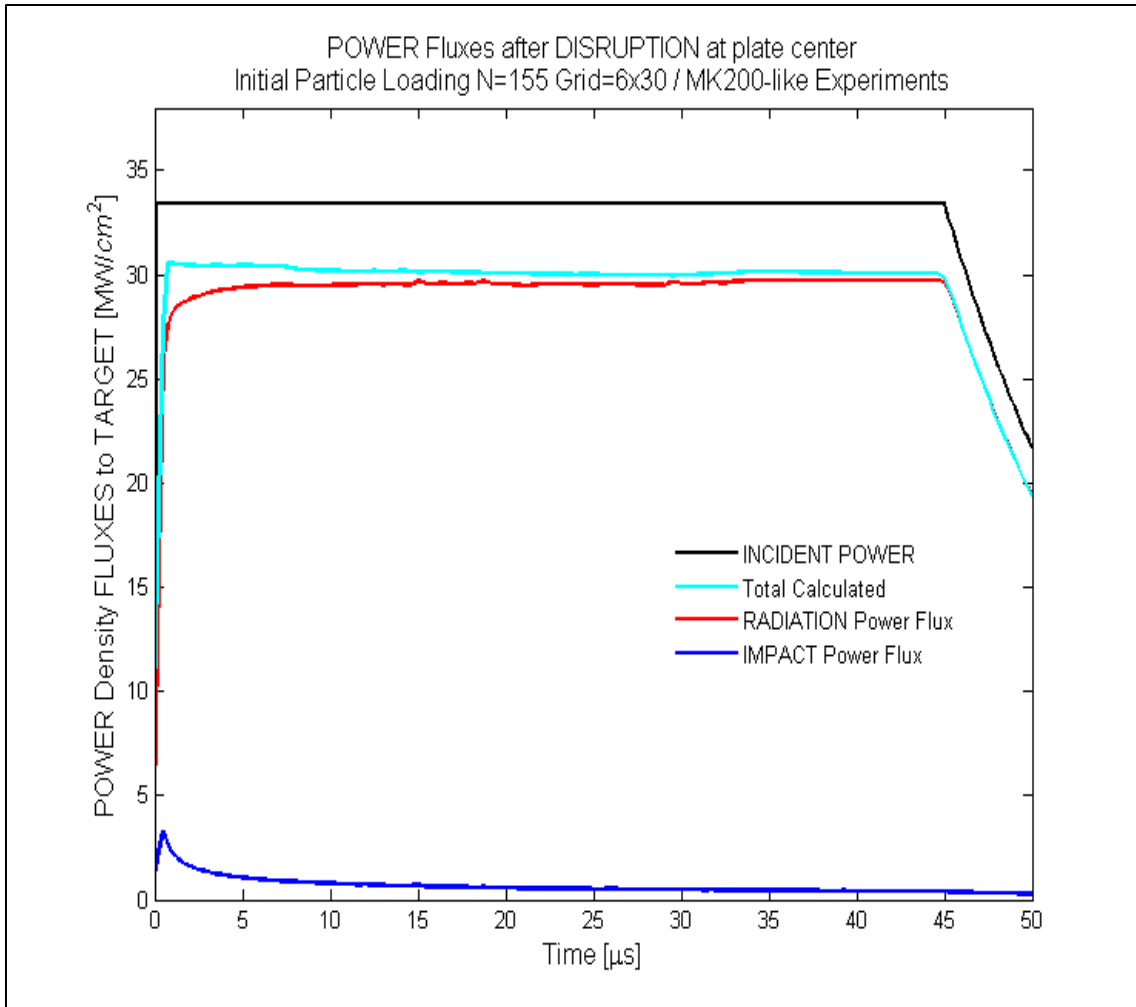


Figure 4.14 Calculated power fluxes evolution at plate center in a typical MK-200 experiment simulation with HEIGHTS-PIC (N=155)

The second consideration is that it is important to check also the geometrical distribution and evolution of the power fluxes. In particular figure 4.15 and 4.16 describe the calculated and assigned beam power fluxes at 45 μs (end of the full beam) and at 50 μs (end of the simulation and beam operation).

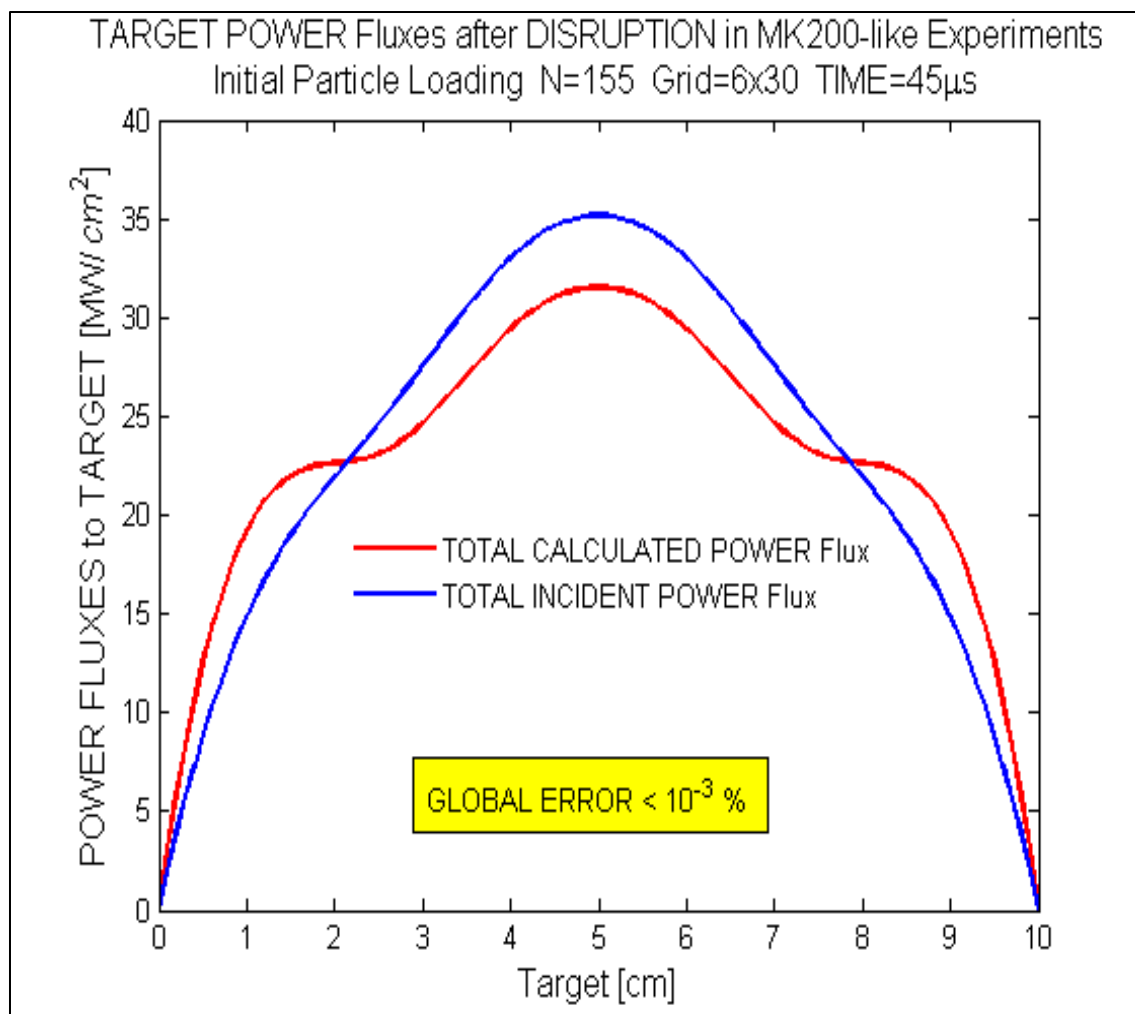


Figure 4.15 Calculated power fluxes along the target at 45  $\mu$ s in a typical MK-200 experiment simulation with HEIGHTS-PIC (N=155)

In both cases even though the global error is very low, it is evident an underestimation of the total values of the central cells (where more energy is damped) combined with and over estimation of the most distant ones onto the grid itself. At the end it is useful to get a more complete picture to observe the trend produced by the simulation using only 5 particles as initial loading.



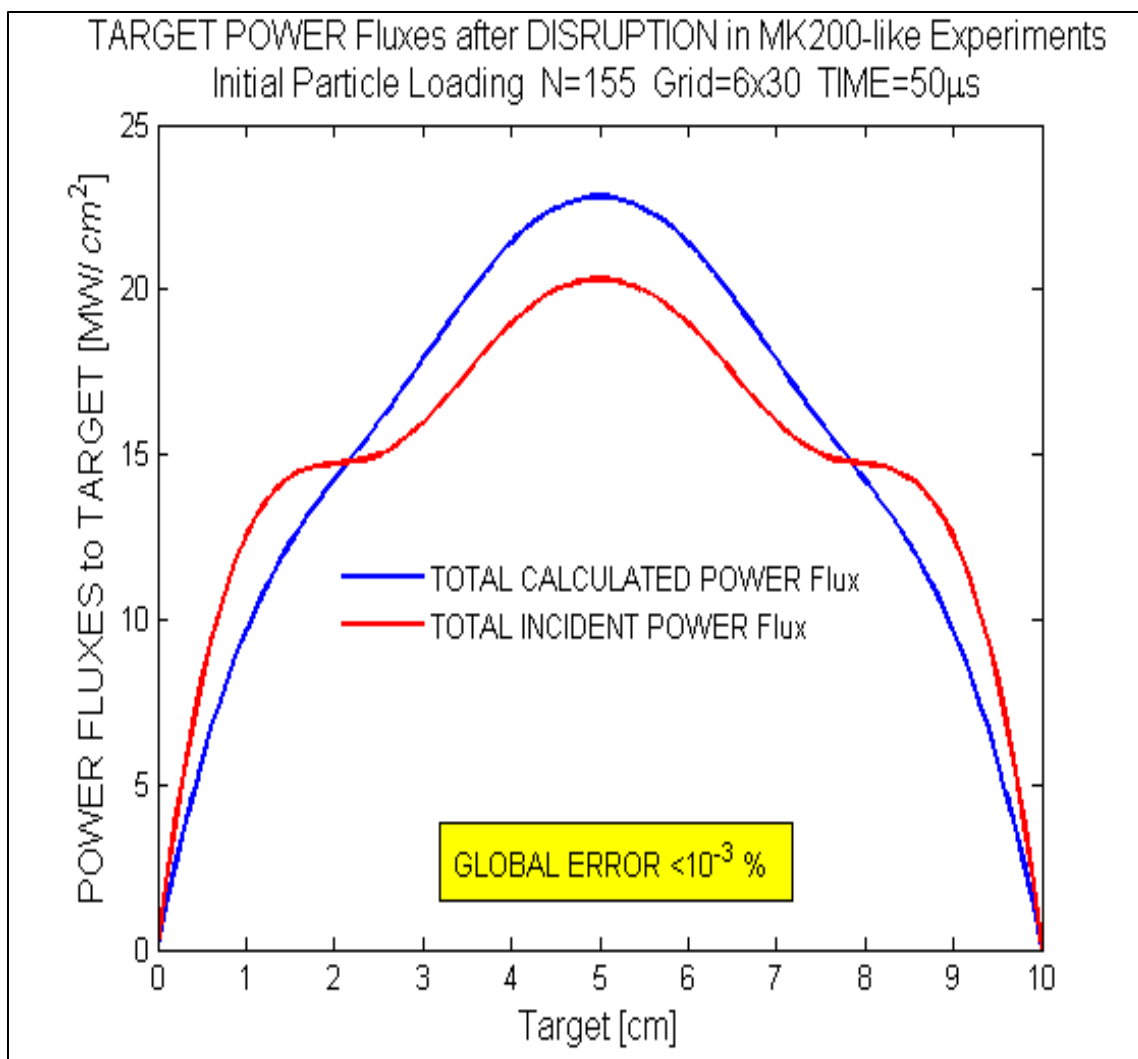


Figure 4.16 Calculated power fluxes along the target at 50  $\mu$ s in a typical MK-200 experiment simulation with HEIGHTS-PIC (N=155)

Even if the trend looks the same, it is worth noticing that the calculation is much more unstable and produces especially for the effective absorbed power flux into plate peak values below the ones provided into the N=155 simulation.

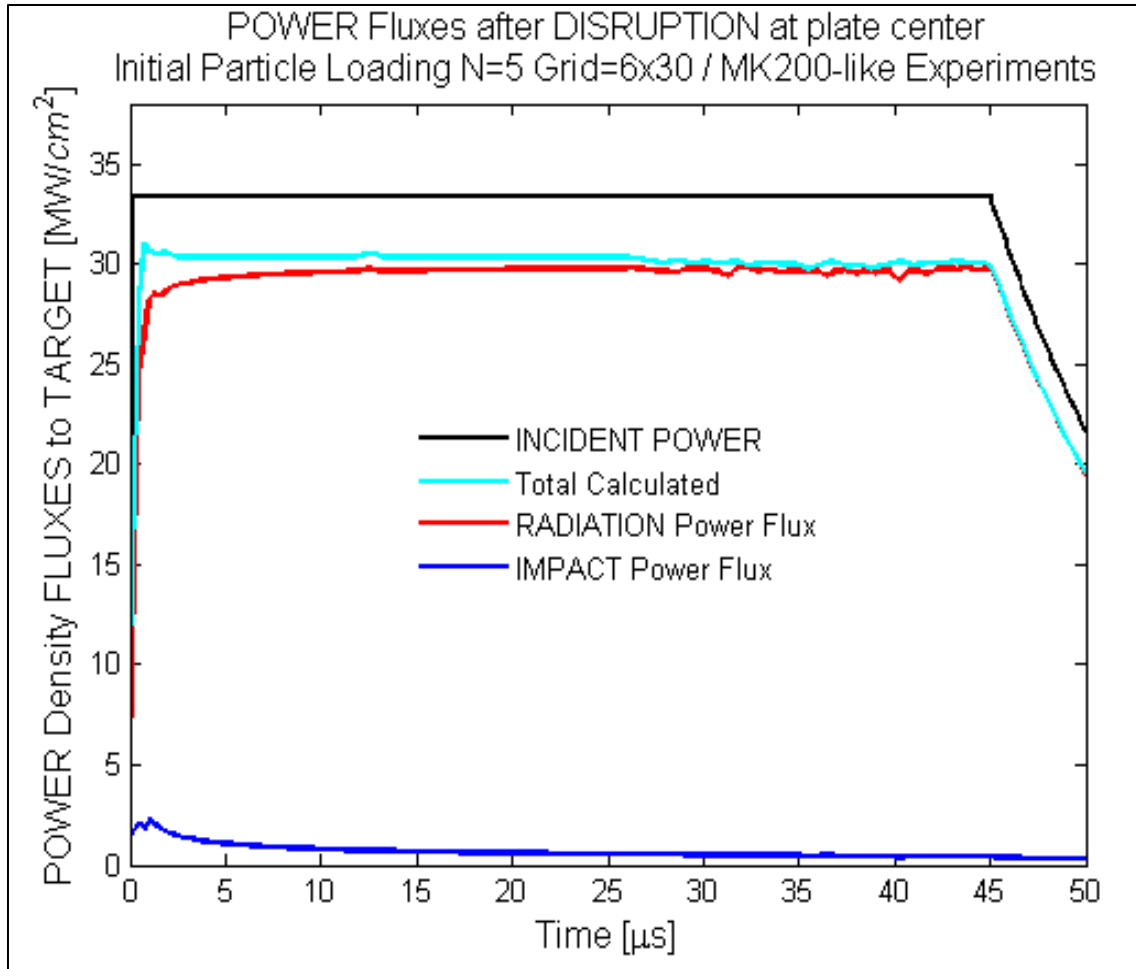


Figure 4.17 Calculated power fluxes evolution at plate center in a typical MK-200 experiment simulation with HEIGHTS-PIC (N=5)

Comparing with the results proposed by FOREV-1/FOREV-2, it is evident that there are important differences. First of all the calculated peak of the target radiation flux in HEIGHTS-PIC is about 3 times higher than the one calculated with the other computer package. The impact power flux appears also to be different as well as the timing for the

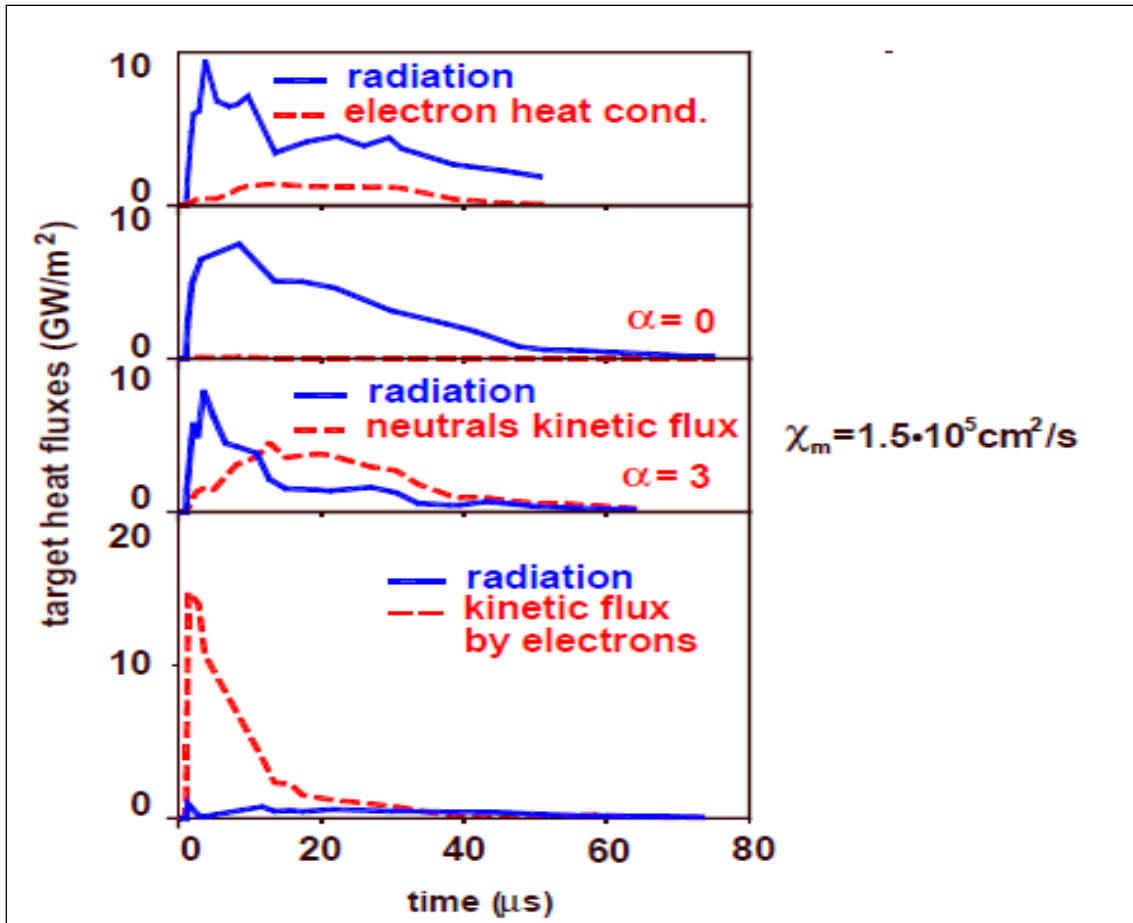


Figure 4.18 Calculated power fluxes evolution at plate center in a typical MK-200 experiment simulation with FOREV-1/FOREV-2 [6] (reproduced with permission)

peaking. In HEIGHTS-PIC, for each computational cell at each time step, both the plasma absorption and emission coefficient are evaluated and the radiation transport equation solved. This methodology is definitely much more accurate and precise than the one used in FOREV-1/FOREV-2 (69 Group Planck opacities and forward reverse method for the solution of radiation transport problem). Besides, there is no comparison with the full beam power flux, so it is difficult to effectively compare the two results.

The evolution of temperature in the plasma vapor cloud can be followed with the following figures looking at both the evolution close to the plate and for the center of the plasma along time. Already at  $1 \mu\text{s}$ , the Temperature has raised up to 3 eV and has the

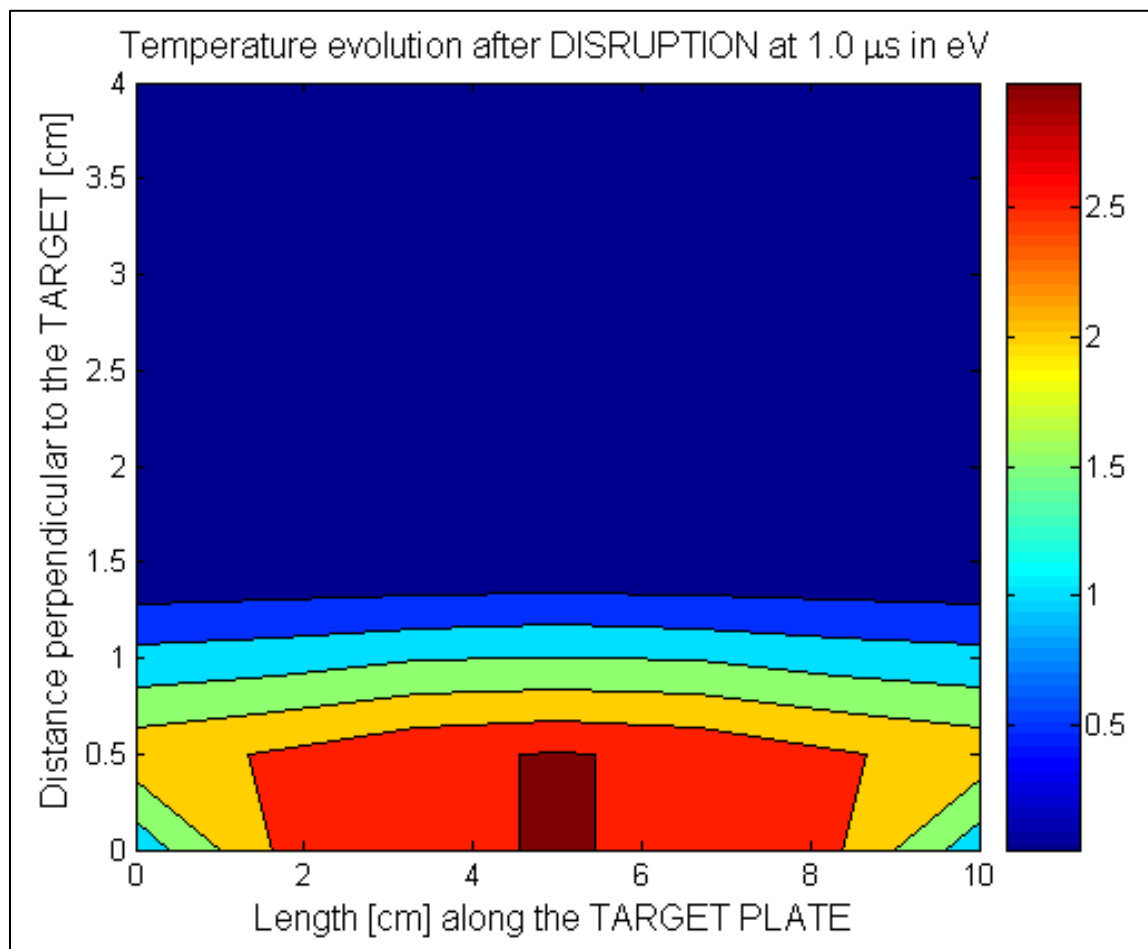


Figure 4.19 Calculated plasma Temperature evolution over the target in a typical MK-200 experiment simulation with HEIGHTS-PIC (at  $1 \mu\text{s}$ )

typical Gaussian shape. Around  $3 \mu\text{s}$ , following the same trend found for the evolution of density, the highest temperature is found very close to the target center, while for hydrodynamics effects, “wings” start to appear. (Fig. 4.20)

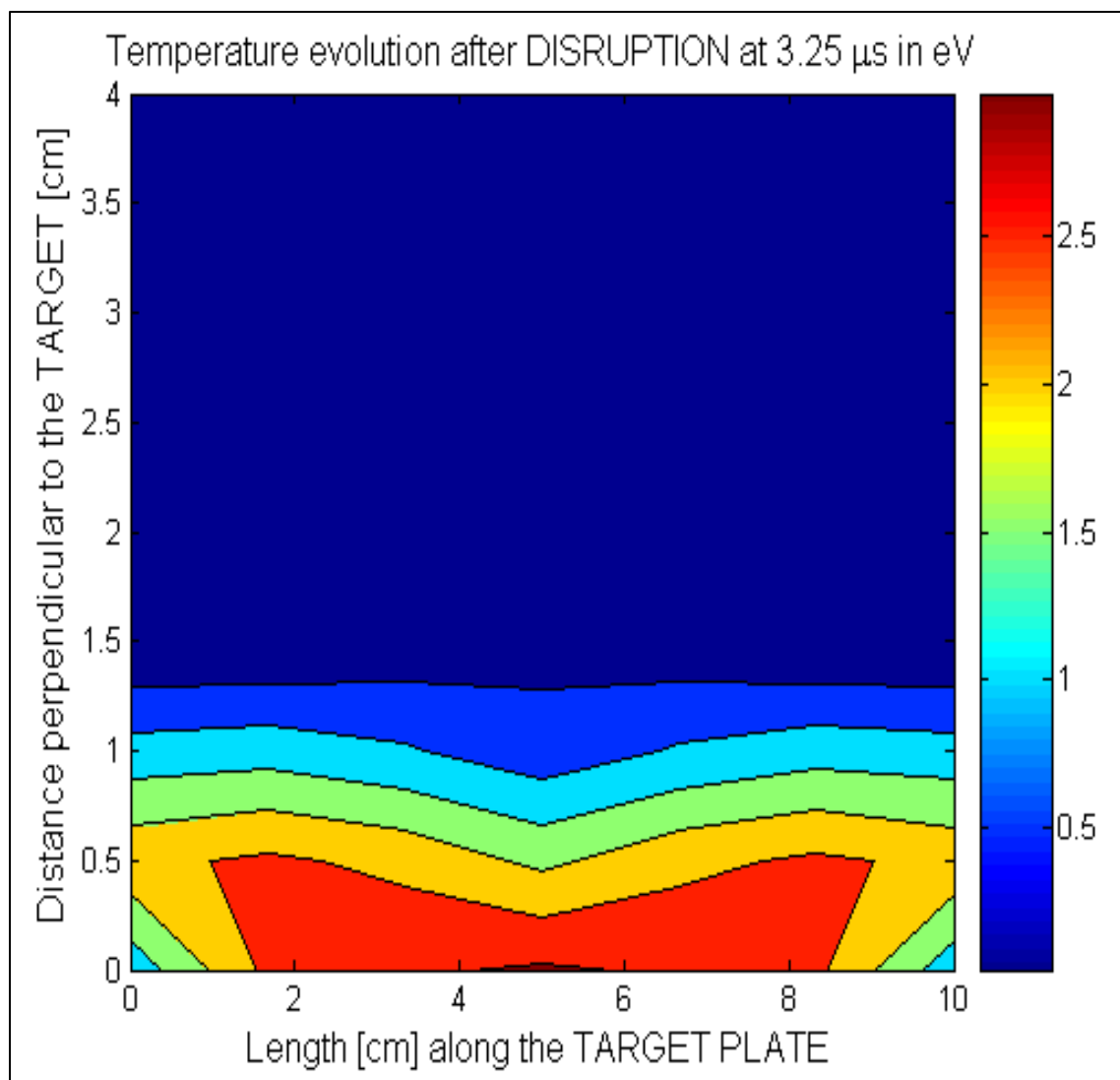


Figure 4.20 Calculated plasma Temperature evolution at the target in a typical MK-200 experiment simulation with HEIGHTS-PIC (at 3.25  $\mu$ s)

After the first microseconds the temperature of the established vapor cloud over the target reaches some eV, being higher in the middle as expected (fig. 4.21).

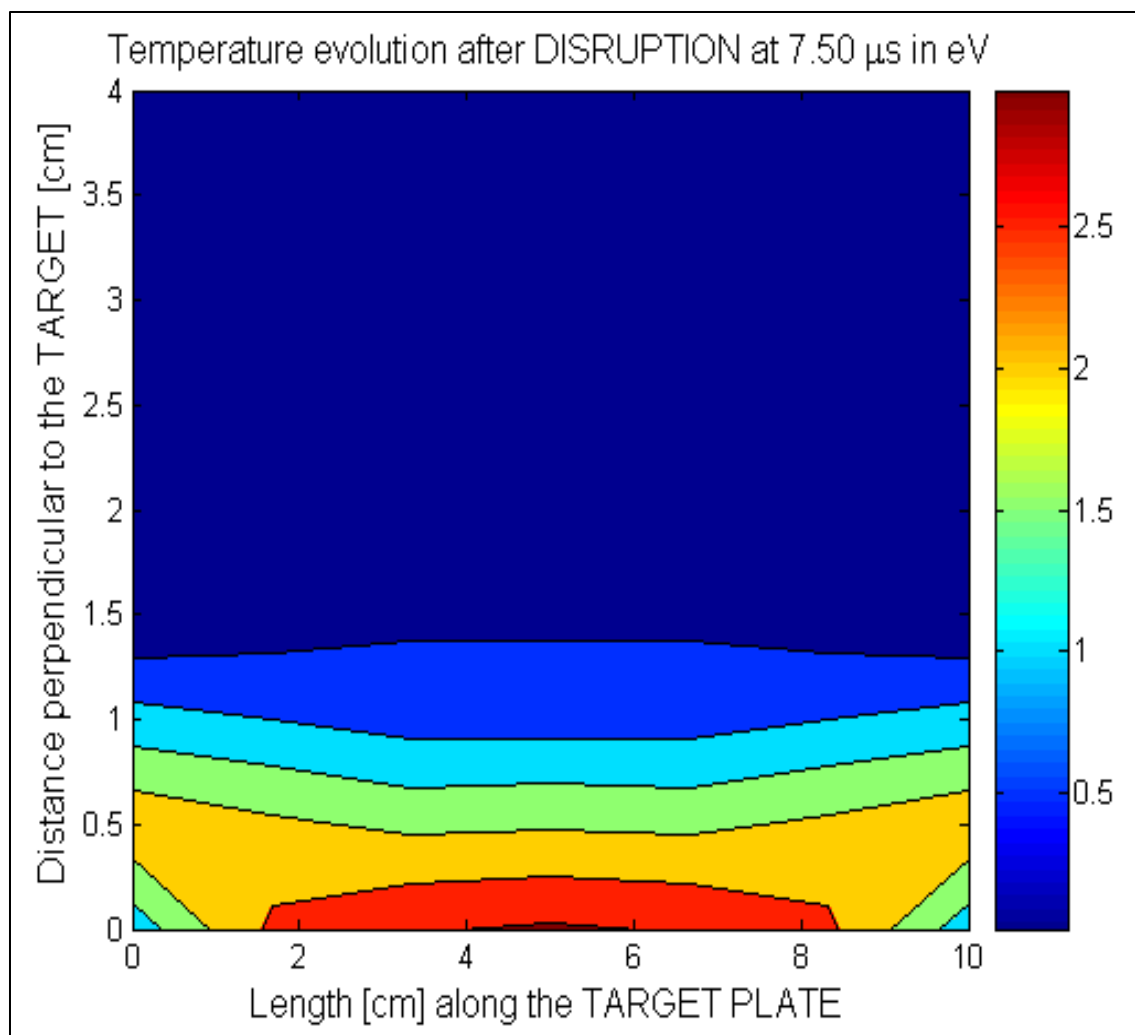


Figure 4.21 Calculated plasma Temperature evolution at the target in a typical MK-200 experiment simulation with HEIGHTS-PIC (at 7.50  $\mu\text{s}$ )

As time progresses (10 and 25  $\mu\text{s}$ ) temperature close to the target stays relatively constant: it is evident the formation of a relatively cooler layers of plasma-vapor material very close to the target plate proving that the self-screening effect is already in place and working well. Plasma in this phase has already started expanding starting to create a cooler layer close to the target.

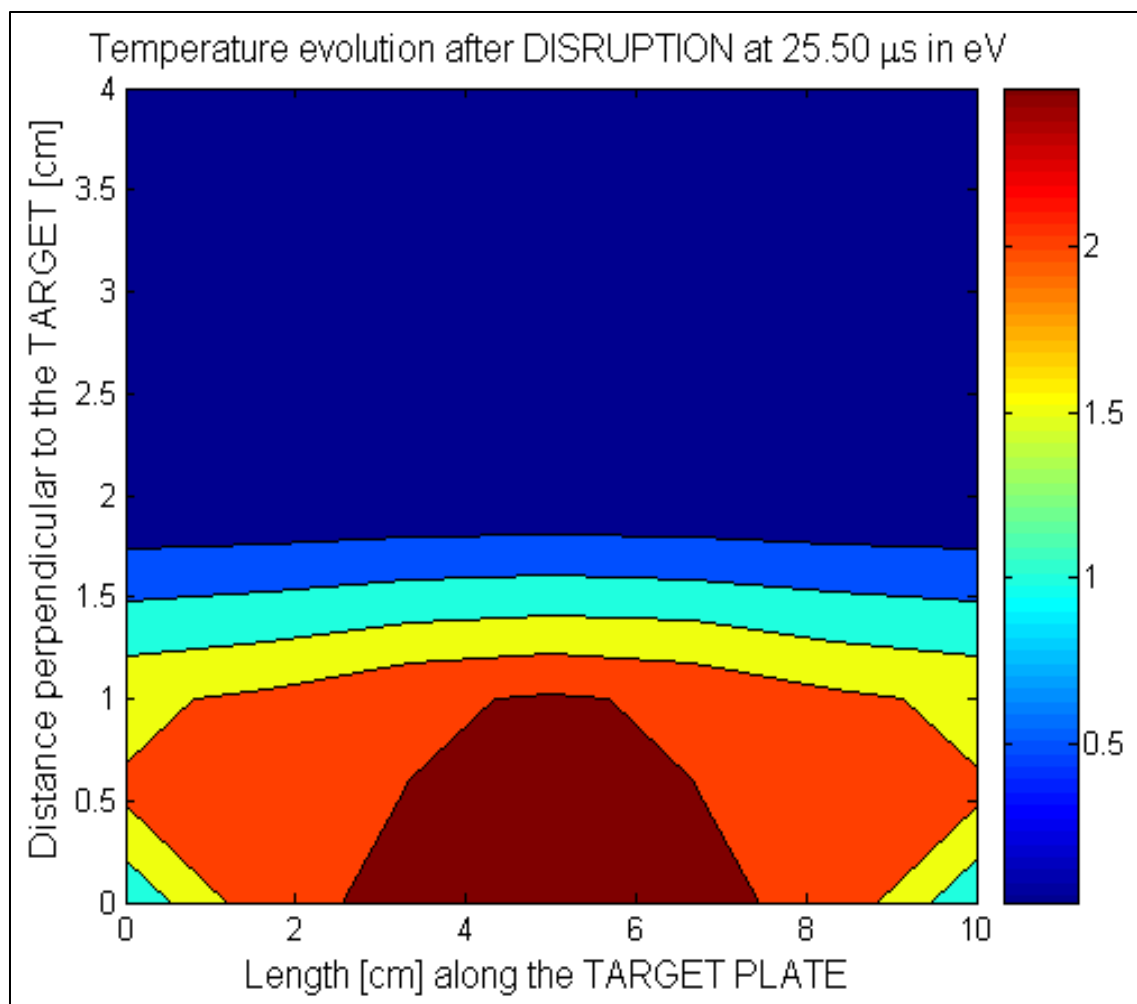


Figure 4.22 Calculated plasma Temperature evolution at the target in a typical MK-200 experiment simulation with HEIGHTS-PIC (at 25.50  $\mu\text{s}$ )

The central layer close to target remains also cool (around 2 eV) and tends to increase in thickness due to upward movement of the ionized particles following the magnetic field. Most of the energy damped onto the system at this point is transformed into radiation towards the target (minimal) and above all away from the target.

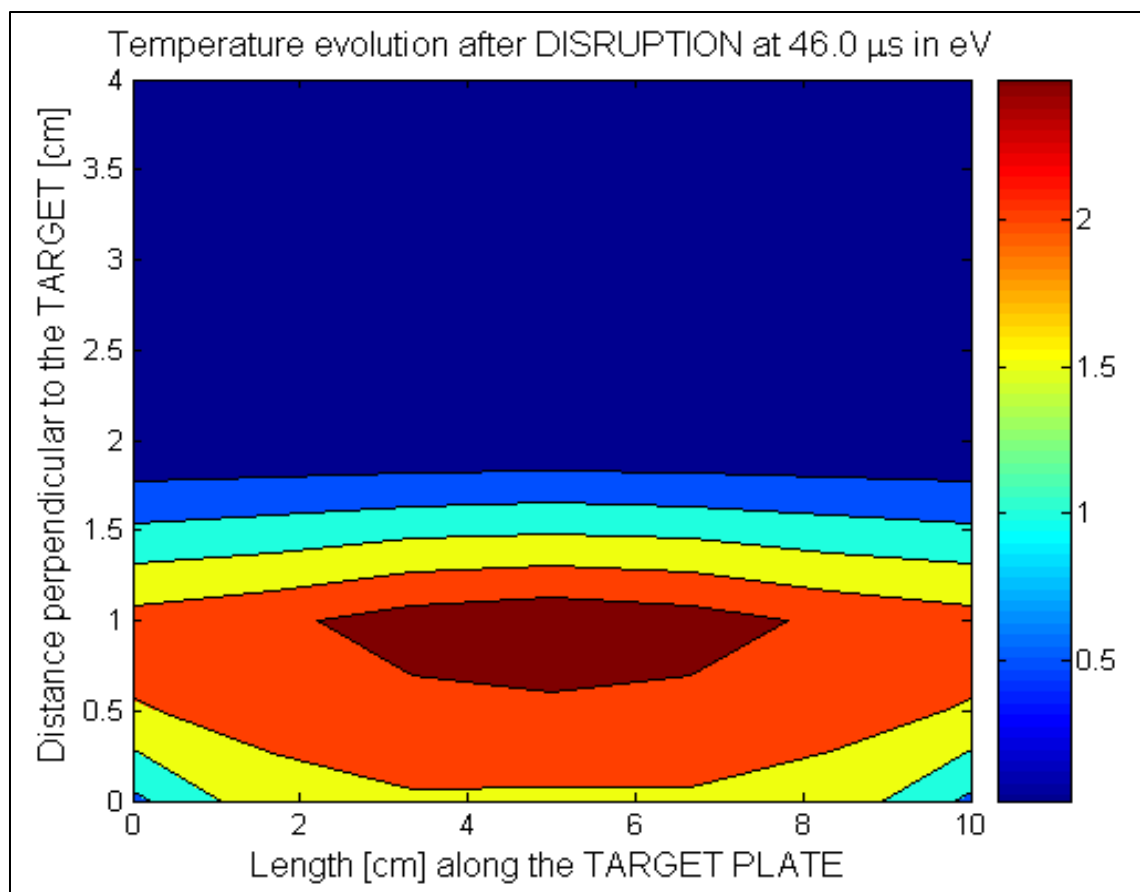


Figure 4.23 Calculated plasma Temperature evolution at the target in a typical MK-200 experiment simulation with HEIGHTS-PIC (at 46.0  $\mu$ s)

It has to be noticed that examining the values calculated for both plasma density and temperature, only one of the two predicted regimes (Radiation losses in FOREV) is found. The region close to carbon plasma has high density but low temperature (the maximum value reached is below 4 eV) while the coronal plasma which is typically with  $T = 40-70$  eV and much smaller densities, is not found in the outer layer of the carbon plasma [4, 13-15]. This evidence is discussed and analyzed further in chapter 5.



### 4.2.3 Pressure, density & electron density of the plasma vapor cloud

It is very important to examine and understand the behavior of the plasma vapor cloud along time both far and in the vicinity of the target. The plasma shield dynamics depends on the pressure distribution inside the plasma shield itself and on the externally applied magnetic field. Its geometry and intensity is influenced by plasma shield through the diamagnetic effect and by its diffusion coefficient in the plasma vapor cloud. Since two layers of plasma are with time formed (hot low dense plasma and cold but dense in the proximity of the target) both contributing to the diamagnetic effect. The evolution of the calculated target plate total pressure at the center is shown in the figure 4.24

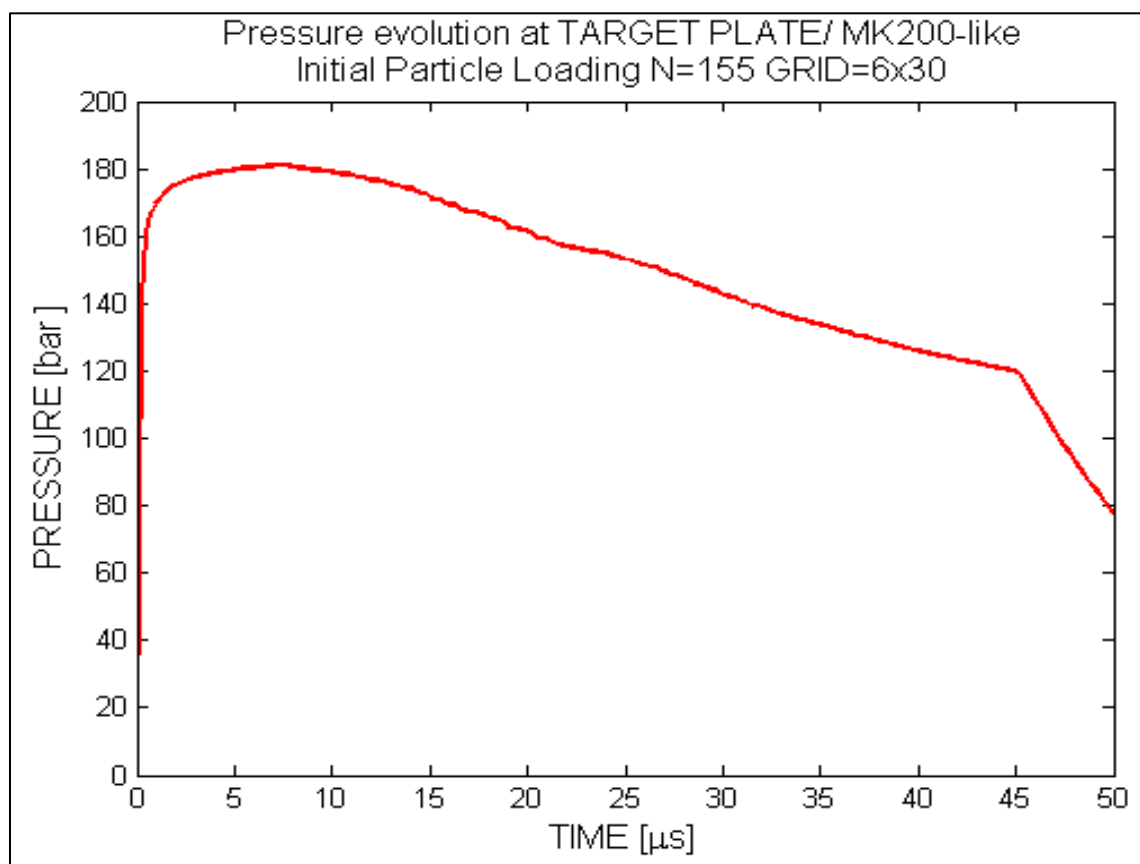


Figure 4.24 Calculated pressure evolution at plate center in a typical MK-200 experiment simulation with HEIGHTS-PIC

At the beginning, pressure increases rapidly following the step rise in power flux reaching the plate. Around 2  $\mu\text{s}$  pressure has reached its peak around 180 bar and remains roughly constant up to 6-7  $\mu\text{s}$ . At this point, when the vapor start expanding pressure is reduced with a liner trend till  $t=45 \mu\text{s}$ . After this time the reduction in pressure follows almost perfectly the exponential decay. This behavior is very important because the variation of the pressure in front of the target is related directly to the variation of the erosion of the plate through the formulation [33-34]:

$$\begin{aligned}
 F_{net} &= Flux_{OUT} - Flux_{IN} \\
 \text{with } Flux_{OUT} &= c_{VAP} \cdot 10^{\left(\frac{T_{FLUX}}{T_{SURFACE}} + T_{COEFF}\right)} \cdot \sqrt{T_{Surface}} \\
 T_{SATUR} &= \frac{T_{FLUX}}{(T_{COEFF} - \log_{10}(P))} \\
 \text{and } Flux_{IN} &= c_{VAP} \cdot P / \sqrt{T_{SATUR}}
 \end{aligned} \tag{4.1}$$

It is also important to look at the calculated geometrical evolution of the pressure in front the target and verify that the Gaussian profile is respected at all times (figures 4.25 and 4.26).

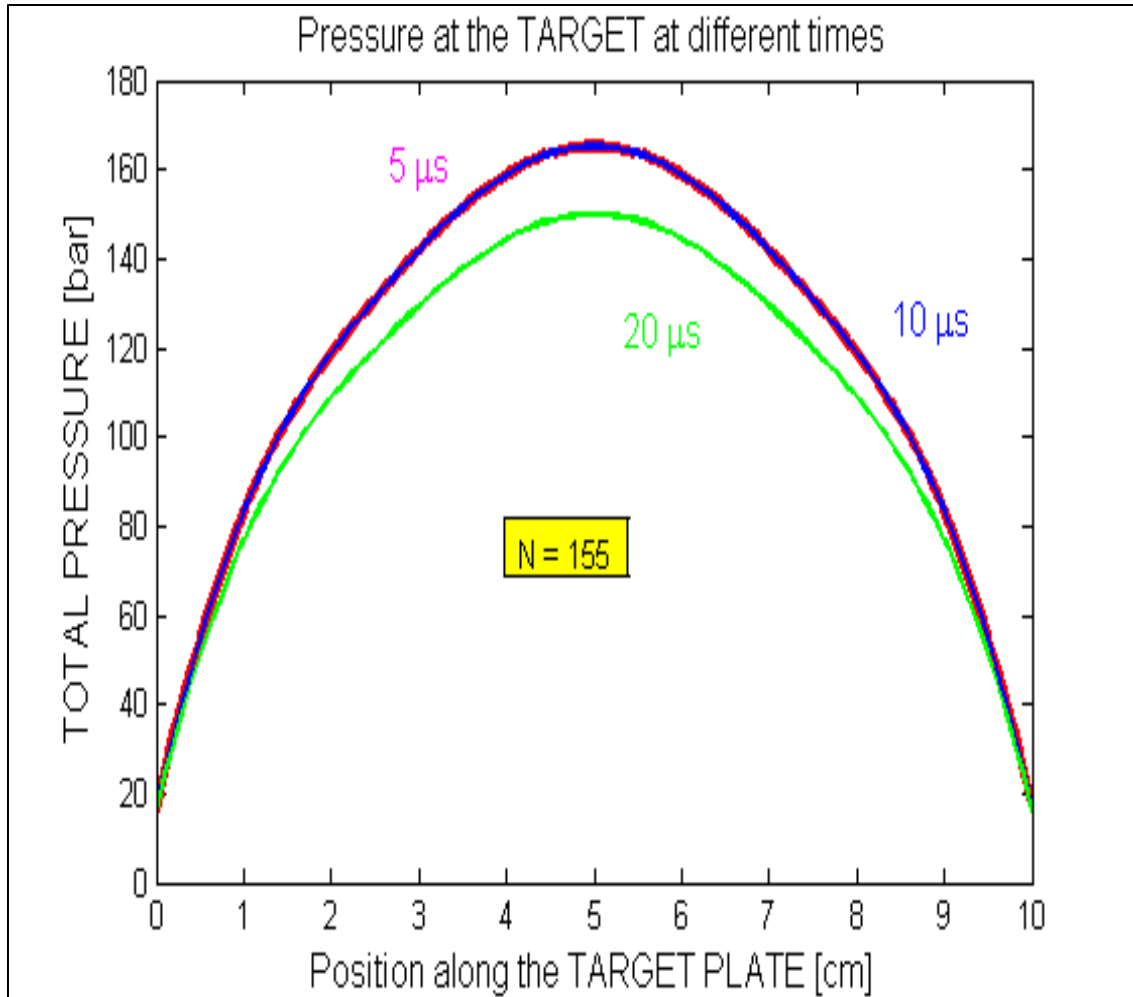


Figure 4.25 Calculated pressure evolution at target plate in a typical MK-200 experiment simulation with HEIGHTS-PIC for different times along the plate ( $t=5-20 \mu\text{s}$ )

At the beginning, the pressure increases as new particles are produced. As soon as they become partially ionized, due to the B field in the vertical direction, they tend to move upward creating a diamagnetic effect. This effect which tends to reduce partially and locally the magnetic field, produces a reduction in the pressure gradient of the total pressure. This resulting pressure gradient drives on outward movement of the cold plasma away from the center of the plate.

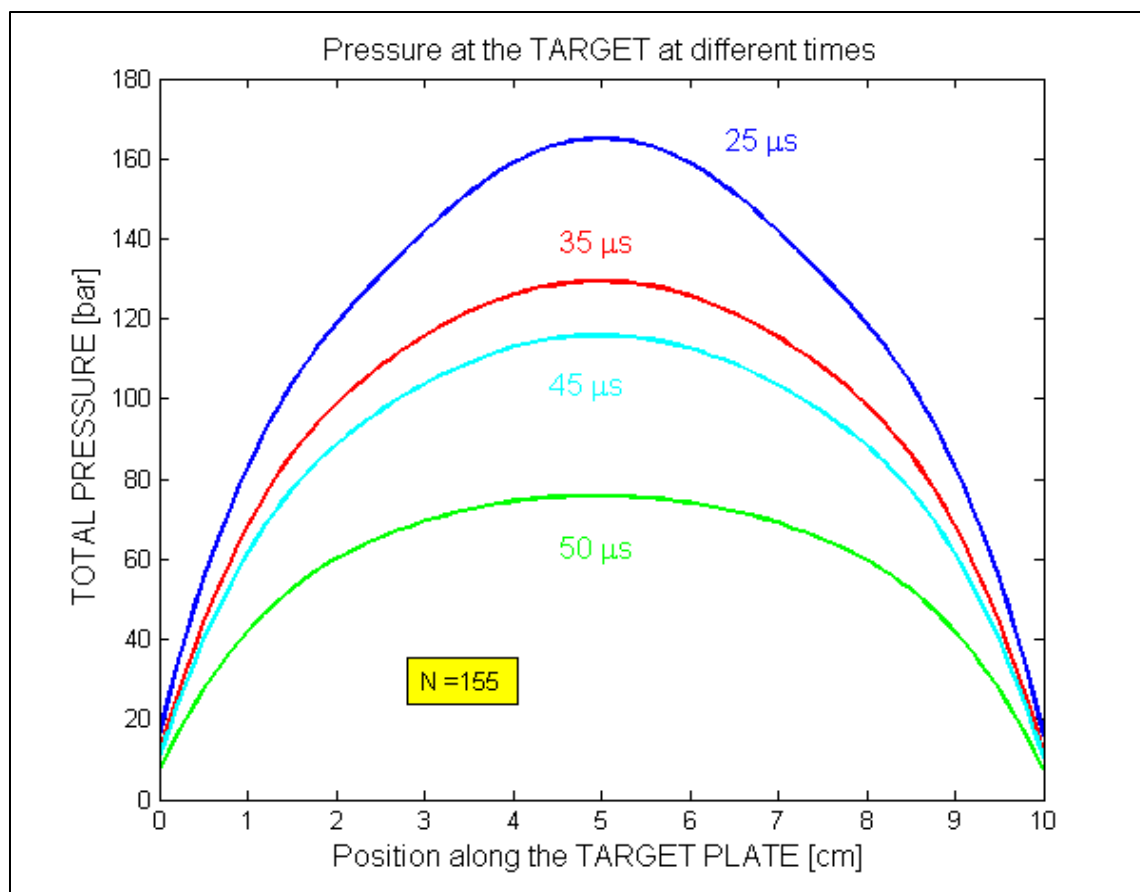


Figure 4.26 Calculated pressure evolution at target plate in a typical MK-200 experiment simulation with HEIGHTS-PIC for different times along the plate ( $t=25-50 \mu\text{s}$ )

At later times the outward movement is reduced because of the decreased plasma shield pressure and due to the diffusion across the perpendicular lines of the magnetic field, pressure tends to be relatively higher in the external “wings” (very visible also in the density and temperature profiles) and low in the middle. Comparing these calculated results with the ones proposed by the FOREV-1/FOREV-2 (Fig. 4.27), the biggest difference appears to be in the maximum values reached at similar instants. HEIGHTS-

PIC pressure is always constantly higher (with peak around 180 bar) than the one calculated in [6] (peak around 35-40 bar) and maintains the Gaussian shape at all times.

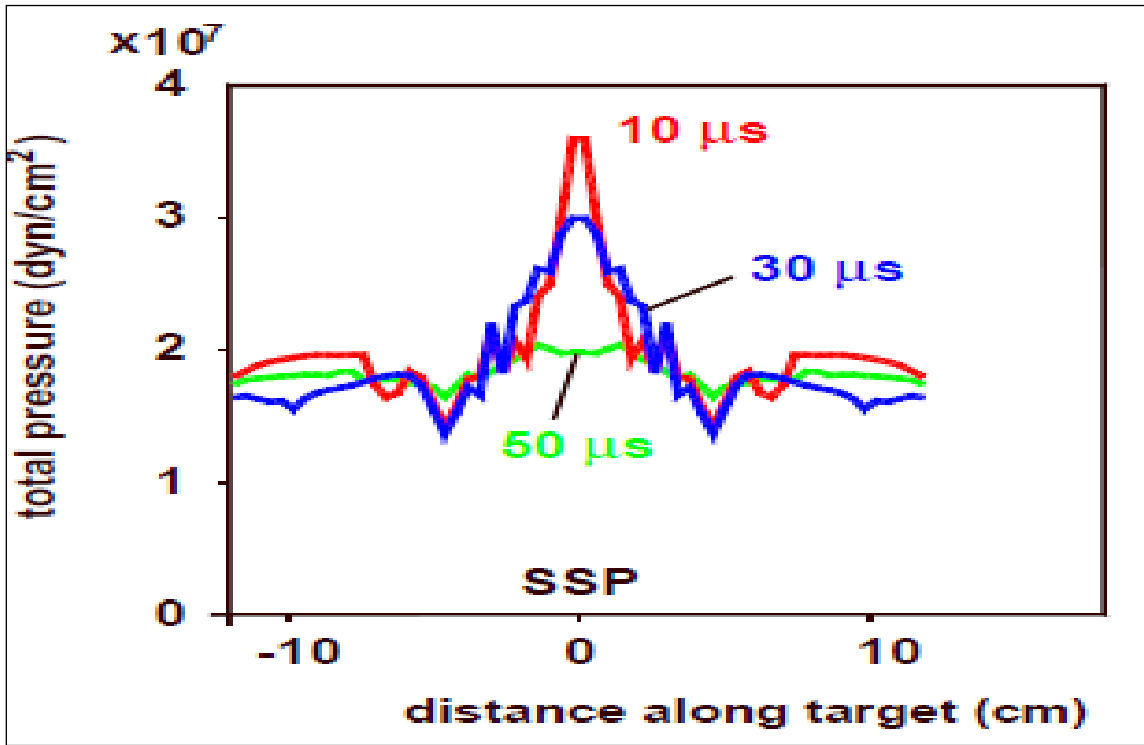


Figure 4.27 Calculated total pressure evolution at the target in a typical MK-200 experiment simulation with FOREV-1/FOREV-2 [6] (reproduced with permission)

Considering the y-component of the momentum equation:

$$\frac{\partial \rho V_y}{\partial t} + \vec{\nabla} \rho V_y \vec{V} + \frac{\partial}{\partial y} \left( P + \frac{B^2}{2\mu_0} \right) - \frac{1}{\mu_0} \left( \vec{B} \vec{\nabla} \right) B_y = 0 \quad (4.2)$$

it is clear that a lateral plasma motion (y direction) occurs only if the magnetic field along y changes from the initial zero value and if there is a the total pressure change:

$$\frac{\partial P_{tot}}{\partial y} = \frac{\partial}{\partial y} \left( P + \frac{B^2}{8\pi} \right) \quad (4.3)$$

The evolution of plasma density is described in the following figures.

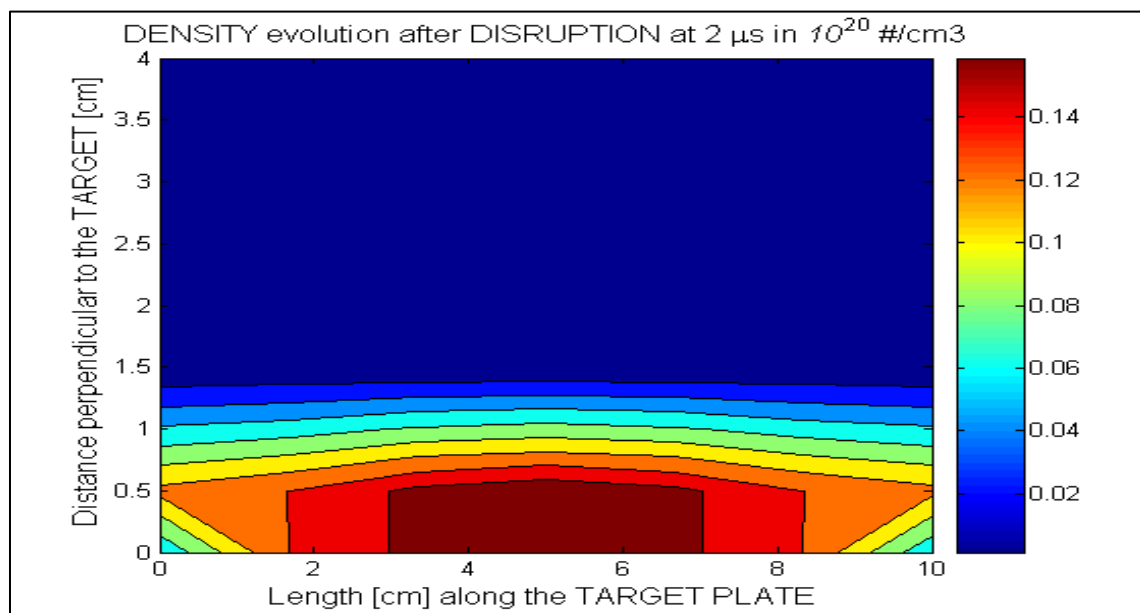


Figure 4.28 Calculated plasma density evolution at the target in a typical MK-200 experiment simulation with HEIGHTS-PIC (at 2  $\mu\text{s}$ )

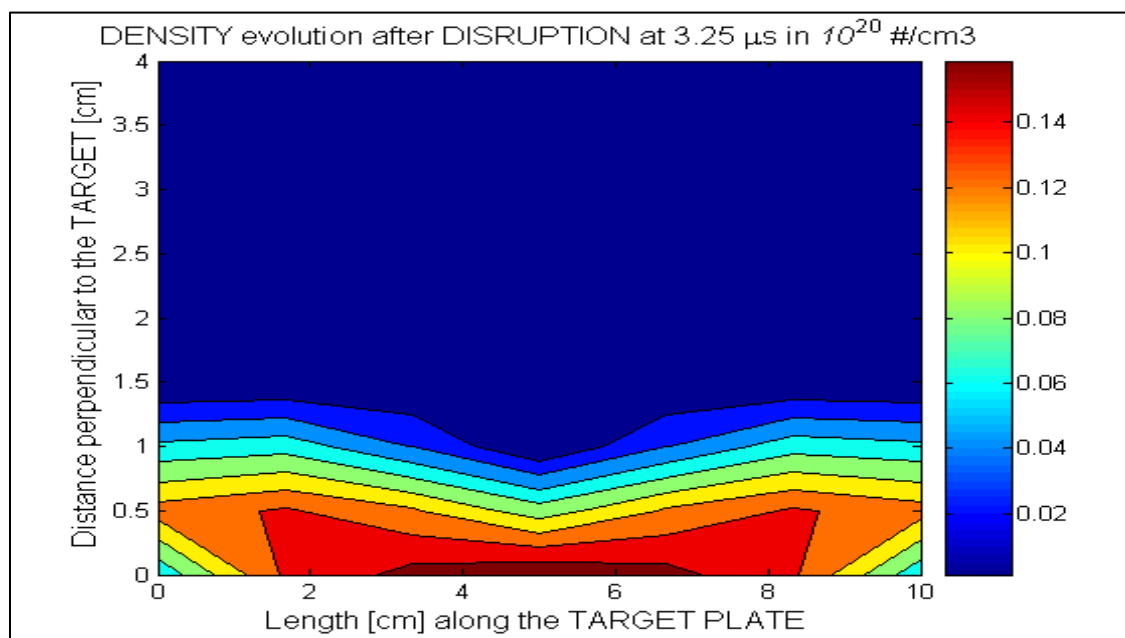


Figure 4.29 Calculated plasma density evolution at the target in a typical MK-200 experiment simulation with HEIGHTS-PIC (at 3.25  $\mu\text{s}$ )

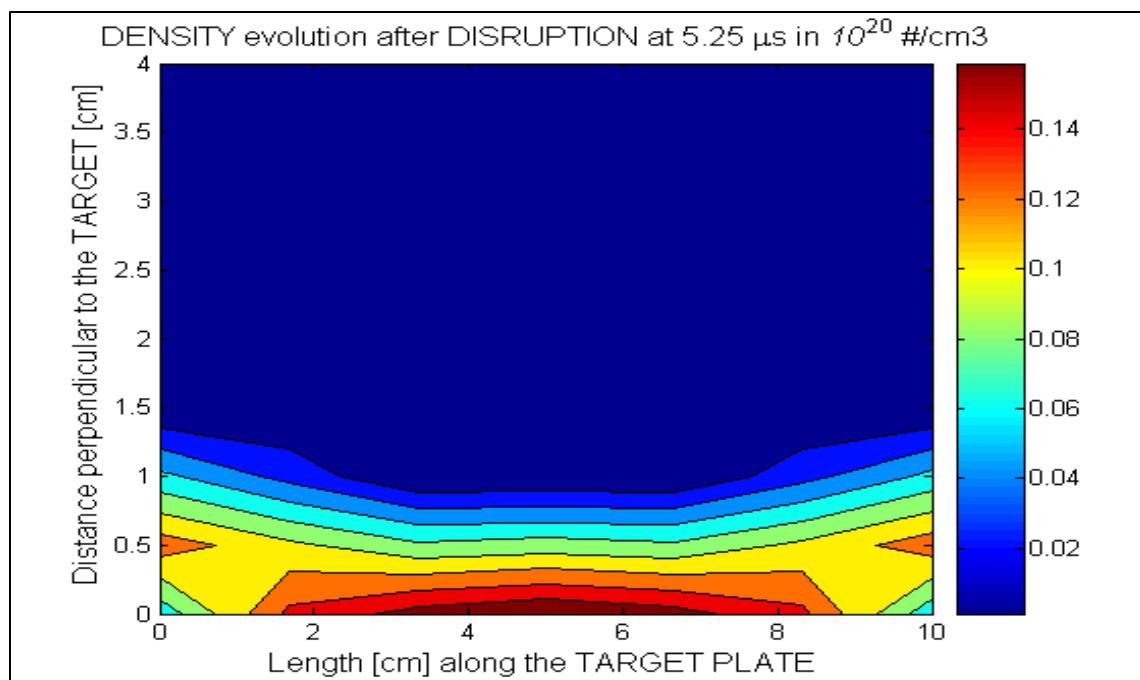


Figure 4.30 Calculated plasma density evolution at the target in a typical MK-200 experiment simulation with HEIGHTS-PIC (at 5.25  $\mu\text{s}$ )

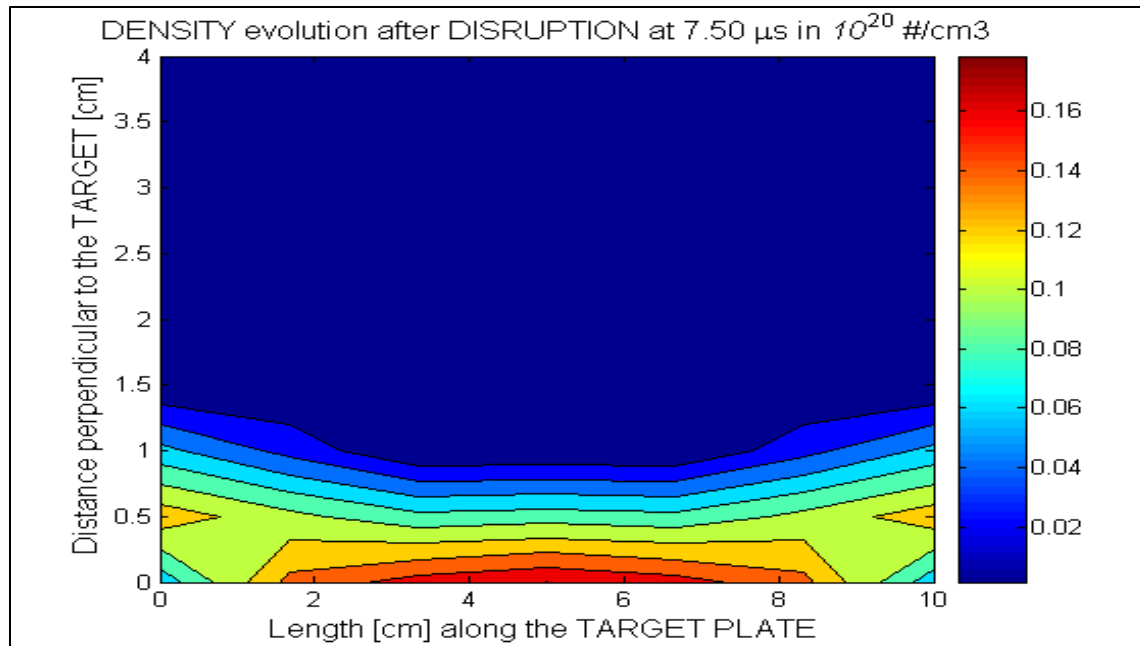


Figure 4.31 Calculated plasma density evolution at the target in a typical MK-200 experiment simulation with HEIGHTS-PIC (at 7.50  $\mu\text{s}$ )

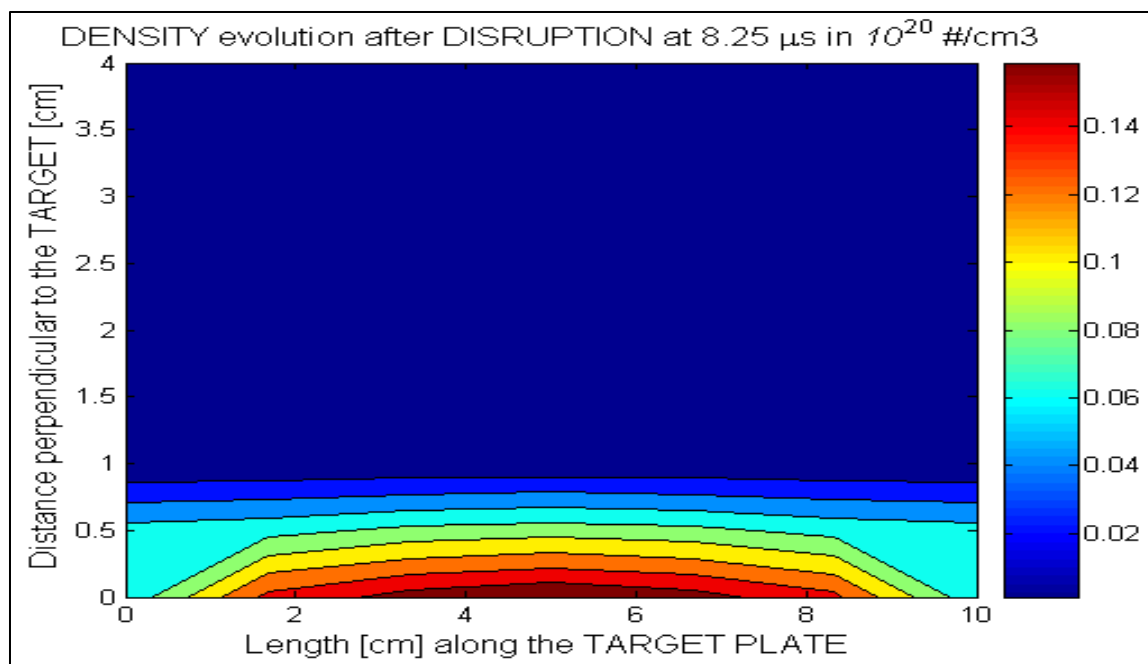


Figure 4.32 Calculated plasma density evolution at the target in a typical MK-200 experiment simulation with HEIGHTS-PIC (at 8.25  $\mu\text{s}$ )

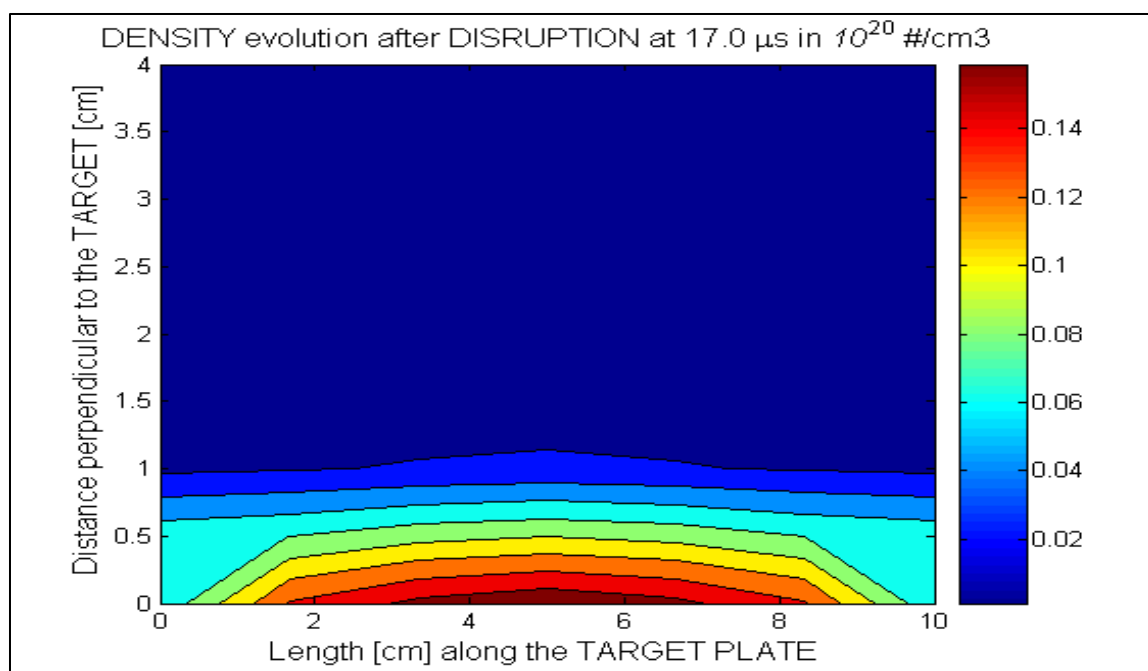


Figure 4.33 Calculated plasma density evolution at the target in a typical MK-200 experiment simulation with HEIGHTS-PIC (at 17.0  $\mu\text{s}$ )



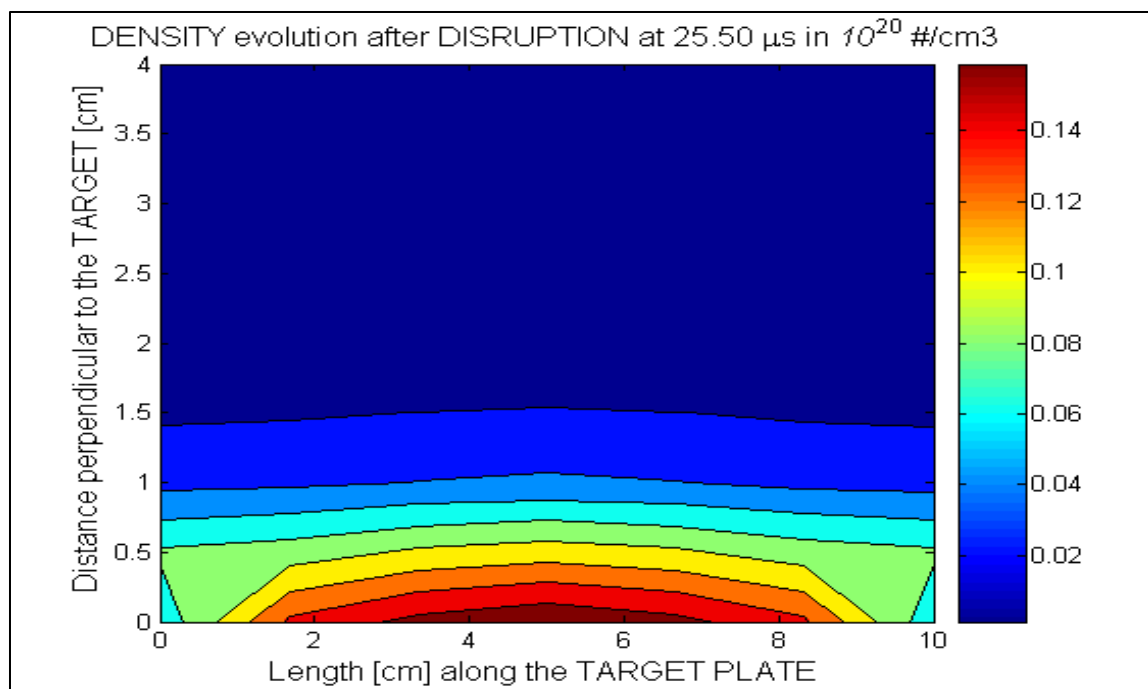


Figure 4.34 Calculated plasma density evolution at the target in a typical MK-200 experiment simulation with HEIGHTS-PIC (at 25.50  $\mu\text{s}$ )

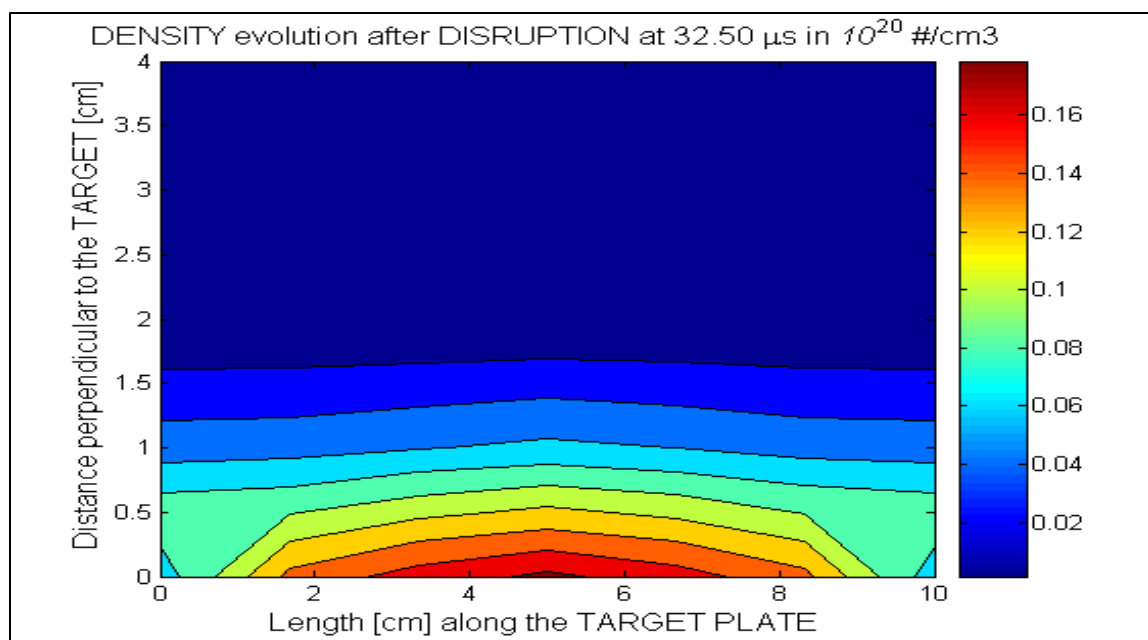


Figure 4.35 Calculated plasma density evolution at the target in a typical MK-200 experiment simulation with HEIGHTS-PIC (at 32.50  $\mu\text{s}$ )

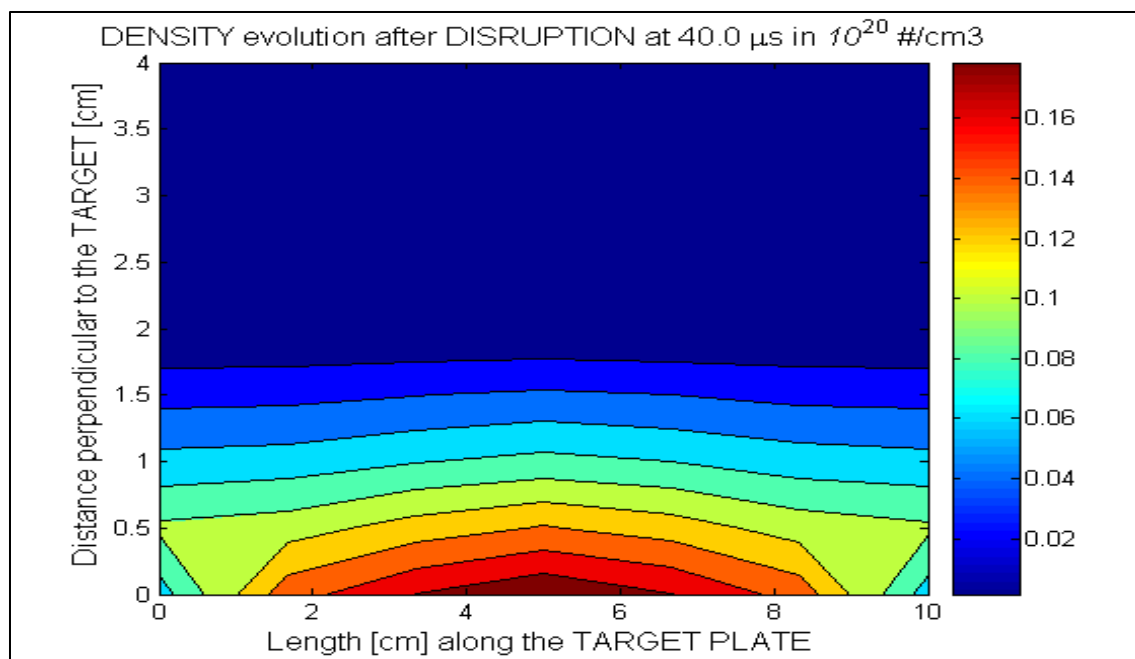


Figure 4.36 Calculated plasma density evolution at the target in a typical MK-200 experiment simulation with HEIGHTS-PIC (at 40.0  $\mu\text{s}$ )

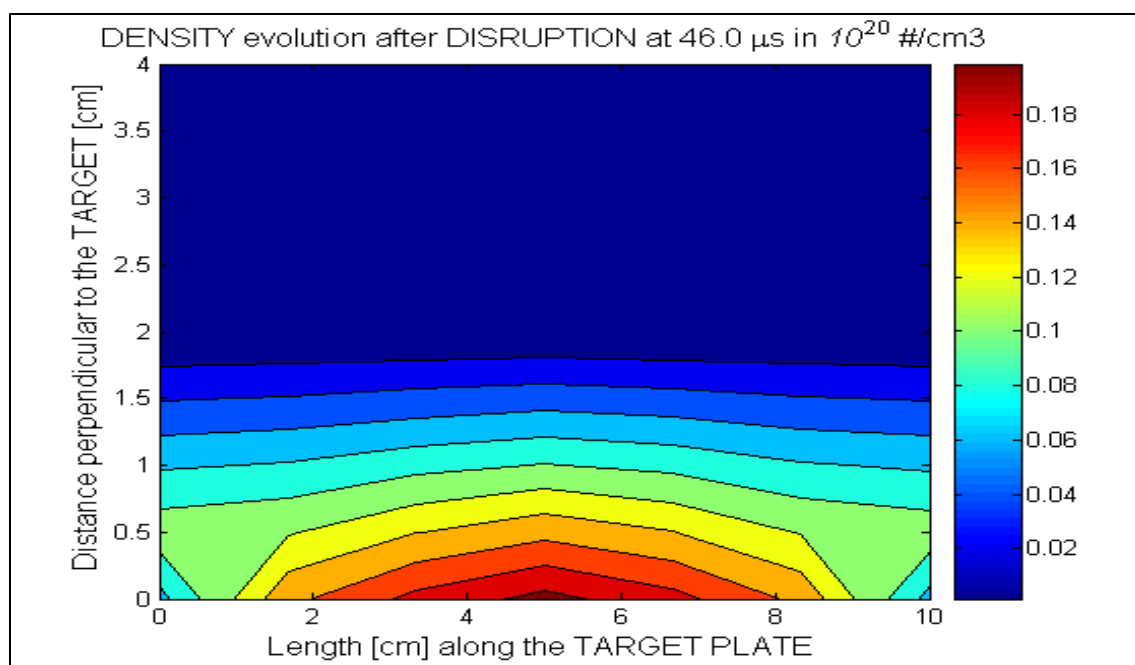


Figure 4.37 Calculated plasma density evolution at the target in a typical MK-200 experiment simulation with HEIGHTS-PIC (at 46.0  $\mu\text{s}$ )

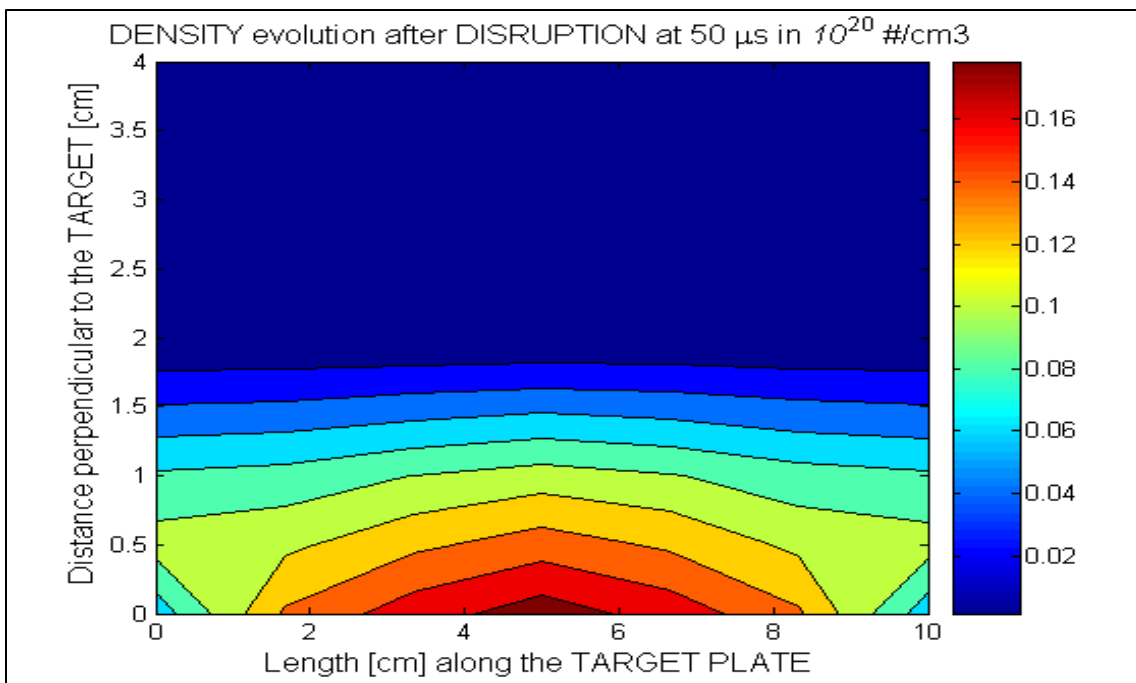


Figure 4.38 Calculated plasma density evolution at the target in a typical MK-200 experiment simulation with HEIGHTS-PIC (at 50.0  $\mu\text{s}$ )

As expected, with time, density close to the target increases due to the vaporized carbon from the material that tends then to expand and mix with the incoming plasma particles. As time progresses, a thick layer of vapor is formed in front of the plate allowing the target plate to be screened from direct plasma impingement. Around 3  $\mu\text{s}$  and up to 8  $\mu\text{s}$  formation of “wings” at the sides is evident and confirmed also by a similar behavior in the calculations performed by FOREV-1/FOREV-2 even though at much later time( recall that the time evolution of the beam here it is different since HEIGHTS-PIC is using a step rise). As time progresses there is an outward flow of carbon particles that makes the density of the outermost layers almost an order of magnitude lower with respect to the cooler and denser material close to the target Once

the particles pushed aside of the computational mesh are numerically lost at the boundaries, the Gaussian shape of the density evolution becomes very evident as in the early instants of the plasma production. After  $9 \mu\text{s}$  or so, since the erosion has already stabilized at very low rate, the expansion of the plasma takes place with almost constant density close to the target. The values reached at the peak by the density are close to  $2 \cdot 10^{19} \text{ \#/cm}^3$ . Looking instead at the electron density close to the plate, we see that the peak values are close to  $3 \times 10^{18} \text{ \#/cm}^3$  so similar to the reported values in the literature and also similar at least in the order of magnitude to the ones calculated with FOREV-1/FOREV-2 [6]. No coronal plasma is found in our calculations, or an expansion of several centimeters from target as reported by other computer packages [6].

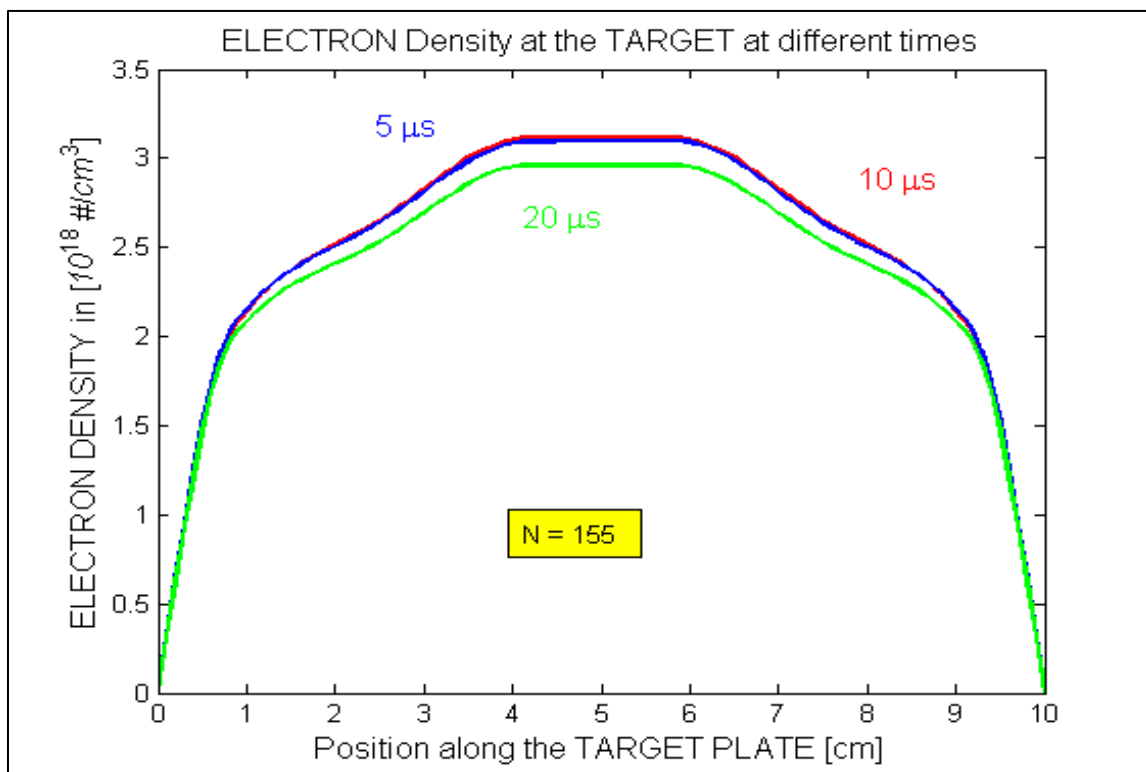


Figure 4.39 Calculated ELECTRON density of the plasma at the target plate in a typical MK-200 experiment simulation with HEIGHTS-PIC (N=155) (5-20  $\mu\text{s}$ )

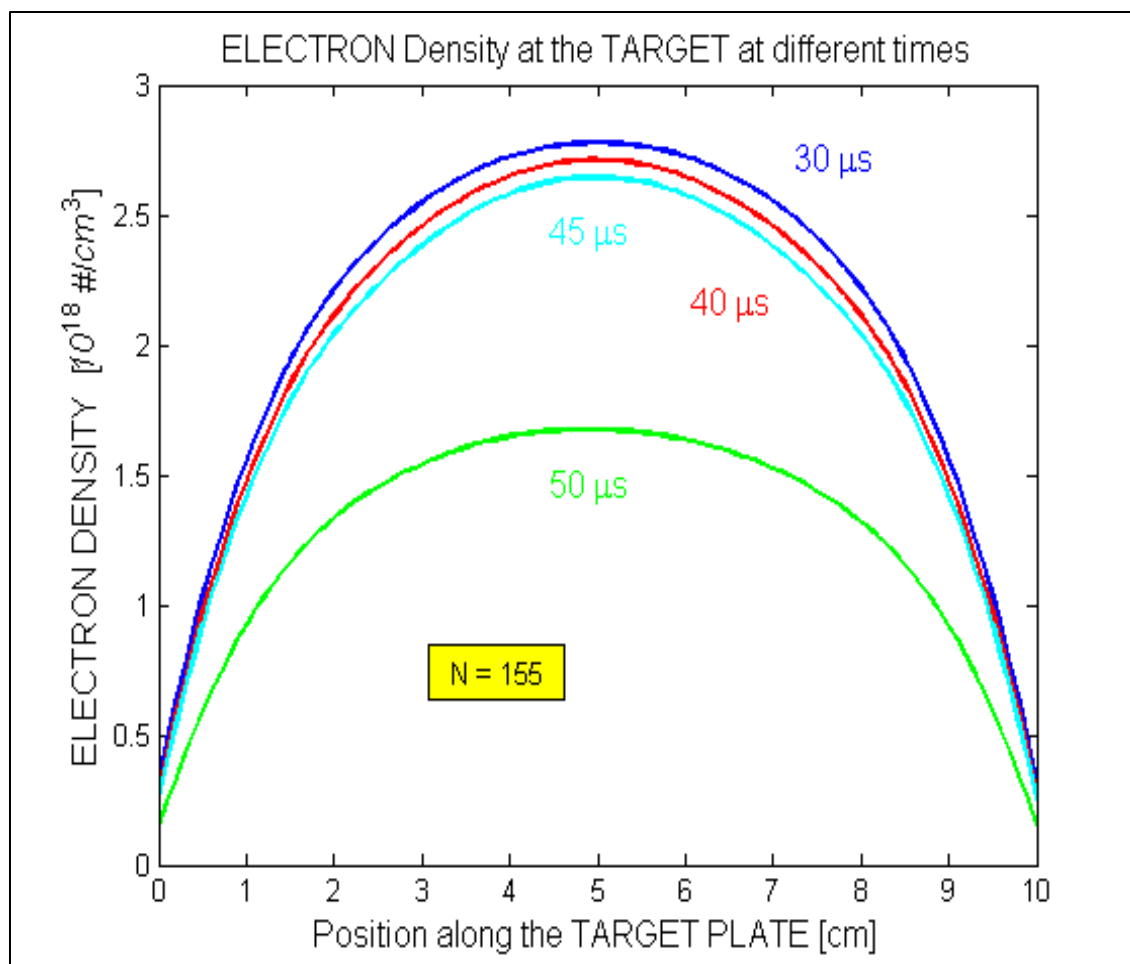


Figure 4.40 Calculated ELECTRON density of the plasma at the target plate in a typical MK-200 experiment simulation with HEIGHTS-PIC (N=155) (30-50  $\mu$ s)

Examining the position of the carbon plasma vapor front, the maximum distance from the plate is not more than few centimeters. This can be probably justified considering that HEIGHTS-PIC beam doesn't have mixing of plasma DT with the Carbon plasma front [35]. The effects of the DT cloud accumulated front are then absent and cannot be evaluated with this model compared to previous HEIGHTS work [35-36].

#### 4.2.4 Benchmarking results with different temporal Beam Evolutions

In this section some other benchmarking calculations are presented. In particular the beam linear rise of 5  $\mu\text{s}$  and 10  $\mu\text{s}$  are used in this section. At the base of the choice for a different temporal evolution of the MK200-like beam stands the fact that there is uncertainty on how the machine itself reaches the full beam of 35  $\text{MW}/\text{cm}^2$  and it is highly probably that the full power flux is not reached immediately but with some type of rise most probably linear. In addition to that, aim of these different simulations was to verify if there were significant differences in the erosion calculation and plasma evolution. At the end of this analysis it will be shown they are not significant and this can be related to the fact that different temporal beam evolutions provide also slightly different energies to the target plate.

Looking at the evolution of the calculated maximum erosion versus time, it is noticeable that the plateau is reached close to the point in which the beam is at full power and it is smaller than the STEP RISE case. Once the plasma expansion starts, erosion increases smoothly and at a slower pace showing that the screening effect is taking place. Erosion stops growing just before the beam start its fading phase.

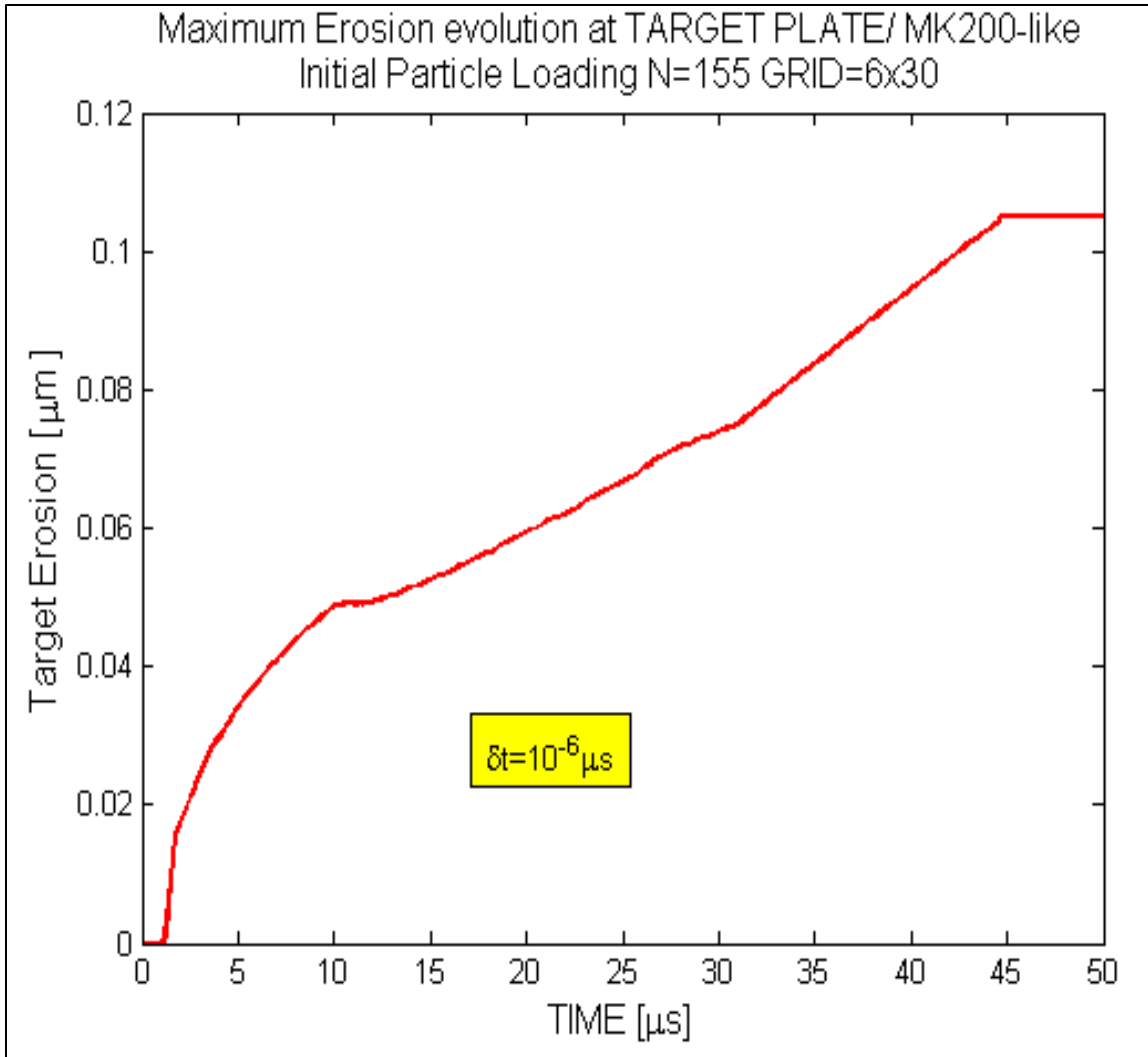


Figure 4.41 Calculated erosion profile evolution (10  $\mu s$  linear rise) in a typical MK-200 experiment simulation with HEIGHTS- PIC (N=155 sample particles initial loading).

A very similar trend is developed with the 5  $\mu s$  LINEAR RISE. The final values for both simulations are very close to each other providing for the first simulation  $\delta X_{\text{erosion}} = 0.105 \mu m$  and  $\delta X_{\text{erosion}} = 0.1125 \mu m$  for the 5  $\mu s$  LINEAR RISE.

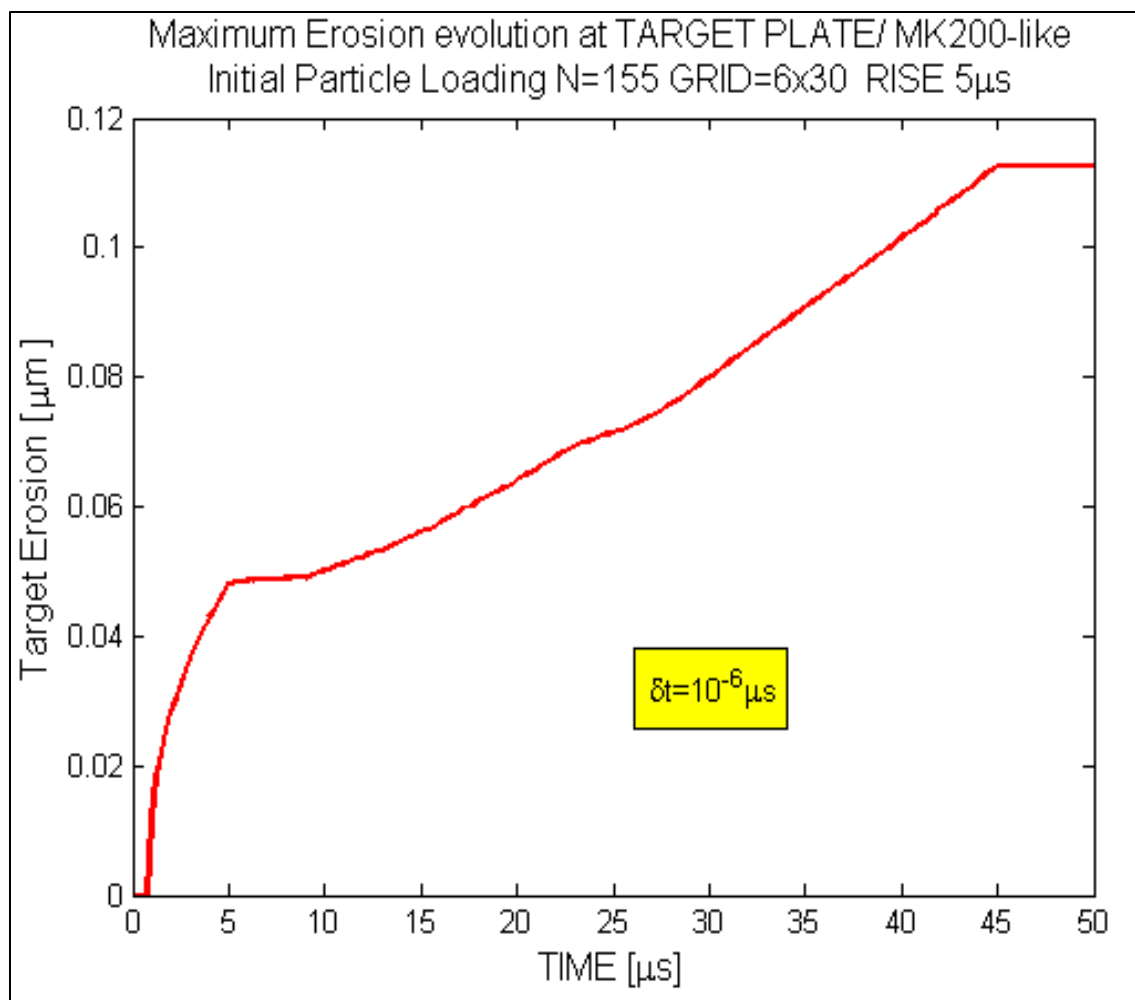


Figure 4.42 Calculated erosion profile evolution (5 μs linear rise) in a typical MK-200 experiment simulation with HEIGHTS- PIC (N=155 sample particles initial loading).

The error also calculated for different initial particle loadings (N=5 vs N=155) is comparable with the one shown before for the STEP RISE (19.3 % vs. 17%) in both cases. In the following figure the 5μs LINEAR RISE is presented.



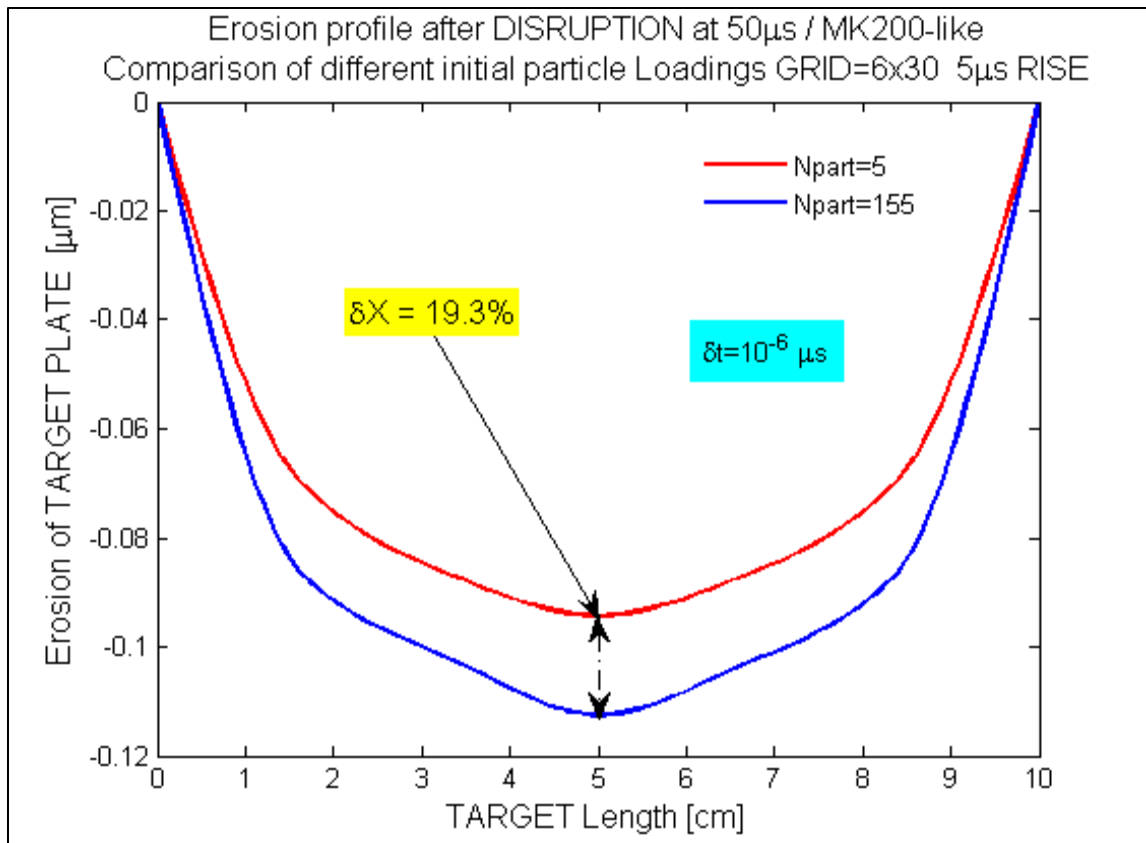


Figure 4.43 Calculated erosion profile (5  $\mu$ s rise) in a typical MK-200 experiment simulation with HEIGHTS-PIC (5 vs. 155 sample particles initial loading).

For the calculation of the maximum temperature into the plate, both simulations reach maximum values around 5300 K (5341 K for 5  $\mu$ s LINEAR RISE 5342 K for 10 $\mu$ s LINEAR RISE) and are very comparable to the STEP RISE simulation (i.e., 5339 K). The main difference stands in when the peak is reached: it corresponds for both cases at the time when the maximum power flux is effectively reached. For example here it is shown the evolution of the maximum target temperature of the 10  $\mu$ s LINEAR RISE.

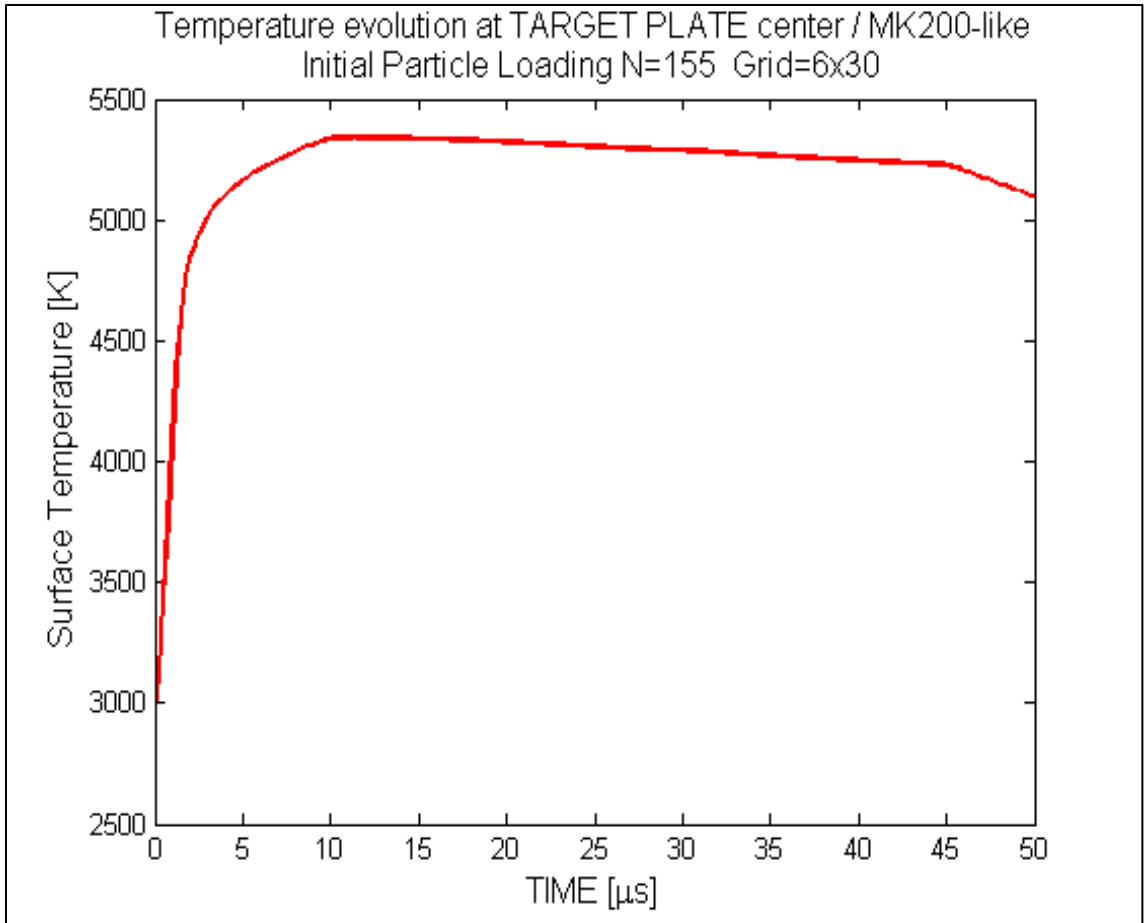


Figure 4.44 Calculated temperature evolution in a typical MK-200 experiment simulation with HEIGHTS-PIC (N=155 Particles/ 10 $\mu$ s linear rise)

Looking for both cases at the power fluxes at the center of the plate (figures 4.45 and 4.46), they show a similar trend for both cases and comparable again with the STEP RISE case. Also in this case and as expected the peak of the calculated power flux is reached at 5  $\mu$ s or 10  $\mu$ s. The trends appear quite smooth and this due essentially to the very small  $\delta t$  used for the simulation (i.e., 1 ps).

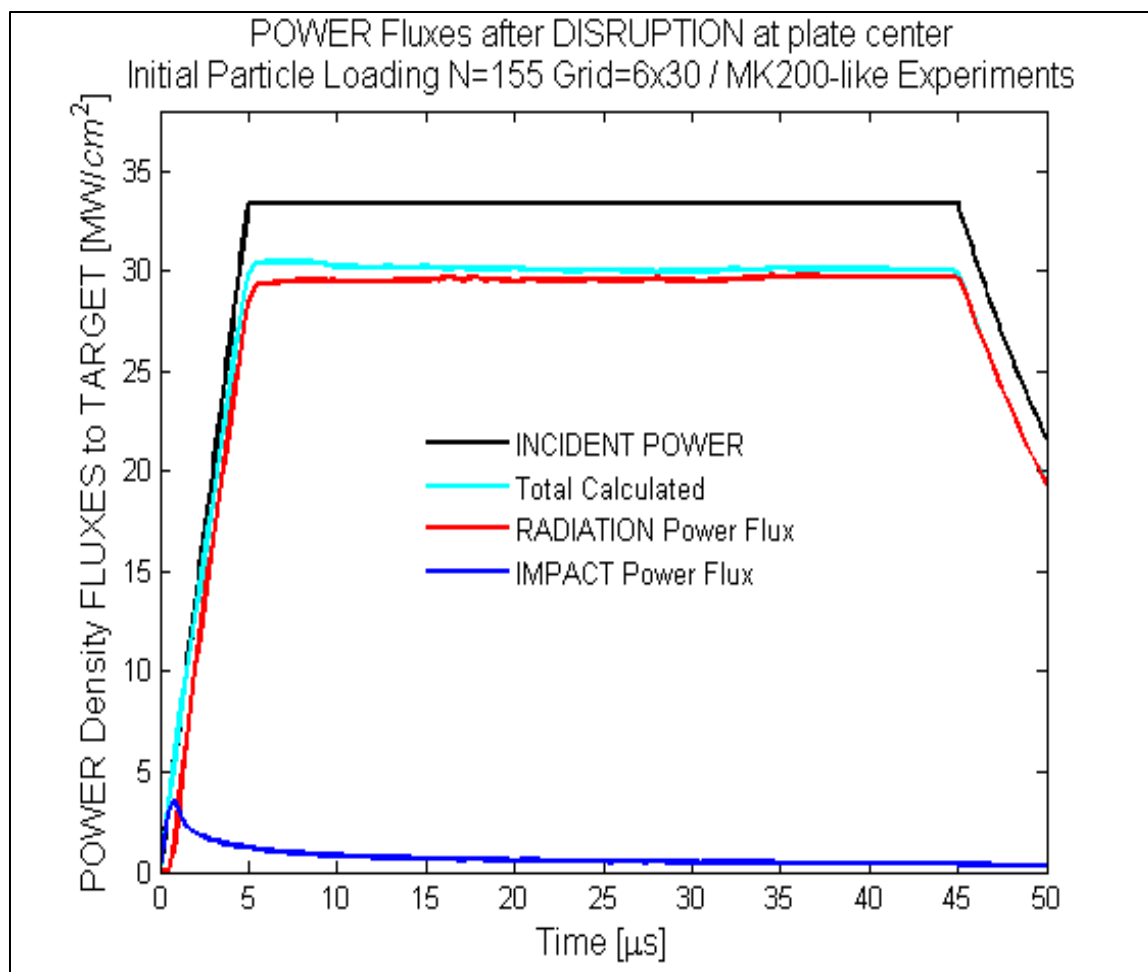


Figure 4.45 Calculated power fluxes evolution at plate center in a typical MK-200 experiment simulation with HEIGHTS-PIC (N=155/ 5  $\mu$ s rise)

As for the STEP RISE case, the use of relatively coarse grid (6x30) induces some difference between the input power beam (black line) and the total calculated (cyan line). This difference as seen before will be strongly reduced one the number of cells used for solving the radiation transport equation will be increased (12x30 and even better 18x30).

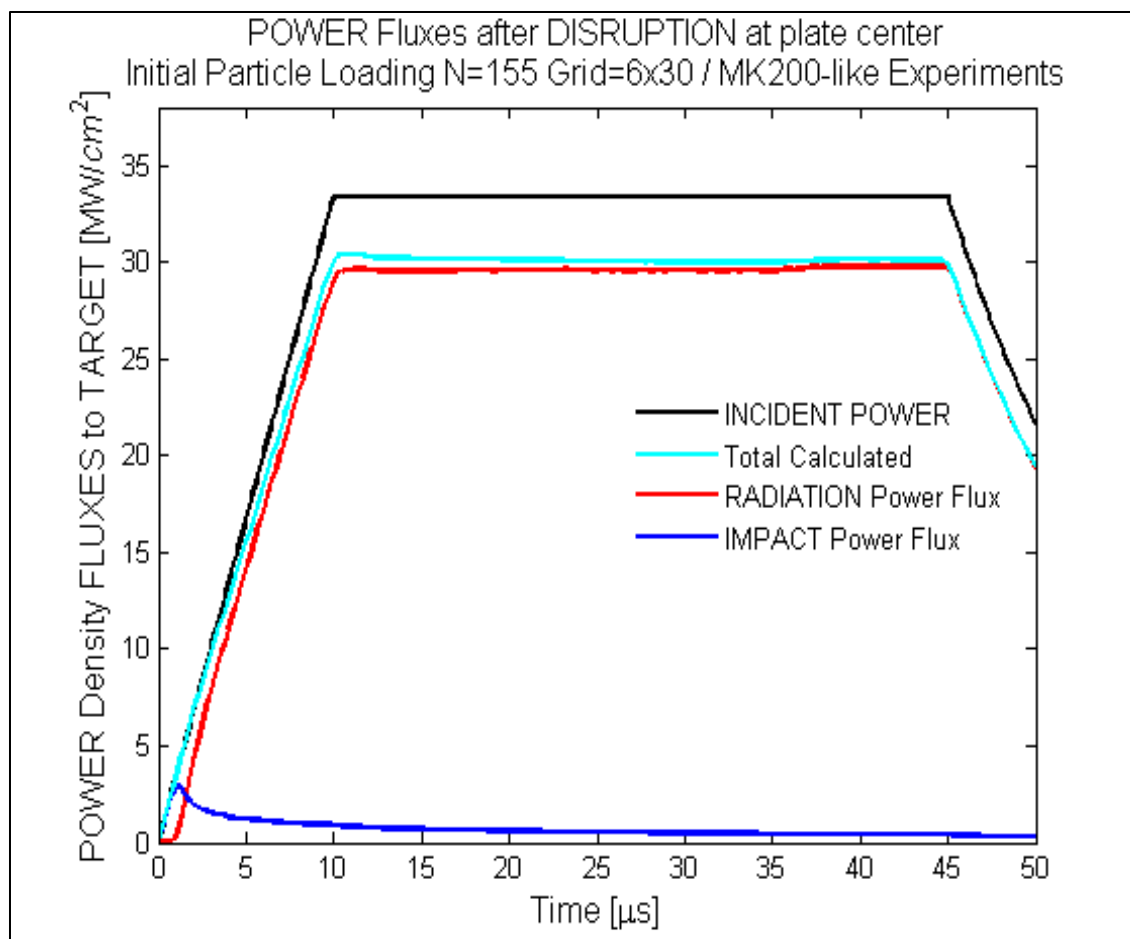


Figure 4.46 Calculated power fluxes evolution at plate center in a typical MK-200 experiment simulation with HEIGHTS-PIC (N=155 / 10 μs rise)

Also the geometrical distribution of the total calculated beam with respect to the originally inputted/assigned one is similar to the STEP RISE case. Looking at figure 4.47 also in this case an underestimation of the central power flux is present. At the same time the wings present an overestimation of the power flux leaving though to total difference with the original beam very small and in the same order of magnitude seen for the STEP RISE case.

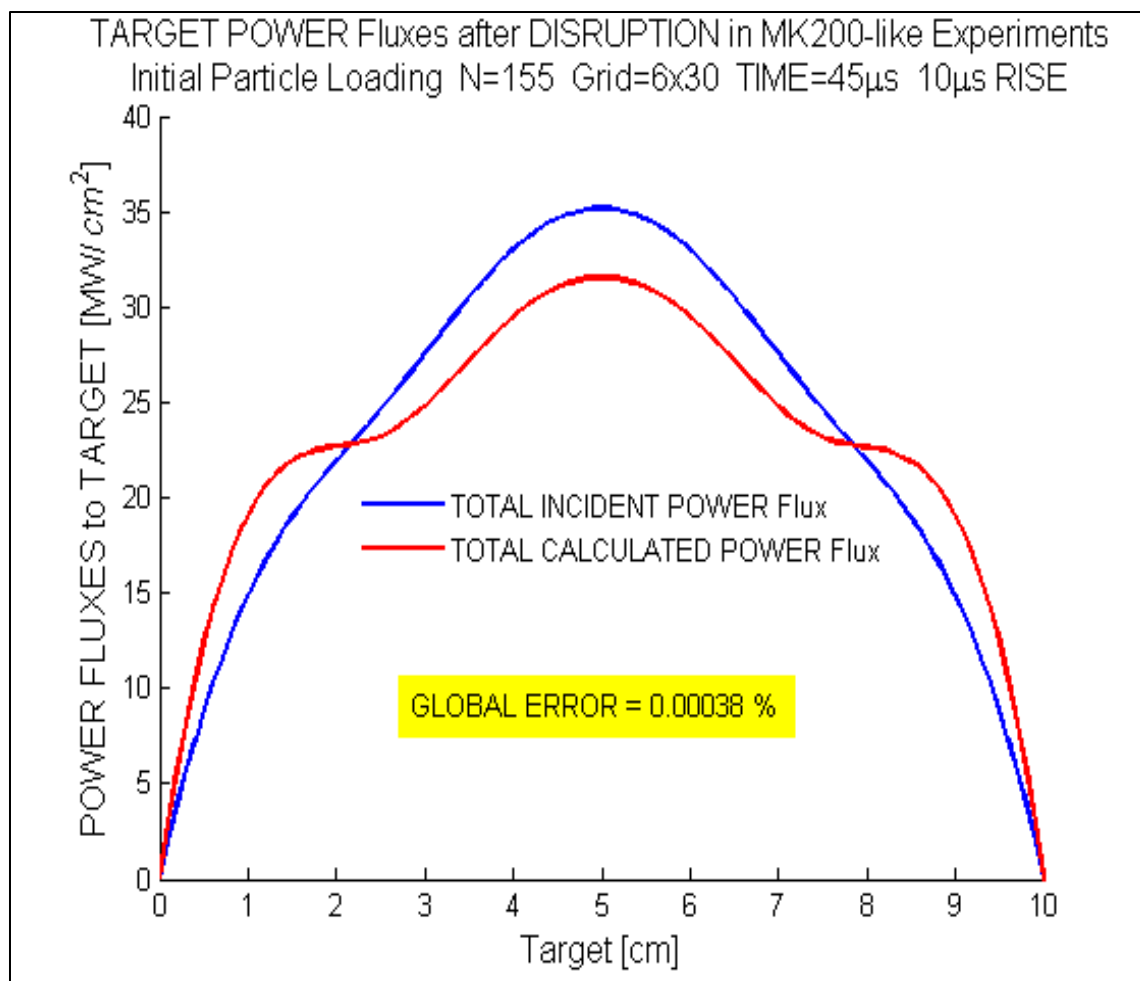


Figure 4.47 Calculated power fluxes along the plate at 45  $\mu$ s in a typical MK-200 experiment simulation with HEIGHTS-PIC (N=155 / 10  $\mu$ s rise)

The trends for both pressure and temperature look very similar to the STEP RISE case. It is important to notice that in both cases (figure 4.48 and 4.49) there are no significant oscillations or numerical instabilities. Both trends look very similar and reach roughly the same value of maximum pressure at their respective power flux peak (5  $\mu$ s and 10  $\mu$ s).

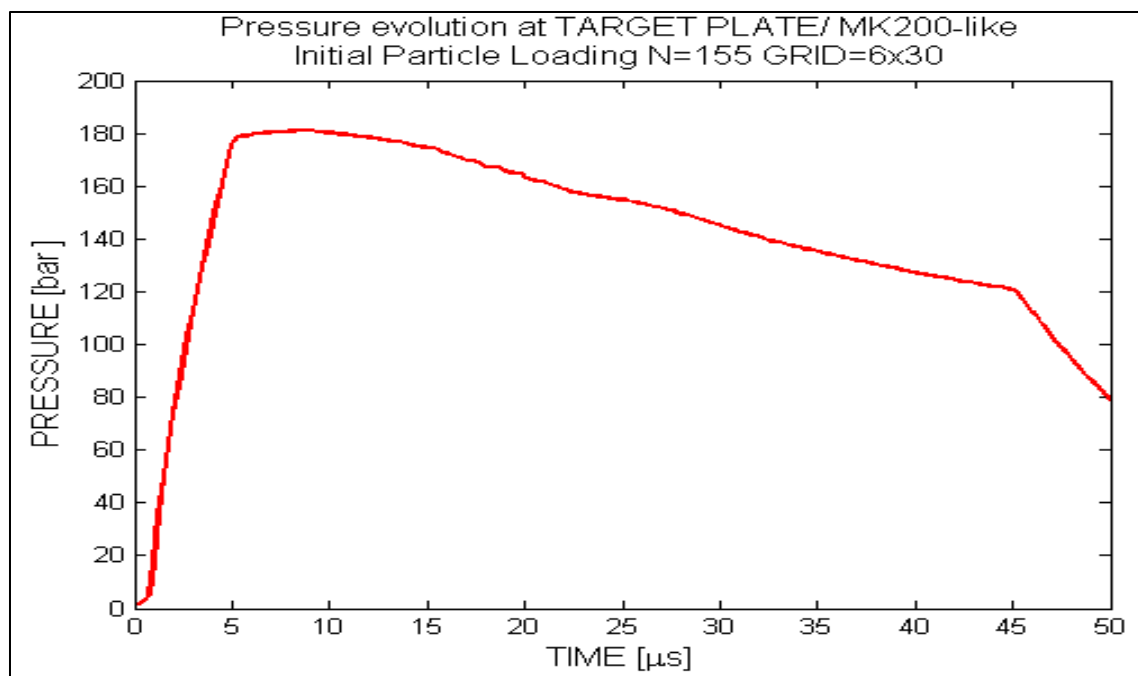


Figure 4.48 Calculated evolution of pressure at TARGET plate center in a typical MK-200 experiment simulation with HEIGHTS-PIC (N=155 / 5  $\mu$ s rise)

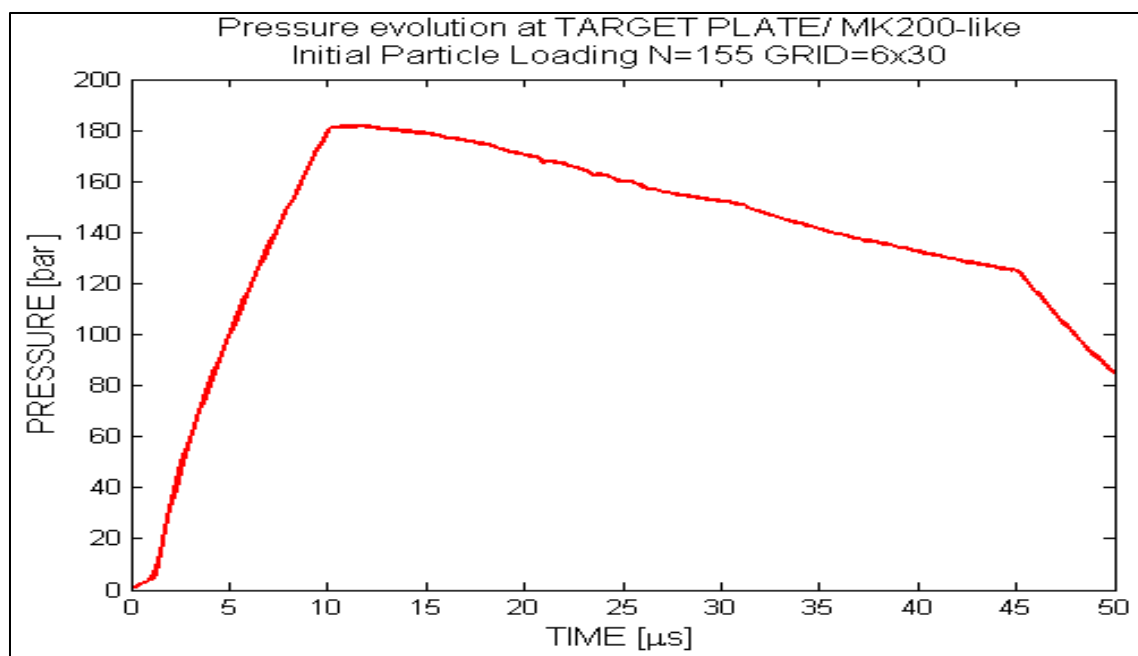


Figure 4.49 Calculated evolution of pressure at TARGET plare center in a typical MK-200 experiment simulation with HEIGHTS-PIC (N=155 / 10  $\mu$ s rise)

Evolution of the plasma density and temperature are similar to the STEP RISE case. The main difference is in when the maximum temperature is reached (still though equal to roughly 3 eV) given the different beam temporal beam evolution. In conclusion it can be confirmed as anticipate before that changing the temporal evolution of the beam profile (using for example different LINEAR rises) does not change significantly any of the main parameters calculated not alter the behavior of the plasma itself.

#### 4.3 Benchmark with the HEIGHTS Computer Package

Simulations have been run with HEIGHTS-PIC in order to reproduce some of the published results by HEIGHTS regarding giant ELM impacting on the divertor using ITER-like conditions. In particular using the ‘ITER-FEAT Outline Design Report’ [10] as basic geometry for our simulations, carbon material divertor was assumed as target plate. The magnetic field intensity used is 5 T and the inclination of the field with respect to the target plate is 5°. The ELM impinging plasma has been simulated assuming an exponential beam shape with the maximum power density profile at the strike point. For duration of 0.1 ms, a total of 12.6 MJ of energy (roughly 10% of the total pedestal energy, i.e., Giant ELM) reaches the target plate [35]. The e-fold length of the power profile above the divertor is 6.7 cm. At the strike point the power density profile peaks at 4.6 MW/cm<sup>2</sup> with a minimum at the e-fold length of 1.692 MW/cm<sup>2</sup>. The ITER major radius is of 6.5 m while the assumed initial plasma temperature is of  $E_0=3.5$  keV. The computational domain taken into account extends then for 6.7 cm along the target plate and for 15 cm perpendicular to it: 300 cells are used in the following ELM simulation

making the cell dimensions of 0.67 cm for 0.5 cm. In the second simulation presented 600 cells were used making the cell dimensions 0.335 cm by 0.5 cm. No poloidal magnetic field is assumed in HEIGHTS-PIC simulations.

#### 4.3.1 Erosion of the divertor plate & Fluxes

Erosion of the divertor plate is highly influenced by the beam intensity, duration, and geometrical distribution above the target [11, 16-17]. Recent studies have pointed out that the plasma energy flux reaching the target plate through the scrape off layer has a non-symmetrical shape similar to an exponential decay. The maximum erosion is then expected close to the strike point where the highest power flux is concentrated. Time considered for a typical ELM event (100  $\mu$ s) is too small to allow significant heat transfer through the material, so that most of the energy released is spent for the carbon erosion and its hydrodynamics movement in the plasma-vapor cloud above the surface.



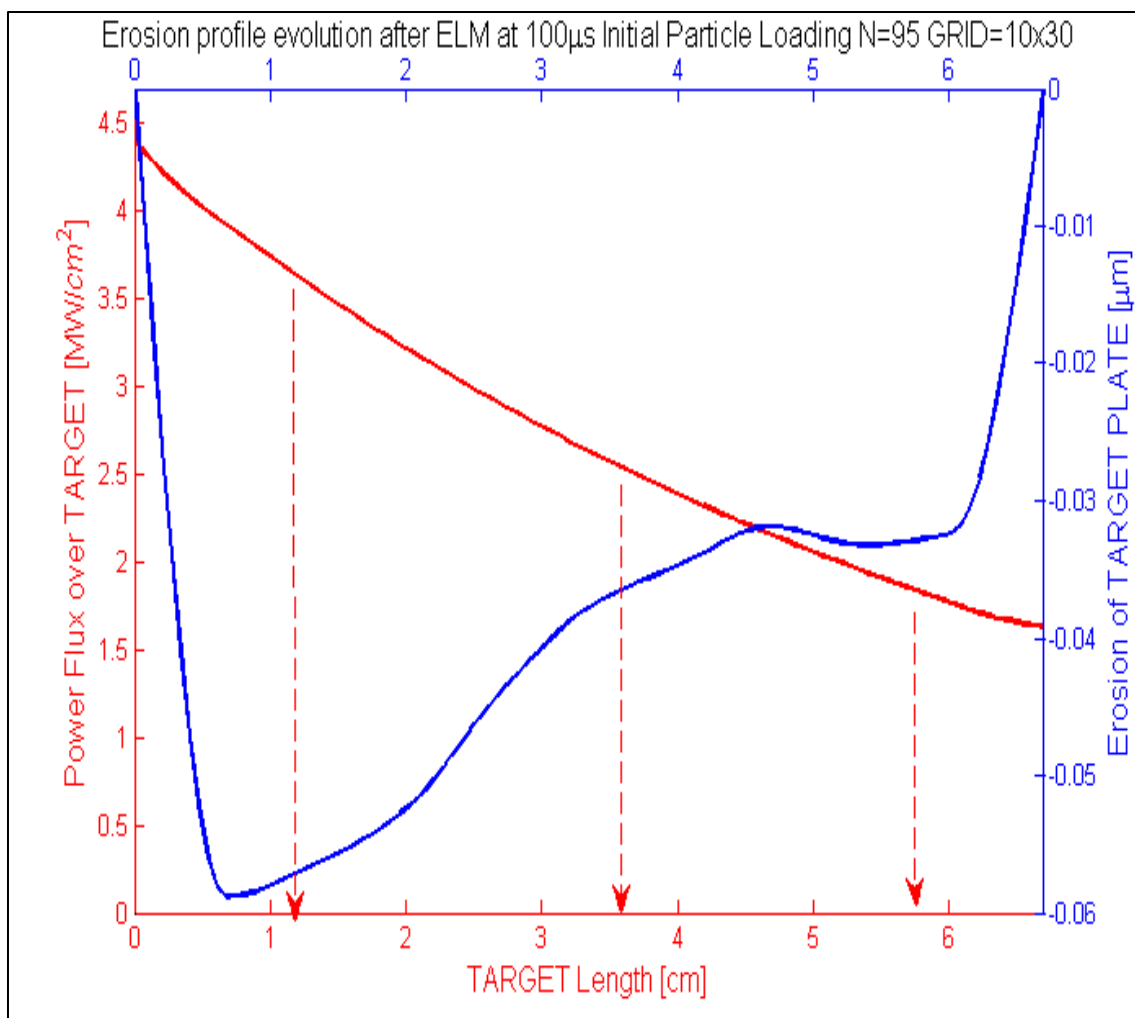


Figure 4.50 HEIGHTS-PIC calculated divertor erosion in carbon plasma during a giant ELM in ITER-like conditions (GRID 10x30 N=95) [39]

The profile at the end of the simulation performed with 95 sample particles (initial loading Figure 4.50) and a grid of 10 cells along the target and 30 cells perpendicular to it, shows a maximum erosion value slightly less than 0.06  $\mu$ m close to the strike point. As expected erosion is much less where the beam power deposition is less close to the end of examined plate length in correspondence to the lower power fluxes of the beam.

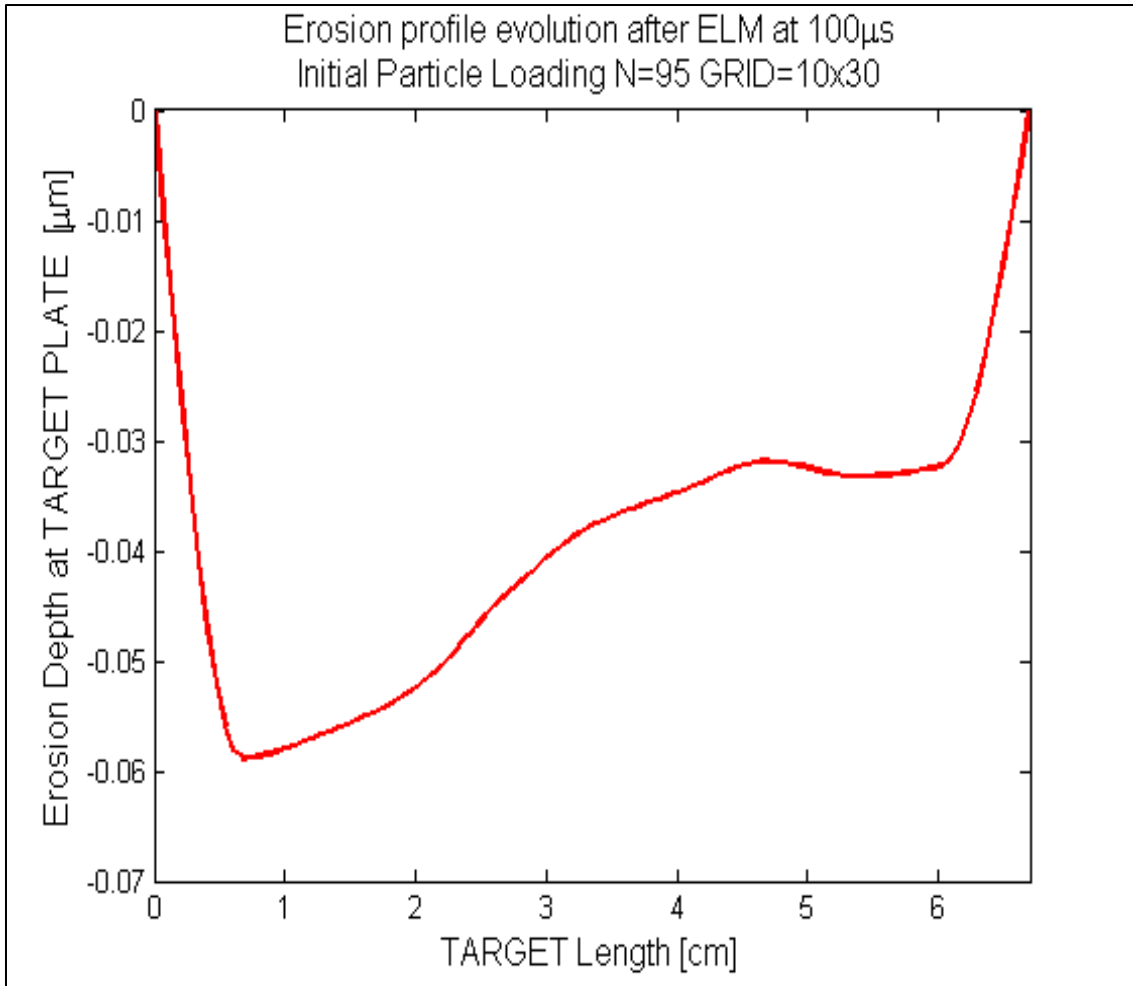


Figure 4.51 HEIGHTS-PIC calculated divertor erosion in carbon plasma during a giant ELM in ITER-like conditions (GRID 10x30 N=395)

A very similar profile can be obtained with an increased number of cells leading to a final maximum erosion close to 0.07  $\mu$ m. Comparing the obtained results with the ones produced by the original HEIGHTS package (figure 4.52,[9]), two things are evident: the maximum erosion profile is larger than the one predicted with HEIGHTS-PIC while the area covered by the profile itself seems to be wider probably due to more energy reaching effectively the surface.

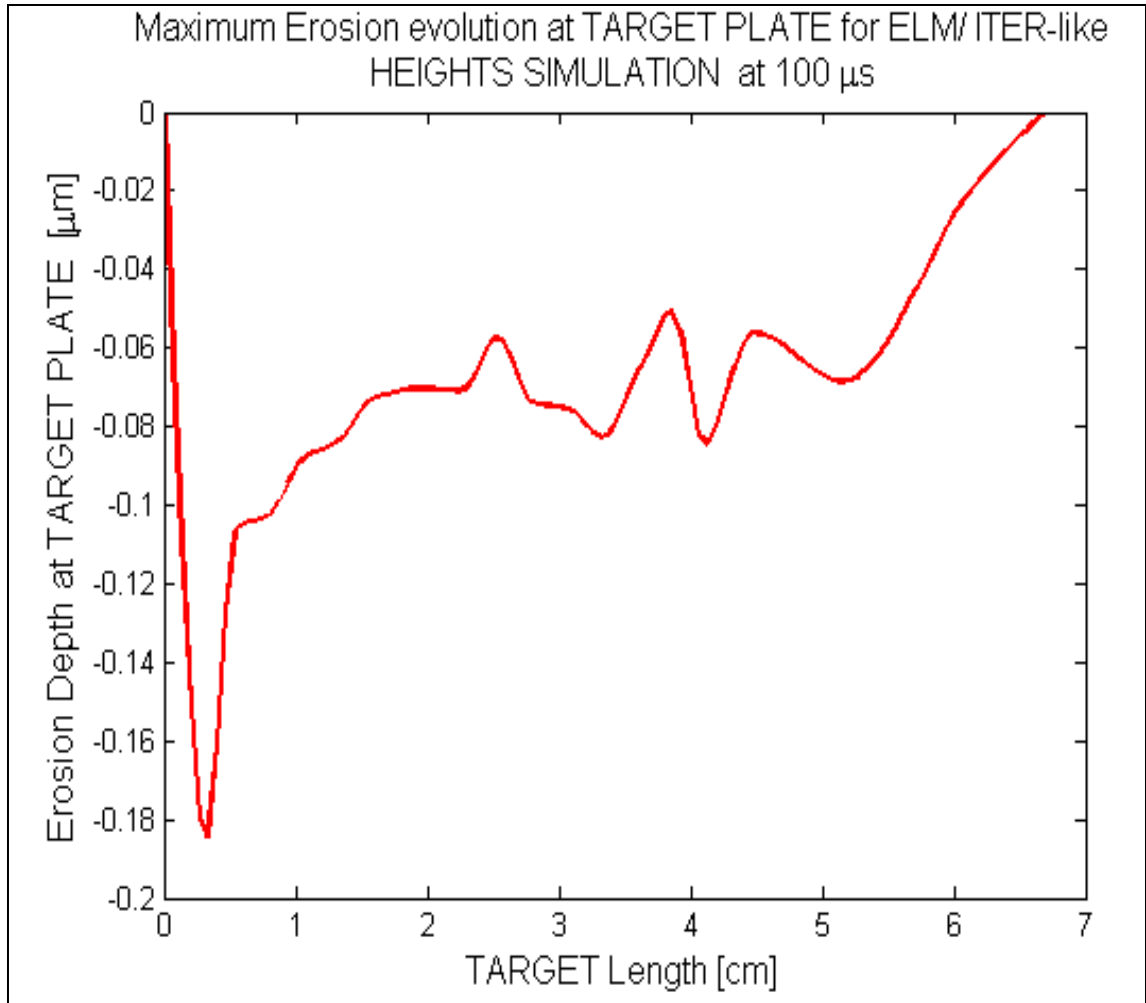


Figure 4.52 HEIGHTS calculated divertor erosion in carbon plasma during a giant ELM in ITER-like conditions [9]

Looking at the evolution of the maximum erosion (close to the striking point) versus time (figure 4.54), we see that particles starts being produced very fast (the plate starting condition is 3000 K): Three main parts can be distinguished: a first one with a relatively fast rise and two more where the rate of growth of erosion is less significant showing a more and more efficient screening effect. No flattening can be seen (at least up to 100  $\mu$ s) even though it would appear to be close.

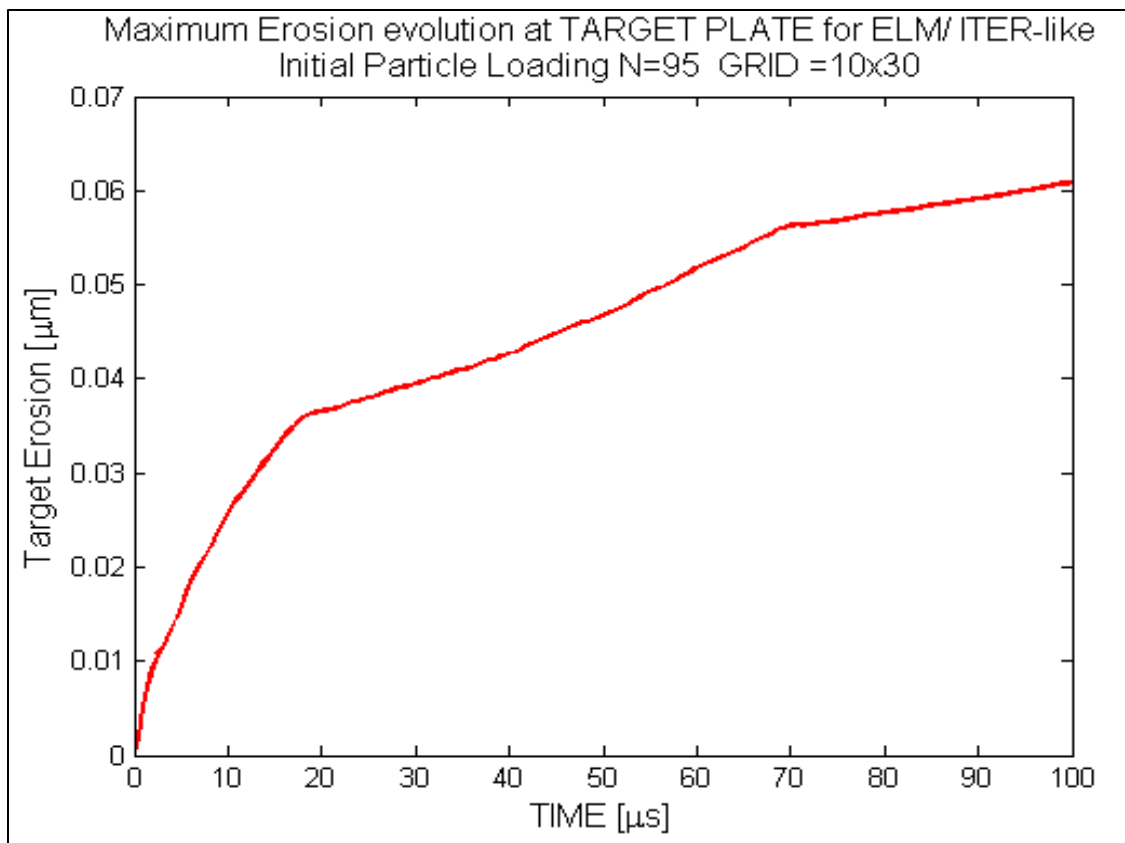


Figure 4.53 HEIGHTS-PIC calculated divertor erosion time evolution in carbon plasma during a giant ELM in ITER-like conditions [39]

Examining the integrated energy profiles deposited onto the target, differences are evident. The peak of the energy flux to the target plate is as predicted close to the strike point and reaches values of 425 J/cm<sup>2</sup>. Along the plates then, decays similarly to the exponential profile of the power beam deposition. The impact energy flux has also a peak similar to the radiation energy flux and never overcomes 50 J/cm<sup>2</sup> while the radiation to the ground reaches a peak for the striking point close to 200 J/cm<sup>2</sup>. Looking at the integrated energy profile calculated using HEIGHTS, large differences appear to be present (figure 4.55).

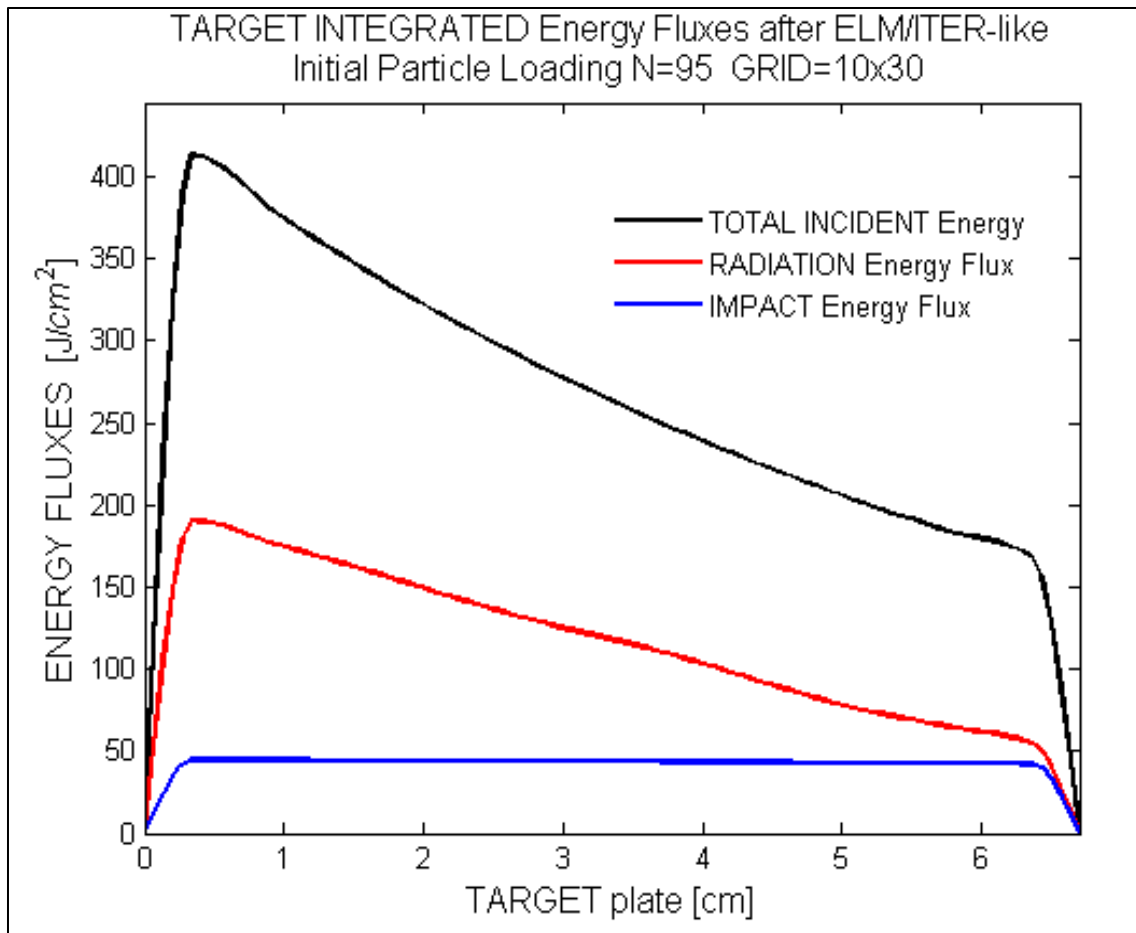


Figure 4.54 HEIGHTS-PIC calculated divertor impinging energy fluxes in carbon plasma during a giant ELM in ITER-like conditions (GRID 10x30) [39]

The calculated integrated radiation profile in the original HEIGHTS [9] appears to be much lower than the HEIGHTS-PIC calculated as the peak for the impact energy flux. It is difficult to say why those differences are so large. One explanation might be in the fact that HEIGHTS-PIC has a fixed geometry which does not compute anything out of the assigned boundary. So being the plate a roughly 7 cm long, no other portion of space is considered. The total energy is fully “trapped” into the computational mesh so designed

and does not expand as it would seem into HEIGHTS package where there are significant amount of energy released or transported to both the left and above all the right of the

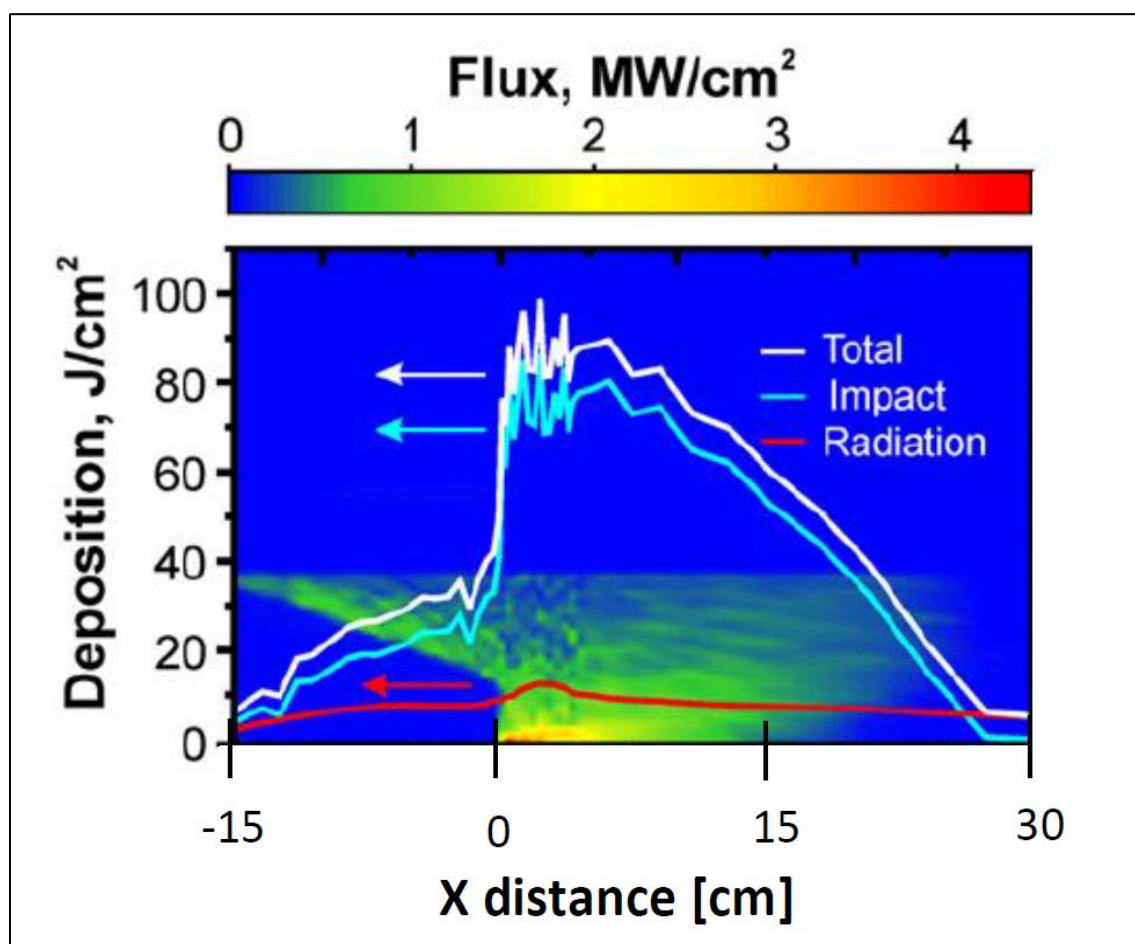


Figure 4.55 HEIGTS calculated divertor impinging energy fluxes in carbon plasma during a giant ELM in ITER-like conditions [9]

ideal computational mesh used by HEIGHTS-PIC. Looking at the power flux profile calculated using HEIGHTS-PIC for the striking point region, it is evident how the fluxes are distributed. Of the total power flux provided (black line), only a small part effectively reaches the plate (blue line) while the total radiation especially for later times would appear to be consistently higher than calculated by HEIGHTS and expected for an ELM

type of event. Consistent differences are also reported in the maximum temperature of the plasma vapor cloud for HEIGHTS-PIC. This value is close to 19 eV which though it is less than 65 eV calculated by HEIGHTS and similar values found in tokamaks experiments [9, 14, 37]. At the same time examining closely the power fluxes distribution

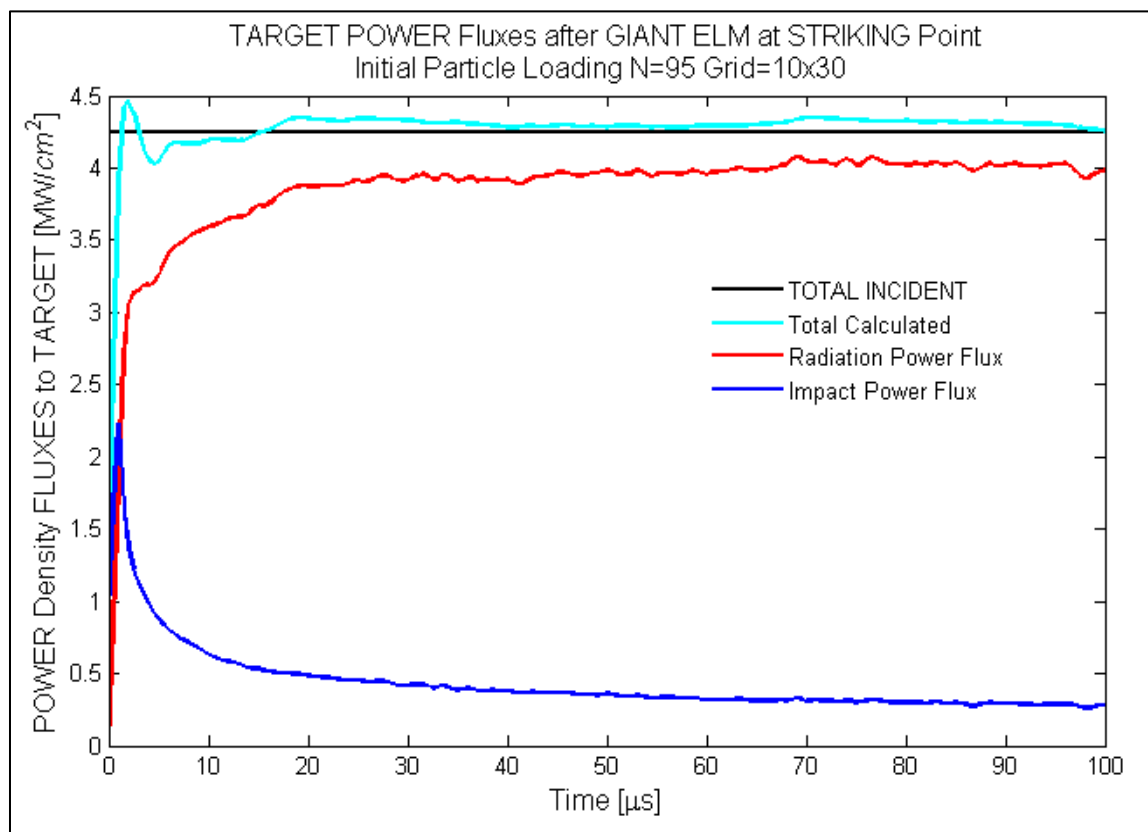


Figure 4.56 HEIGHTS PIC calculated divertor impinging power fluxes into target during a giant ELM in ITER-like conditions [39]

close to the striking point, a behavior more similar to a disruption is effectively encountered since the distribution between the effectively impinging power flux (blue line figure 4.56) and full radiation (red line) indicate a high predominance of radiation transport effects.

### 4.3.2 Density of the plasma vapor cloud

It is also important to look at the evolution of the density in proximity of the target plate. As the energy impacts over the plate, it starts heating it up and as time progresses production of carbon vapor starts (figure 4.57). As expected at the beginning most of the

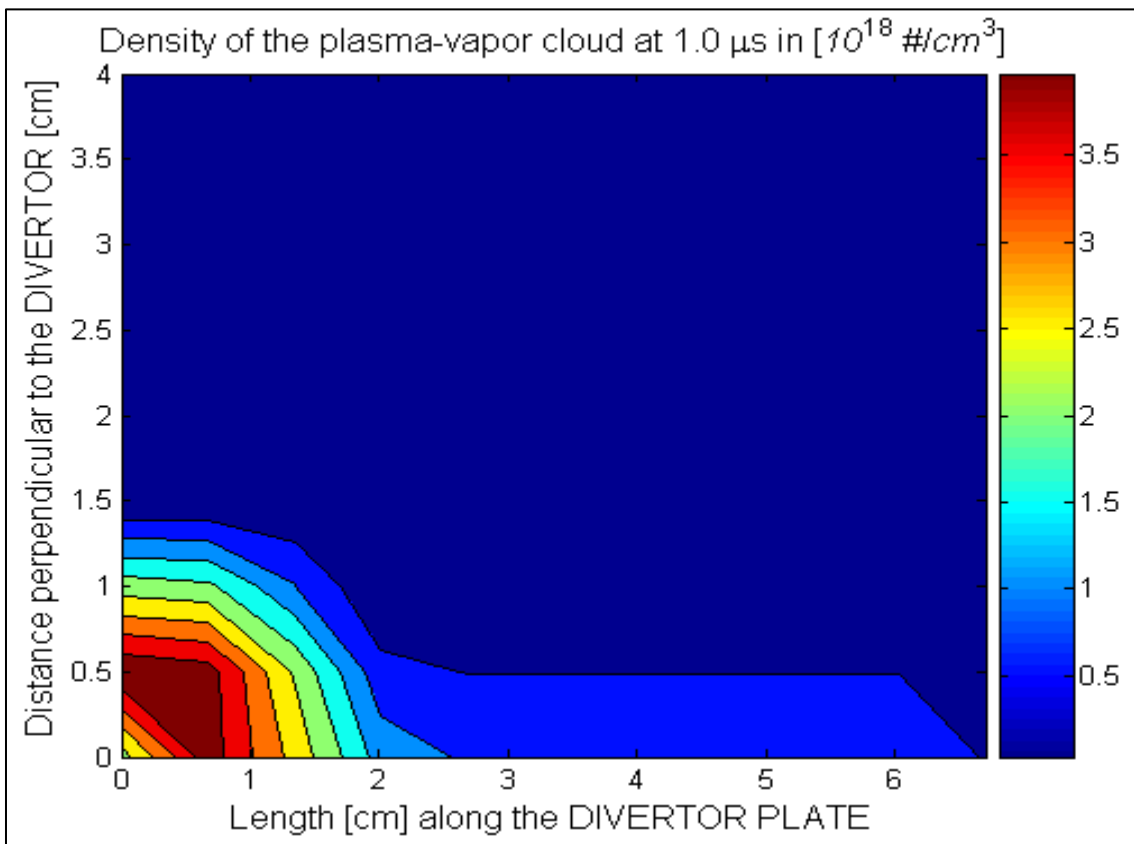


Figure 4.57 HEIGHTS PIC calculated density in carbon plasma during a giant ELM in ITER-like conditions (at  $1\mu\text{s}$ )

particle production is very close to the striking point where the power flux is higher [39]. As time progresses, other particles start being produced along the plate and the profile of the plasma density enlarges (figure 4.58): As time keeps progressing (figure 4.59 – 4.62), the carbon plasma vapor cloud tends to expand in both the X and Y direction.



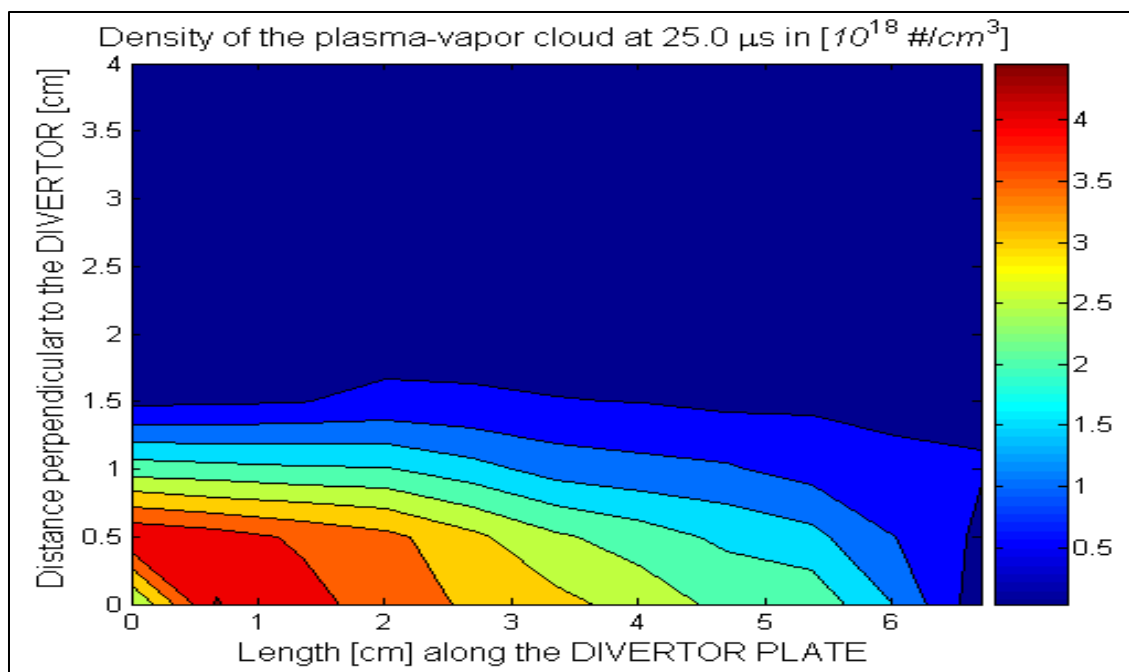


Figure 4.58 HEIGHTS PIC calculated density in carbon plasma during a giant ELM in ITER-like conditions (at 25 $\mu\text{s}$ )

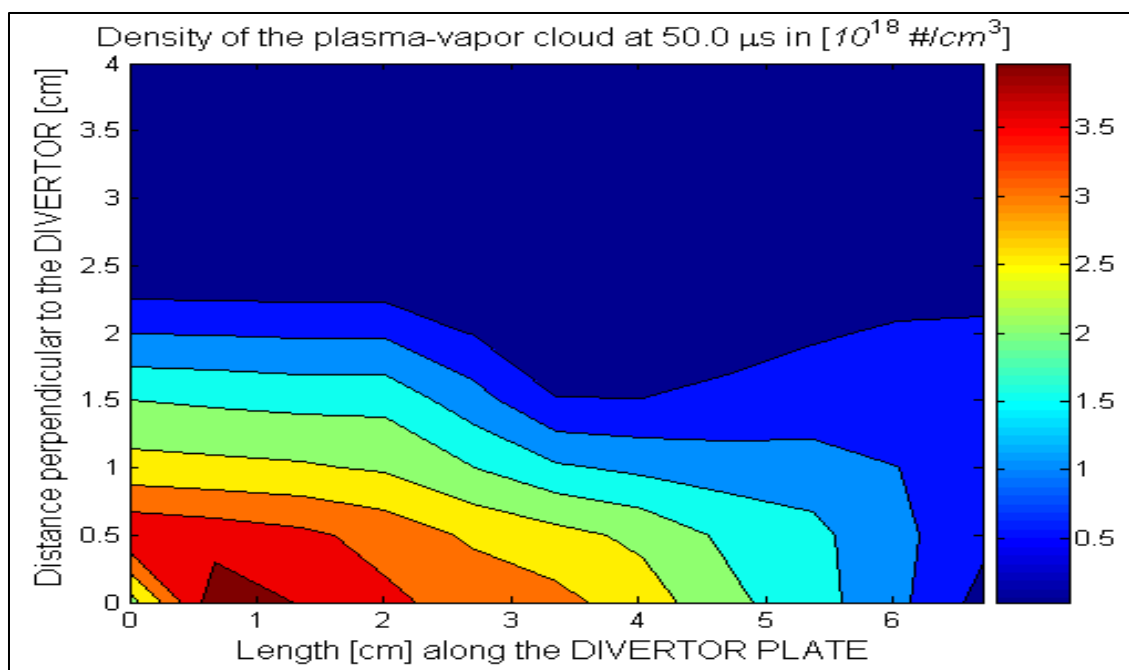


Figure 4.59 HEIGHTS PIC calculated density in carbon plasma during a giant ELM in ITER-like conditions (at 50 $\mu\text{s}$ )

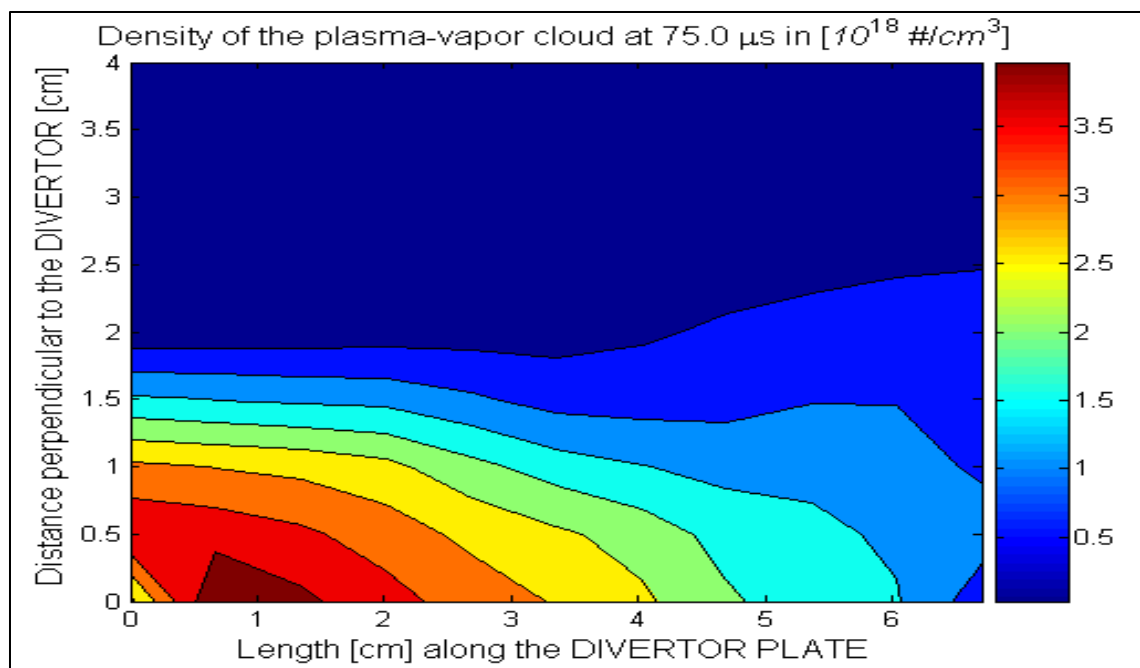


Figure 4.60 HEIGHTS PIC calculated density in carbon plasma during a giant ELM in ITER-like conditions (at 75 $\mu\text{s}$ )

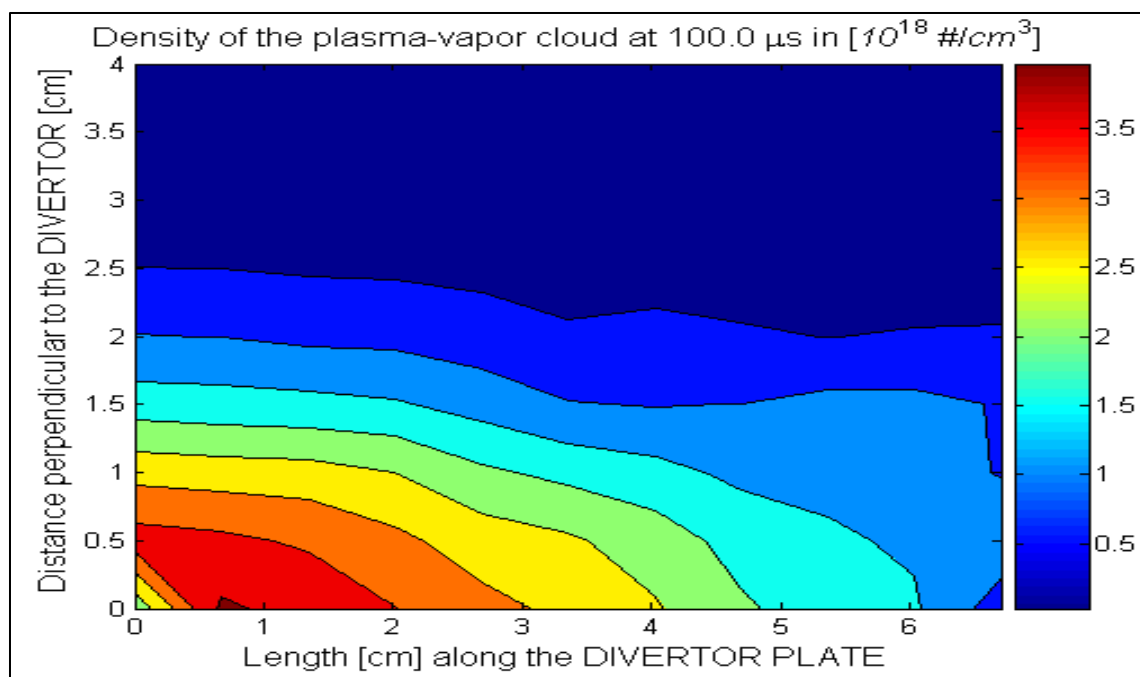


Figure 4.61 HEIGHTS PIC calculated density in carbon plasma during a giant ELM in ITER-like conditions (at 100 $\mu\text{s}$ )

At the end of the simulation the carbon plasma/vapor front has reached about 3 cm distance from the plate while the cloud is relatively stationary over the divertor plate. This distance is close to the evaluation provided for carbon vapor cloud [35].

#### 4.4 Benchmark with LASER Theoretical and Experimental DATA

In order to have more benchmarking comparisons, HEIGHTS-PIC has been modified to be able to perform numerical laser beam simulation to compare with experimental data available into the literature as well as theoretical laser-produced plasma approaches.

Laser ablation is a well-known method for removing any material from a target surface whenever it is irradiated with a high intensity laser. The process of laser ablation involves a complex series of physical events starting from a rapid evaporation of the target forming a thin layer of very dense gas made of neutrals electrons and ions. As time progresses the formed plasma starts interacting with the incoming laser beam photons increasing its pressure and temperature rapidly. This interaction is so important that governs strongly the ablation rate [17-18]. The plume in fact can become so dense that can hinder the laser radiation from reaching the target effectively screening it from further damage. This phenomenon is also very similar to the one present in similar conditions during disruptions and off-normal tokamak events [4].

The geometry used is very similar to the one adapted into HEIGHTS-PIC for the MK200 facility. The source of the laser is ideally impinging perpendicularly onto the carbon plate and the plasma so formed develops being coupled with both the incoming energy of the laser and the magnetic field still present (figure 4.63).

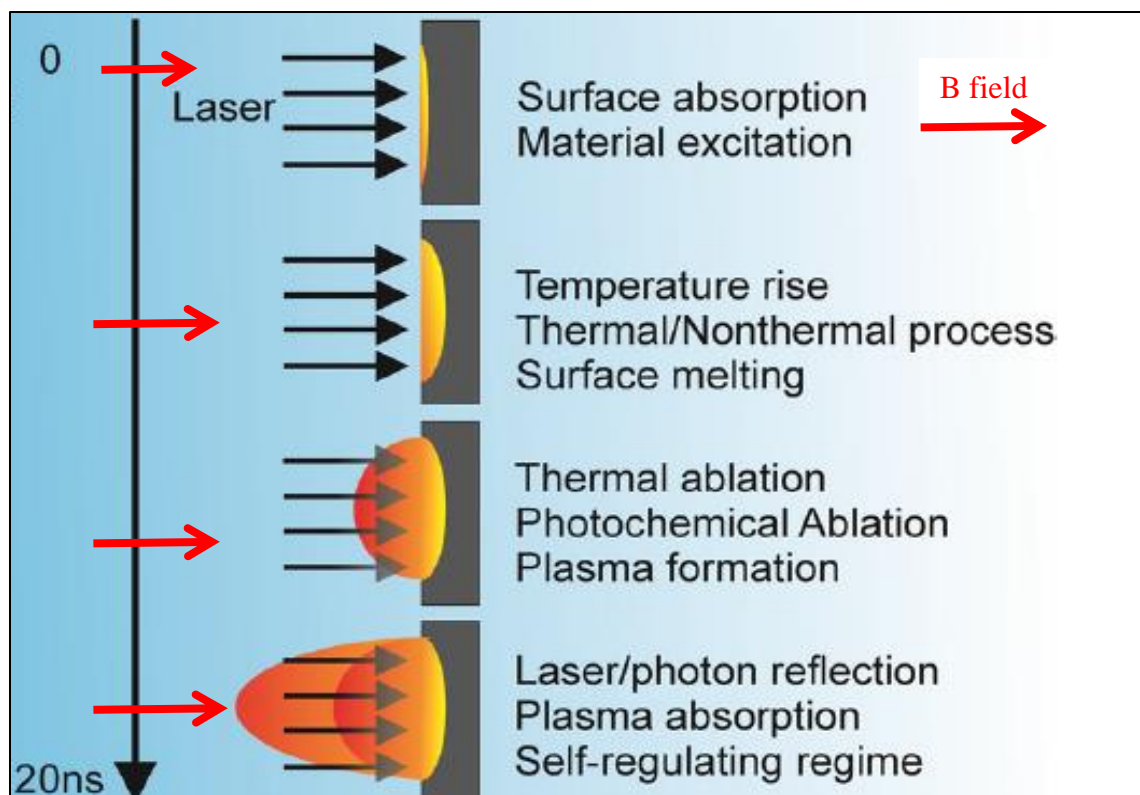


Figure 4.62 Schematics of the processes involved in ns laser ablation during the first instants of the experiment with approximate timeline of events (similar to [19]) and addition of the magnetic field B

The beam used into HEIGHTS-PIC has been modified to mimic numerically a ND:YAG laser operating with a Gaussian beam shape at its fundamental wavelength of 1064 nm with pulse energy of 400 mJ and 30 ns and total pulse duration 30 ns with FWHM of 10 ns. The laser spot size on the target has a diameter of 0.1784 cm (area of  $2.5 \text{ mm}^2$ ) with a laser total energy flux close to  $16 \text{ J/cm}^2$  with intensity of  $1.6 \text{ GW/cm}^2$ . The total duration of the analysis was 40 ns (fig.4.43). The numerical grid used was coarse being formed by a  $6 \times 10$  while the number of particles used for the initial loading was  $N=20$ . The cells then

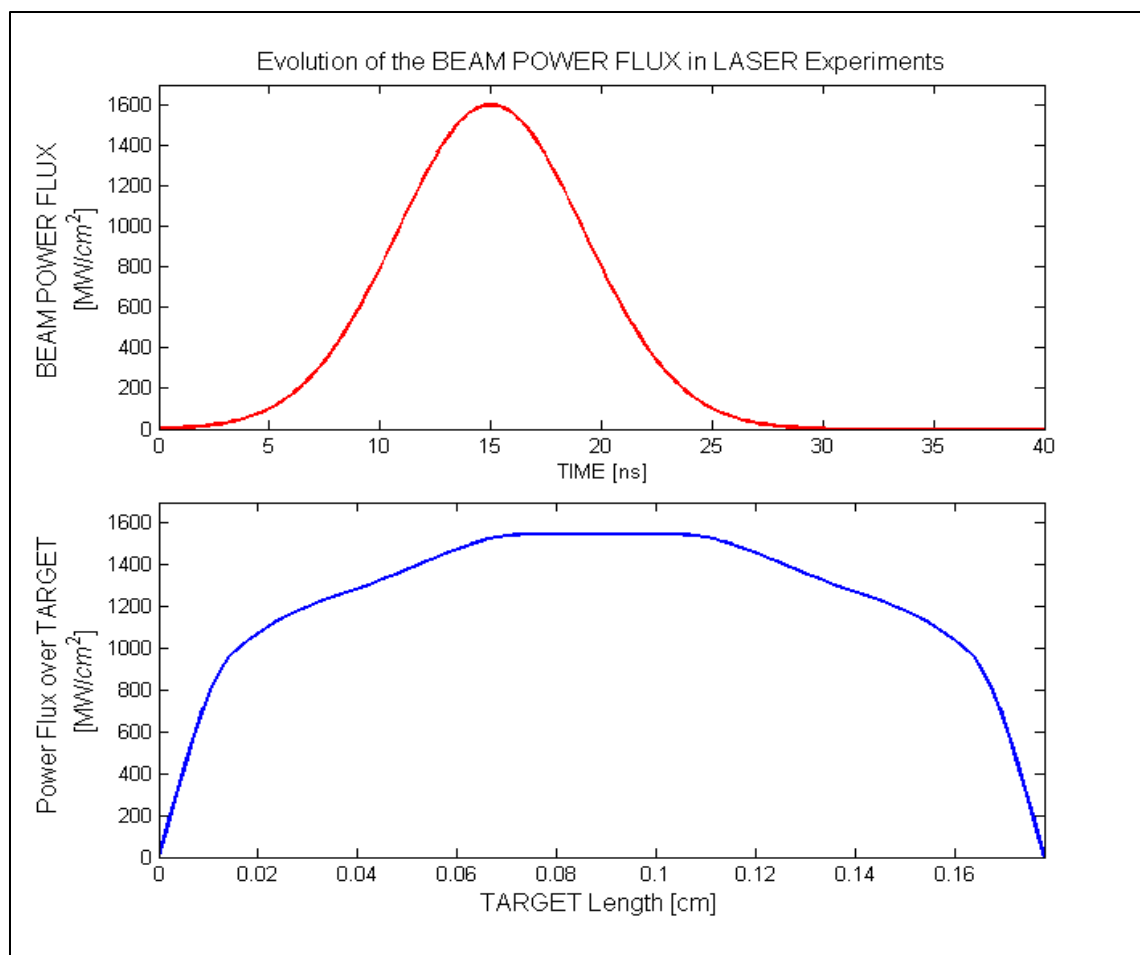


Figure 4.63 Temporal and geometrical laser beam evolution for HEIGHTS-PIC laser numerical experiments

have dimension of 0.0296cm x 0.033 cm. with the latter one the dimension of the plasma expansion. The magnetic field strength was set at 0.5 T.

#### 4.4.1 Theoretical Additions to the original HEIGHTS-PIC models

The equations of conservation of mass, momentum, and energy are solved in 2D representation (x-y plane) allowing for the plasma characteristics to be evaluated per each

cell on the top of the target itself. The target heating by the laser beam is described by the equation:

$$\rho c_p \frac{\partial T}{\partial t} = \nabla \cdot (K \nabla T) + (1 - R) \alpha I_s e^{(-\alpha y)} \quad (4.2)$$

where T is the temperature,  $c_p$  is the specific heat,  $\rho$  is the density, K is the thermal conductivity, R is the target reflectivity of laser photons,  $\alpha$  is the graphite absorption,  $I_s = I_0 \exp(-\int \kappa dy)$  with  $I_0$  is maximum laser intensity,  $\kappa$  plasma absorption coefficient, and y is the axial coordinate.

There are three main mechanisms for absorption of energy from a laser beam: photoionization, electron-ion inverse Bremsstrahlung and electron-neutral inverse Bremsstrahlung. While the first one is already considered into our CRE model applied into HEIGHTS-PIC, the other two are not. This is due to the fact that for the given energies, temperatures and pressures typically present into tokamaks plasmas, the inverse Bremsstrahlung radiation contribution is extremely small and so often neglected. This is not the case when a laser pulse is applied. For this reason the inverse Bremsstrahlung radiation absorption coefficient is calculated as follows [20-21]:

$$\alpha_{IB} = 1.37 \times 10^{-35} \lambda^3 n_e^2 T_e^{-1/2} \quad (4.3)$$

where  $\lambda$  is the wavelength of the laser expressed in  $\mu\text{m}$ ,  $n_e$  is the electron density while  $T_e$  is the temperature of electrons.

#### 4.4.2 Erosion and Fluxes onto target

The calculated erosion crater formed by the impinging laser and subsequent irradiation from the vapor cloud is shown in the figure 4.65. As expected it is fully symmetrical reaching a maximum erosion value of  $0.3355 \mu\text{m}$ . This value is very close to erosion

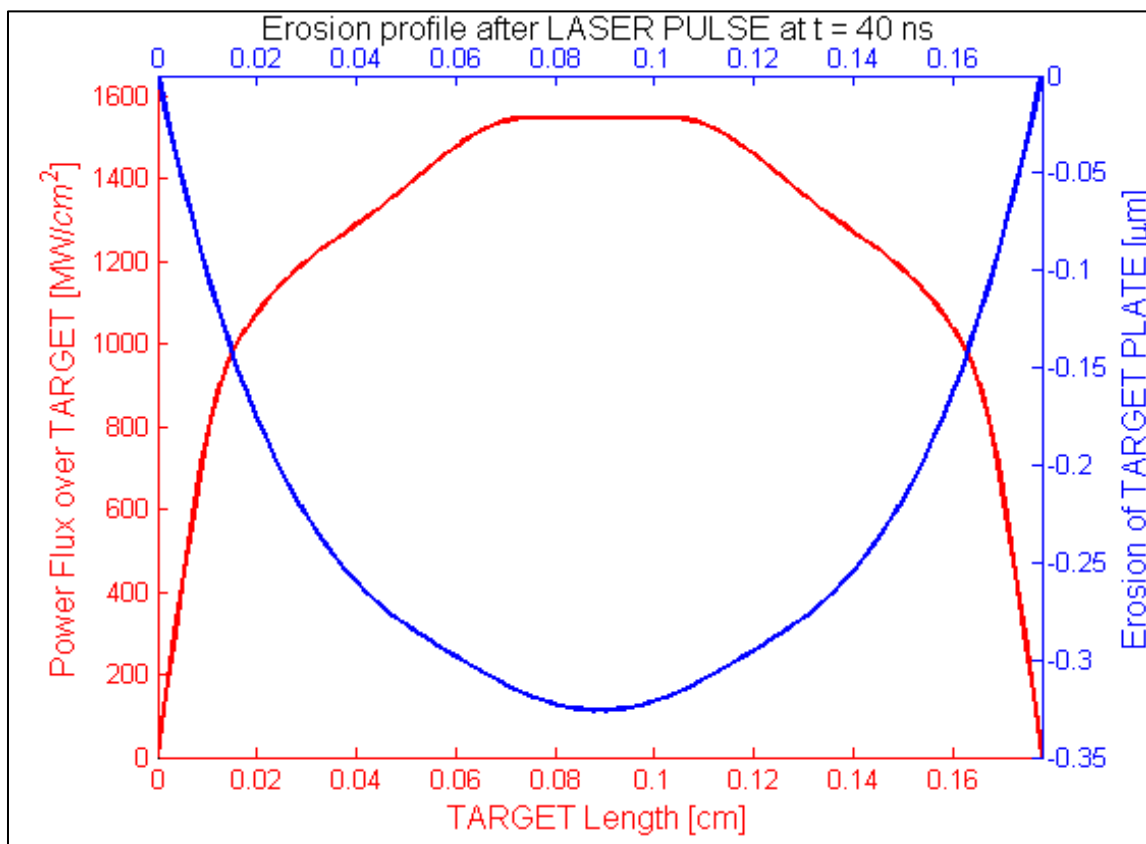


Figure 4.64 Calculated carbon erosion along the plate at 40 ns and after laser pulse

values provided in literature both theoretically and experimentally for similar conditions [24,27,32]. Those values were respectively equal to crater depth =  $0.36 \mu\text{m}$ , crater depth= $0.382 \mu\text{m}$  and crater depth =  $0.25 \mu\text{m}$ . In all these cases erosion was calculated based on the amount of ablated matter using several laser shots ranging from 500 to 3000 and then averaging the final values. The erosion calculated using HEIGHTS-PIC is also

very similar to the value of crater depth =  $0.40\ \mu\text{m}$  predicted by the well-known and well benchmarked HEIGHTS-LPP package [30] for similar conditions. Looking at the evolution of the maximum depth of the crater along time, it is evident that erosion starts only when enough energy has been stored into the target plate around 10.8 ns. Once plasma starts being produced, erosion increases almost linearly. Close to 17 ns, the rate trend bends reaching a saturation point that shows perfect screening from the laser energy still quite large at this point. Erosion has reached its maximum point and does not change till the end of the simulation.

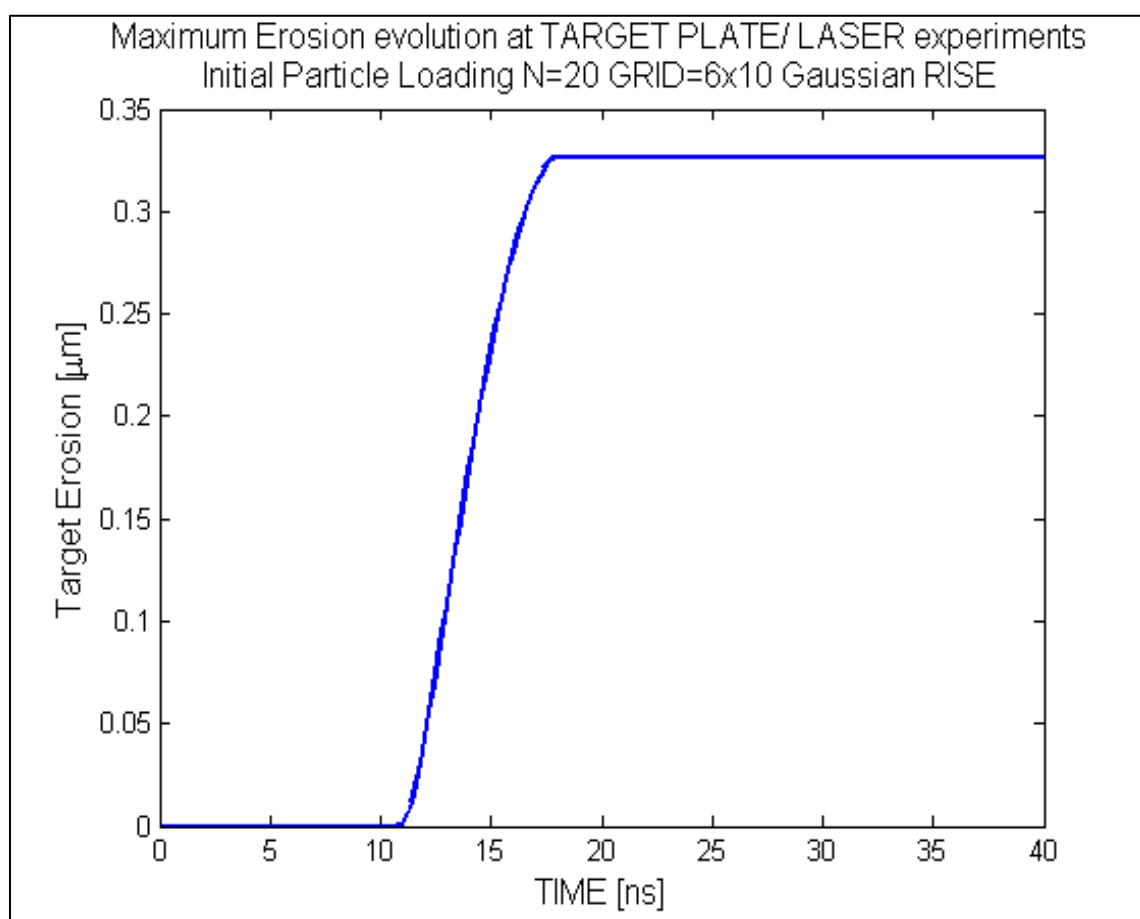


Figure 4.65 Calculated carbon erosion evolution with time during Laser pulse



The value of laser reflectivity used for these simulations is taken from [25-26] and provides the variation of carbon reflectivity as a function of the surface temperature. The relationship is expressed by:

$$R(t) = 0.21 - 2.83 \times 10^{-5} (T - 300) \quad (4.4)$$

and it is equal to  $R = 0.21$  at the beginning ( $T=300$  K) and becomes very small at higher temperatures (less than 0.05 for  $T > 6000$  K). When plasma starts being formed around 11 ns, the carbon plate has already reached a surface temperature close to 5000K (as shown in figure 4.66) so that its reflectivity according to [25] is calculated roughly equal to 0.08 and rapidly diminishing. Since there is still some uncertainty on how carbon reflectivity behaves under laser pulse conditions, other possibilities have been examined.

It has been reported [26, 31] that at ambient temperature reflectivity can be measured as equal to values ranging from 0.40 to 0.29. In tokamaks environment carbon materials due to their high porosity show lower values ( $R = 0.22$ ) and seems that reflectivity behaves almost independently from surface temperature. For this reason HEIGHTS-PIC has been run also with different values of reflectivity, which was kept constant for all simulation. Looking at figure 4.67 the differences are immediately evident and are consistent with what expected. If the reflectivity remains constant, more energy will be reflected back into the plasma screening better the target plate.

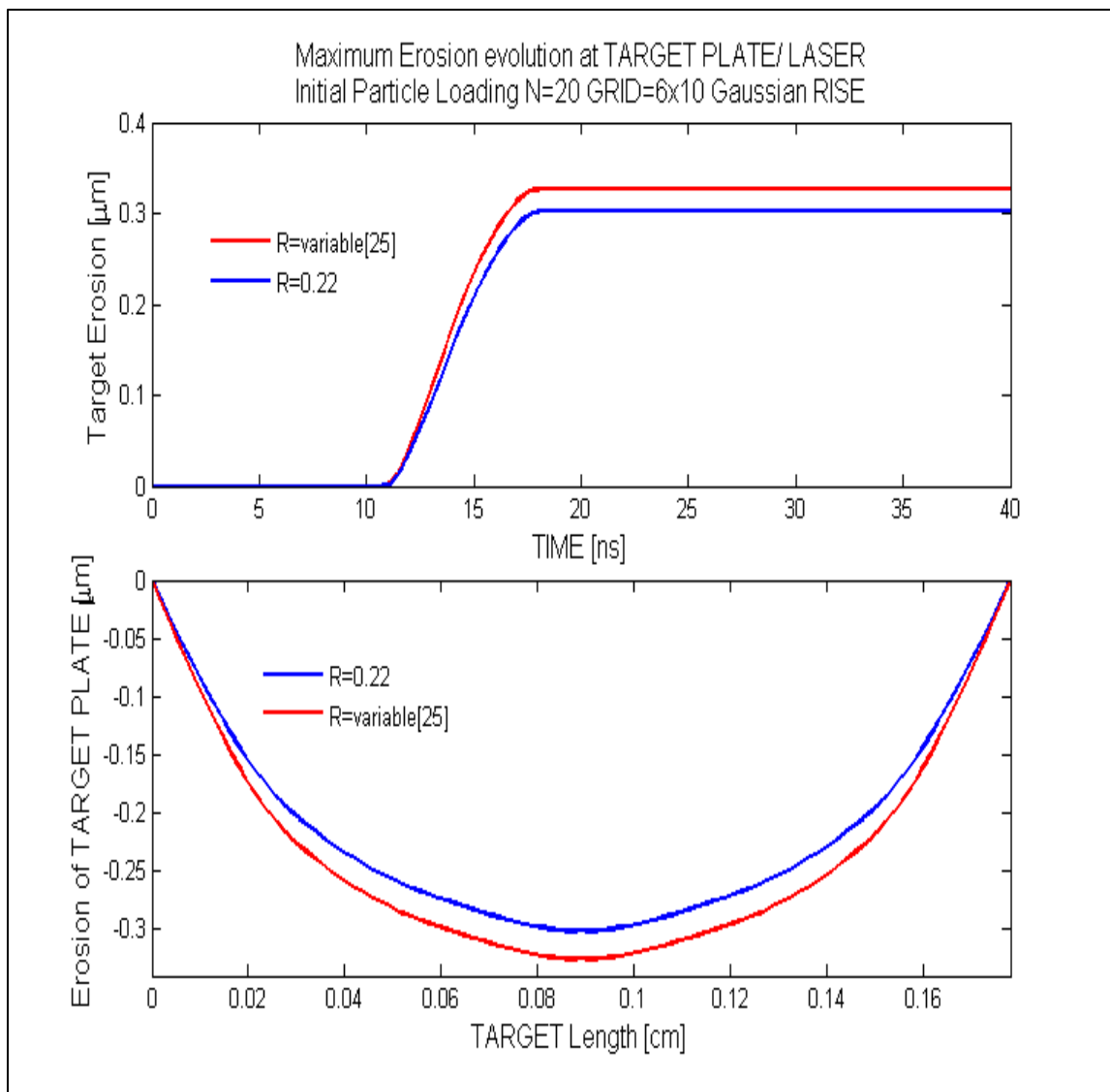


Figure 4.66 Calculated carbon erosion evolutions with time during with different reflectivity values

With constant reflectivity values ( $R = 0.40$  or  $R = 0.22$ ) particle production is reduced, while for  $R$  variable according to [25], especially at higher temperatures and close to the peak of the pulse almost none of the energy is reflected back.

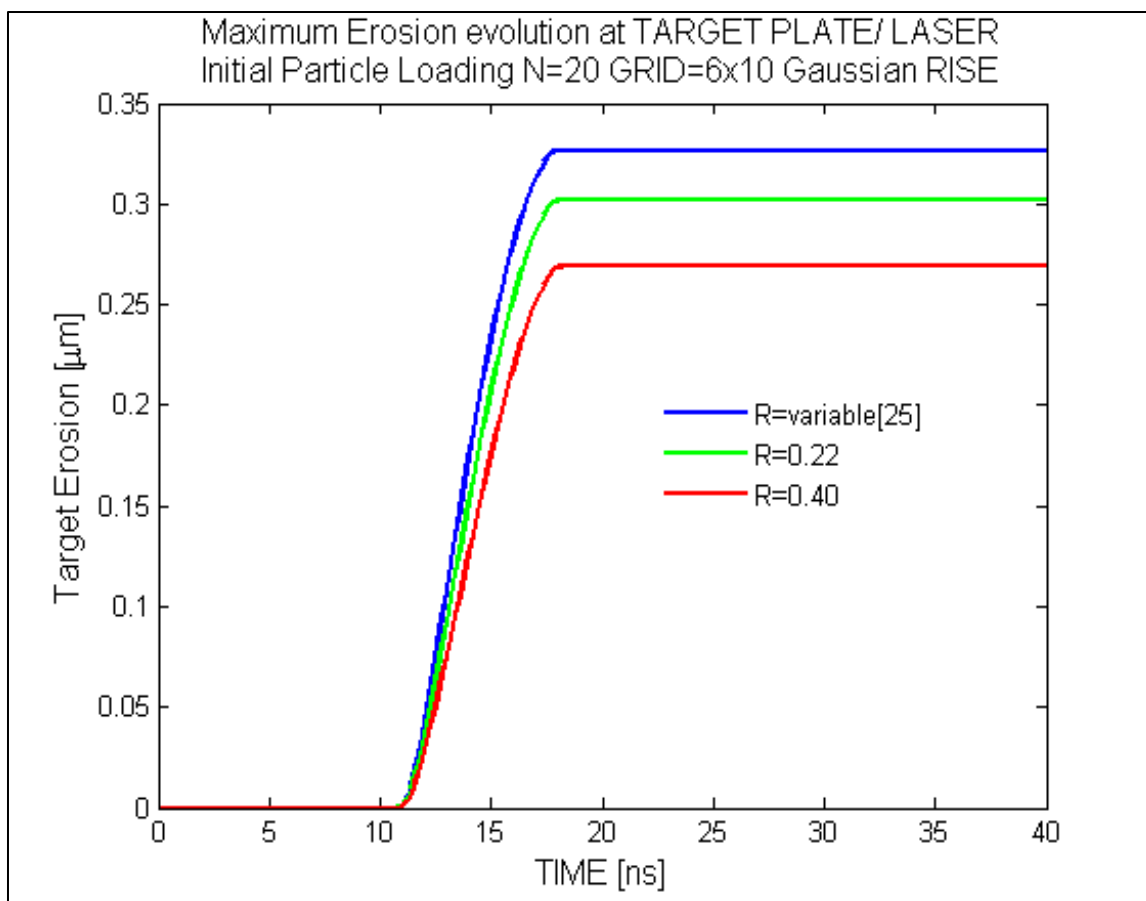


Figure 4.67 Calculated carbon erosion evolutions with different reflectivity values

( $T_{\text{solid}}$  initial = 300 K for all 3 cases)

In this case it is very important to examine the evolution of the power fluxes as shown in figure 4.69. In fact in the very first nanoseconds of the pulse and up to the time in which the temperature in the target has been raised enough to vaporize the material and eject particles from the surface (i.e., 10.8 ns), the total laser power flux goes into the target which absorbs it fully. Once carbon plasma is formed and vapor particles are produced and emitted into the system, some of the incoming laser power flux starts being absorbed

into the plasma itself through photon interaction, reducing the effective amount of power reaching the plate.

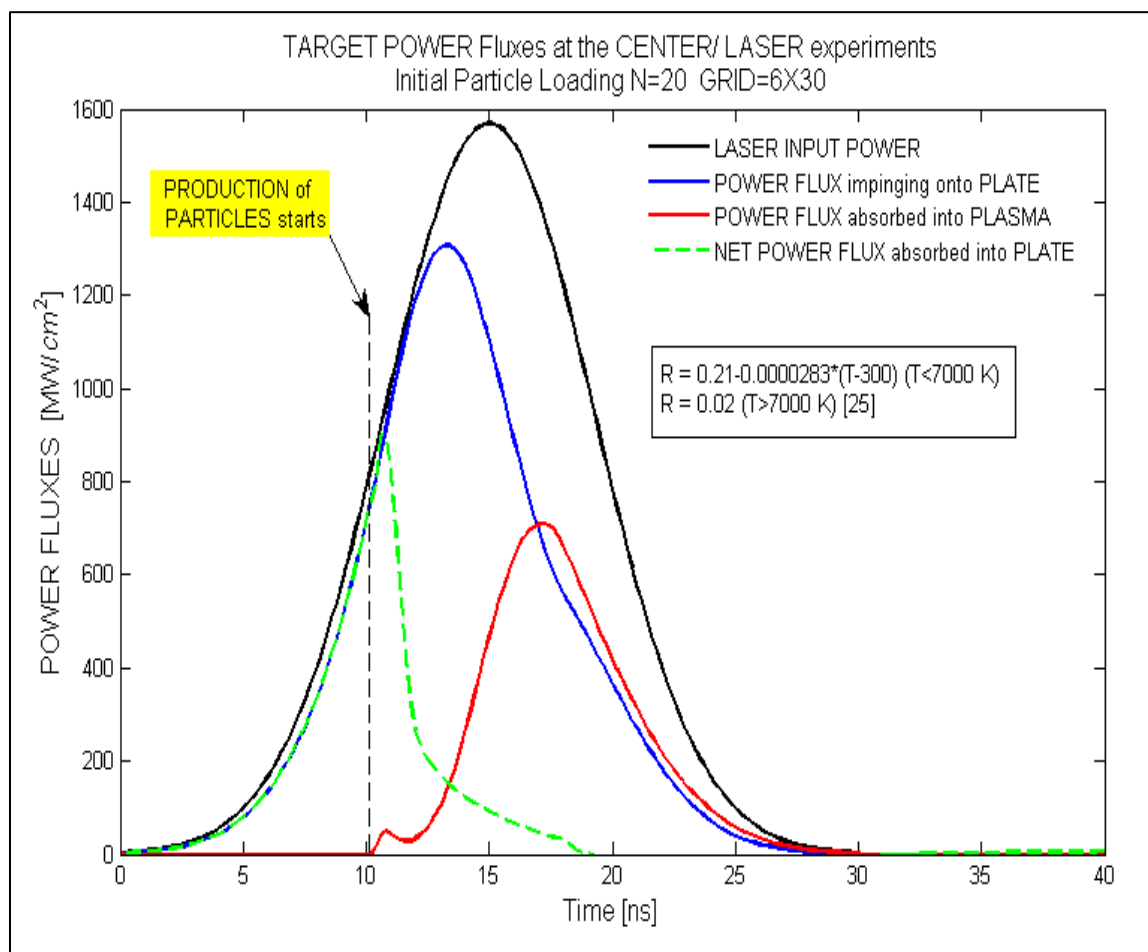


Figure 4.68 Calculated power fluxes up to 40ns [42].

As this phenomenon becomes more and more significant, more and more energy is absorbed into the plume effectively producing no further damage. The effectively laser absorbed power intensity into target drops rapidly towards zero up to a point in which the target is totally screened from it and further erosion is eventually produced by the radiation only as shown in Fig. 4.68. Integrated energy fluxes versus time are plotted in

figure 4.69. At the end of the pulse, it is noticeable that of the entire energy provided (100% blue line) only 22% (red line) has been effectively absorbed into the plate. All the rest (black line/ 78%) has been shielded, partially reradiated back (33%) and partially absorbed into the plasma itself (45 % cyan line).

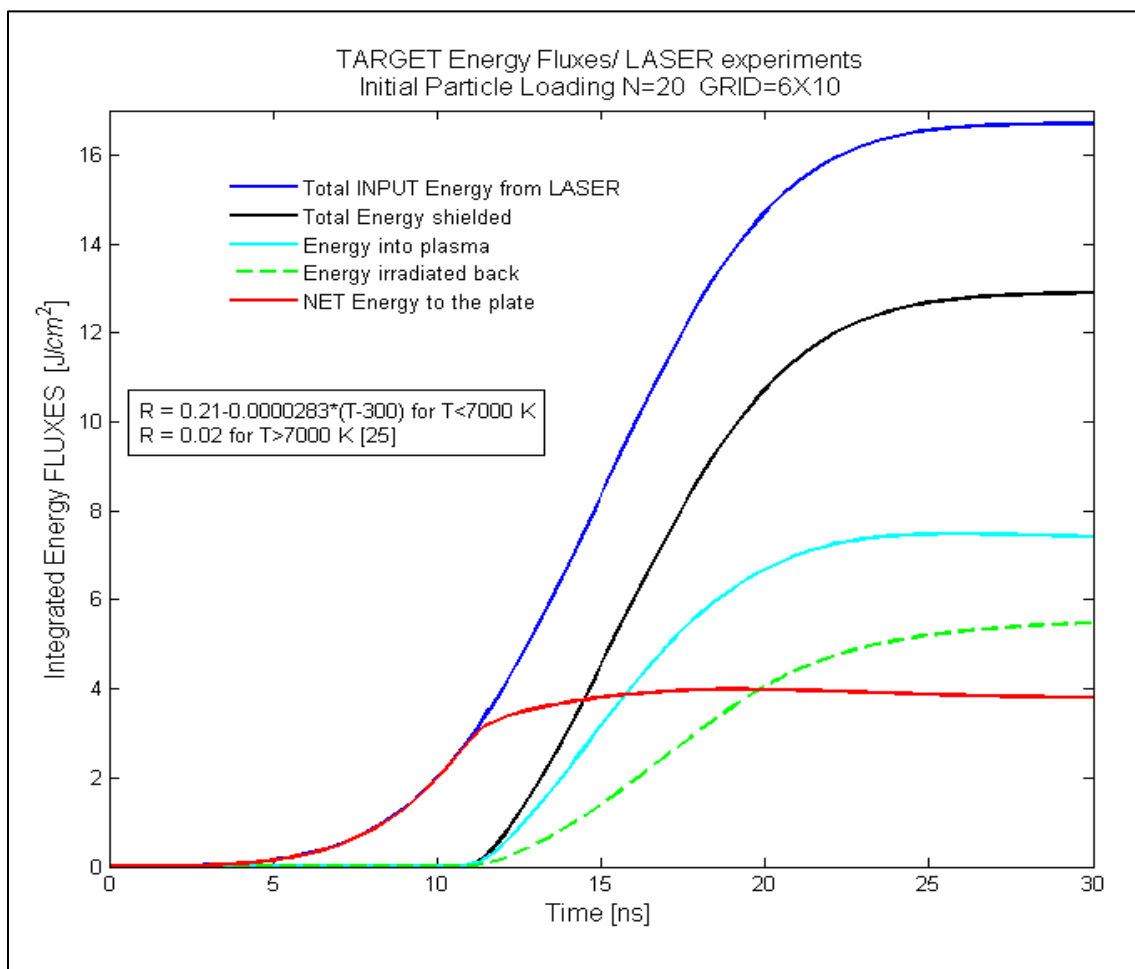


Figure 4.69 Calculated integrated energy fluxes along time [42].

This plot shown how efficient is the screening effect and how energy distribute during the carbon plume evolution. This energy distribution is also similar to other theoretical

models [23]. Radiation intensity is enhanced with respect to the no B field case due to the improvement of radial plasma confinement [39].

#### 4.4.3 Carbon Surface Temperature, Plasma density & Temperature

Temperature in the target evolving along time is plotted in figure 4.71. The temperature is calculated at different distances from the plate center and is in agreement with the

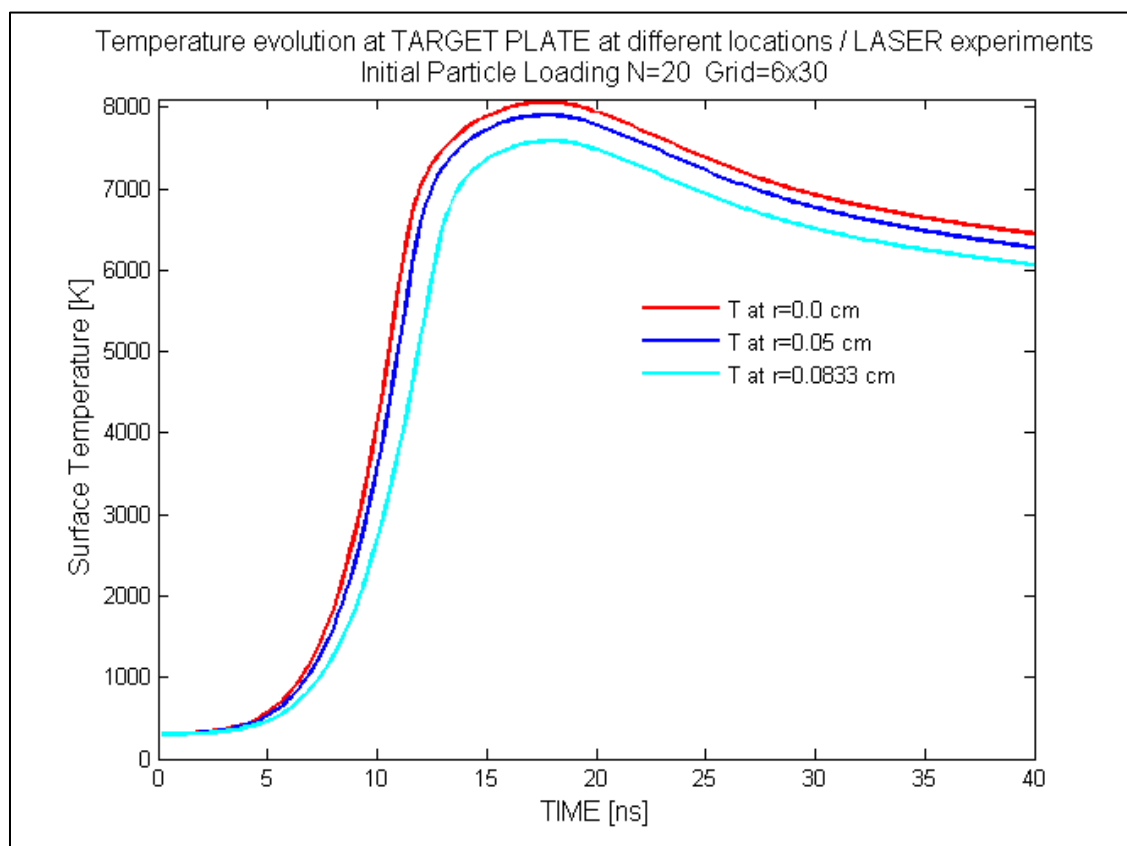


Figure 4.70 Evolution of the calculated target temperature along time at different locations [42].

Gaussian laser-beam profile. The peak of the temperature is in the middle and close to 8060 K, value very similar to the one reported in [23] for similar laser conditions. It is

important to notice that the peak of the temperature is slightly delayed in time with respect to the peak of the laser beam and this is due to the diffusion into bulk material: the rate of heat transfer into the material follows the characteristics of the material and needs some time for the energy to penetrate.

Values of the electron density and temperature of the plasma are calculated along the entire mesh and for each time step. At 40 ns the profile of temperature close to the target still has a Gaussian shape. The peak of temperature for the plasma very close to target is around 6.6 eV and drops with distance as expected [28]. The comparison with experimental data for similar conditions is quite good given the experimental error of  $\pm 15\%$  for the electron temperature.

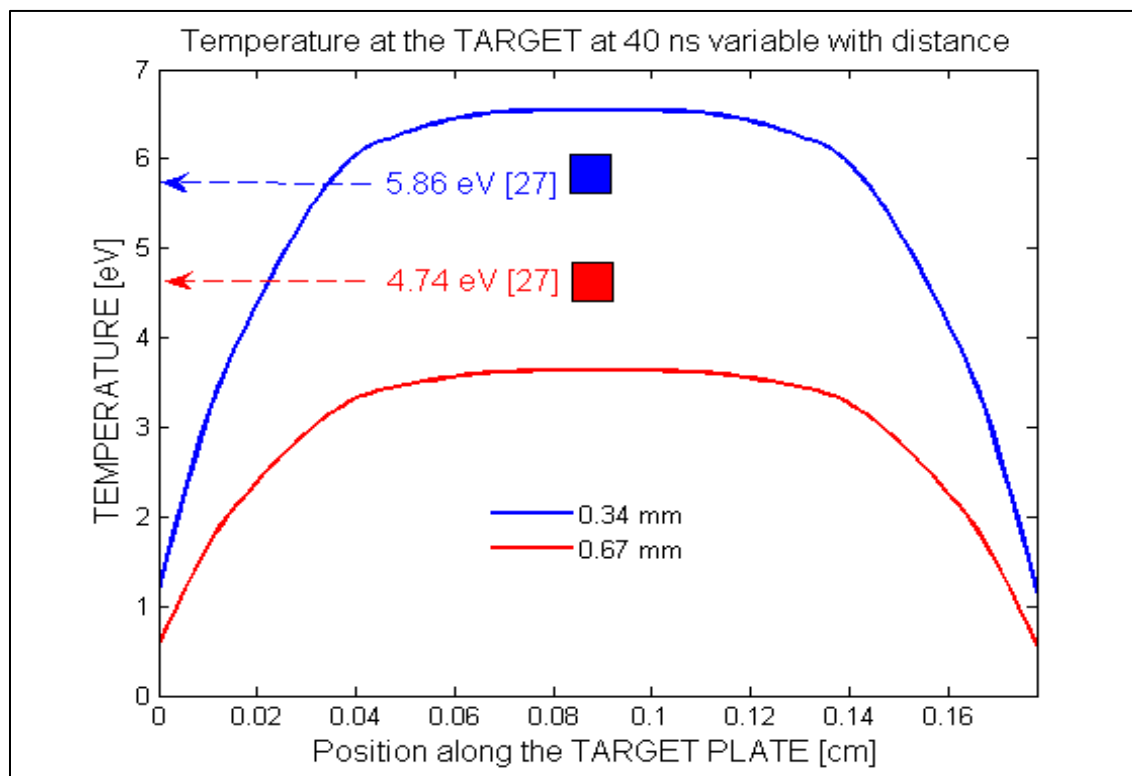


Figure 4.71 Calculated plasma temperature profiles close to the target at 40 ns and comparison with experimental data [27, 42]

Electron density has a similar profile. The experimental values provided into literature report at such close distance to target an error of the measurements around 50-60% for electron density [27] so that the comparison can be considered fair.

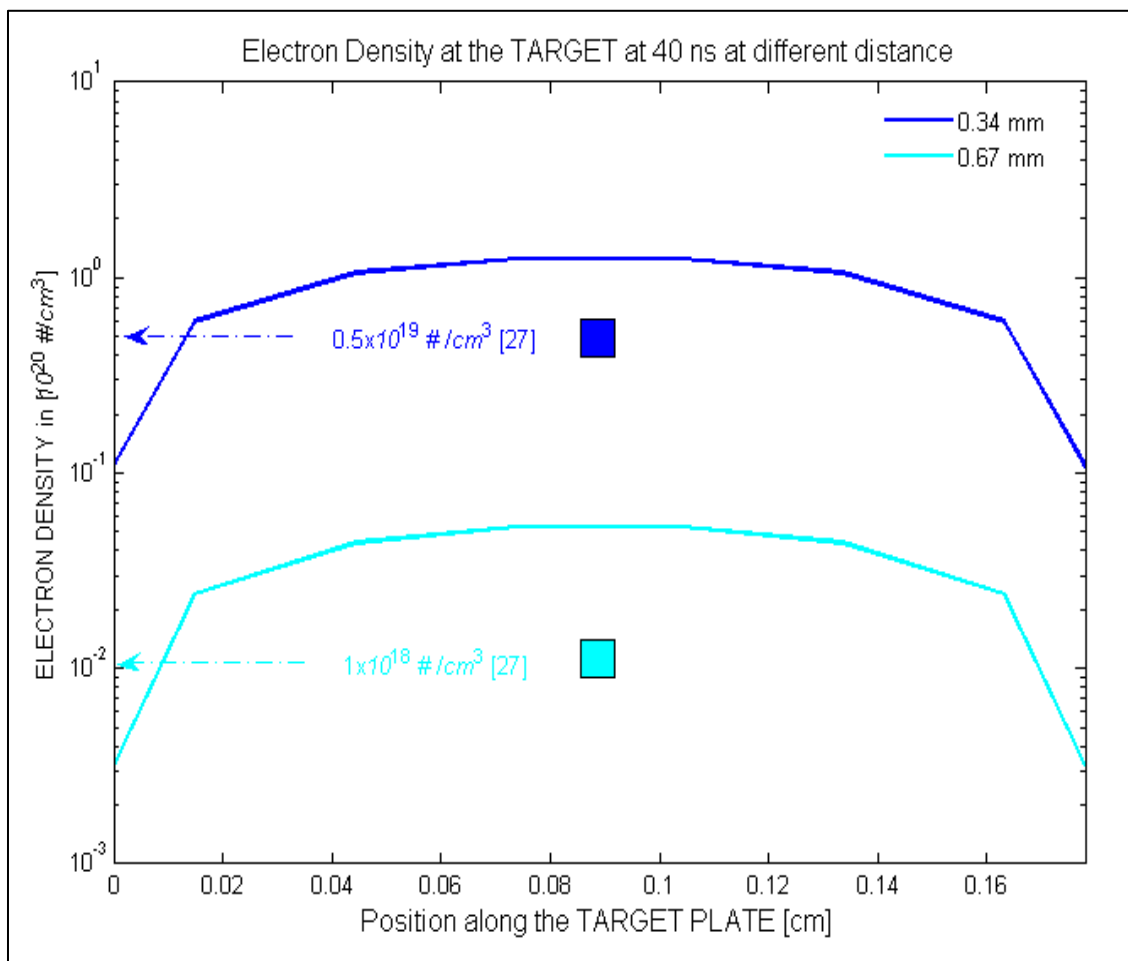


Figure 4.72 Calculated electron density profiles close to the target at 40 ns and comparison with experimental data [27, 42]

It should be pointed out, that HEIGHTS-PIC has, into the solution of the hydrodynamics equations, the implementation of the contribution of the magnetic force. As observed already [22,29] the presence of the  $\vec{J} \times \vec{B}$  magnetic force changes the



behavior of the plasma plume with respect to the one expanding for example into vacuum having a strong influence on the ionization characteristics as well as on the velocity of the plume itself. This translates for axial magnetic field as for HEIGHTS-PIC in a stronger confinement close to target. In the experiments examined and compared numerically with HEIGHTS-PIC, no magnetic field was considered or used.

## References

1. N.I. ARKHIPOV, et al., Fusion Technology 1994, Vol. 1, p. 423, 1995.
2. N.I. ARKHIPOV et al., "Study of structure and dynamics of shielding layer for inclined incidence of plasma stream at MK-200 facility", J. Nuclear Materials, 233- 237, p. 767-770, 1996.
3. N.I. ARKHIPOV et al., Fusion Technol. in: C. Varandas, F. Serra (Eds.), p. 507, 1996
4. V.G. BELAN, "Features of dynamics and structure of the shielding layer at the interaction of plasma flow with target", Journal of nuclear materials, 233-237,763-766, 1996.
5. H. WURZ et al., "Hot Plasma Target Interaction and Quantification of Erosion of the ITER Slot Divertor during Disruptions and ELM", 1999, FZKA 6198 , Karlsruhe , Germany, 1999.
6. H. WURZ et al., "Damage and Evaluation of Vertical targets and first walls during ITER-FEAT off-normal events", FZKA 6582, Karlsruhe, Germany, 2001.
7. N.I. ARKHIPOV et al., "Erosion mechanism and erosion products in carbon based materials" , J. Nuclear Materials, 307- 311, p. 1364-1368, 2002.
8. V. SAFRONOV et al., "Macroscopic erosion of divertor materials under plasma heat loads typical for ITER hard disruptions", Problems of Atomic Science and Technology,N.5, Series: Plasma Physics 8,27-29 , 2002
9. V. SIZYUK, A. HASSANEIN, "Damage to nearby divertor components of ITER-like devices during giant ELMs and disruptions", J. of Nuclear Fusion, 50,11500, 2010.

10. R. AYMAR, "ITER R&D: Executive summary: Design overview." *Fusion Engineering and Design* 55(2-3): 107-118, 2001.
11. A. HASSANEIN, "Modeling and key issues of plasma/surface interactions in future Tokamaks", *Fusion Engineering and Design* 69, 781-787. 60, PII S0920-3796(02)00006, 2002
12. V. SAFRONOV, et al., "Evaporation and vapor shielding of CFC targets exposed to plasma heat fluxes relevant to ITER ELMs", *Journal of Nuclear Materials*, 386-388,744-746 , 2009.
13. S. PESTCHANYI et al., "Radiation losses from ITER SOL due to divertor material plasma" ,31<sup>st</sup> EPS Conference on Plasma Physics, London ECA , vol. 28 , 1.135, 2004.
14. N.I. ARKHIPOV et al., "Formation of shielding layer near a solid target under the action of high-power plasma flow", *Plasma Physics Report*, vol. 25 , N.3,236-245 , 1999.
15. N.I. ARKHIPOV et al., "Energy balance in the interaction of intense High-Temperature Plasma Flows with solid Targets", *Plasma Physics Report*,.vol. 28 , N.3,432-443 , 2002.
16. L.E. GARKUSHA et al., "The latest Results from ELM-simulation experiments in plasma accelerators", *Physica Scripta*, T138, 014054, 2009.
17. F. GENCO, A. HASSANEIN, "Modeling of Damage and Lifetime Analysis of Plasma Facing Components During Plasma Instabilities in Tokamaks", *Fusion Science & Technology* 60, 339-343, 2011.
18. S.S. HARILAL et al., " The effect of excitation wavelength on dynamics of laser-produced-plasmas, *Journal of Applied Phys* 109:063306,2011.

19. A.E. HUSSEIN, P.K. DIWAKAR , SS. HARILAL and A. HASSANEIN "The role of laser wavelength on plasma generation and expansion of ablation plumes in air" , Journal of Applied Physics , 113 ,143305, 2013
20. J.J. CHANG , B.E. WARNER, "Laser Plasma Interaction during visible laser ablation of methods" , Applied Phys. Lett. , 69, 473, 1996
21. Y. ZEL'DOVICH and Y. RAIZER, " Physics of Shock Waves and High Temperature Hydrodynamics Phenomena" , Academic, New York , 1966
22. K. PATHAK, A. CHANDY, " Laser Ablated carbon plume flow dynamics under magnetic field, Journal of Applied Physics 105, 084909, 2009
23. N.M. BULGAKOVA, A.V. BULGAKOV, L.P., BABICH, "Energy balance of pulsed laser ablation: thermal model revised", Appl Phys A:Mater Sci Process 79: 1323-1326, 2004
24. A.V. BULGAKOV, N.M. BULGAKOVA, " Thermal model of pulsed laser ablation under the conditions of formation and heating of a radiation-absorbing plasma", Quantum Electronics ,29: 433-437, 1999.
25. N.M. BULGAKOVA, A.V. BULGAKOV, " Pulsed laser ablation of solids: transition from normal vaporization to phase explosion", Appl Phys A:Mater Sci Process 73: 199-2082004, 2001
26. A.M. MALVEZZI, N. BLOEMBERGEN, " Time resolved picosecond optical measurements of laser-excited Graphite", Physical Review Letters 57:146-149, 1986
27. J. HOFFMAN, T. MOSCICKI T., Z. SZYMANSKI, "The effect of laser wavelength on heating of ablated carbon plume", Appl. Phys. A: Mater. Sci. Process 104:815-819, 2011

28. S.S. HARILAL.,” Electron Density & Temperature Measurements in a Laser Produced Carbon Plasma, Journal of Applied Physics 82:2140-2146, 1997
29. A. NEOGI, R.K., THAREJA, “Laser Ablated carbon plume flow dynamics under magnetic field”, Appl Phys B ,72, 231-235, 2001
30. V. SIZYUK, A. HASSANEIN, T. SIZYUK," Three-dimensional simulation of laser-produced plasma for extreme ultraviolet lithography applications”, Journal of Applied Physics ,100, 103106, 2006
31. A. SEMEROK, S.V. FOMICHEV, J-M. WEULERSSE, F. BRYGO, P.Y. THRO and C. GRISOLIA, “Heating and ablation of Tokamak graphite by pulsed nanoseconds ND:YAG lasers”, Journal of Applied Phys., 101, 084916, 2007
32. J. HOFFMAN, T. MOSCICKI T., Z. SZYMANSKI, “The effect of laser wavelength on laser-induced carbon plasma”, Journal of Applied Physics 114:083306, 2013
33. A. HASSANEIN, G.L. KULCINSKI and W.G. WOLFER, “Vaporization and Melting of Materials in Fusion Devices”, 2nd Top. Mtg. Fusion Reactor Materials, Seattle, WA, August 9 1981, J. Nucl. Mater., 103 & 104, 311, 1981
34. A. HASSANEIN, G.L. KULCINSKI and W.G. WOLFER, “Dynamics of Melting, Evaporation, and Resolidification of Materials Exposed to Plasma Disruptions”, J. Nucl. Mater. 111 & 112, 554, 1982
35. A. HASSANEIN and I. KONKASHBAEV, "Comprehensive modeling of ELMs and their effect on plasma-facing surfaces during normal tokamak operation." Journal of Nuclear Mat. 313: 664-669, 2003

36. A. HASSANEIN and I. KONKASHBAEV, "Physics of collisionless scrape-off-layer plasma during normal and off-normal Tokamak operating conditions," Report No. ANL/FPP/TM-296, 1999
37. A. HASSANEIN, V. SIZYUK V. and T. SIZYUK, "Extreme Conditions for Plasma-Facing Components in Tokamak Fusion Devices", IEEE Trans. Plasma Science 39 2880 , 2011
38. V. SAFRONOV et al., "Material erosion and erosion products under plasma heat loads typical for ITER hard disruptions", Journal of Nuclear Materials, 290-293, 1052-1058, 2001
39. V.N. LITUNOVSKY et al., "Experimental study of radiation power flux on the target surface during high heat plasma irradiation ", Journal of Nuclear Materials, 290-293, 1112-1116, 2001
40. F. GENCO and A. HASSANEIN, "Particle-in-Cell (PIC) Methods in predicting materials behavior during high power deposition". Submitted to Laser and Particle Beams, Cambridge University Press, Accepted for Publications, November 2013
41. F. GENCO and A. HASSANEIN, "Particle-in-Cell (PIC) Simulations of damage to Tokamaks Plasma Facing Components during Intense Power Deposition". Submitted to Fusion Engineering and Design, IOP Science, Under Review, 2013
42. F. GENCO and A. HASSANEIN, "Numerical Simulations of Laser Ablated Plumes Using Particle-in-Cell (PIC) Methods". Submitted to Laser and Particle Beams, Cambridge University Press, Under Review, 2013

## CHAPTER 5. DISCUSSION OF RESULTS & LIMITS OF THE MODEL

### 5.1 Numerical Stability

HEIGHTS-PIC numerical stability is very important and needs to be discussed. At each time step, before the solution is advanced, the Courant Condition is verified in order to have a reference  $\delta t$  of time. It is worth recalling that in mathematics, the Courant–Friedrichs–Lewy condition (abbreviated as CFL condition or simply Courant condition) is a necessary condition for convergence while solving certain partial differential equations (for example hyperbolic PDE) with a numerical approach using finite differences to approximate the physical quantities. [1]. Typically once the time step has been defined and the length scale also, their ratio has to be smaller than a pre-established value in order for the systems of equations to be solved without producing incorrect results. HEIGHTS-PIC evaluates the Courant condition, but the numerical  $\delta t$  used for advancing the calculations is taken much smaller. In fact the Courant condition is a necessary one but not sufficient to get stable solutions. Several simulations have been run using HEIGHTS-PIC with several  $dt$  (orders of magnitude different) in order to compare the results and establish which configuration provided the most numerically stable ones. The typical values considered were ranging from  $\delta t = 10^{-4} \mu s$  (just below the smallest Courant value calculated which was around  $10^{-3} \mu s$ ) to  $\delta t=10^{-8} \mu s$ . Results here presented are from  $\delta t =10^{-5} \mu s$  and  $\delta t =10^{-6} \mu s$ . The latter values is the one used for most of the

simulations since it is the one that ensures stability of the solution differing from  $\delta t = 10^{-7}$   $\mu\text{s}$  and  $\delta t = 10^{-8}$   $\mu\text{s}$  for a value of less than 3%. It will be important also to evaluate the computational time used but the machine once difference  $\delta t$  are applied.

In the following figures (5.1 and 5.2), it is possible to see the final calculated erosion geometrical evolution over the target plate as well as the temporal profile. The case here presented is the STEP RISE or quadratic beam for the MK200 geometry with an initial loading of  $N = 155$  as the previous case presented in chapter 4.

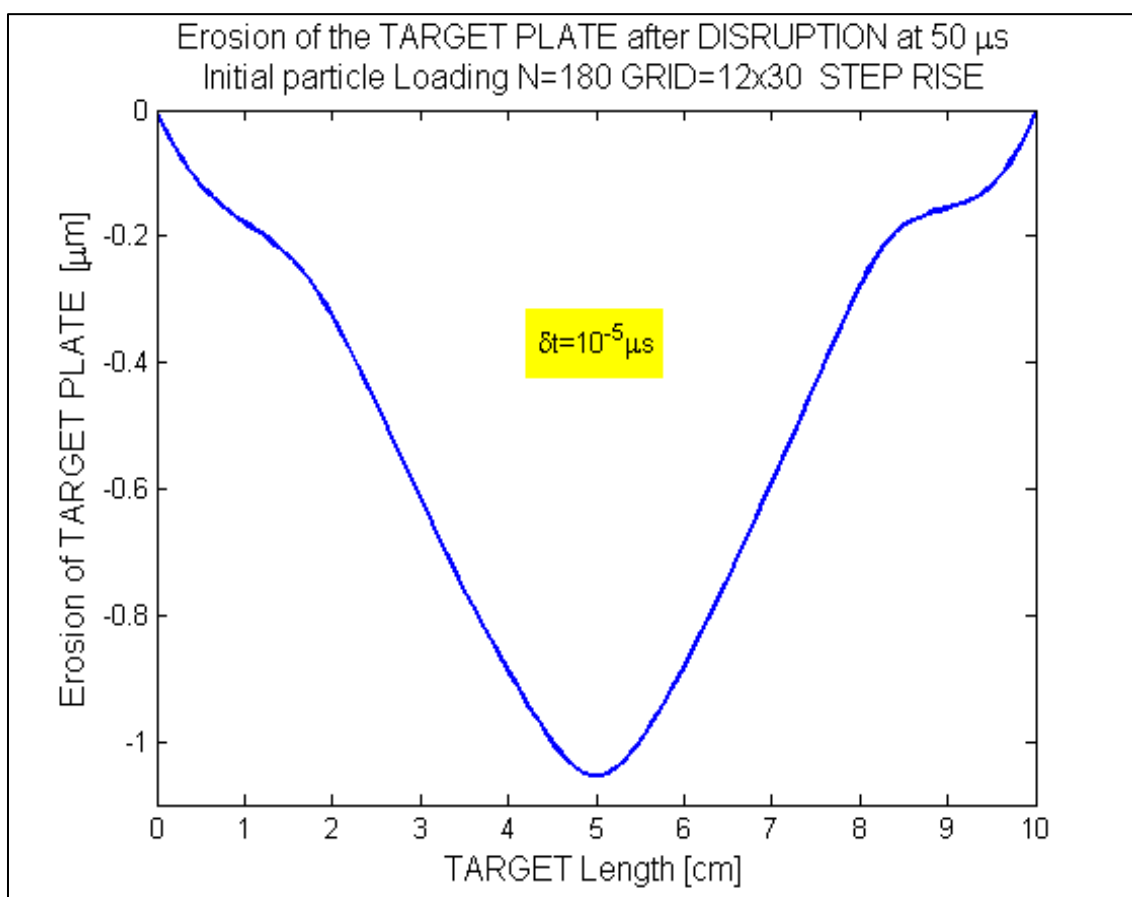


Figure 5.1 Calculated carbon erosion crater at 50  $\mu\text{s}$  in MK200-like conditions simulation using HEIGHTS-PIC



Two main considerations can be done. First of all the final shape of the erosion crater appears to be more triangular than before not really recalling the Gaussian shape of the beam itself. Second, the final value is about  $1.012 \mu\text{m}$  which, is roughly 10 times larger than the one previously calculated. Looking at the temporal evolution of the erosion,

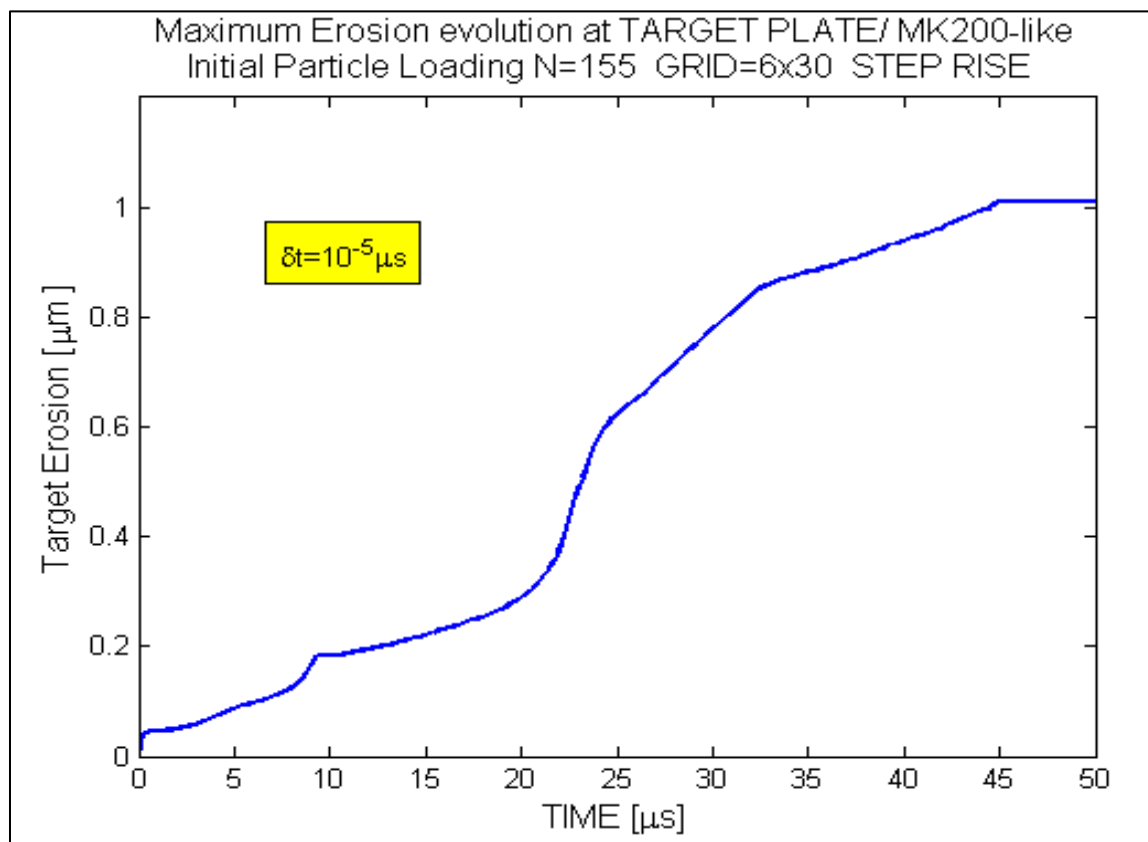


Figure 5.2 Calculated carbon erosion evolution of plate center in a MK200-like conditions simulation using HEIGHTS-PIC (step rise)

it is evident that numerical instabilities prevent the system to have a smooth growth, despite the relatively high number of particles initially loaded into the system. This plot reveals clearly how important is the use of appropriate  $\delta t$  for advancing the entire

calculation. In the next figure (5.3), the comparison between the two different simulations ( $\delta t=10^{-5}$   $\mu\text{s}$  vs.  $\delta t=10^{-6}$   $\mu\text{s}$ ) clearly points out the big difference already noticed.

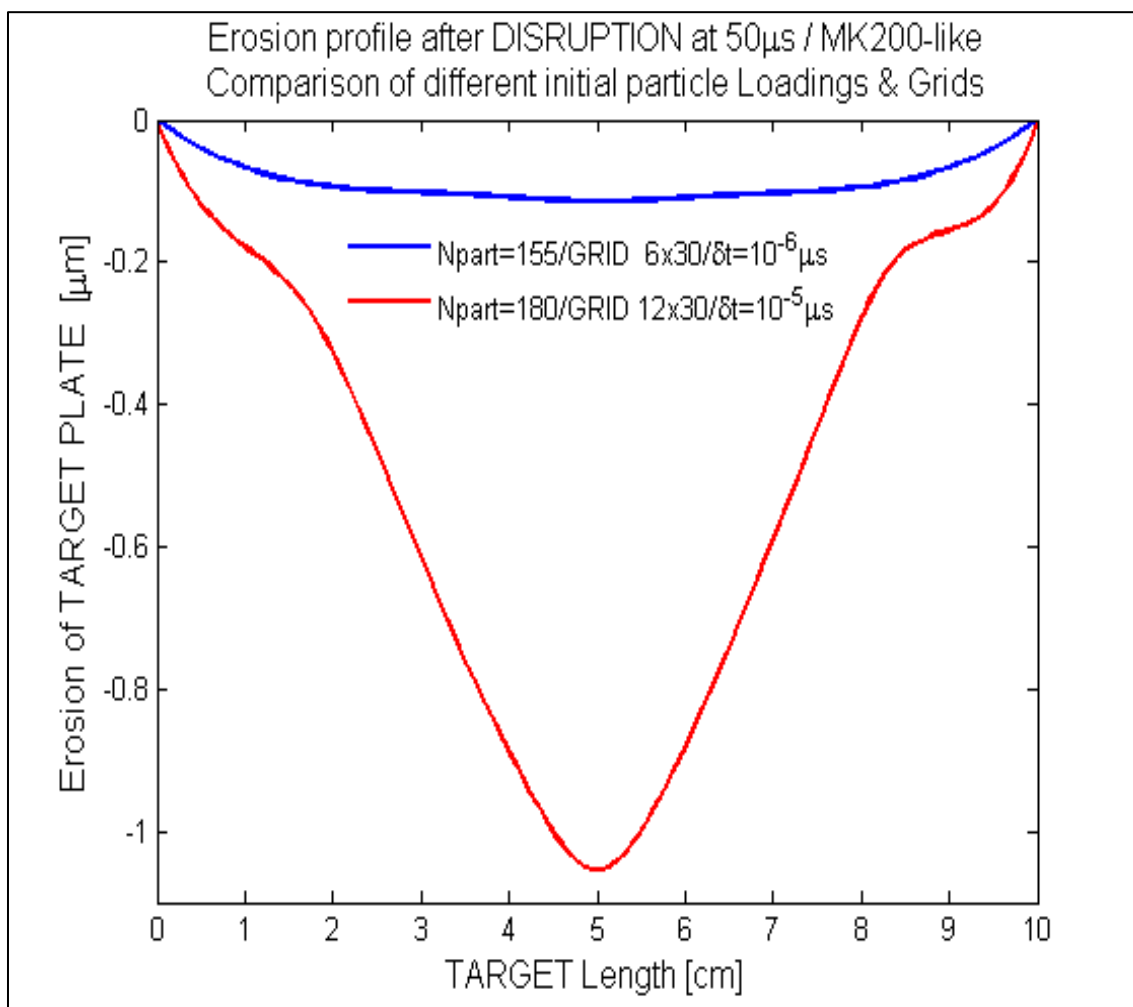


Figure 5.3 Calculated carbon erosion evolution of plate center in MK200-like conditions simulation using HEIGHTS-PIC (step rise) with different  $\delta t$

The very different behavior for the calculation of the erosion between the two different timings used can be well explained looking at the stability of the calculation for the pressure of the immediately close to target cells. As explained before, especially in the

expansion phase, any inaccuracy into the calculation of the pressure, changes drastically the erosion rate of the carbon plate. Looking at figure 5.4 this unstable trend is evident.

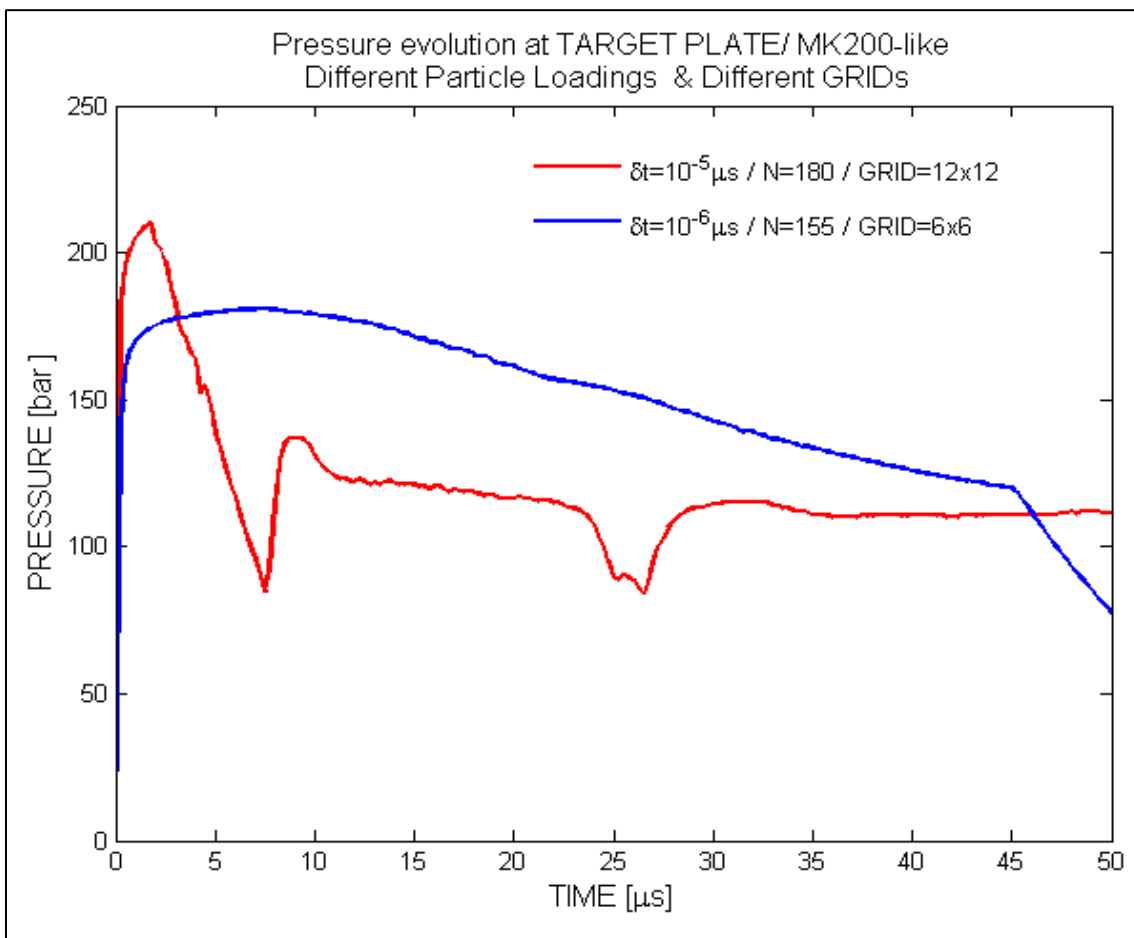


Figure 5.4 Calculated pressure evolution of plate center in MK200-like conditions simulation using HEIGHTS-PIC (step rise) with different  $\delta t$

As we can notice, even though in the maximum value differences are relatively small, it is in the evolution that no physical justification can be found to explain the two sudden drops present in the profile. Also, the profile (red line  $\delta t = 10^{-5} \mu s$ ) seems not to catch the exponential drop into the laser beam. Looking at the geometrical evolution of pressure

along the plate, the instability in the calculated values is again very evident at all times considered (figure 5.5 and 5.6):

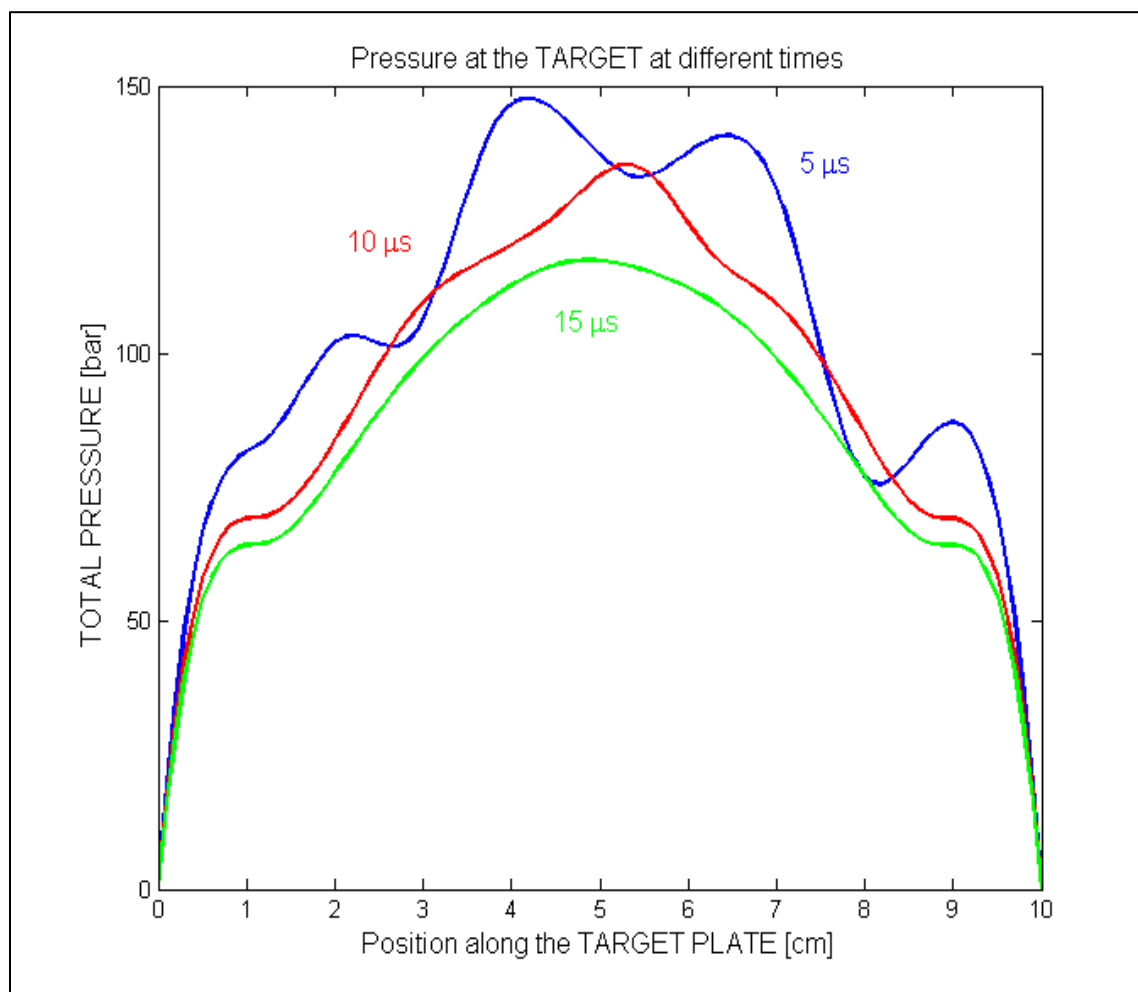


Figure 5.5 Calculated pressure evolution of plate center in MK200-like conditions simulation using HEIGHTS-PIC (step rise) with  $\delta t = 10^{-5} \mu s$  (5-15  $\mu s$ )

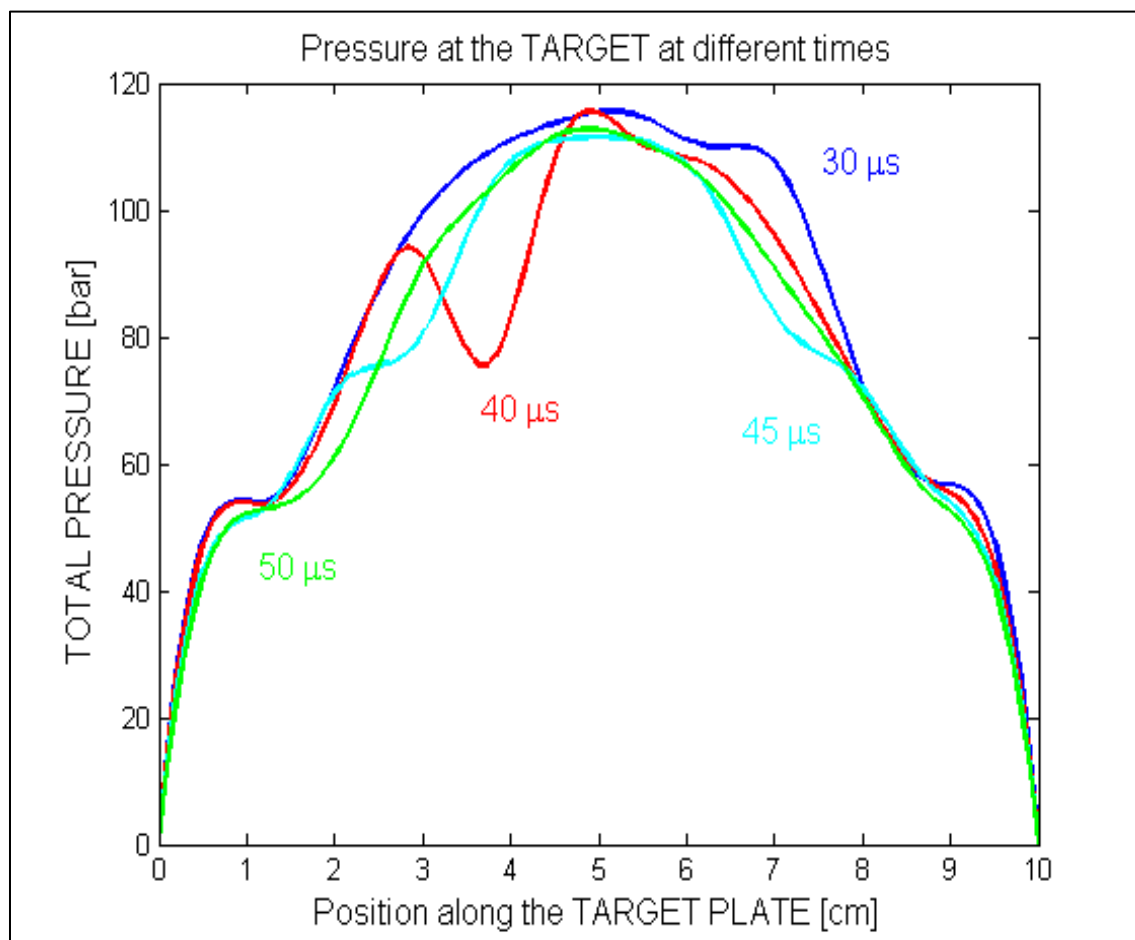


Figure 5.6 Calculated pressure evolution of plate center in MK200-like conditions simulation using HEIGHTS-PIC (step rise) with  $\delta t = 10^{-5} \mu s$  (30-50  $\mu s$ )

A similar behavior emerges also from other simulations run for the MK200 case with both the linear rise of 5  $\mu s$  and 10  $\mu s$ . No differences instead exist in both the trend and stability of simulation which, were run with  $\delta t = 10^{-7} \mu s$  leading to almost identical results in both pressure and final erosion.

## 5.2 Accuracy of the calculation with increasing N

Once the stability of the solution has been determined being produced with  $\delta t = 10^{-6} \mu\text{s}$  or less, several simulation have been run in order to evaluate the accuracy of the solutions with different values of the initial particle loadings. In fact, changing the ratio of the mass representing per each cell the carbon plasma particles, different but similar simulations can be run. Obviously increasing the “representativeness” of the plasma particles, the results become more and more accurate despite a considerable increase of computational time. Each numerical loop and calculations becomes longer with respect to computational time, but provides a better mapping of the values calculated.

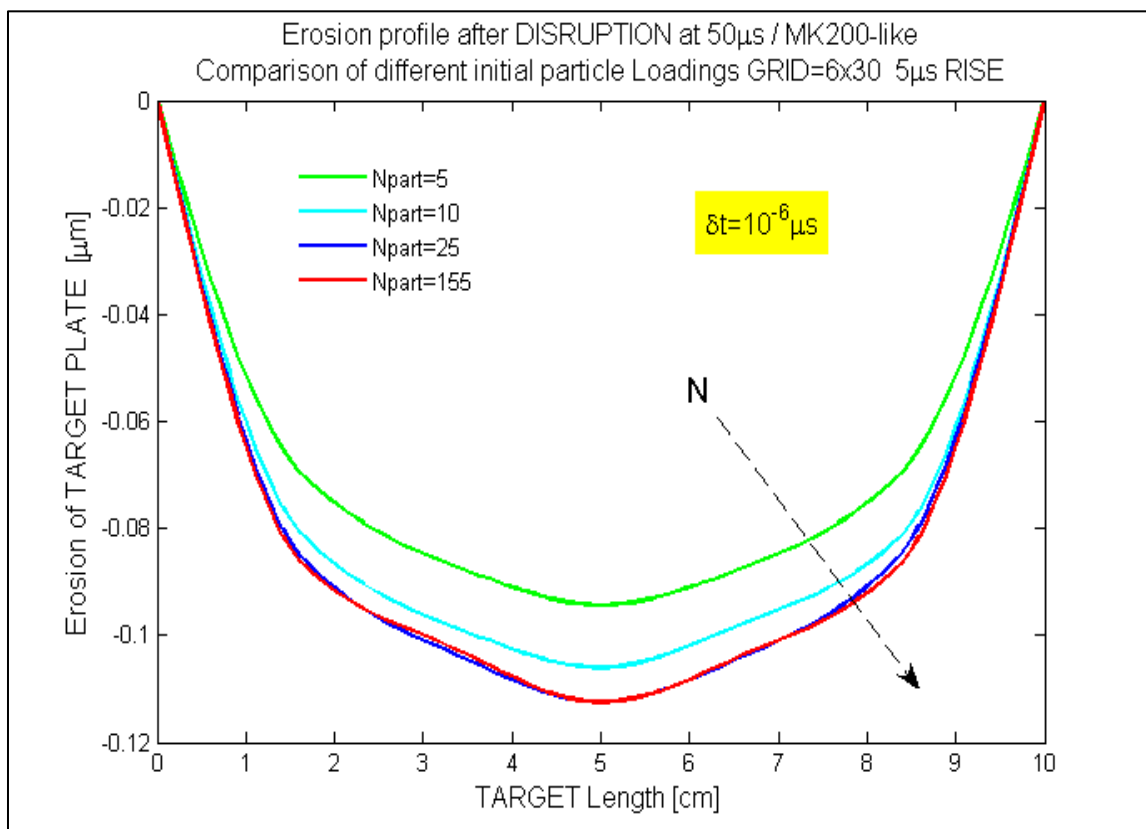


Figure 5.7 Calculated carbon erosion along the plate in MK200-like conditions simulation using HEIGHTS-PIC (5 $\mu$  rise) with different N [22]

The Erosion geometrical evolution along the plate is shown in figure 5.7 with different initial particle loadings. As  $N$  increases, the erosion value becomes more and more accurate as expected. Already for a low number of super particles ( $N = 25$ ), the value appears to be almost as the final one without major differences. For  $N = 155$ , the profile almost does not change. It is also important in this case to evaluate for the stability and accuracy of the solution, the profiles calculated at the center of the plate for the pressures involved (figure 5.8).

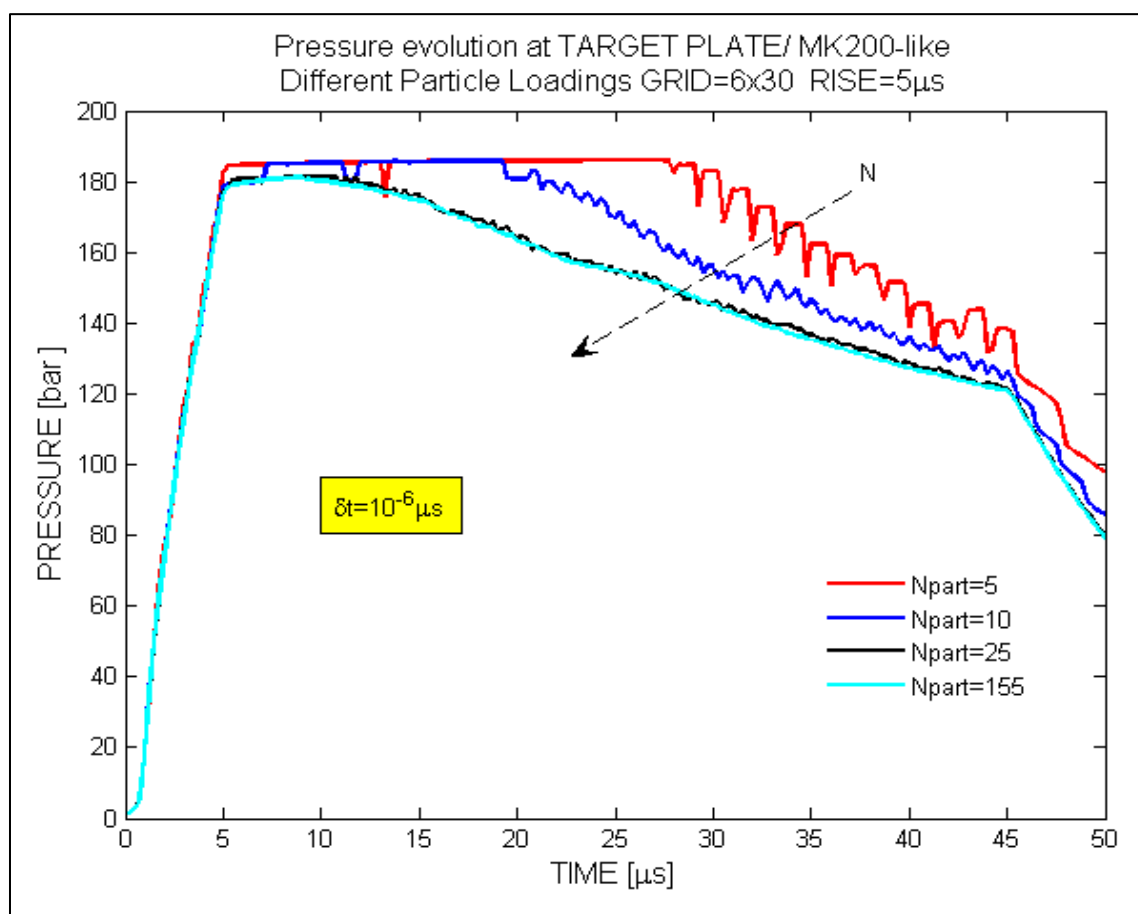


Figure 5.8 Calculated pressure evolution of plate center in MK200-like conditions simulations using HEIGHTS-PIC ( $5\mu$  rise) with different  $N$  [22]

The profiles for  $N = 25$  and  $N = 155$  look very smooth and almost the same. Instead for both  $N = 5$  and  $N = 10$ , they appear to be different and a bit unstable making the final calculation of erosion not that accurate.

It also interesting to examine another case (step rise) for the same problem (figure 5.9)

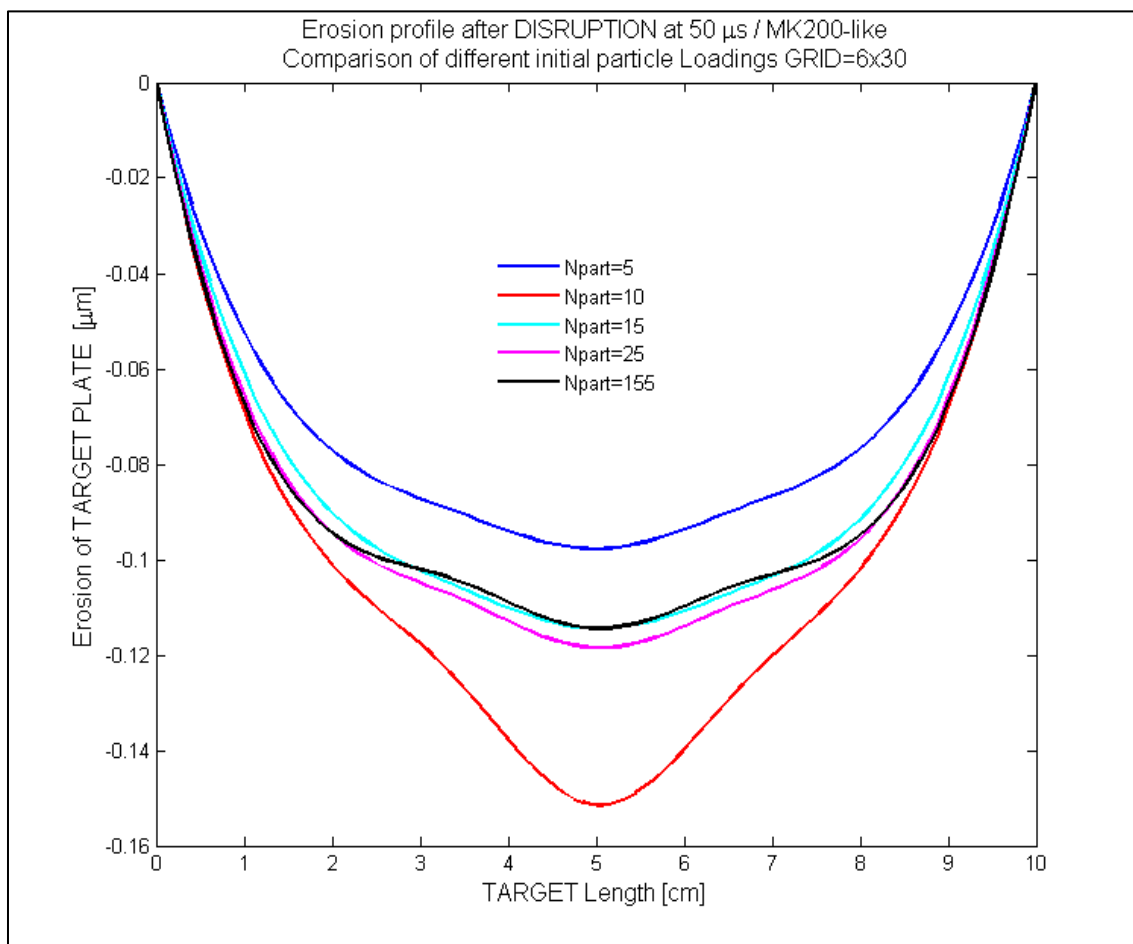


Figure 5.9 Calculated carbon erosion along the plate in MK200-like conditions simulations using HEIGHTS-PIC (step rise) with different  $N$

In this plot, the value provided by the calculation with  $N=10$  it clearly in contrast with the others and shows an overestimation of the final erosion. This trend can be justified



(showing the sensitivity of the calculation to the pressure) looking at the relative plot for the evolution of the pressure in front of the plate (figure 5.10):

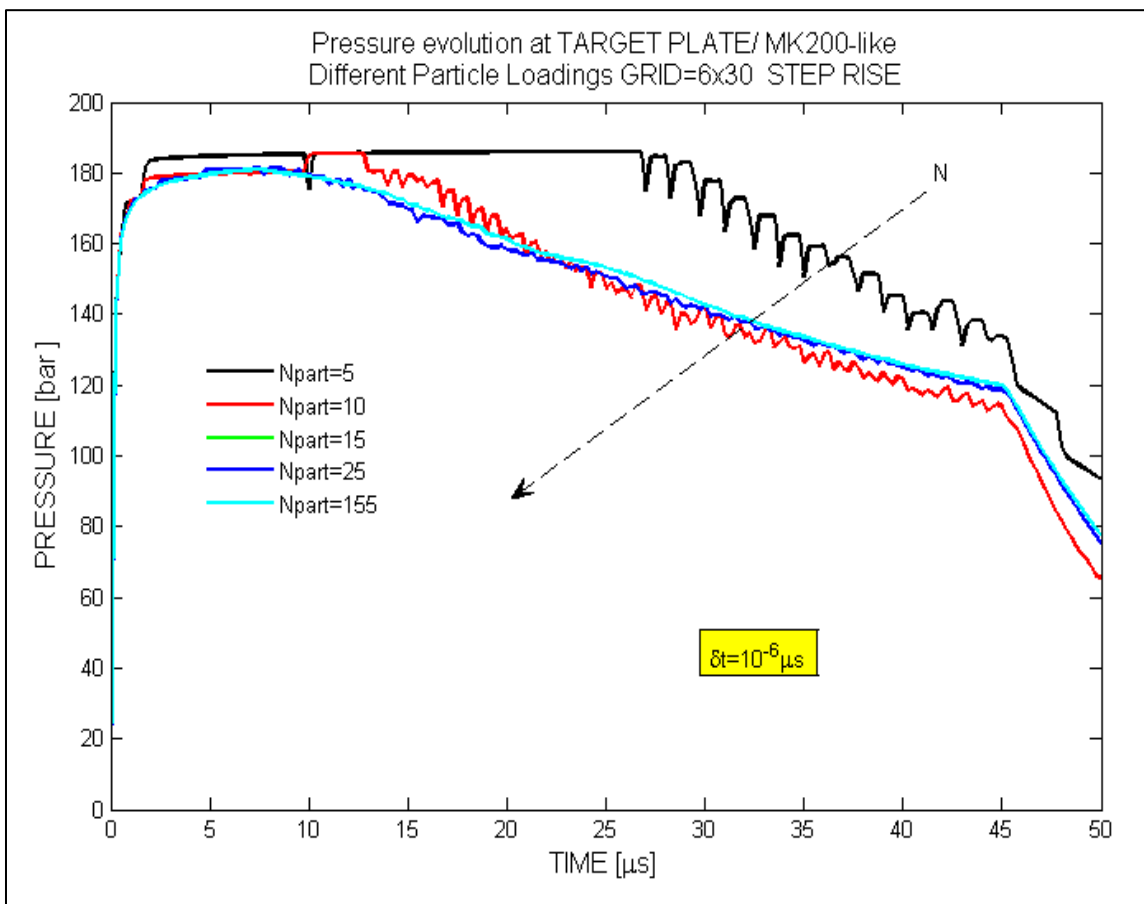


Figure 5.10 Calculated pressure evolution at plate center in MK200-like conditions simulations using HEIGHTS-PIC (step rise) with different N

Looking at the pressure trend, we notice that even though for  $N=10$  it is similar to the ones for higher values, it remains unstable with multiple oscillations. The oscillations are still evident but much smaller for  $N=25$  while disappear totally for  $N=155$  as expected.

As final note it is worth noticing that even for higher values of  $\delta t$ , increasing the number of particles plays a role towards getting more accurate results. In the following figure

(5.11) it appears evident that in both cases ( $N=75$  and  $N=180$ ) the expected Gaussian shape for the erosion crater is not respected but a consistent difference exist in the final value which is roughly 67% of the originally calculated. This 33 % reduction in the final estimate has been reached increasing the initial particle loading from 75 to 180 particles and so with an increase of 140% of particle loading.

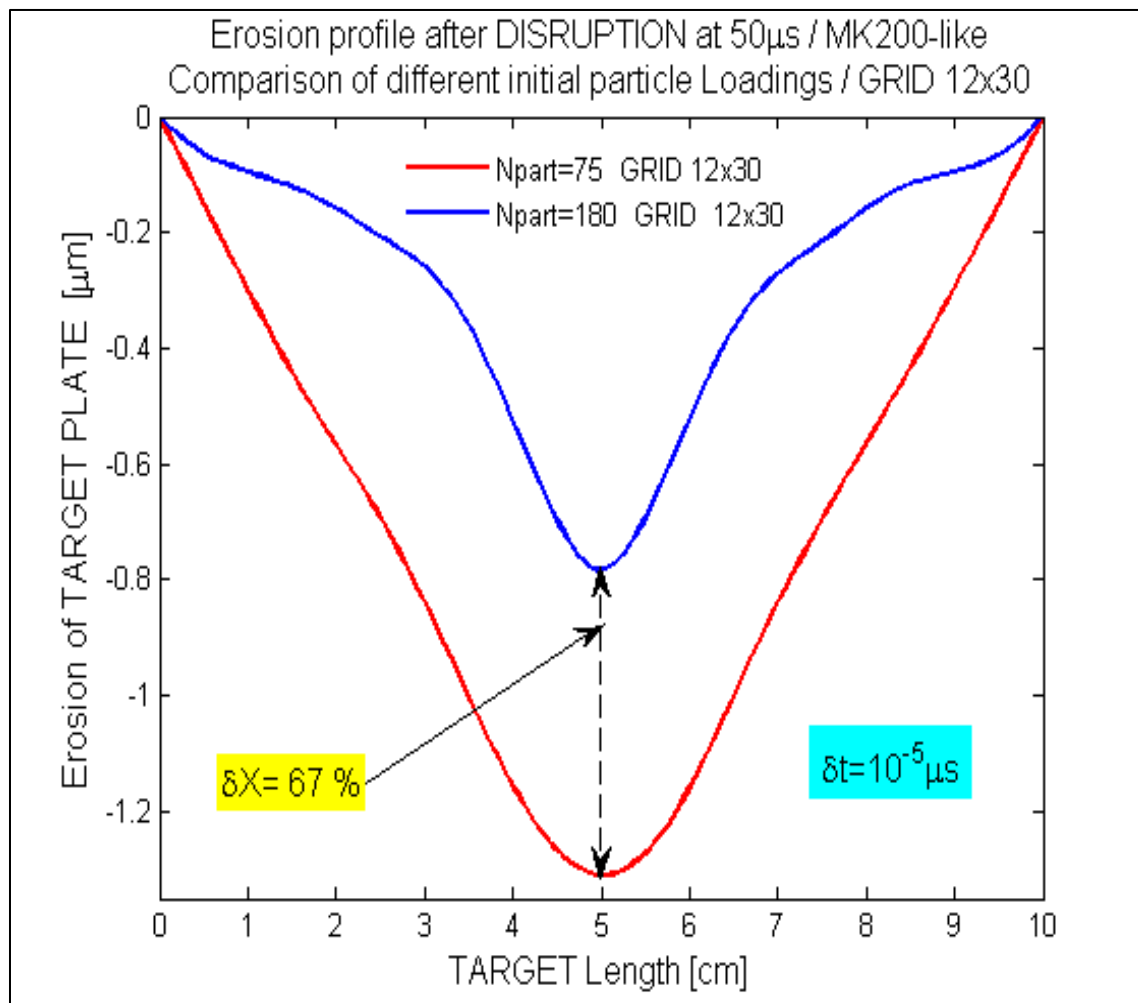


Figure 5.11 Calculated erosion evolution of plate center in MK200-like conditions simulations using HEIGHTS-PIC ( $10 \mu\text{s}$  rise with  $\delta t = 10^{-5} \mu\text{s}$ ) with different  $N$

### 5.3 Computational mesh vs numerical stability and computational time

Another important aspect to examine with attention, is to understand how much changing the initial computational grid can influence the stability of the calculation and accuracy of the solutions. Also in this case several simulations have been run with HEIGHTS-PIC to verify some of these characteristics. There is in fact no doubt that increasing the refinement of the computational mesh, more accurate results can be reached. Several factors though play a role as the  $\delta t$  chosen for advancing the calculation as well as the initial number of particles. As seen already in figure 5.9, the use of more refined grid (12x30 with respect to 6x30 of the previous simulations) not necessarily leads to more accurate results in absence of the proper  $\delta t$  and N. Looking instead at simulations using  $dt=10^{-6} \mu s$ , two main cases have been studied and compared with the original simulations for the MK200 (case 6x30): a computational grid of 12x30 and 18x30 have been used and all three cases for the evolution of the beam have been examined : step rise , linear rise of 5  $\mu s$  and linear rise of 10  $\mu s$ . As for the previous simulations an exponential decaying part has been used starting at 45  $\mu s$  and ending at 50  $\mu s$ . Here results from the 10  $\mu s$  rise are presented and compared.

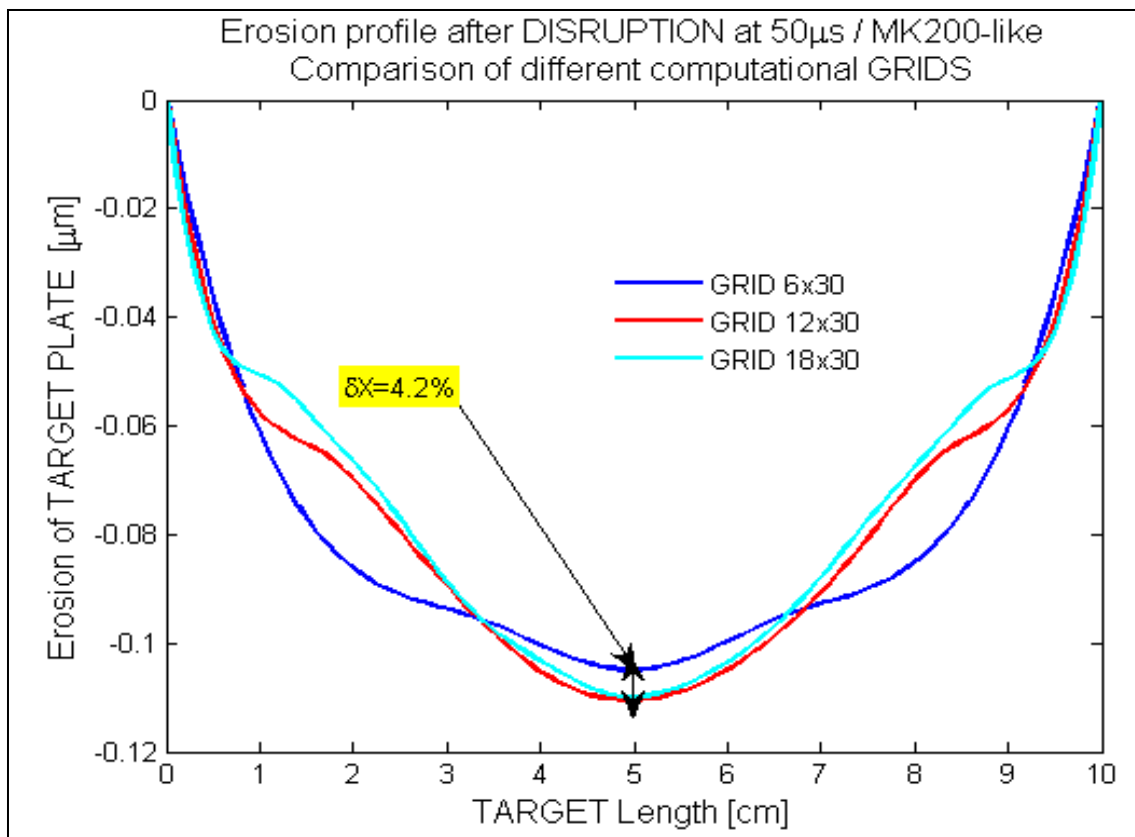


Figure 5.12 Calculated geometrical erosion evolutions along the plate in MK200-like conditions simulations using HEIGHTS-PIC (with  $\delta t = 10^{-6}$   $\mu$ s and 18x30 grids)[21]

As figure 5.12 shows, as expected increasing the number of cells into the computational mesh makes the results smoother and increasingly more accurate. In particular it is evident the difference into the geometrical shape which becomes increasingly more resembling the expected Gaussian shape originated from the beam itself. It is also important to notice that while the difference is relatively marked from 6x30 to 12x30, not much of a difference exists with 12x30 to 18x30 meaning that the saturation level for accuracy has been reached. Altogether the improvement in terms of calculated final erosion is only of 4.2%. A similar behavior exists looking at the evolution of maximum erosion along time:

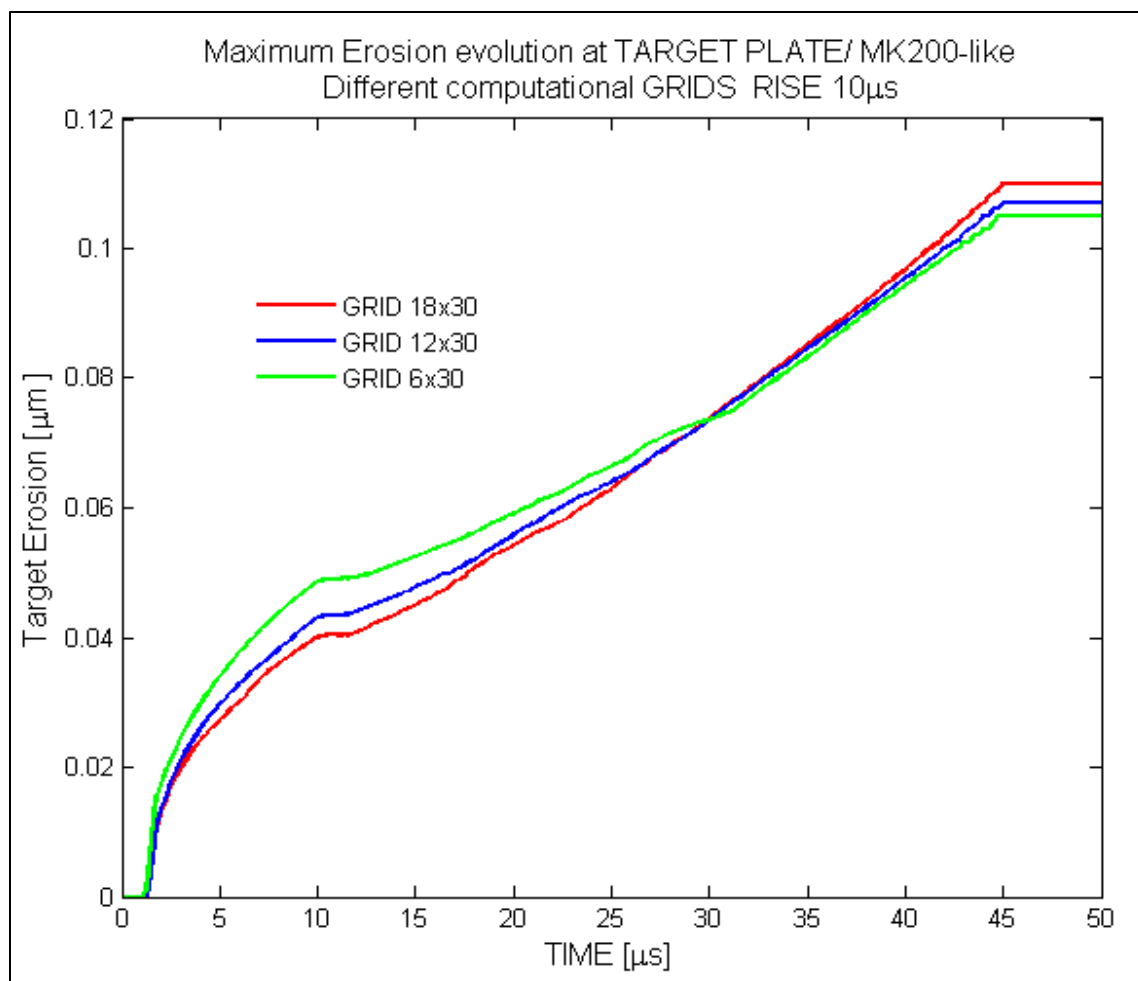


Figure 5.13 Calculated erosion evolutions with time of plate center in MK200-like conditions simulations using HEIGHTS-PIC (with  $\delta t=10^{-6}$  μs and 18x30 grids)

In fact in figure 5.13 particles in all 3 cases (6x30, 12x30 and 18x30) start being produced around 1 μs while erosion increase rapidly up to the end of the linear rise and then evolve almost linearly till the fading phase of the beam. Not much difference so exist between 6x30 and 18x30 calculations being the latter only much more smoother as it is visible from the following figure:

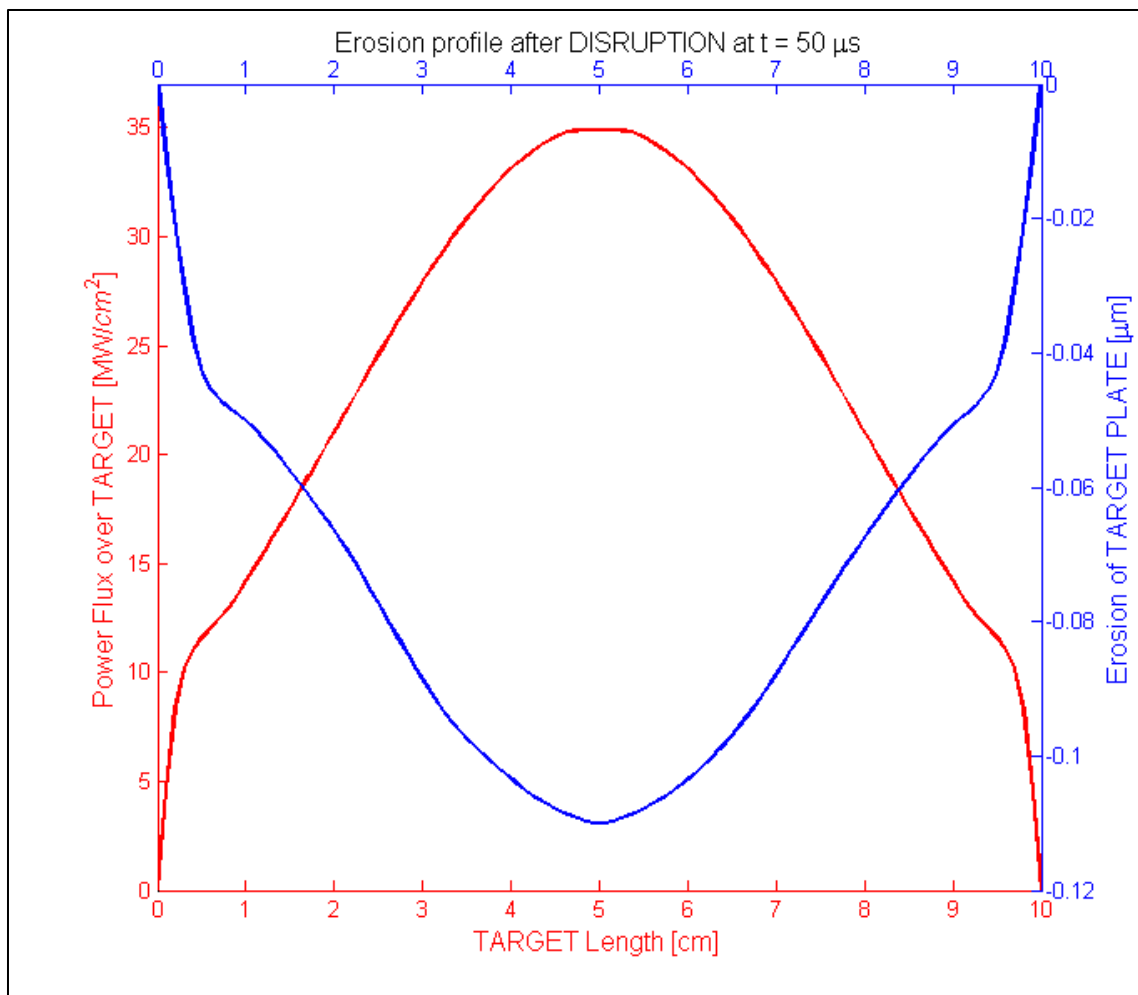


Figure 5.14 Calculated geometrical erosion evolution at plate in MK200-like conditions simulations using HEIGHTS-PIC (with  $\delta t=10^{-6}$   $\mu$ s and 18x30 grid)

Examining the geometrical calculated power flux and comparing it with the input from the beam (Figure 5.15) it is evident that the augmented number of cells spanning the space the results are better and almost perfectly matching the original beam taken in this case at 45  $\mu$ s. The global error also has reached a value of  $10^{-5}$  % which, is a good improvement of the already good  $10^{-3}$  % for similar condition for 6x30 grid.

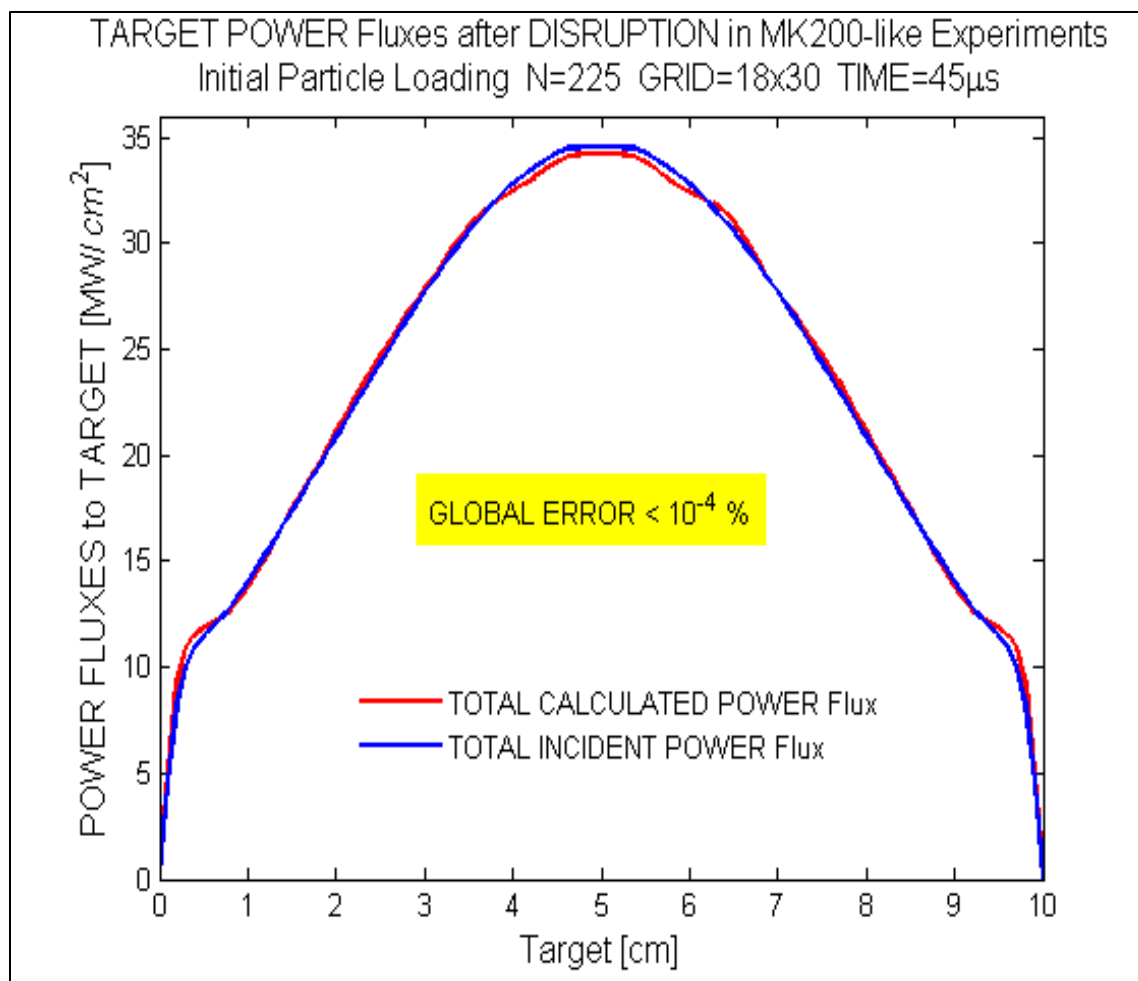


Figure 5.15 Calculated power fluxes along the plate in MK200-like conditions simulations using HEIGHTS-PIC (with  $\delta t=10^{-6}$   $\mu$ s , 18x30 grid at 45  $\mu$ s)

It is worth also analyzing the power fluxes profile and compare them. In fact this comparison reveals that as expected the 18x30 case calculated total power flux is much closer to effective input power than the 6x30 case. Hence the higher accuracy in the value calculated (Figure 5.16).

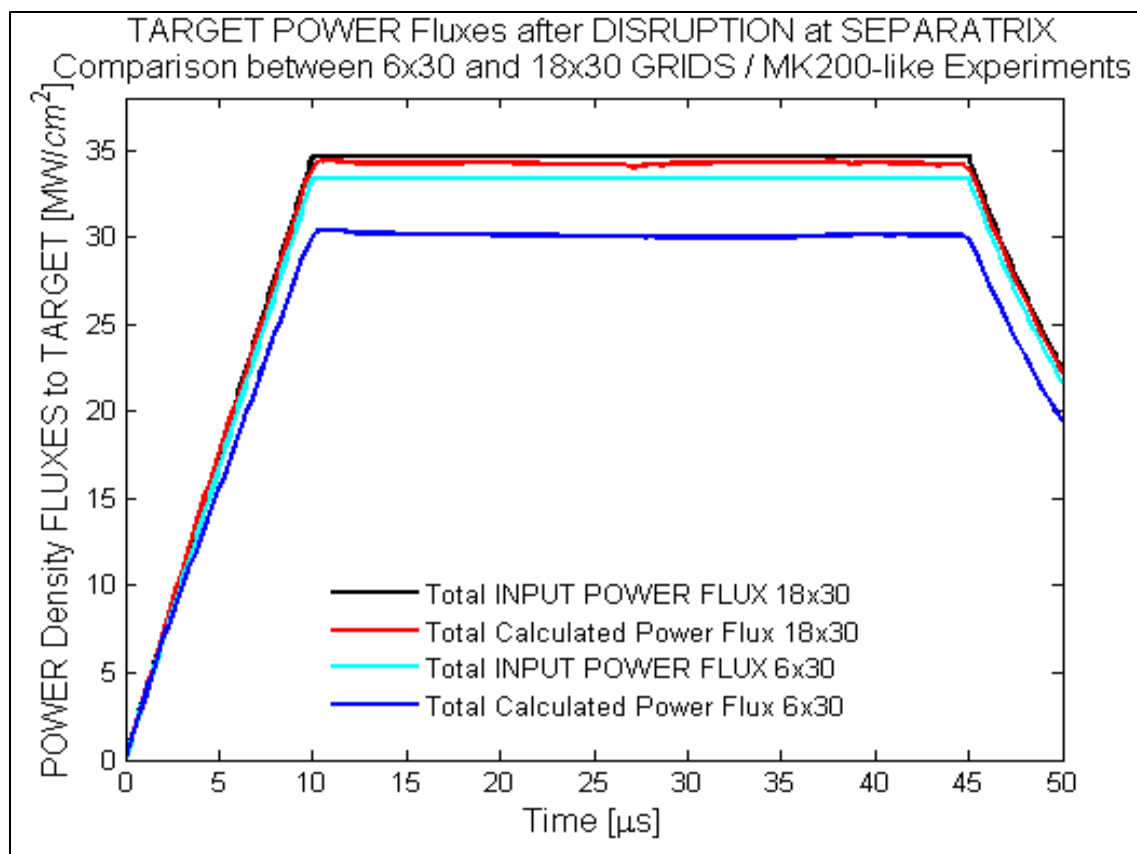


Figure 5.16 Calculated power fluxes at plate center in MK200-like conditions simulations using HEIGHTS-PIC (with  $\delta t=10^{-6}$   $\mu s$  , 18x30 grid and 6x30 grid)

In the end some considerations must be done regarding the total machine computational time. In fact, so far HEIGHTS-PIC behavior fully respects the particle in cell methodology. The increase in computational cells in order to provide more accurate and stable results works perfectly but has a strong limitation common to many similar techniques: the increase in computational time used by the same machine is not a linear factor but has more exponential type of trend. Improved accuracy is reached at the cost of increasing in a large amount the computational time. This can be related to the increased cost of solving at each time step for each cell, for each energy group, for each transition



line, for each of the eight angles chosen the radiation transport equation which uses quadrangular grids (i.e. 6x6 , 12x12 or 18x18) covering the entire space. The solution of the radiation transport equation in fact takes about 96% of the computational time. Using HEIGHTS-PIC in its serial version and running it on the CMUXE computational server assembled with Quad sockets AMD Opteron(TM) 6274 Interlagos 2.2GHz having 16 cores for a total of 64 cores CPU total, the machine time for each simulation has been recorded. In figure 5.17 the comparisons for the smaller computational grid (i.e. 6x30) are plotted.

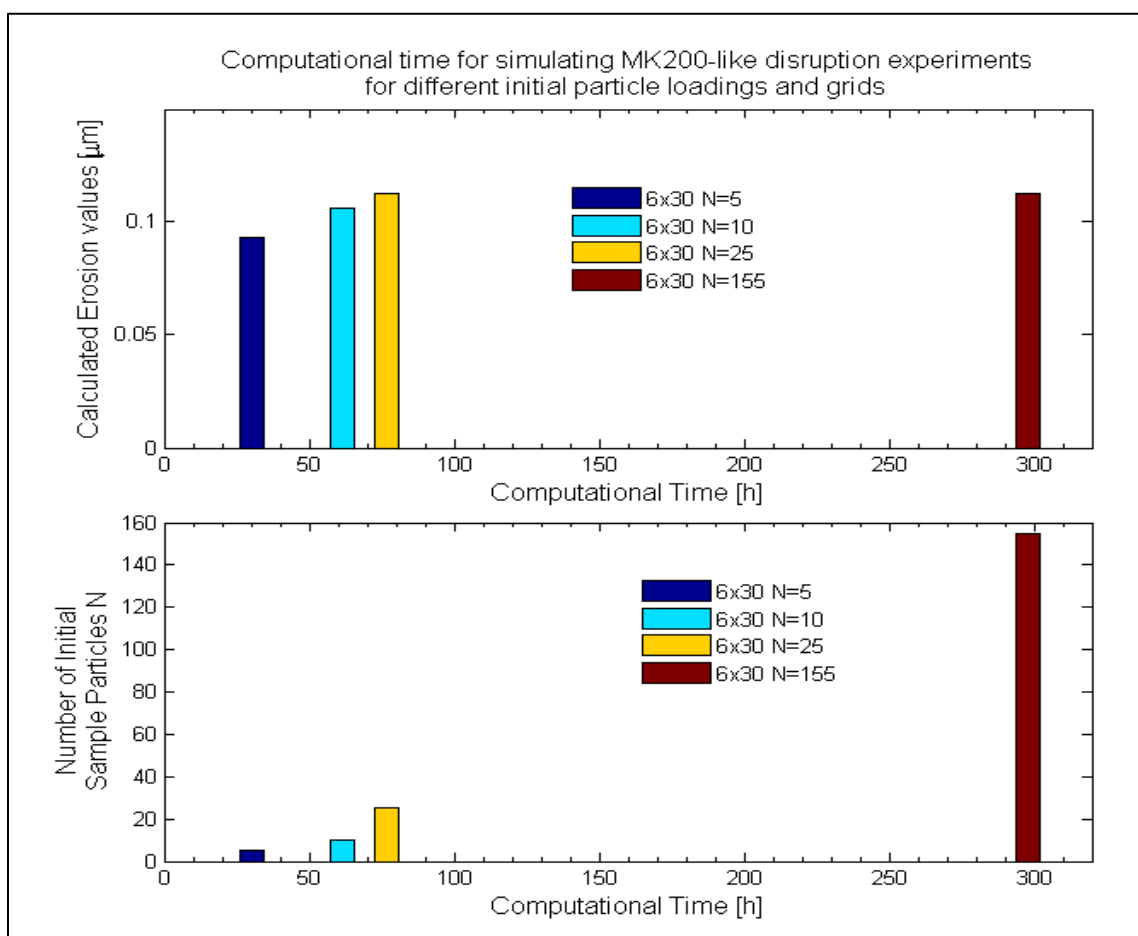


Figure 5.17 Calculated computational time in MK200-like conditions simulations using HEIGHTS-PIC on the CMUXE Server (different particle loadings for 6x30 grid) [22].

Looking at the different values of erosion calculated, as expected for very few particles loaded ( $N=5$  to  $N=25$ ) the total machine time is relatively small: it goes from 34 hours for the first case, till 75 hours for  $N=25$ . For the complete solution of the last case ( $N=155$ ) the machine time taken is of roughly 300 hours (i.e., 294 hours). In the same plot, the maximum erosions can be also extrapolated showing that the increase of particles produces more accurate results but at the expense of a largely increased computational time. It is also interesting to see how the trend is absolutely not linear and has 2 distinctive phases: the first one is between  $N=5$  to  $N=25$  (with similar global errors). In fact an increase of 5 times the number of loaded initial particles, does not produce 5 times increase in the computational time that goes from 34 to 75 hours.

The second phase from  $N=25$  to  $N=155$  shows another trend where still increasing the number of loaded particles 6 times produces only about 4 times the increase in computational time. More evident are those differences if erosion calculations are taken into account. In fact as shown before, there is not much of a difference between  $N=25$  and  $N=155$  while comparing  $N=5$  and  $N=155$  for an accuracy increase of 16 % there is a cost of almost 900% of computational power. To be complete the analysis has to include not only the number of particles for a fixed computational grid but also a study of different grids with roughly the same initial number of particles. This is plotted into figure 5.18 where the variation of calculated erosion is plotted against computational time and number of particles. As it can be seen for almost identical values of final target erosion and for relatively high number of particles there is a net increase of computational time which though does not appear to be justified given the level of

accuracy already reached. It is impressive to see that 18.x30 grid for 225 particles loaded needs more than 1600 hours of machine time to produce the needed results.

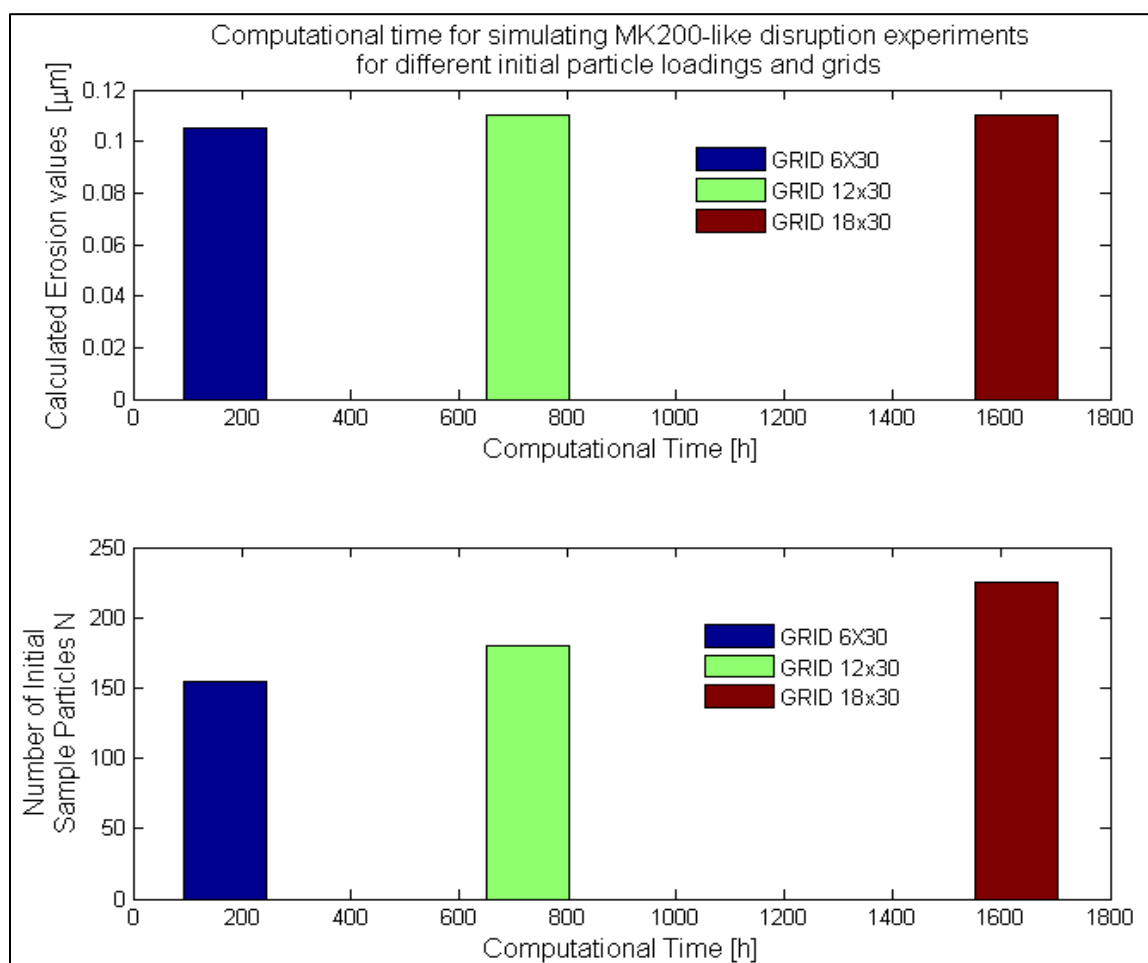


Figure 5.18 Calculated computational time in MK200-like conditions simulations using HEIGHTS-PIC on the CMUXE Server (Comparisons 6x30, 12x30 and 18x30) [21].

This scales of about 6 times the same time needed for the same simulation using 6.x30 grid and  $N=155$  particles.

Taking into account what it has been explained so far, it appears clear that there is no “winning factor” in terms of preferring one characteristic over the other. This is a

complex problem that requires a “trade off” type of approach always looking at the final goal which, is to produce accurate erosion results and plasma information but in a reasonable amount of time. Increasing the number of “super particles” increases the “quality” of the information produced up to a point where saturation is reached. Increasing further the number of particles will not produce more accurate results, just increase computational time (for example as shown in a 6x30 grid simulation passing from 25 to 155 initially loaded particles). On the other end, while increasing the number of cells will increase the “refinement” of the calculations, if used with  $\delta t$  too big (case of 12x30 but  $dt=10^{-5}$   $\mu s$ ) will not produce any effect and not provide the aimed accuracy. At the same time though, it has to be considered that especially when evaluating a new geometrical configuration, results significantly close to the final ones can be provided also but a relative coarse grids as shown especially for the calculation of erosion. So, in the end the choice is in the scientist who applies the rules and has to judge wisely.

#### 5.4 Application of different B fields

To complete the study of the plasma evolution, several other simulations have been run in order to define the characteristics of the plasma and its erosion for different magnetic field with respect to the benchmarking conditions.

The geometry considered for evaluating possible effects one the B field is changed from the original configuration studied , are both the MK-200 like and the ELM type. In particular the focus has been to identify significant changes in the plasma behavior. For the MK200-like experiment [3-5, 9], the magnetic field was set at  $B=0.50$  T (4 times less than the previous calculations) while all the rest was left unchanged. Looking at the

erosion provoked onto the plate (figure 5.19) it is evident that the trend already seen before is not significantly changed.

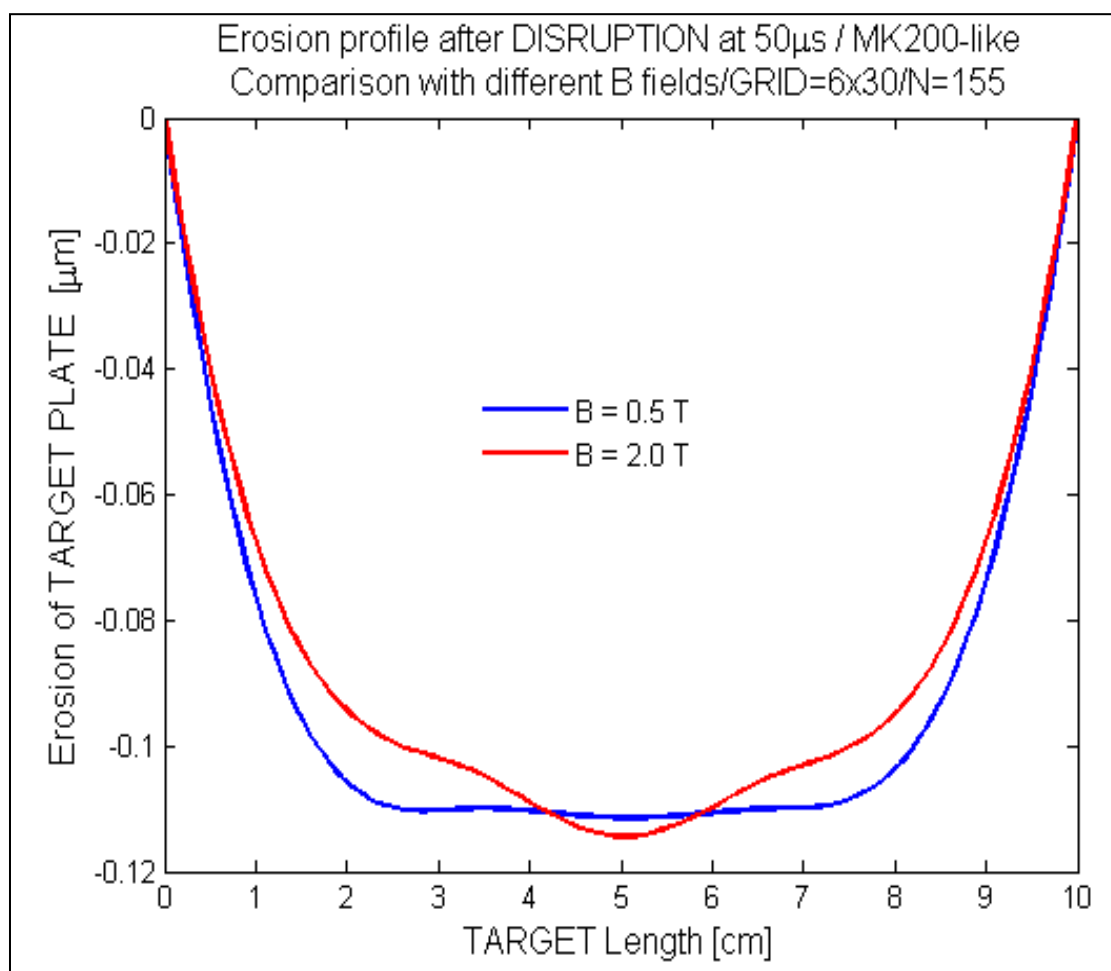


Figure 5.19 Calculated erosions along the plate at 50  $\mu$ s in MK200-like conditions simulations using HEIGHTS-PIC for different B fields (N=155)

Very similar also appear to be the evolution along time with the reduced B field (figure 5.20) without major changes and using all the same parameters.

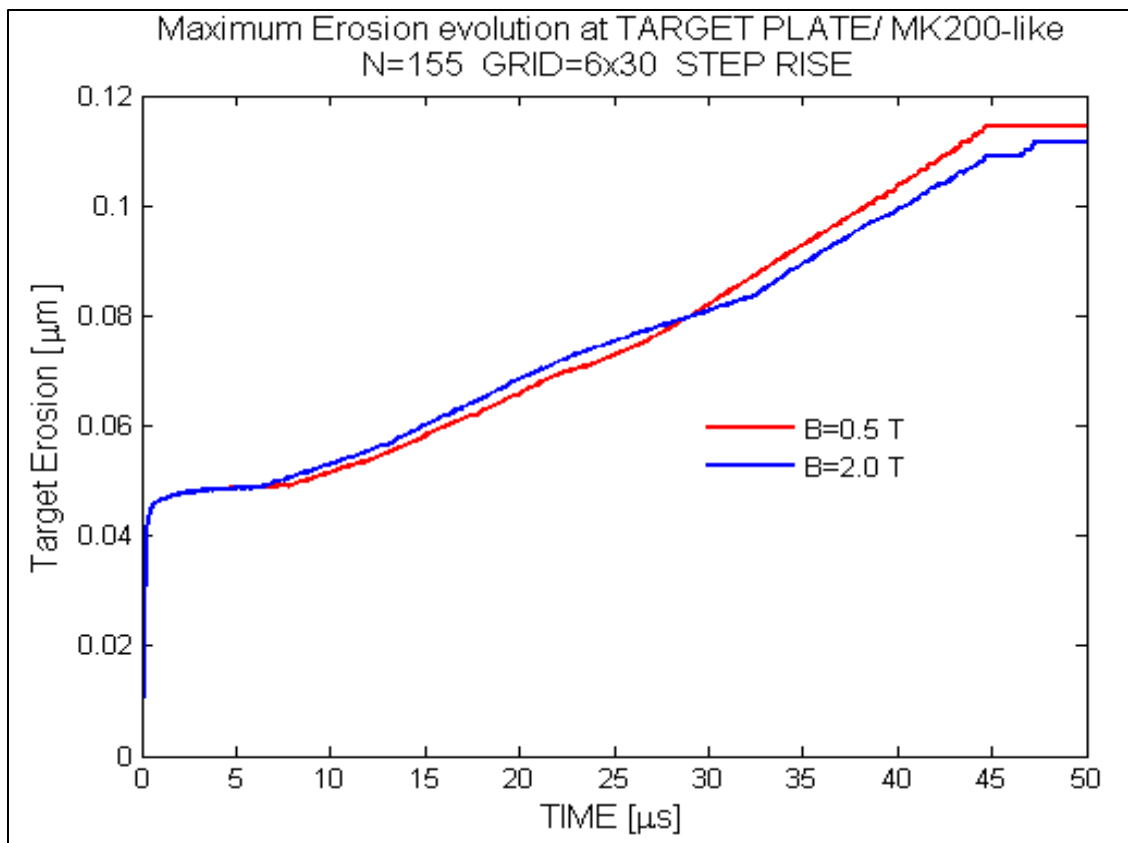


Figure 5.20 Calculated erosions evolutions along time in MK200-like conditions simulations using HEIGHTS-PIC for different B fields (N=155)

This very similar trend can be justified by the relatively short time of plasma evolution. The reduced confinement provided by the smaller B field in the MK200 geometry (B perpendicular to the plate) produces a slightly wider erosion footprint but does not significantly change the original considerations. At the same time though it has to be considered that since typically ELM events as disruptions events have duration of several hundred  $\mu$ s [2-6, 11, 13, 19], the hydrodynamics effects of a reduced magnetic confinements can be seen producing evident differences acting only after a much longer time than the one here examined. Similar behaviors in fact are also found in the density

profiles, temperature profiles, and power fluxes. The configuration used is the same of the previous chapter and recalls the ITER geometry [11-12, 19]. Differences in all cases do exist but are minors and do not show a “completely different” plasma behavior. In order to confirm this result, also ELM simulations have been run. This time the magnetic field intensity has been chosen equal to  $B=1$  T and so 5 times less than the previous simulations. Also in this case all the rest was left unchanged (figures 5.21-22)

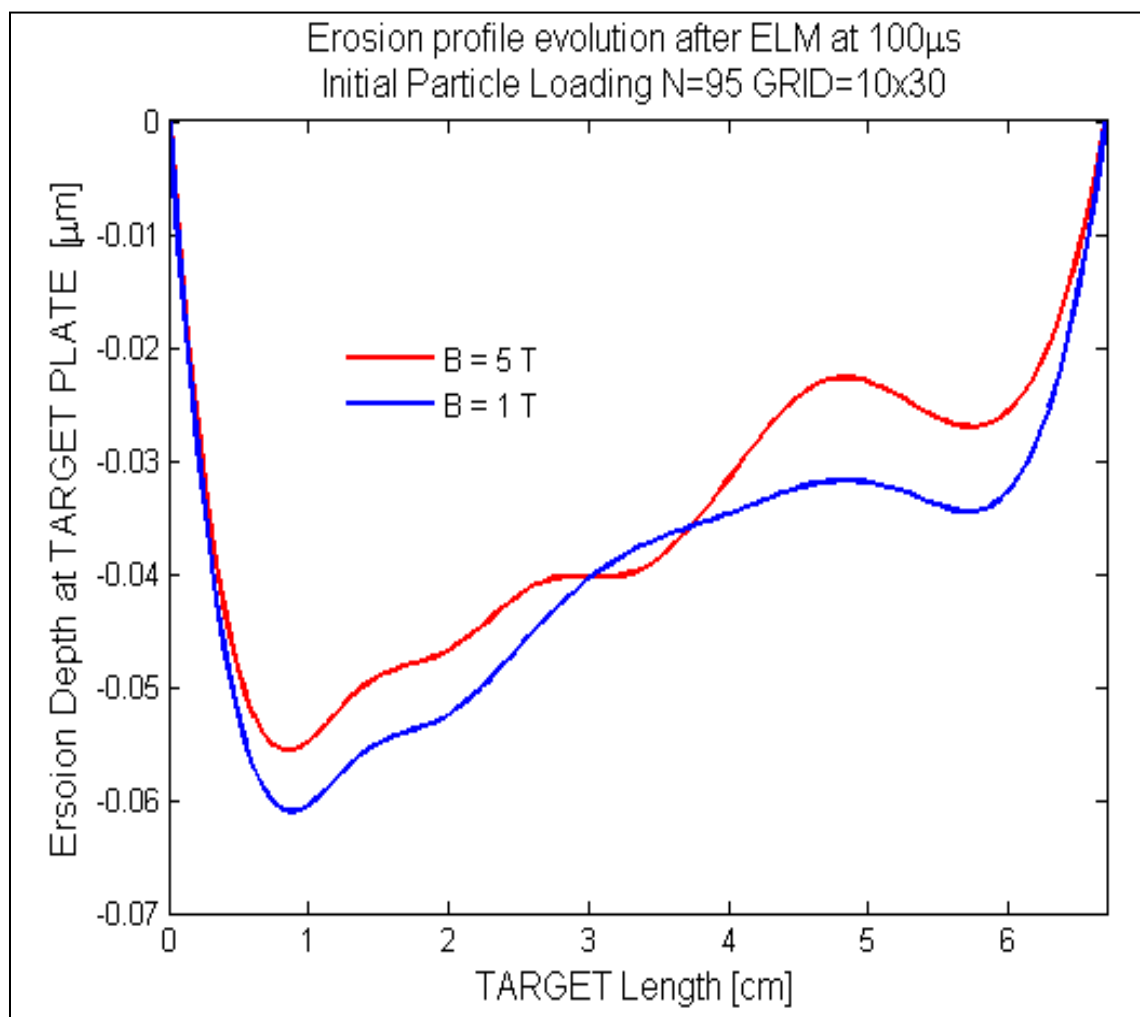


Figure 5.21 Calculated erosions along the plate at  $100 \mu\text{s}$  in ITER-like conditions ELM simulations using HEIGHTS-PIC for different B fields ( $N=95$ )

As predicted, differences in the erosion are small and evident only at much later times (from 60-70  $\mu\text{s}$ ). For the ELM case the very shallow angle of the magnetic field will affect the evolution of the plasma vapor cloud on top of the plate affecting both plasma expansion and radiation [6, 11, 14-16]. In the end as proven in [11] the target plate will have a wider erosion footprint due to the less screening provided by the cloud.

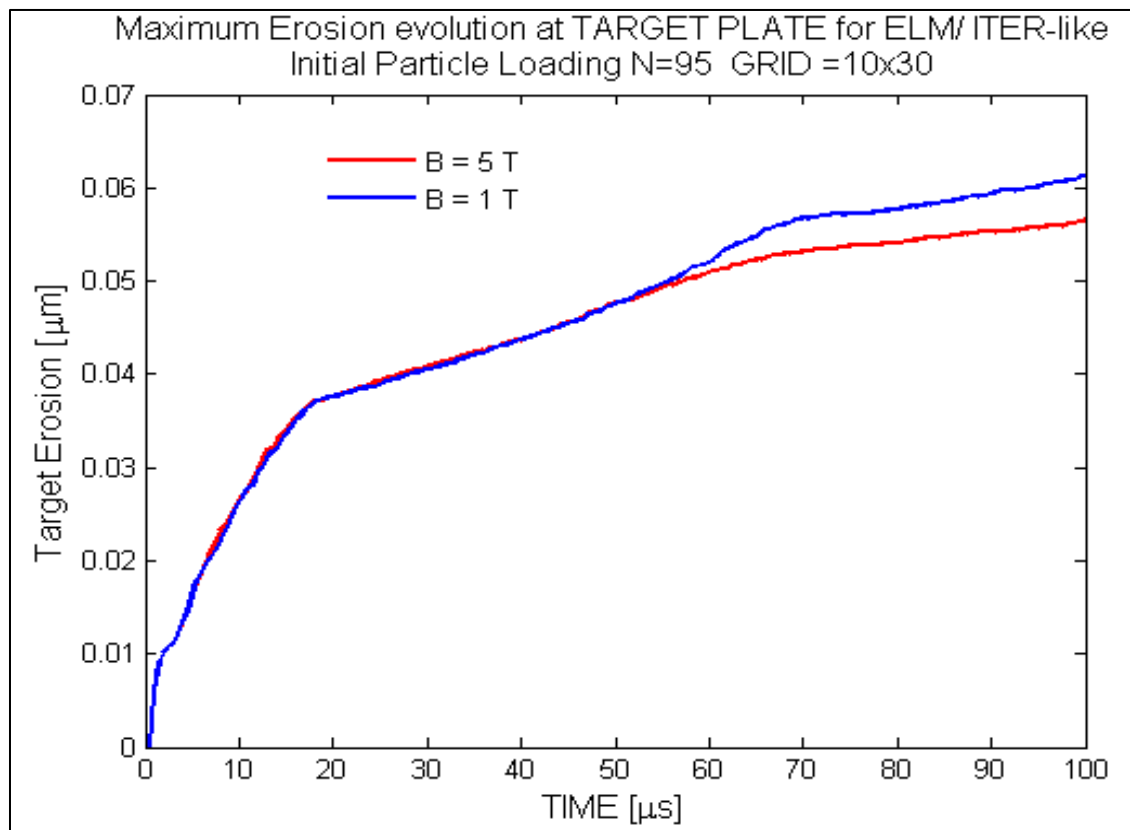


Figure 5.22 Calculated erosions along time in ITER-like conditions ELM simulations using HEIGHTS-PIC for different B fields (N=95)

This phenomenon is evident in both cases (ELM and MK200) looking at both the final densities of the plasma vapor cloud and velocities associated with the super particles. Velocities along Y axis are consistently higher (roughly one order of magnitude) when B



is weaker producing less dense (roughly 20 to 30 %) and protective vapor clouds allowing a faster escape of the particles out of the boundaries.

### 5.5 Limitations of the model

Looking at the results and comparisons so far here presented, some aspects regarding the model have emerged. In fact, looking at HEIGHTS-PIC computer package, there are several improvements that can be implemented and would reduce some of the limitations of the present model. HEIGHTS-PIC has been designed with a fixed geometry in mind. Its application to other geometries, more complex and closer to the entire tokamak environments would require a redesigning process. In this way also damages created to nearby components (the dome for example close to the divertor) would be examined providing a more accurate picture of the entire phenomenon.

Another important improvement that can be inserted into HEIGHTS-PIC is the presence of the poloidal magnetic field. Even though not large in magnitude (about 1/10 of the original toroidal one), its presence as well orientation with respect to the plate and to the geometry under investigation, may allow to produce higher velocities of the plasma vapor cloud onto the Y-axis direction. In fact, all the movements along the plate during the events examined are essentially driven by magnetic diffusion events which would results in higher velocities than those calculated if there was a poloidal component. This is important especially with respect to the study of “indirect” erosion driven by the effect of radiation to the ground and outside the original imprint provided by the beam. In the studies done with HEIGHTS-PIC, the values of the radiation to the original exposed surface for those cells out of the original imprint of the beam, produce a power flux

always below the threshold proven experimentally [14, 18] to produce intense evaporation (and so super particles) which, is around  $0.20 \text{ MJ/m}^2$ . This value has been also confirmed in our models as the bare minimum to be reached in order to start "cumulating" significant vapor mass that will lead to the formation of particles.

It is also very important to define better the beam components. As it is now, HEIGHTS-PIC has a beam which creates essentially a thermal imprint onto the target plate. Though very flexible in its use, this way of "interpreting" the incoming SOL plasma is not necessarily a perfect tool. In HEIGHTS-PIC simulations in fact while the carbon vapor front is well interpreted providing a close to target high dense and cool plasma [7-8,14-17,19] is unable to provide information about the plasma corona which extend much further from the target (several cm) showing much higher temperatures and low densities and essentially formed by DT ions, electrons and neutral particles.

Another consideration should be done regarding the processes that bring to the destruction of the carbon-graphite surface under intense power deposition. In fact, experimentally [9-10] it has been proven that cracks develop leading to a brittle type of failure of the material. At the same time due to the presence of the B field, re-deposition of melted material is possible as well as re-deposition from initially ejected chunks of material [20]. HEIGHTS-PIC does not have any brittle destruction mechanism or any splashing physics into its models and this justifies the existing differences for erosion with some specific graphite like the MPG8, which are doped and exhibit a rather sensitive behavior to brittle destruction.

In order to further improve accuracy a new computational strategy for solving the radiation transport equation must be found. This is not just a need for a purely parallel

code, but rather for a parallel code which balances efficiently the great amount of computational power needed for the accurate solution of all components being able to distinguish among different “beam zones”. In both the exponential and Gaussian beam geometry, the cells interested by higher fluxes generate much more particles which translates into more time for each processor involved leaving the “less loaded” lingering.

## References

1. R. COURANT, K. FRIEDRICHS, H. LEWY, "Über die partiellen Differenzgleichungen der mathematischen Physik", *Mathematische Annalen* (in German) 100 (1): 32–74 , 1928.
2. V.M. SAFRONOV et al., "Evaporation and vapor shielding of CFC targets exposed to plasma heat fluxes relevant to ITER ELMs", *Journal of Nuclear Materials*, 386-388, 744-746, 2009.
3. N.I. ARKHIPOV, et al., *Fusion Technology* 1994, Vol. 1, p. 423, 1995.
4. N.I. ARKHIPOV et al., "Study of structure and dynamics of shielding layer for inclined incidence of plasma stream at MK-200 facility", *J. Nuclear Materials*, 233- 237, p. 767-770, 1996.
5. N.I. ARKHIPOV et al., *Fusion Technol.* in: C. Varandas, F. Serra (Eds.), p. 507, 1996
6. V.G. BELAN, "Features of dynamics and structure of the shielding layer at the interaction of plasma flow with target", *Journal of nuclear materials*, 233-237,763-766, 1996.
7. H. WURZ et al., "Hot Plasma Target Interaction and Quantification of Erosion of the ITER Slot Divertor during Disruptions and ELM", 1999, FZKA 6198 , Karlsruhe , Germany, 1999.
8. H. WURZ et al., "Damage and Evaluation of Vertical targets and first walls during ITER-FEAT off-normal events", FZKA 6582, Karlsruhe, Germany, 2001.
9. N.I. ARKHIPOV et al., "Erosion mechanism and erosion products in carbon based materials" , *J. Nuclear Materials*, 307- 311, p. 1364-1368, 2002.

10. V. SAFRONOV et al., "Macroscopic erosion of divertor materials under plasma heat loads typical for ITER hard disruptions", Problems of Atomic Science and Technology, N.5, Series: Plasma Physics 8, 27-29, 2002
11. V. SIZYUK, A. HASSANEIN, "Damage to nearby divertor components of ITER-like devices during giant ELMs and disruptions", J. of Nuclear Fusion, 50, 11500, 2010.
12. R. AYMAR, "ITER R&D: Executive summary: Design overview." Fusion Engineering and Design 55(2-3): 107-118, 2001.
13. A. HASSANEIN, "Modeling and key issues of plasma/surface interactions in future Tokamaks", Fusion Engineering and Design 69, 781-787. 60, PII S0920-3796(02)00006, 2002
14. V. SAFRONOV, et al., "Evaporation and vapor shielding of CFC targets exposed to plasma heat fluxes relevant to ITER ELMs", Journal of Nuclear Materials, 386-388, 744-746, 2009.
15. S. PESTCHANYI et al., "Radiation losses from ITER SOL due to divertor material plasma", 31<sup>st</sup> EPS Conference on Plasma Physics, London ECA, vol. 28, 1.135, 2004.
16. N.I. ARKHIPOV et al., "Formation of shielding layer near a solid target under the action of high-power plasma flow", Plasma Physics Report, vol. 25, N.3, 236-245, 1999.
17. N.I. ARKHIPOV et al., "Energy balance in the interaction of intense High-Temperature Plasma Flows with solid Targets", Plasma Physics Report, vol. 28, N.3, 432-443, 2002.
18. L.E. GARKUSHA et al., "The latest Results from ELM-simulation experiments in plasma accelerators", Physica Scripta, T138, 014054, 2009.

19. A. HASSANEIN and I. KONKASHBAEV, "Comprehensive modeling of ELMs and their effect on plasma-facing surfaces during normal tokamak operation." *Journal of Nuclear Mat.* 313: 664-669, 2003
20. K. OHYA and K. INAI, "Hydrocarbon redeposition on Plasma Facing Walls Intersecting Magnetic Field at Shallow Angles", *Japanese Journal of Applied Physics*, 49, 096201, 2010
21. F. GENCO and A. HASSANEIN, "Particle-in-Cell (PIC) Methods in predicting materials behavior during high power deposition". Submitted to *Laser and Particle Beams*, Cambridge University Press, Accepted for Publications, November 2013
22. F. GENCO and A. HASSANEIN, "Particle-in-Cell (PIC) Simulations of damage to Tokamaks Plasma Facing Components during Intense Power Deposition". Submitted to *Fusion Engineering and Design*, IOP Science, Under Review, 2013

## CHAPTER 6. CONCLUSIONS

In this thesis, new methodologies based on particle-in-cell (PIC) technique for the study of the effects of plasma instabilities such as Edge Localized Modes, Disruptions, VDE, and Runaway Electrons on plasma facing components in a tokamak environment were presented.

The importance of a full understanding of the evolution of plasma under those off-normal conditions cannot be stressed enough. In fact plasma facing components are subjected during those events to great thermal stresses, fatigue, erosion, sputtering, blistering, and structural damage which in the end compromise their lifetime expectancy, their performance as well as the ability for the tokamak itself to maintain an effective plasma inside the toroidal chamber . With this work we have updated and developed a new computer package, i.e., HEIGHTS-PIC, able to examine in a self-consistent way each aspect of the physical problem present: a) heat transfer, melting and evaporation of the carbon target surface b) plasma material interaction over the surface under power flux and c) radiation transport in the plasma vapor cloud.

Initially a very detailed computational framework was developed in order to properly interpret the very complex physical phenomena involved in such phenomena based on similar treatments done already with the original HEIGHTS package (chapter 2).

Radiation transport solution models developed based on the direct solution of the radiation transport equation with calculation at each time step for each zone of the computational mesh of the absorption and emission coefficient have been used to accurately solve the physical problem involving plasma material interaction. A new approach of the particle-in-cell technique based on use of a fluid dynamic interpretation of the plasma produced upon energy imping on a target plate has been updated and developed and proposed in this work. The algorithm developed uses super particles introduced via a dynamically changing boundary (the target plate) and stacks them in each cell according to cell birth position. The particles are 1-D dimensional along the Y direction (partition decided at the start of the run) but non-dimensional along the X direction perpendicular to the target plate. In order to benchmark HEIGHTS-PIC computer package (chapter 4) three main approaches have been followed. The first one used the experimental data available for the MK200 plasma gun facility in Troisk, Russia in attempt to verify the quality and accuracy of the erosion predictions. Several numerical experiments have been conducted using the same experimental configuration. Some of the results have also been compared with other computer packages based on different numerical methods and have shown also good agreement. The second approach has consisted in comparing HEIGHTS-PIC with the original HEIGHTS computer package.

Even if the methodologies used are also in this case different (Monte Carlo versus direct solution of the radiation transport equation, Lagrangian versus particle in cell for the solution of the hydrodynamics, and so on) the general agreement can be considered very good. Finally, laser produced experimental and theoretical data have also been used in a modified version of HEIGHTS-PIC and have shown excellent agreement (chapter 4).



This leads to some more considerations related to the technique in general. In fact, this modified version of particle-in-cell technique coupled with the direct solution of the radiation transport equation can be applied in principles to any area of plasma physics, from the study of galaxies to the analysis of plasma thrusters for satellites. The flexibility and capacity to produce minimum numerical diffusion errors is also very important as the possibility to decide a priori the level of complexity and accuracy desired via the initial loading of super particles. Numerical stability of the integrated systems can also be reached using a wise decision making when establishing the computational step for advancement of the calculation well below the simple Courant condition (chapter 5). The interpretation of plasma as a fluid provides also more flexibility in the choice of where to engage the computational power that in HEIGHTS-PIC is done providing a direct solution of the very complex equations

The models can be expanded transforming them in a fully operating system working on a similar fashion of cloud computing which would allow more sophisticated geometries as well a three-dimensional approach to the problem. Given the importance of different materials for tokamak environments and graphite performance, HEIGHTS-PIC should be also integrated with the atomic data for both tungsten and beryllium. The accurate solution of the radiation transport can be used to predict once expanded to full tokamak geometry, the effective amount of impurities tolerable by the system as well as their impact on a local scale and more extended one. Introducing into the models plasma turbulent mixing would allow following even more precisely the general behavior and study the overall feasibility of the magnetic fusion concept for future energy production. Future work to be developed, starting from the actual development of HEIGHTS-PIC,

should have in mind the full spectrum of the actual limitations of the model and build up from there. The full parallelization of the code needs to be done in order to pursue more complex geometries. More advanced geometries might consider not only the damage on the divertor plate, but also other plasma facing components far from the actual strike point. Dust particles and their motion might be also considered into the new models. For carbon material, brittle destruction as well as cracking must be implemented and integrated into HEIGHTS-PIC: redeposition of the carbon macroscopic particles emitted should also be evaluated especially far from the original impact area. Introducing plasma mixing into the models would allow for much better understanding and tracking of the plasma far from the facing components and possibly evaluation of direct effects into the bulk plasma of tokamaks.

## APPENDICES

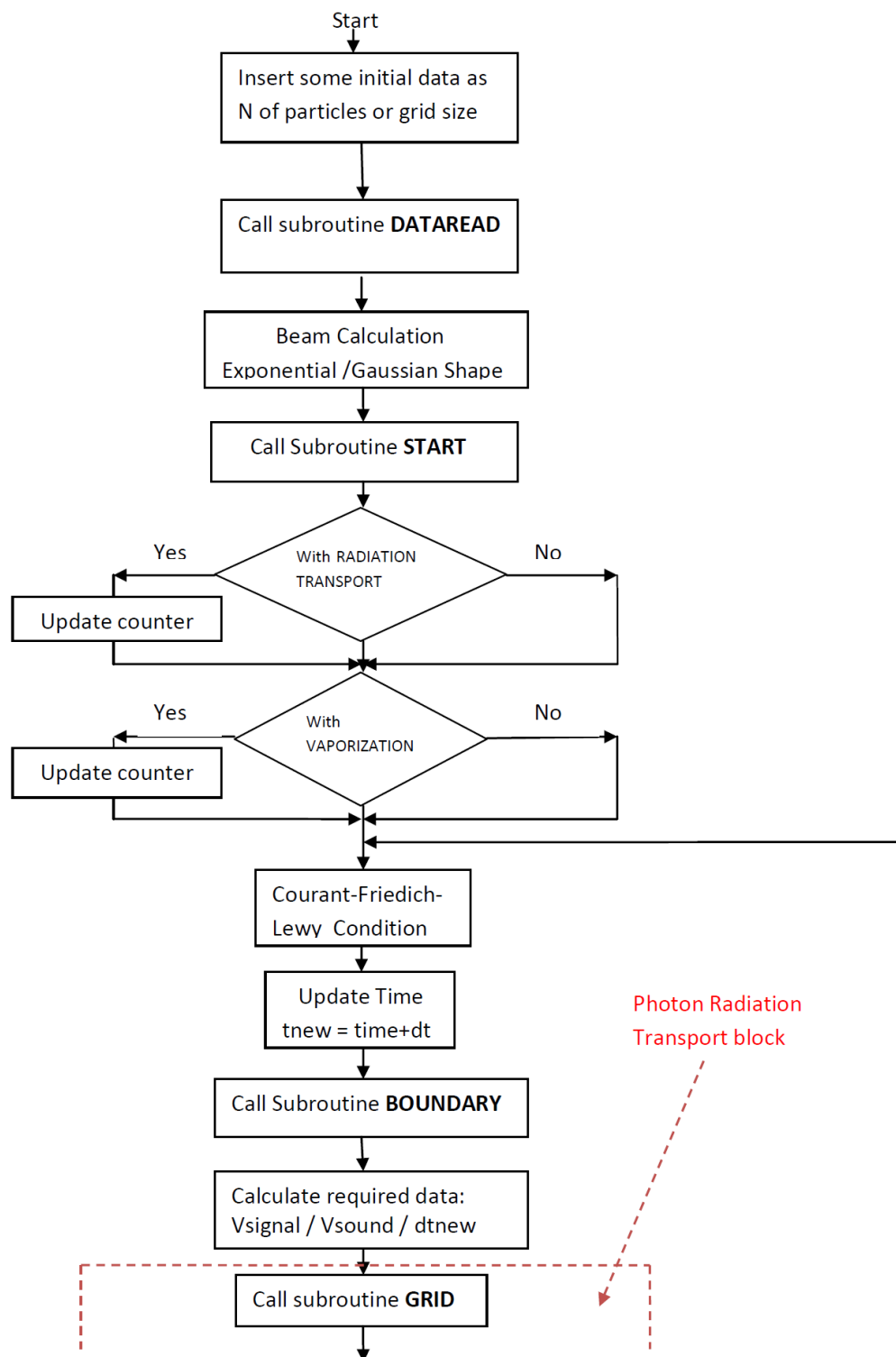
## Appendix A Flow Charts of HEIGHTS-PIC/Hydrodynamics

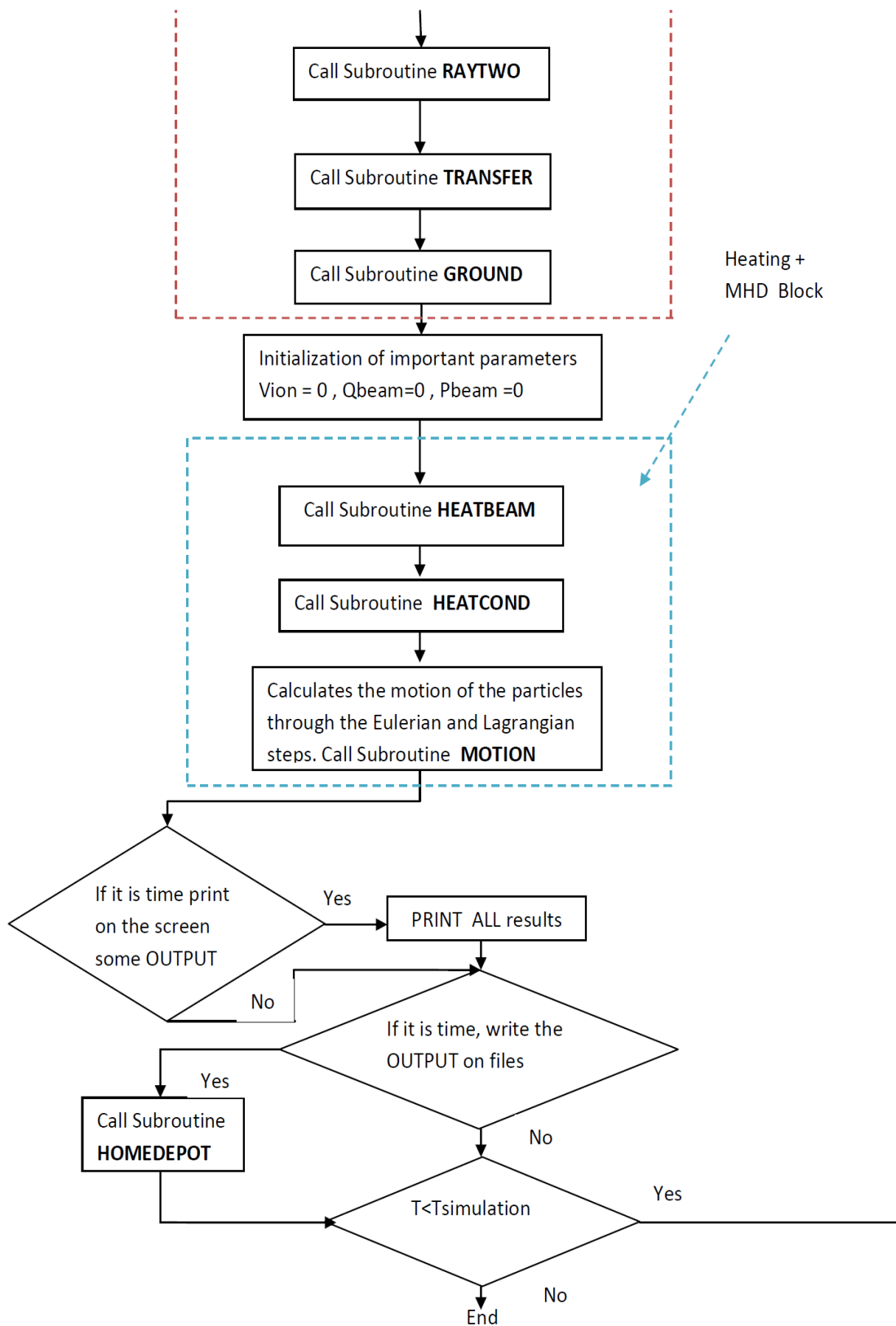
### **A1) Main Program**

In this section, the main program is explained. Initially some data are assigned or loaded using the subroutine DATAREAD where many of the code structure are taken from the initial unpublished HEIGHTS-PIC code and the parameters needed for the calculation are defined or assigned. Among the data provided, the angle of the divertor plate is assigned with respect with the XYZ natural axis as well as the type or shape of the beam. A very important parameter is dmP0, which is the amount of real particles represented by a sample one. The magnetic angle, intensity of the B field and the number of particles originally loaded in the cells are also provided. In the main program also the original subdivision of the entire domain along the X and Y direction is assigned defining the number of cells along those directions. Then once the beam parameters (energy of the particles, shape of the beam, and intensity of the impinging power flux) have been provided, the program calculates per each cell of the domain above the divertor the local intensity and influence on the system. These data will be used for evaluating the energetic balance into the cells as well as for the solution of the heat conduction problem into the material. Among the several options available we can write in output files the required results or execute the radiation transport part. In this case, before calling the subroutine in charge for the solution of the radiation transport part, the Courant-Friedrich-Lewy condition is also checked to make sure that the new time step calculated is below this value for the stability of the solution. Then in order the subroutines GRID, RAYTWO, TRANSFER and GROUND are called to solve the radiation transport inside the plasma-

vapor cloud. As a result, the value of the radiation power is known in each cell and can be applied later for the calculation of the energy transferred to the target material. Then the subroutine HEATBEAM and HEATCOND are called: the first subroutine evaluates the power and energy deposited by the beam of plasma onto the divertor plate, while the second calculates all the energy transferred cell by cell by conduction. Finally the subroutine MOTION is called: in this subroutine all the hydrodynamic evolution of the plasma and vapor is calculated, as well as the new sample particles eventually generated by the erosion of the material. For each cell, velocity, pressure, density, energy is calculated. The position of the particles inside the mesh is also evaluated at each time step. The subroutine MOTION contains both the Eulerian step and the Lagrangian step typical of the PIC technique. In these Appendices only some of the most important subroutines are presented with flow chart.

## FLOW CHART MAIN PROGRAM





It is anyway described in a detailed manner later in this section. Before restarting the loop for next time step evaluation, the code checks if it is time to write the partial results into the subroutine HOMEDEPO as well if it is time to write in a more extended form those results on the screen for viewing by the operator. The flow chart of the MAIN is described above.

## **A2) Subroutine MOTION**

This subroutine is very important because contains all the hydrodynamics of the system and calls several other subroutines to solve single parts of the problem. At the beginning it calculates the magnetic field diffusion coefficient in each cell of the domain:

$$diff = \frac{diff - 0}{T \sqrt{T}}$$

The values are inversely proportional to the local temperature T.

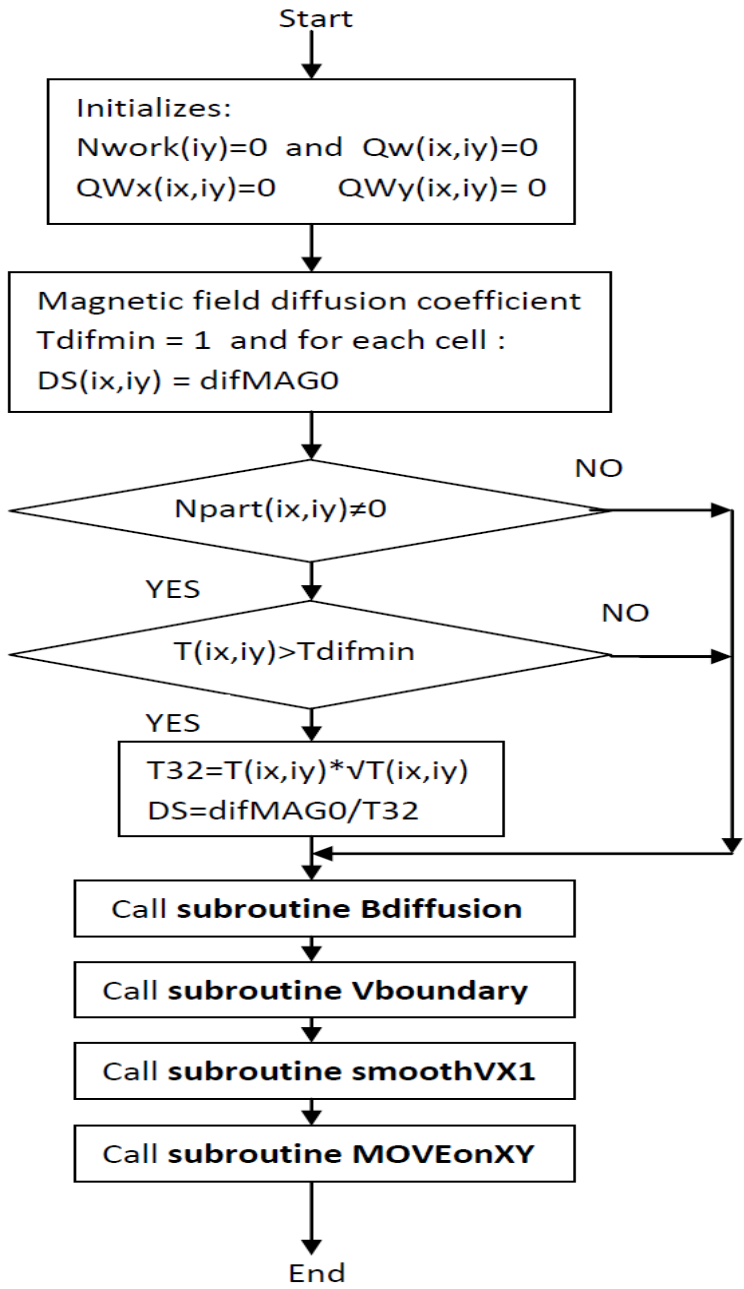
Then in sequence calls the subroutine BDIFFUSION , VBOUNDARY and MOVEonXY.

Into the first subroutine the magnetic field and pressure are calculated in each single cell.

In the VBOUNDARY subroutine, the velocity of the cloud upper front is calculated using the Godunov's limitation into the rarefacting wave. The Eulerian step of the PIC technique is also developed in this subroutine. Finally in the subroutine MOVEonXY (explained in detail in the following section) , the motion of the particles in the mesh is calculated and the Lagrangian step completed.



## FLOW CHART SUBROUTINE MOTION



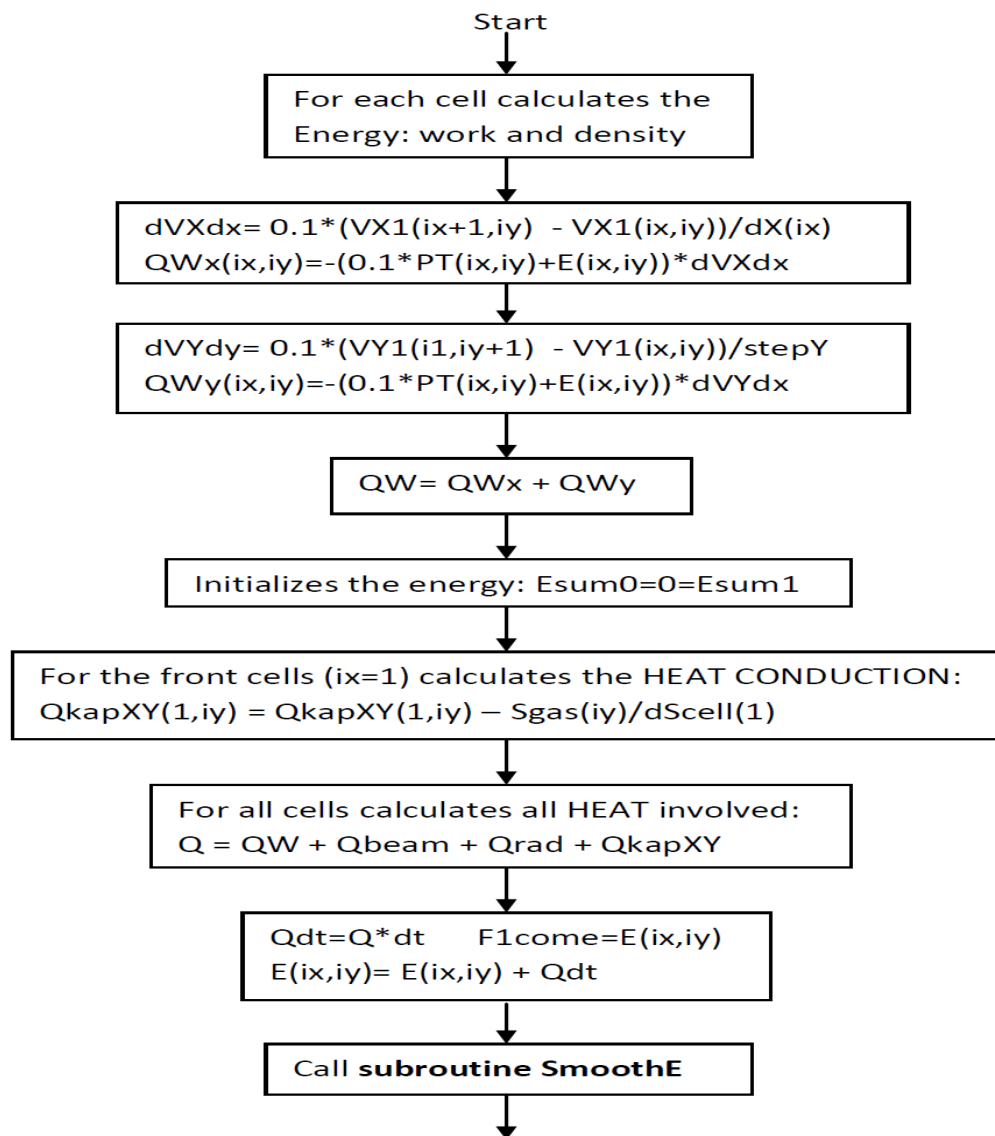
### A3) Subroutine MOVEonXY

This subroutine calculates for each single cell the energy exchanged and contained. The value can be evaluated through:

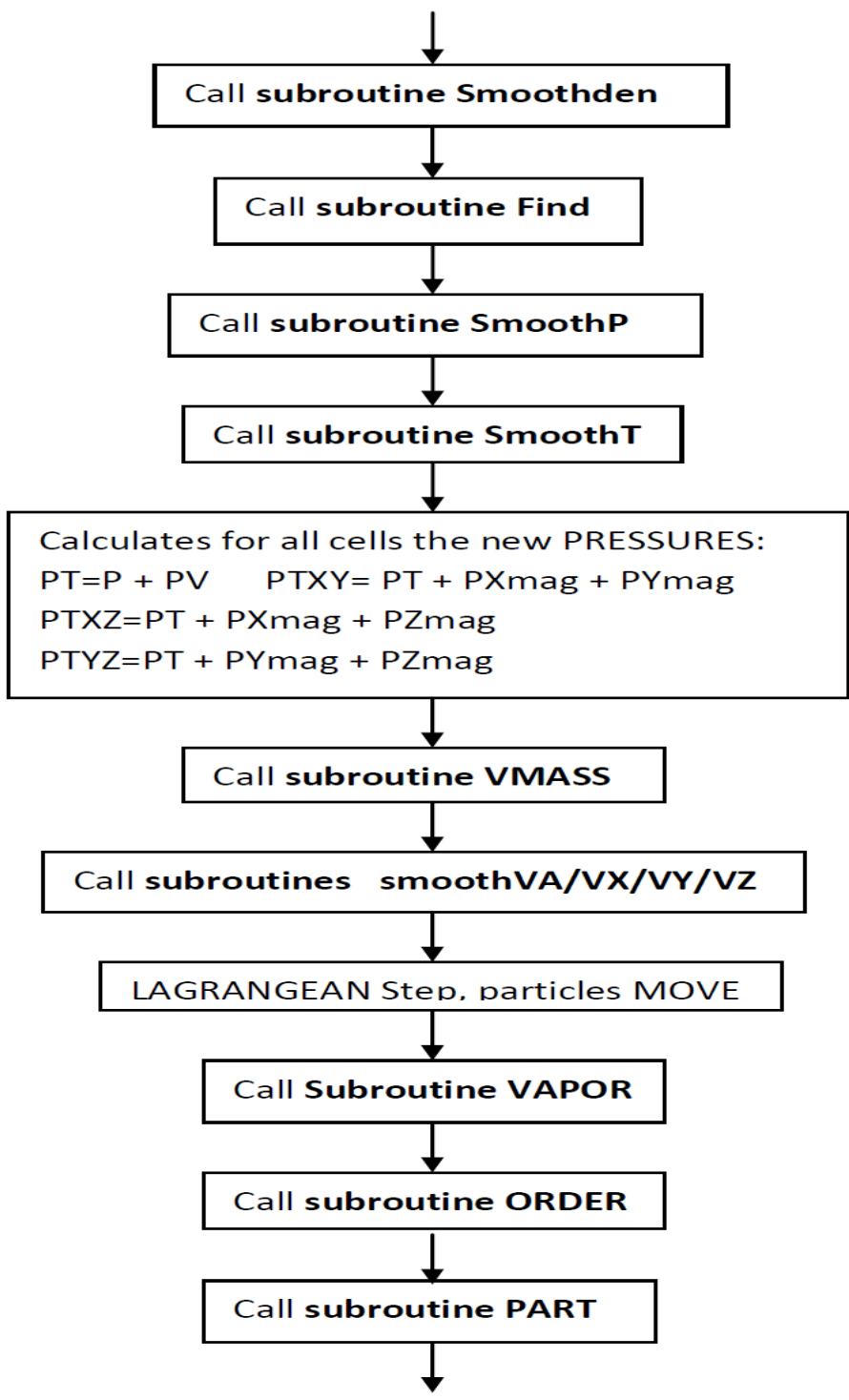
$$Q_{TOT} = Q_{BEAM} + Q_{RADIATION} + Q_{WORK \text{ performed on the FLUID}} + Q_{CONDUCTION}$$

Then the value of both the energy and density are smoothed with the use of the subroutines SMOOTHE and SMOOTHDEN. The subroutine FIND is called to search iteratively for each cell for the new value of the temperature which can be calculated knowing the energy of the entire cell. Also the values of the temperature T and the pressure P are smoothed using the subroutines SMOOTHT and SMOOTHP.

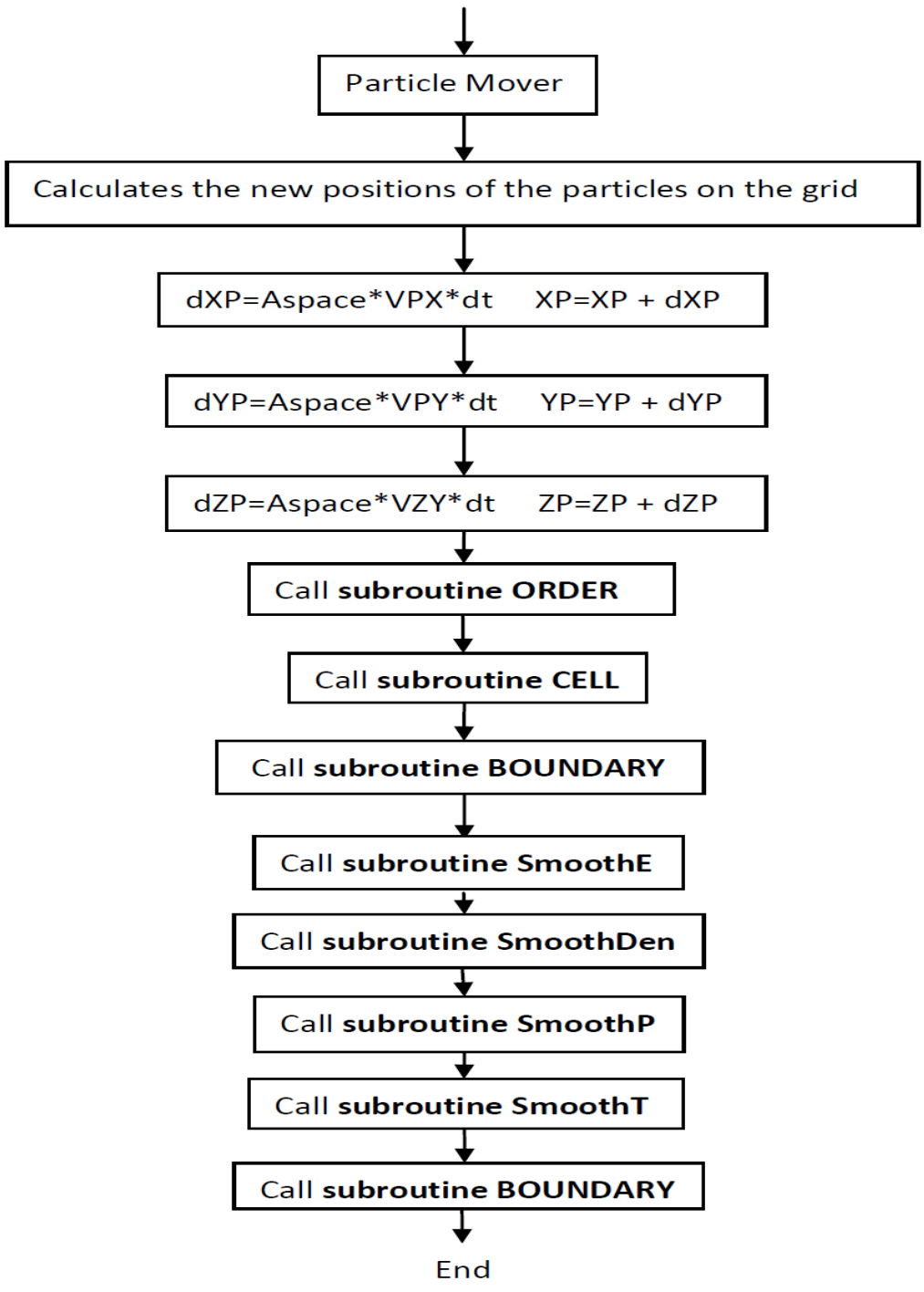
### FLOW CHART SUBROUTINE MOVEonXY



Values of the pressure inside each cell are then re-calculated a summation of the magnetic pressure along the X and Y axis and the vapor pressure.



Just before starting the Lagrangian step, the subroutine VMASS is called: it provides information about the velocities associated with the inner cells  $V_x, V_y, V_z$  calculating also the thermal and magnetic pressure.



In the Lagrangian step, the particles move once they are eventually produced by the subroutine VAPOR. In this subroutine at the same time the heat conduction equation is solved implicitly providing also information about the target temperature and the values of the fluxes incoming and out-coming from the surface itself. The subroutines ORDER and PART are called just after. The first one evaluates the position of the particles front (along X and Y) with respect to the position in the mesh and for those that remained in the same cell, upgrades, if necessary, the number of particles present in the cells. Subroutine PART instead, calculates the new particle parameters on the old net cells. In this case the new velocities associated with the cells are calculated as well as the new values of the fluxes.

Then the subroutine CELL is called: it evaluates the new mesh values after the particles move on the new net. Values of the velocities, fluxes, masses, magnetic forces, B field and energy for each cell are recalculated. Finally before calling the smoothing subroutines, the subroutine BOUNDARY is called to evaluate the same properties for the ghost points along the boundaries.

#### A4) Subroutine VAPOR

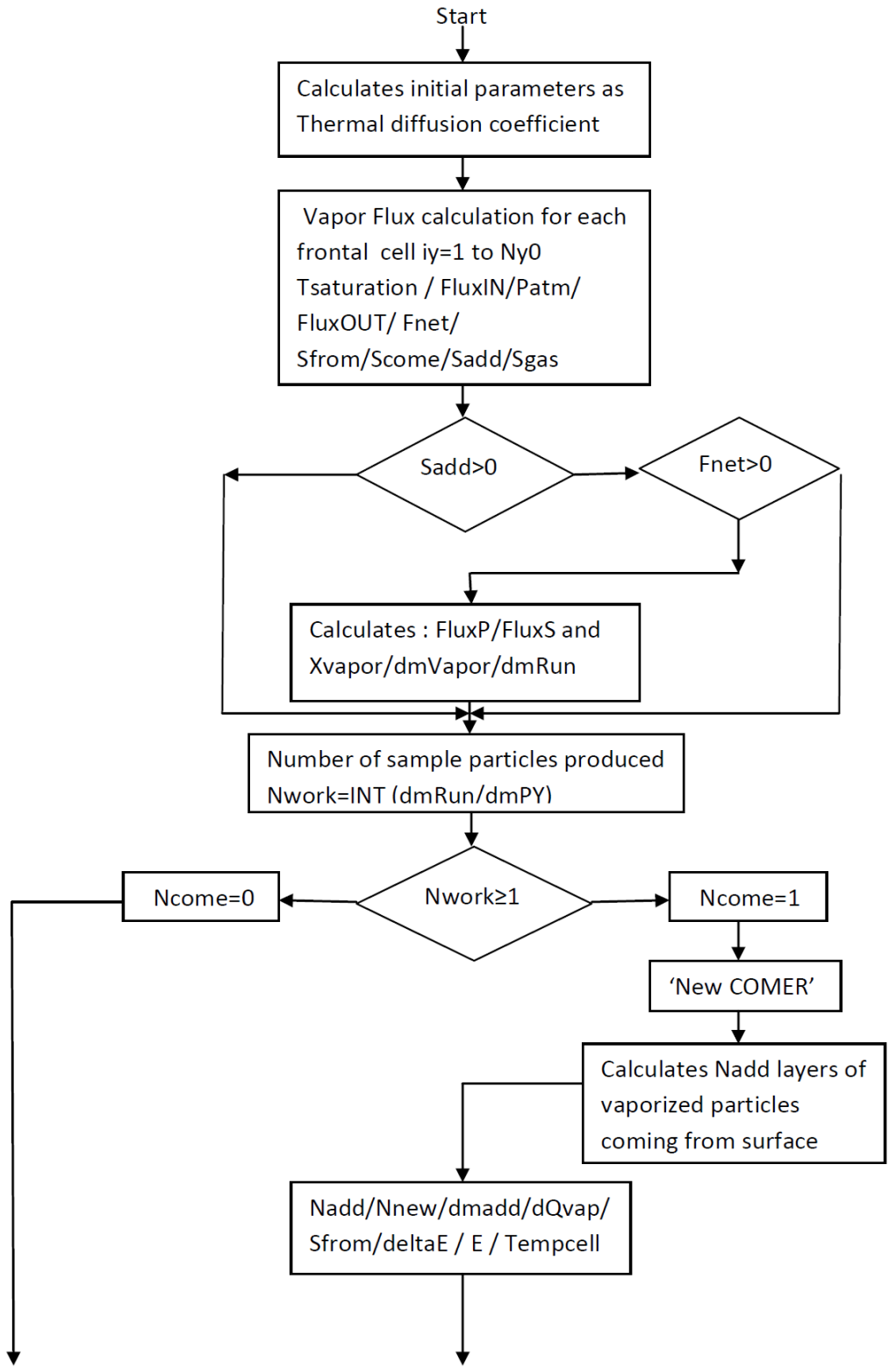
This subroutine is a very important one. The vapor flux is calculated using the model explained in a previous section. Once the incoming flux and outgoing flux are calculated, it is possible to calculate the net flux, as well as how energy is effectively reaching the surface.

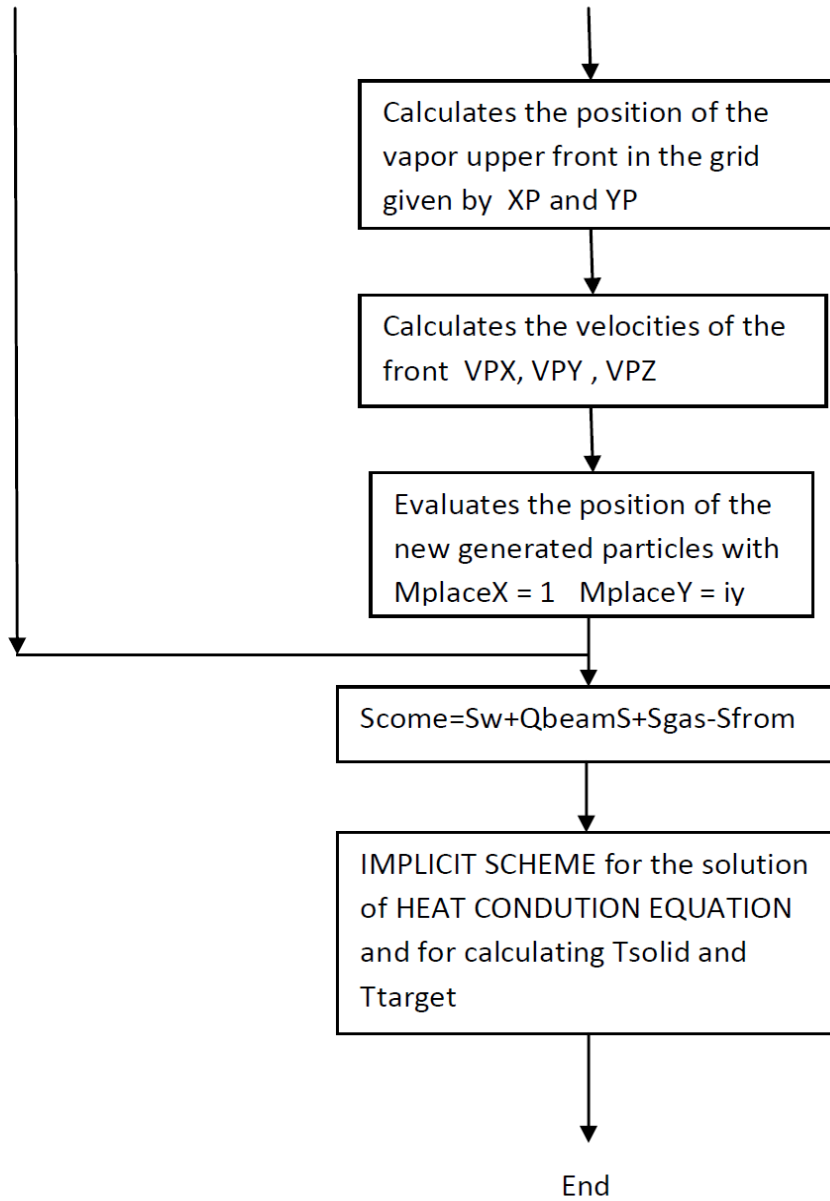
$$\begin{aligned}
 P_{atm} &= 10^{\left(\frac{T_{FLUX}}{T_{TARGET}} + T_{COEFF}\right)} \\
 Flux_{OUT} &= 10^{-6} \cdot c_{VAP} \cdot P_{atm} \cdot \sqrt{T_{TARGET}} \\
 P_{COEF} &= \log_{10}(P) \\
 T_{SATUR} &= \frac{T_{FLUX}}{(T_{COEFF} - \log_{10}(P))} \\
 Flux_{IN} &= 10^{-6} \cdot c_{VAP} \cdot P / \sqrt{T_{SATUR}} \\
 F_{net} &= Flux_{OUT} - Flux_{IN} \\
 S_{GAS} &= \frac{1}{4} \cdot Flux_{IN} \cdot c_A \cdot (T - T_{TARGET}) \\
 S_{FROM} &= Flux_{OUT} \cdot Q_{VAP} \cdot c_A (T_{SOLID}) \\
 S_{12} &= K \cdot \Delta T \\
 S_{COME} &= S_{RADIATION} + S_{BEAM} + S_{GAS} - S_{FROM} \\
 S_{ADD} &= S_{COME} - S_{12}
 \end{aligned}$$

This is done taking into account also the contribution from the gas above the surface, the plasma cloud and the beam. In this contest the new added erosion thickness can be calculated as mass of material lost by the target surface.

$$\begin{aligned}
 F_P &= F_{NET} \cdot dt \\
 X_{THICKNESS} &= F_P / \text{density} \\
 dm_{VAPOR} &= F_P \cdot \text{platesize} / N_{Y\text{ CELLS}}
 \end{aligned}$$

### FLOW CHART SUBROUTINE VAPOR





If the mass produced is enough in this time step to produce with the previous “cumulated” a new sample particle, then this is added to the system according to the location of generation along the divertor plate.

$$N_{ADD} = dm_{VAPOR} / dm_{MASS\ OF\ 1\ LINE\ IN\ 1\ CELL}$$

$$dm_{ADD} = N_{ADD} \cdot dm_{MASS\ OF\ 1\ LINE\ IN\ 1\ CELL}$$

$$dQ_{VAPOR} = (Q_{VAPOR} + c_A T_{TARGET}) \cdot dm_{ADD}$$



The corresponding energy is also added to the cell and the particle added to the layers of particles eventually already “sitting” in layers on top of the material. The position along the grid (X and Y) of the new particle is recorded as well as the velocities associated. In the end, the implicit method is used to calculate the new temperature of the solid material at the new surface and inside the material itself for a depth corresponding up to 100 sample particles.

#### **A5) Subroutine BDIFFUSION**

In the subroutine BDIFFUSION, the magnetic field and pressure are calculated for the entire mesh. Initially the dt used for the increment of time is checked versus the Courant condition. In case the dt of time produced by the Courant condition is less than the used dt for the calculation than this becomes the dt to be used:

$$dt_{PROBE} = Courant \cdot dX^2 / diff$$

The diffusion coefficients are evaluated as an average between bordering cells. Four coefficients are calculated according to the direction of the axis (X or Y) and if the mean is evaluated backwards or forwards. In this way the solution for the diffusion coefficient is smoothed according to the presence or not of particles inside a cell.

$$diff_{11} = \frac{1}{2} (diff_{ix,iy} + diff_{ix,iy-1})$$

$$diff_{12} = \frac{1}{2} (diff_{ix,iy} + diff_{ix+1,iy})$$

$$diff_{13} = \frac{1}{2} (diff_{ix,iy} + diff_{ix,iy+1})$$

$$diff_{14} = \frac{1}{2} (diff_{ix-1,iy} + diff_{ix,iy-1})$$

For calculating the values along X, Y and Z for the B field and for the diffusion across it, we need to calculate several subparts. The subroutine starts with the calculation of  $\nabla X$  ( $diff \bullet \nabla X \vec{B}$ ); in order to evaluate the partial derivatives along X, Y and Z other partial results are required: in fact all values of the B field are averaged for each cell with the neighboring cells. In this part of the subroutine BXdot, BYdot and BZdot are calculated as follows:

$$BX_{DOT\ 11} = \frac{1}{2}(BX_{ix,iy} + BX_{ix,iy-1})$$

$$BX_{DOT\ 13} = \frac{1}{2}(BX_{ix,iy} + BX_{ix,iy+1})$$

$$dB12 = BX_{ix+1,iy} - BX_{ix,iy}$$

$$dB14 = BX_{ix,iy} - BX_{ix-1,iy}$$

$$BX_{DOT\ 12} = BX_{ix,iy} + dB12 \bullet dX_{ix} / (dX_{ix+1} + dX_{ix})$$

$$BX_{DOT\ 14} = BX_{ix-1,iy} + dB14 \bullet dX_{ix-1} / (dX_{ix} + dX_{ix-1})$$

$$dBR2 = BX_{ix+1,iy+1} - BX_{ix,iy+1} = \Delta(BX_{FORWARD\ X})$$

$$dBR1 = BX_{ix,iy+1} - BX_{ix-1,iy+1} = \Delta(BX_{BACKWARD\ X})$$

$$BX_{DOT\ 12R2} = BX_{ix,iy+1} + dBR2 \bullet dX_{ix} / (dX_{ix+1} + dX_{ix})$$

$$BX_{DOT\ 14R1} = BX_{ix-1,iy+1} + dBR1 \bullet dX_{ix-1} / (dX_{ix} + dX_{ix-1})$$

In an analogous way we can calculate:

$$dBL2 = BX_{ix+1,iy-1} - BX_{ix,iy-1} = \Delta(BX_{FORWARD\ X})$$

$$dBL1 = BX_{ix,iy-1} - BX_{ix-1,iy-1} = \Delta(BX_{BACKWARD\ X})$$

$$BX_{DOT\ L2} = BX_{ix,iy-1} + dBL2 \bullet dX_{ix} / (dX_{ix+1} + dX_{ix})$$

$$BX_{DOT\ L1} = BX_{ix-1,iy-1} + dBL1 \bullet dX_{ix-1} / (dX_{ix} + dX_{ix-1})$$

Finally the intermediate results can be put together:

$$\begin{aligned}
BX_{DOT1} &= \frac{1}{2}(BX_{DOT L1} + BX_{DOT14}) \\
BX_{DOT2} &= \frac{1}{2}(BX_{DOT L2} + BX_{DOT12}) \\
BX_{DOT3} &= \frac{1}{2}(BX_{DOT R1} + BX_{DOT14}) \\
BX_{DOT4} &= \frac{1}{2}(BX_{DOT R2} + BX_{DOT12})
\end{aligned}$$

These partial results will be used later to calculate the values of the partial derivatives.

Also, along Y and Z axis the formulation of the partial results is the same. At his point, it

is possible to calculate the values of the partial differentials as  $BX_{XX}$ ,  $BX_{XY}$ ,  $BX_{YY}$  and

similarly for  $BY_{XX}$ ,  $BY_{XY}$ ,  $BY_{YY}$ :

$$\begin{aligned}
u2 &= diff_{12} \bullet (BX_{ix+1,iy} - BX_{ix,iy}) \bullet 2 / (dX_{ix} + dX_{ix+1}) = \left( D_{DIFF X} \frac{\Delta B_X}{\Delta X} \right)_{FORWARD} \\
u1 &= diff_{14} \bullet (BX_{ix,iy} - BX_{ix-1,iy}) \bullet 2 / (dX_{ix} + dX_{ix-1}) = \left( D_{DIFF X} \frac{\Delta B_X}{\Delta X} \right)_{BACKWARD} \\
BX_{XX} &= \frac{u2 - u1}{dX_{ix}} = \left( D_{DIFF X} \frac{\Delta B_X}{\Delta X} \right)_{FORWARD} - \left( D_{DIFF X} \frac{\Delta B_X}{\Delta X} \right)_{BACKWARD}
\end{aligned}$$

Note that the following expressions use some of the intermediate results:

$$\begin{aligned}
u2 &= diff_{13} \bullet (BX_{DOT3} - BX_{DOT4}) / (Platesize \bullet NYcells) = D_{DIFF Y} \left( \frac{\Delta BX_{DOT34}}{\Delta Y} \right) \\
u1 &= diff_{11} \bullet (BX_{DOT2} - BX_{DOT1}) / (Platesize \bullet NYcells) = D_{DIFF Y} \left( \frac{\Delta BX_{DOT21}}{\Delta Y} \right) \\
BX_{XY} &= \frac{u2 - u1}{dX_{ix}} = D_{DIFF Y} \left( \frac{\Delta BX_{DOT34}}{\Delta Y} \right) - D_{DIFF Y} \left( \frac{\Delta BX_{DOT21}}{\Delta Y} \right) \\
u2 &= diff_{13} \bullet (BX_{ix,iy+1} - BX_{ix,iy}) / (Platesize \bullet NYcells) = \left( D_{DIFF Y} \frac{\Delta B_X}{\Delta Y} \right)_{FORWARD} \\
u1 &= diff_{11} \bullet (BX_{ix,iy} - BX_{ix,iy-1}) / (Platesize \bullet NYcells) = \left( D_{DIFF Y} \frac{\Delta B_X}{\Delta Y} \right)_{BACKWARD} \\
BX_{YY} &= \frac{u2 - u1}{(Platesize \bullet NYcells)} = \left( D_{DIFF Y} \frac{\Delta B_X}{\Delta Y} \right)_{FORWARD} - \left( D_{DIFF Y} \frac{\Delta B_X}{\Delta Y} \right)_{BACKWARD}
\end{aligned}$$

$$u2 = \text{diff}_{12} \bullet (BY_{ix+1,iy} - BY_{ix,iy}) \bullet 2 / (dX_{ix} + dX_{ix+1}) = \left( D_{DIFF X} \frac{\Delta B_Y}{\Delta X} \right)_{FORWARD}$$

$$u1 = \text{diff}_{14} \bullet (BY_{ix,iy} - BY_{ix,iy-1}) \bullet 2 / (dX_{ix} + dX_{ix+1}) = \left( D_{DIFF X} \frac{\Delta B_Y}{\Delta X} \right)_{BACKWARD}$$

$$BY_{XX} = \frac{u2 - u1}{dX_{ix}} = \left( D_{DIFF X} \frac{\Delta B_Y}{\Delta X} \right)_{FORWARD} - \left( D_{DIFF X} \frac{\Delta B_Y}{\Delta X} \right)_{BACKWARD}$$

$$u2 = \text{diff}_{13} \bullet (BY_{DOT3} - BY_{DOT4}) / (dX_{ix}) = D_{DIFFY} \left( \frac{\Delta BY_{DOT34}}{\Delta X} \right)$$

$$u1 = \text{diff}_{11} \bullet (BY_{DOT3} - BY_{DOT4}) / (dX_{ix}) = D_{DIFFY} \left( \frac{\Delta BY_{DOT34}}{\Delta X} \right)$$

$$BY_{XY} = \frac{u2 - u1}{(Platesize \bullet NYcells)} = D_{DIFFY FORWARD} \left( \frac{\Delta BY_{DOT34}}{\Delta X} \right) +$$

$$- D_{DIFFY BACKWARD} \left( \frac{\Delta BY_{DOT34}}{\Delta X} \right)$$

$$u2 = \text{diff}_{13} \bullet (BY_{ix,iy+1} - BY_{ix,iy}) / (Platesize \bullet NYcells) = \left( D_{DIFF Y} \frac{\Delta B_Y}{\Delta Y} \right)_{FORWARD}$$

$$u1 = \text{diff}_{11} \bullet (BY_{ix,iy-1} - BY_{ix,iy}) / (Platesize \bullet NYcells) = \left( D_{DIFF Y} \frac{\Delta B_Y}{\Delta Y} \right)_{BACKWARD}$$

$$BY_{YY} = \frac{u2 - u1}{(Platesize \bullet NYcells)} = \left( D_{DIFF Y} \frac{\Delta B_Y}{\Delta Y} \right)_{FORWARD} - \left( D_{DIFF Y} \frac{\Delta B_Y}{\Delta Y} \right)_{BACKWARD}$$

At this point it is possible to calculate the value of dB or increment of the B field due to the magnetic diffusion and then evaluate the new value of the B field along the axis X, Y and Z per each cell of the mesh. Before proceeding, geometrical parameters and angles need to be considered recalling also those calculated into the main program:  $\alpha$  magnetic angle (= 5° for ELM or tokamak disruption), plate angle which is the divertor plate inclination in degrees versus Ynat or the radial direction, tangens defined as the tan(plate angle). In addition we need also to recall the definition of  $\sin\theta = \sin(\text{plate angle})$ ,  $\cos\theta = \cos(\text{plate angle})$  and  $\text{tgc}\theta$  defined as  $\text{tgc}\theta = \tan(\text{plate angle})$ . Finally with the partial

results calculated before and recalling these geometrical definitions we can calculate first the increment of the B field and with it  $B_X$ ,  $B_Y$  and  $B_Z$  as follows :

$$\begin{aligned} dB_X DIFF_{XX} &= BX_{XX} \bullet \tan^2(\text{plateangle}) \\ dB_X DIFF_{XY} &= -BX_{XY} \bullet 2 \bullet \tan(\text{plateangle}) \\ dB_X DIFF_{YY} &= BX_{YY} / \cos(\text{plateangle}) \\ dB_Y DIFF_{XX} &= -BY_{YY} \bullet \tan(\text{plateangle}) \bullet (\sin(\text{plateangle}) + \cos(\text{plateangle})) \\ dB_Y DIFF_{XY} &= -BY_{YY} \bullet (1 + 2 \tan^2(\text{plateangle})) \\ dB_Y DIFF_{YY} &= BY_{YY} \bullet \tan(\text{plateangle}) / \cos(\text{plateangle}) \end{aligned}$$

So putting together all the needed elements:

$$\begin{aligned} dB_X &= dB_X DIFF_{XX} + dB_X DIFF_{XY} + dB_X DIFF_{YY} \\ dB_Y &= dB_Y DIFF_{XX} + dB_Y DIFF_{XY} + dB_Y DIFF_{YY} \\ dB &= dB_X + dB_Y \end{aligned}$$

So the values of the B field along X can be evaluated as:

$$B_X = B_X + dt_{DIFFUSION} \bullet dB$$

where  $dt_{DIFFUSION} = dt$ . Similarly for the evaluation of  $B_Y$ , it can be calculated:

$$\begin{aligned} dB_X DIFF_{XX} &= -BX_{XX} \bullet \tan(\text{plateangle}) \\ dB_X DIFF_{XY} &= BX_{XY} / \cos(\text{plateangle}) \\ dB_Y DIFF_{XX} &= BY_{XX} \bullet \cos(\text{plateangle}) \bullet (1 - \tan^2(\text{plateangle})) \\ dB_Y DIFF_{XY} &= BY_{XY} \bullet \tan(\text{plateangle}) \end{aligned}$$

Putting together all the needed elements:

$$\begin{aligned} dB_X &= dB_X DIFF_{XX} + dB_X DIFF_{XY} \\ dB_Y &= dB_Y DIFF_{XX} + dB_Y DIFF_{XY} \\ dB &= dB_X + dB_Y \end{aligned}$$

The value of the B field along the Y axis can then be evaluated as:

$$B_Y = B_Y + dt_{DIFFUSION} \bullet dB$$

For calculating the B value along the Z axis, we need to solve for  $\nabla \times \nabla \vec{B}$ : in order to do so, we need first to evaluate the partial differentials of interest:  $BZ_{XX}$ ,  $BZ_{XY}$ ,  $BZ_{YY}$  and also consider the geometry of the system:

$$u2 = diff_{12} \cdot (BZ_{ix+1,iy} - BZ_{ix,iy}) / (dX_{ix}) = \left( D_{DIFF X} \frac{\Delta B_Z}{\Delta X} \right)_{FORWARD}$$

$$u1 = diff_{14} \cdot (BZ_{ix,iy} - BZ_{ix-1,iy}) / (dX_{ix-1}) = \left( D_{DIFF X} \frac{\Delta B_Z}{\Delta X} \right)_{BACKWARD}$$

$$BZ_{XX} = \frac{u2 - u1}{dX_{ix}} = \left( D_{DIFF X} \frac{\Delta B_Z}{\Delta X} \right)_{FORWARD} - \left( D_{DIFF X} \frac{\Delta B_Z}{\Delta X} \right)_{BACKWARD}$$

Then we need in sequence the other two:

$$u2 = diff_{13} \cdot (BZ_{DOT3} - BZ_{DOT4}) / (Platesize \cdot NYcells) = D_{DIFFY} \left( \frac{\Delta BZ_{DOT34}}{\Delta Y} \right)$$

$$u1 = diff_{11} \cdot (BZ_{DOT2} - BZ_{DOT1}) / (Platesize \cdot NYcells) = D_{DIFFY} \left( \frac{\Delta BZ_{DOT21}}{\Delta Y} \right)$$

$$BX_{XY} = \frac{u2 - u1}{\Delta Y} = D_{DIFFY} \left( \frac{\Delta BZ_{DOT34}}{\Delta Y} \right) - D_{DIFFY} \left( \frac{\Delta BZ_{DOT21}}{\Delta Y} \right)$$

$$u2 = diff_{13} \cdot (BZ_{ix,iy+1} - BZ_{ix,iy}) / (Platesize \cdot NYcells) = \left( D_{DIFF Y} \frac{\Delta B_Z}{\Delta Y} \right)_{FORWARD}$$

$$u1 = diff_{11} \cdot (BZ_{ix,iy} - BZ_{ix,iy-1}) / (Platesize \cdot NYcells) = \left( D_{DIFF Y} \frac{\Delta B_Z}{\Delta Y} \right)_{BACKWARD}$$

$$BZ_{YY} = \frac{u2 - u1}{(Platesize \cdot NYcells)} = \left( D_{DIFF Y} \frac{\Delta B_Z}{\Delta Y} \right)_{FORWARD} - \left( D_{DIFF Y} \frac{\Delta B_Z}{\Delta Y} \right)_{BACKWARD}$$

Finally we can evaluate dB along the Z axis:

$$dB_Z DIFF_{XX} = BZ_{XX} \cdot (1 - \tan^2(\text{plateangle}))$$

$$dB_Z DIFF_{XY} = -BZ_{XY} \cdot 2 \cdot \tan(\text{plateangle})$$

$$dB_Z DIFF_{YY} = BZ_{YY} / (\cos^2(\text{plateangle}))$$

$$dB_Z = dB_Z DIFF_{XX} + dB_Z DIFF_{XY} + dB_Z DIFF_{YY}$$

So, B along Z can be calculated as:

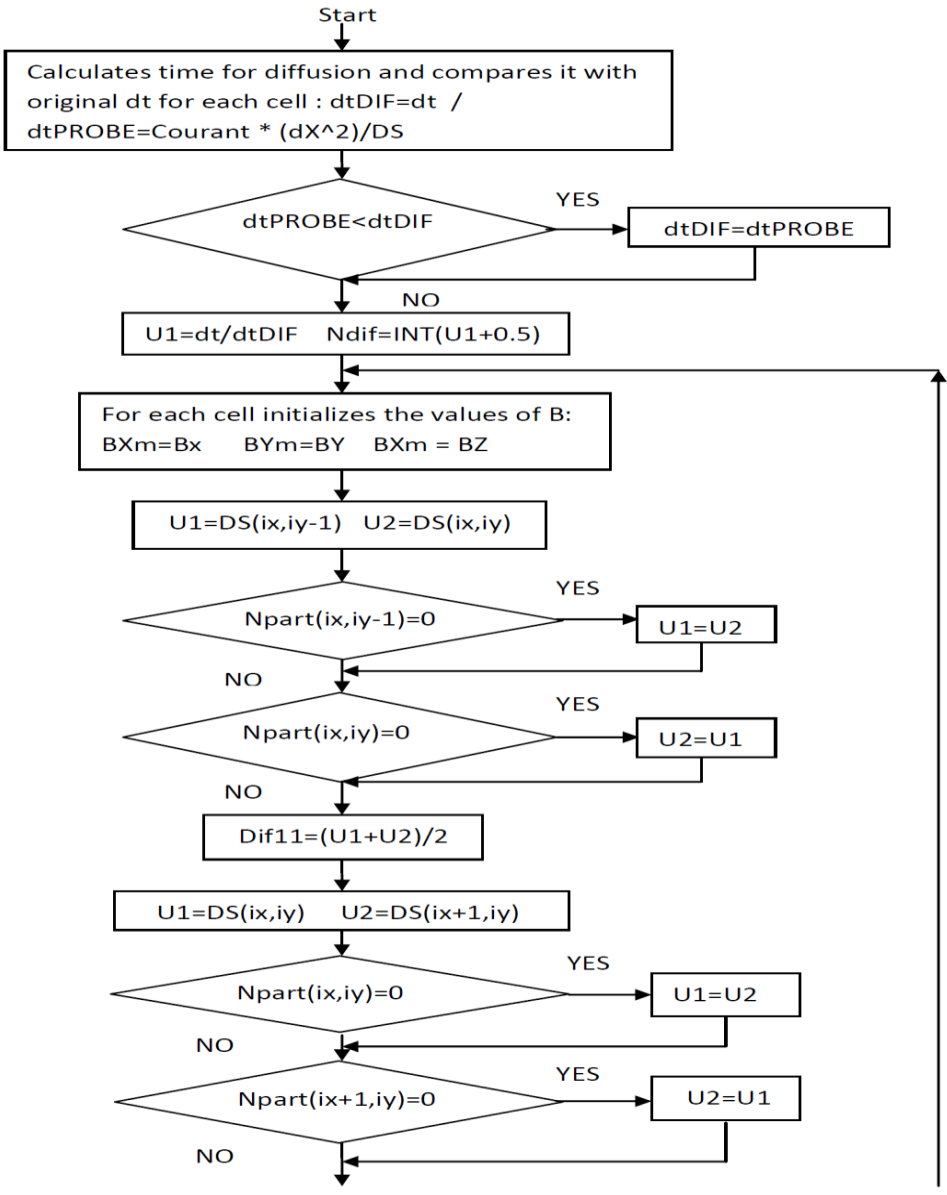
$$B_Z = B_Z + dt_{DIFFUSION} \cdot dB_Z$$

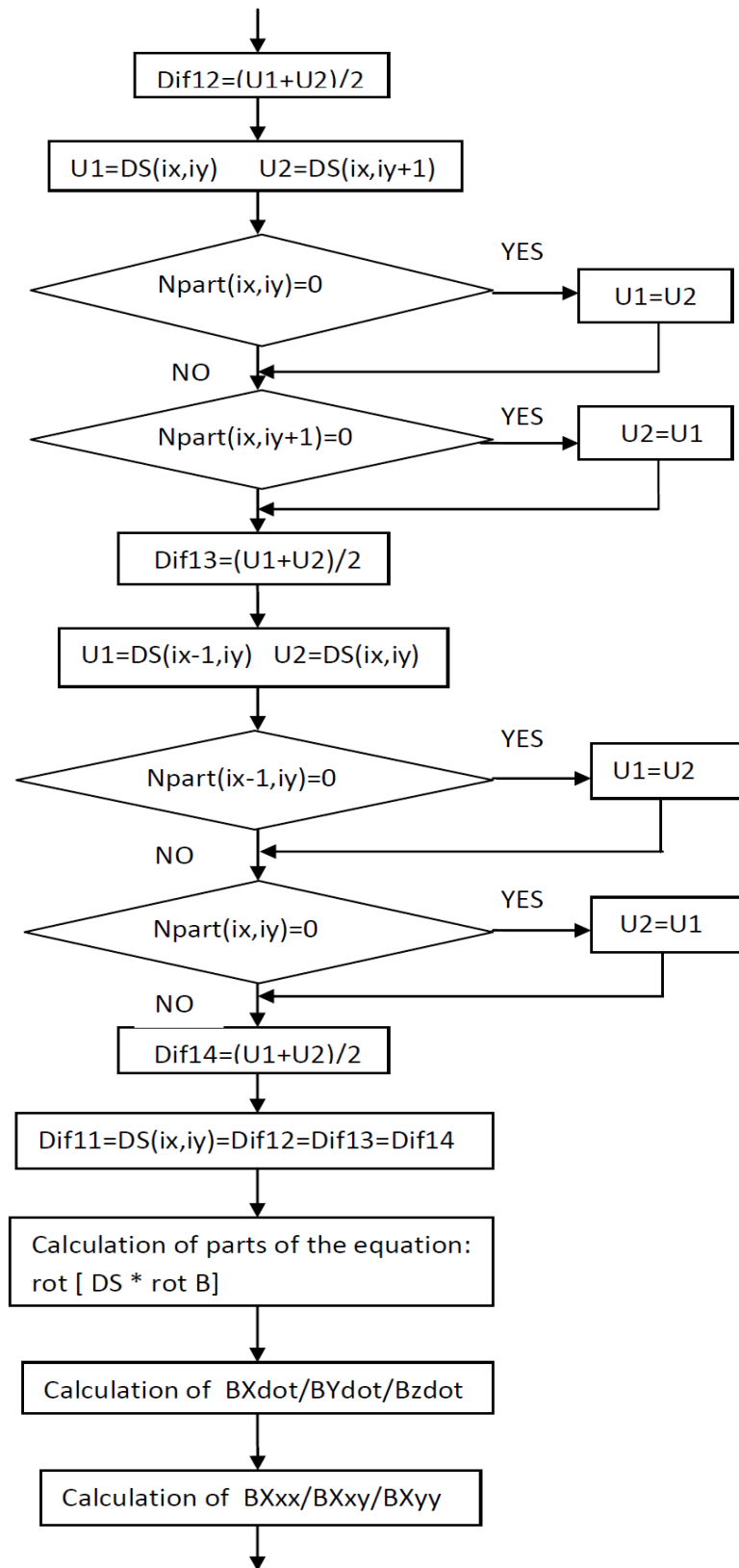
In the end, after calculating the boundary condition for the ghost point, it is possible to calculate also the magnetic force throughout the mesh for each single cell with the use of:

$$F_x\text{mag} = BX \bullet d\text{Scell} \quad ; F_y\text{mag} = BY \bullet d\text{Scell} \quad ; F_z\text{mag} = BZ \bullet d\text{Scell}$$

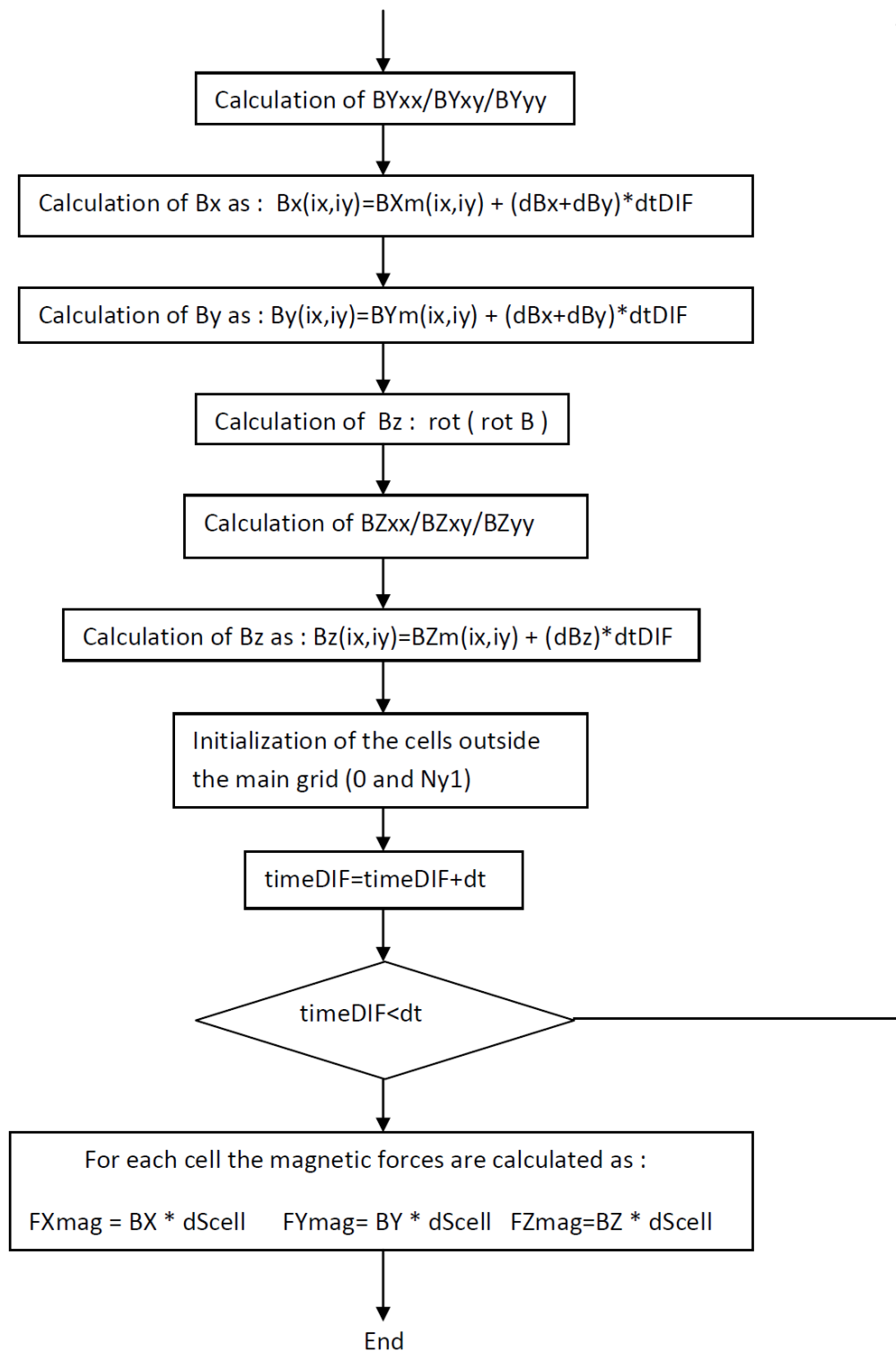
where dScell is the dimension of the cells previous calculated. The slow chart of the subroutine can be seen in the following scheme.

**FLOW CHART SUBROUTINE B DIFFUSION**









### A6) Subroutine HEATBEAM

In this subroutine the energy deposited by the plasma beam (disruption) into the vapor and onto the target surface is calculated. To do so, the velocity of the ions contained in each cell needs also to be known and calculated. The increment or decrement of the velocity of ions contained in a cell can be calculated as the ration between the two quantities pathION and path so defined:

$$pathION = \frac{dX \cdot B_x}{\sqrt{B_x^2 + B_z^2}}$$

$$path = \frac{\text{density of carbon} \cdot \text{beam ion path length for solid density}}{\text{density of cell}}$$

$$dV_{ION} = \frac{pathION}{path}$$

Using these definitions, it is easy to calculate the value of the velocity of the ions per each cell:

$$\Delta V_{ION X} = (1 - dV_{ION})$$

If the new velocity is calculated with a negative value, than it is posed equal to zero. The energy deposited by the beam is calculated proportional to the quadratic value of the ions average velocity according to:

$$Q_{RELATIVE} = (V_{ION EXTERNAL BOUNDARY}^2 - V_{ION}^2) \cdot S_{BEAM Y} \cdot time_{BEAM}$$

where Sbeam0 is the incoming power from the beam. Calculating Q of the beam per each cell as:

$$Q_{BEAM} = \frac{Q_{RELATIVE}}{dS_{CELL}}$$

it is also possible to evaluate the value of the pressure of the beam due to the pressure of the particles in it as:

$$P_{BEAM} = (V_{ION}^{EXTERNAL\ BOUNDARY} - V_{ION}^2) \cdot S_{BEAM\ Y} \cdot time_{BEAM} \cdot P_{BEAM\ 0} / \cos(\text{plate angle})$$

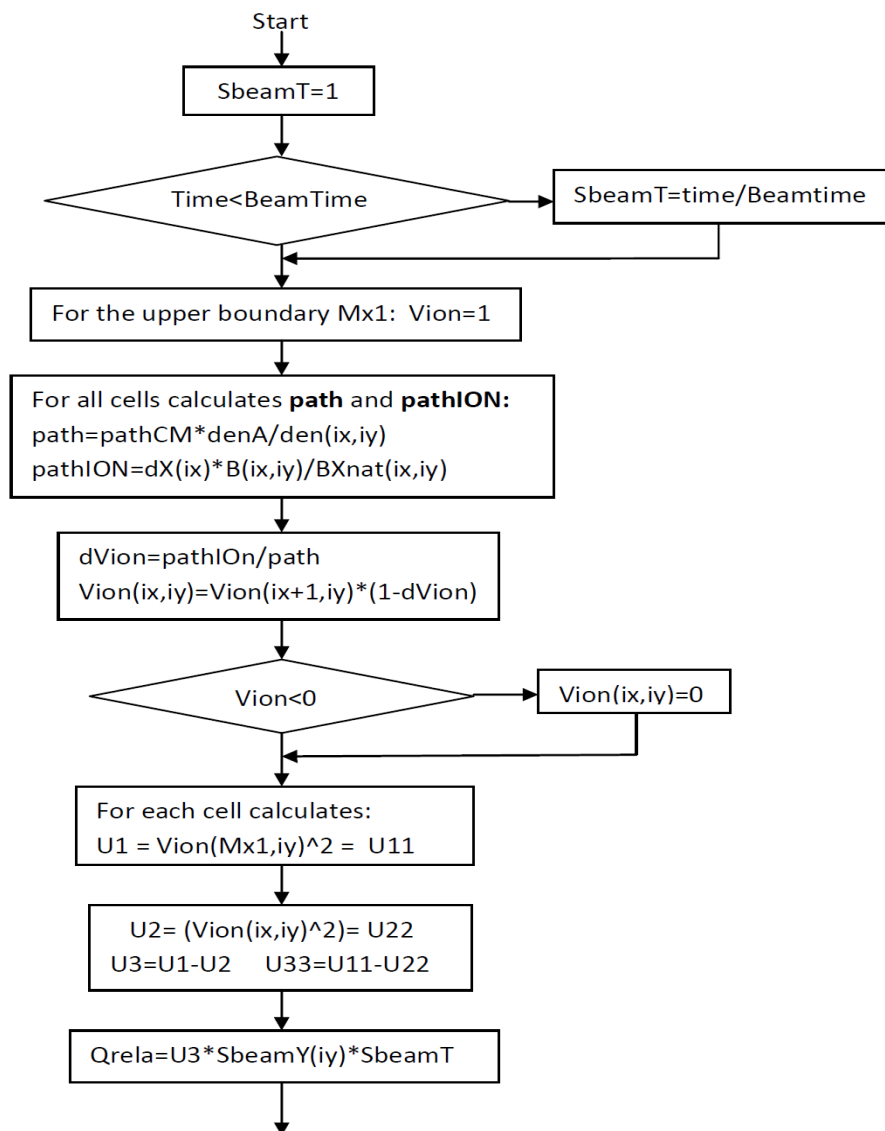
In the end in order to calculate the energy deposited by the beam in each cell of the mesh,

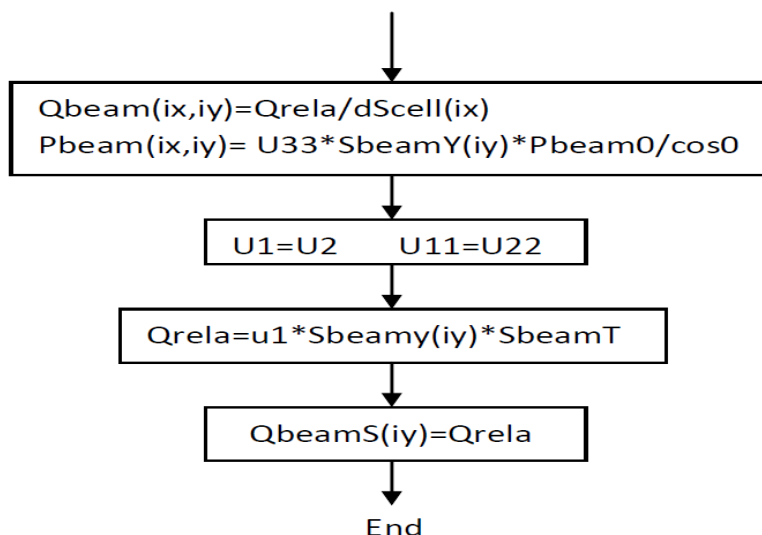
QbeamS is calculated as follows:

$$Q_{BEAM\ S} = (V_{ION})^2 \cdot S_{BEAM\ Y} \cdot time_{BEAM}$$

The flow chart of the subroutine is described here.

### FLOW CHART SUBROUTINE HEATBEAM





At each time step QbeamS is used into the subroutine VAPOR for calculating the energy balance of the facing cells just above the divertor plate and by the subroutine MOTION in order to calculate the energy present in each cell at the end of each time step.

#### A7) Subroutine HEATCOND

In this equation the heat conduction equation into the plasma vapor cloud is solved for each single cell so that the values of the heat and flux are known. For this purpose the values of the density, temperature and atomic number  $Z$  need to be known for each cell.

The main equation to be solved assumed the form in 1D:

$$\frac{dE}{dt} = \frac{\partial}{\partial t} k(T) \frac{\partial T}{\partial l}$$

Before calculating the contribution from the electron and ion conduction, the subroutine evaluates the status of the ionization inside the charge. If this value is less than 0.1, there is no need for calculation the ions and electron contribution. The heat present into the cell then is calculated as follows:

$$Q_{CONDUCTION} = (V_{THERM}) \cdot \sqrt{T_{VAP}} \cdot \sqrt{T_{CELL}}$$

where  $V_{THERM} = \sqrt{\frac{8 kT_{VAP}}{\pi m}}$ . If instead the degree of ionization is not negligible, then

both electron conduction and ion conduction need to be calculated. Using the transport equations for simple plasma, the electron conduction can be calculated as follows:

$$\omega = \left( \frac{B \cdot \sqrt[3]{T}}{density \cdot Z^2} \right)$$

$$\omega_{ELECTRONS} = \left( \frac{B \cdot \sqrt[3]{T}}{density \cdot Z^2} \right) \cdot \omega_0_{ELECTRONS}$$

$$u2 = \omega^2_{ELECTRONS}$$

$$u4 = \omega^4_{ELECTRONS}$$

The thermal conductivities for electrons can be defined as:

$$U_{PARALLEL} = 3.19$$

$$U_{NORMAL} = \left( \frac{u4 + 0.41 \cdot u2 + 9.055}{3.604 \cdot u2 + 2.841} \right)$$

so that aggregating these partial results, the electron heat conduction can be calculated:

$$Q_{ELECTRONS \text{ PARALLEL TO } B} = U_{PARALLEL} \left( \frac{Q_{ELECTRON 0} \cdot \sqrt[5]{T}}{Z} \right)$$

$$Q_{ELECTRONS \text{ NORMAL TO } B} = U_{NORMAL} \left( \frac{Q_{ELECTRON 0} \cdot \sqrt[5]{T}}{Z} \right)$$

With  $Q_{ELECTRON 0} = 9.65$ . In a similar way we can define the main parameters for the ions:

$$\omega = \left( \frac{B \cdot \sqrt[3]{T}}{density \cdot Z^2} \right)$$

$$\omega_{IONS} = (\omega_0_{IONS} \cdot \omega) / Z$$

$$u2 = \omega^2_{IONS}$$

$$u4 = \omega^4_{IONS}$$

The ions thermal conductivities can be defined as:

$$U_{PARALLEL} = 3.91$$

$$U_{NORMAL} = \left( \frac{u^4 + 2.7 \cdot u^2 + 0.677}{2 \cdot u^2 + 2.645} \right)$$

so that aggregating these partial results, the ion heat conduction can be calculated:

$$Q_{IONS \text{ PARALLEL TO } B} = U_{PARALLEL} \left( \frac{Q_{ION 0} \cdot \sqrt[5]{T}}{Z^3} \right)$$

$$Q_{IONS \text{ NORMAL TO } B} = U_{NORMAL} \left( \frac{Q_{ION 0} \cdot \sqrt[5]{T}}{Z^3} \right)$$

with with  $Q_{ION 0} = 0.46 / \sqrt{2 \cdot A_{TARGET}}$  and  $A_{TARGET}$  the molecular weight of target material (= 12 for carbon). At this point the summation of all heat conduction parts, leads to the entire heat conduction along B and perpendicular to it:

$$Q_{PARALLEL \text{ TO } B} = Q_{IONS \text{ PARALLEL TO } B} + Q_{ELECTRONS \text{ PARALLEL TO } B}$$

$$Q_{NORMAL \text{ TO } B} = Q_{IONS \text{ NORMAL TO } B} + Q_{ELECTRONS \text{ NORMAL TO } B}$$

In order to calculate the effective values along the X and Y axis, the geometry of the system needs to be considered:

$$\sin BXZ = BX_{NAT} / B \quad \cos BXZ = \sqrt{1 - \sin^2 BXZ}$$

$$BXZ = \sqrt{BX_{NAT}^2 + BZ_{NAT}^2}$$

$$\sin BX = BX_{NAT} / B \quad \cos BX = \sqrt{1 - \sin^2 BX}$$

$$Q_X = Q_{PARALLEL \text{ TO } B} \cdot \sin BX \cdot \sin BXZ + Q_{NORMAL \text{ TO } B} \cdot \cos BX \cdot \cos BXZ$$

In an analogous manner, the value of the heat conduction along Y can be calculated:

$$\sin BYZ = BY_{NAT} / B \quad \cos BYZ = \sqrt{1 - \sin^2 BYZ}$$

$$BYZ = \sqrt{BY_{NAT}^2 + BZ_{NAT}^2}$$

$$\sin BY = BY_{NAT} / B \quad \cos BY = \sqrt{1 - \sin^2 BY}$$

$$Q_Y = Q_{PARALLEL \text{ TO } B} \cdot \sin BY \cdot \sin BYZ + Q_{NORMAL \text{ TO } B} \cdot \cos BY \cdot \cos BYZ$$

After calculating the boundary condition and the solution for the ghost points, the heat conduction fluxes can be calculated using a backwards type of formulation:

$$Q_{X \text{ AVERAGE}} = \frac{1}{2} \cdot (Q_{ix,iy} + Q_{ix-1,iy})$$

$$S_X = Q_{X \text{ AVERAGE}} \cdot \frac{(T_{ix,iy} - T_{ix-1,iy})}{(dX_{ix} + dX_{ix-1})/2}$$

The same calculation can be performed along the axis Y:

$$Q_{Y \text{ AVERAGE}} = \frac{1}{2} \cdot (Q_{ix,iy} + Q_{ix,iy-1})$$

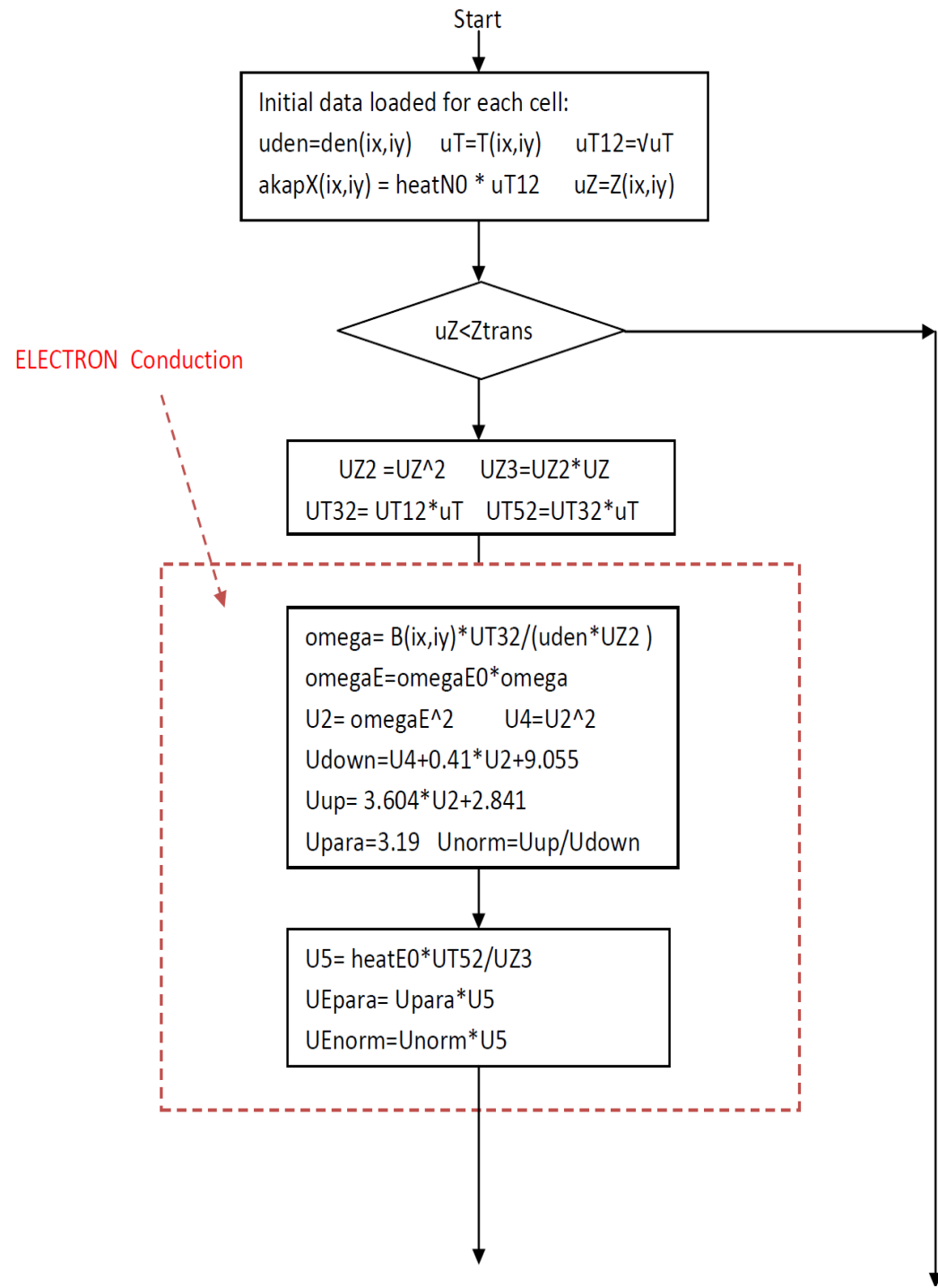
$$S_Y = Q_{Y \text{ AVERAGE}} \cdot \frac{(T_{ix,iy} - T_{ix,iy-1})}{\text{Plate size} / N_{\text{CELLS ALONG Y}}}$$

Finally also the total value as sum of the values of X and Y can be calculated for the heat of conduction:

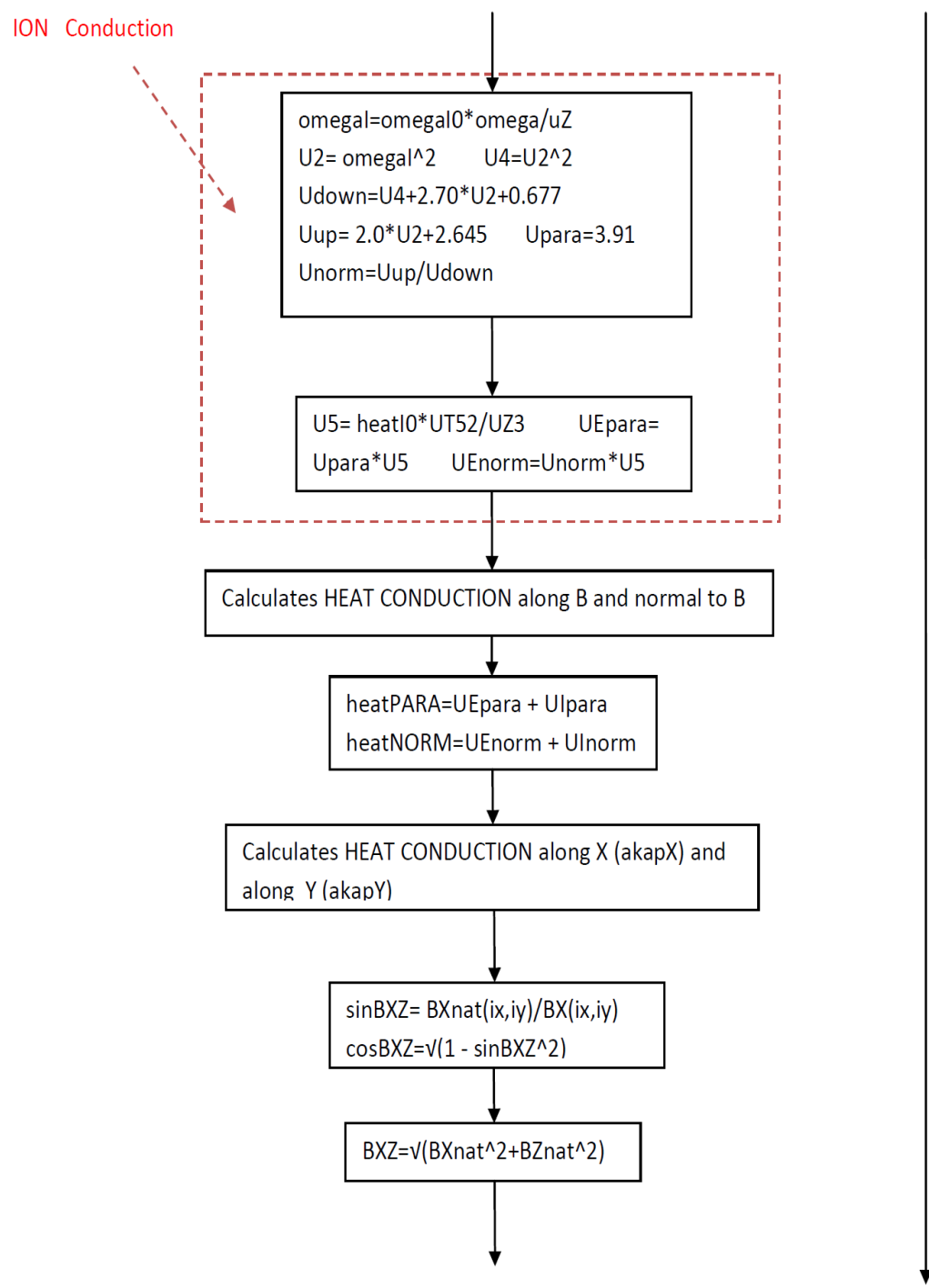
$$Q_{XY} = (Q_X + Q_Y)$$

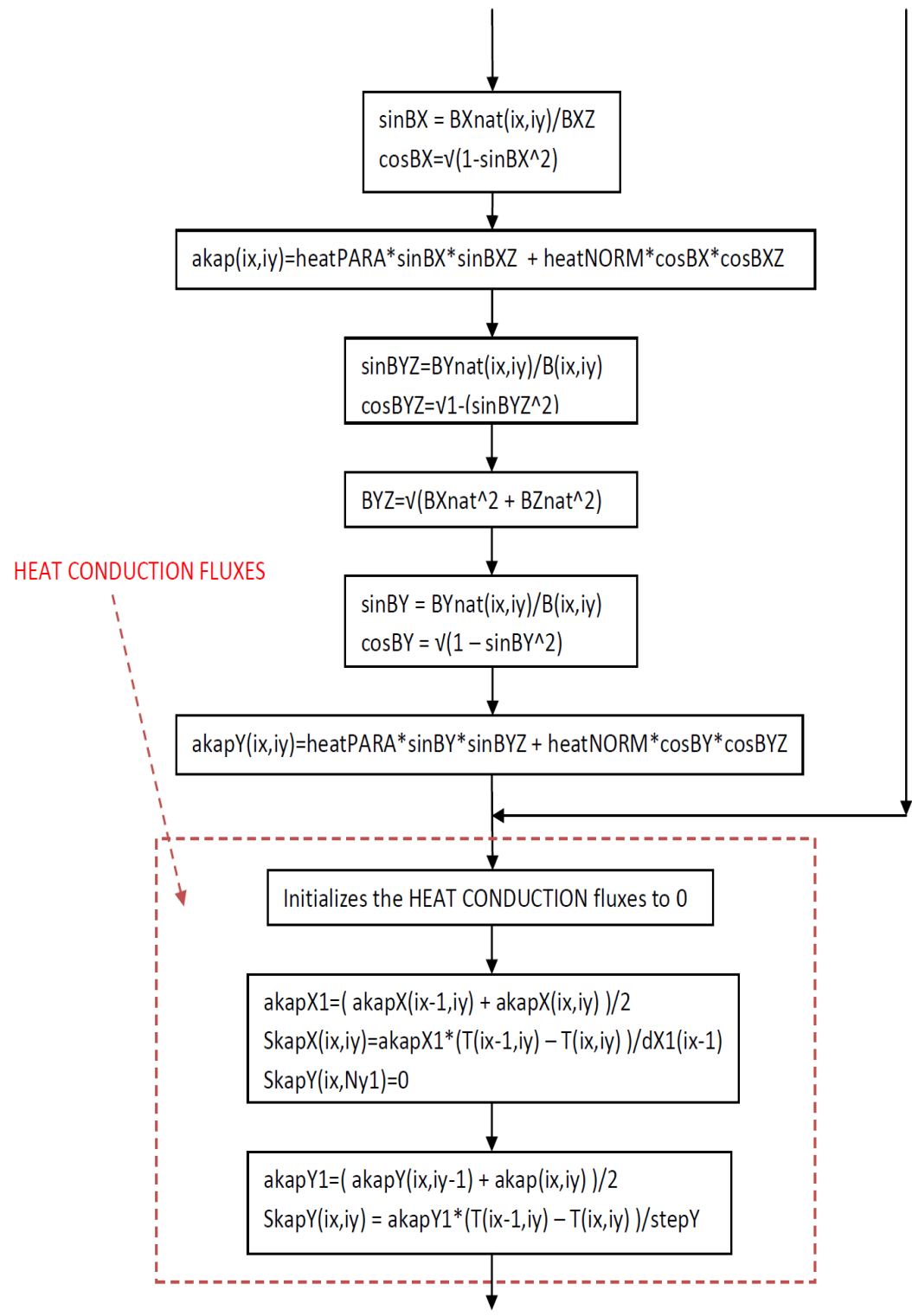
The flow chart of the subroutine is explained in the following pages.

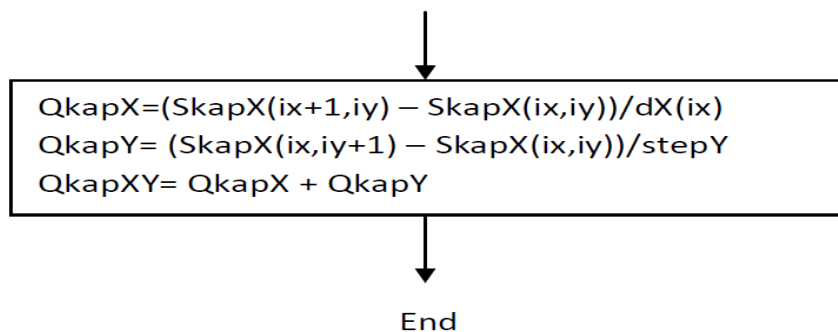
### FLOW CHART SUBROUTINE HEATCOND











### A8) Subroutine PART

This subroutine with the subroutine CELL is the heart of the hydrodynamic part. In this subroutine the new parameters regarding each single cell are calculated using though the old net or mesh. After initializing all the main parameters to be calculated to zero, for the cell of interest, the velocity  $V_{x1}$  and  $V_{y1}$  are calculated. For  $V_{x1}$  the new velocity is provided by:

$$dV_X = \frac{1}{2} \cdot (VX_{ix+1,iy} + VX_{ix-1,iy})$$

$$V_{x1} = V_X + dV_X \cdot \frac{dX_{ix}}{(dX_{ix} - dX_{ix-1})}$$

In a similar way,  $V_{y1}$  is calculated as:

$$V_{y1} = \frac{1}{2} (VY_{ix,iy} + VY_{ix,iy-1})$$

Using the information provided in the subroutine VAPOR about the position of the new vapor particle front, it is possible to calculate the updated values of the front velocity according to their position on the grid ( $ixC$  and  $iyC$ ). Then the new velocities  $VPX$ ,  $VPY$  and  $VPZ$  can be evaluated as follows:

$$dV_x = \Delta VX1 = (VX1_{ixC+1,iyC} + VX1_{ixC,iyC})$$

$$ud_x = \Delta XP / dX$$

$$dVP_x = dV_x \bullet ud_x$$

$$VP_x = VX1 + dVP_x$$

and in an analogous way , it can be calculated:

$$dV_y = \Delta VY1 = (VY1_{ixC,iyC+1} + VY1_{ixC,iyC})$$

$$ud_y = \Delta YP / dY$$

$$dVP_y = dV_y \bullet ud_y$$

$$VP_y = VY1 + dVP_y$$

For the value of V front along the Z axis (VPZ) it is easy to see that:

$$V_{PZ} = V_Z = VZ_{ixC,iyC}$$

Finally the values of the momenta along the 3 axis and the energy for each cell can be calculated. If no particles are in cell, the calculation is skipped:

$$E_p = E_{ixC,iyC} \bullet \frac{dScell}{Nparticles}$$

$$FluxX = \frac{m \bullet Vx}{Nparticles}$$

$$FluxY = \frac{m \bullet Vy}{Nparticles}$$

$$FluxZ = \frac{m \bullet Vz}{Nparticles}$$

Similarly we can calculate:

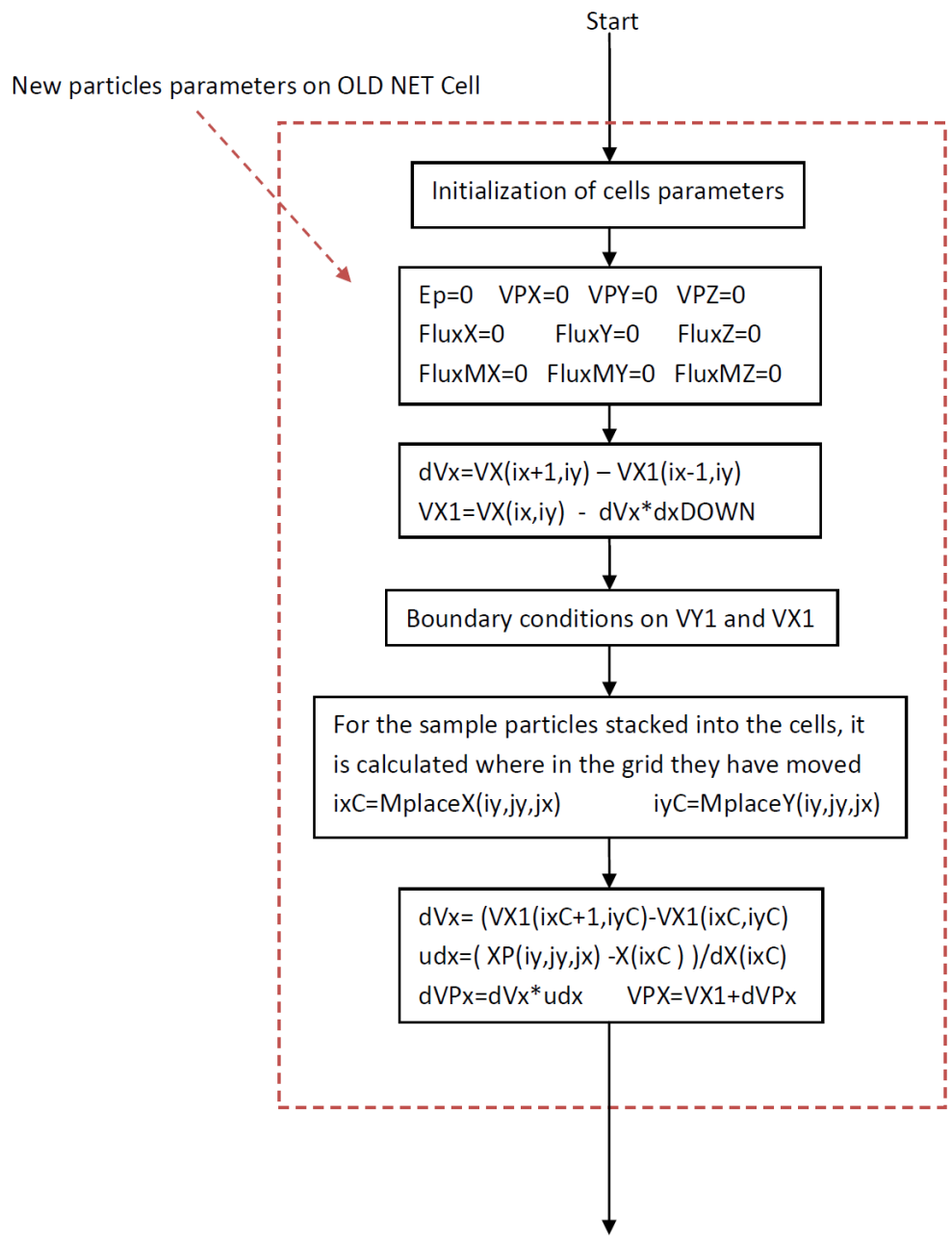
$$FluxMX = \frac{dScell \bullet Bx}{Nparticles}$$

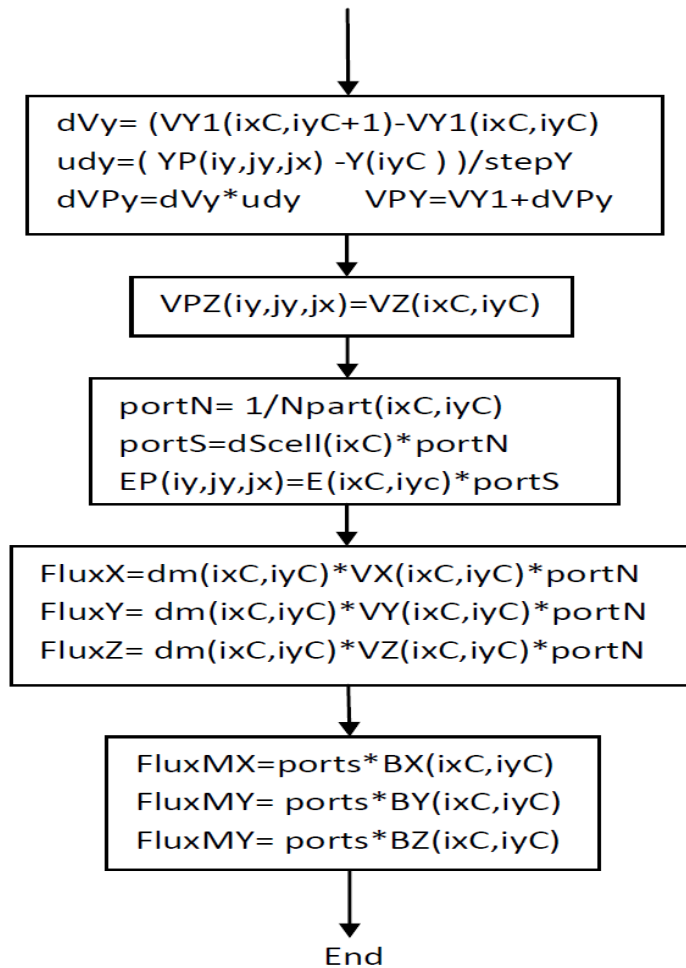
$$FluxMY = \frac{dScell \bullet By}{Nparticles}$$

$$FluxMZ = \frac{dScell \bullet Bz}{Nparticles}$$

All these values will be used later (subroutine CELL) to recalculate the magnetic forces as well as the velocities associated with the cells. The flow chart follows.

### FLOW CHART SUBROUTINE PART



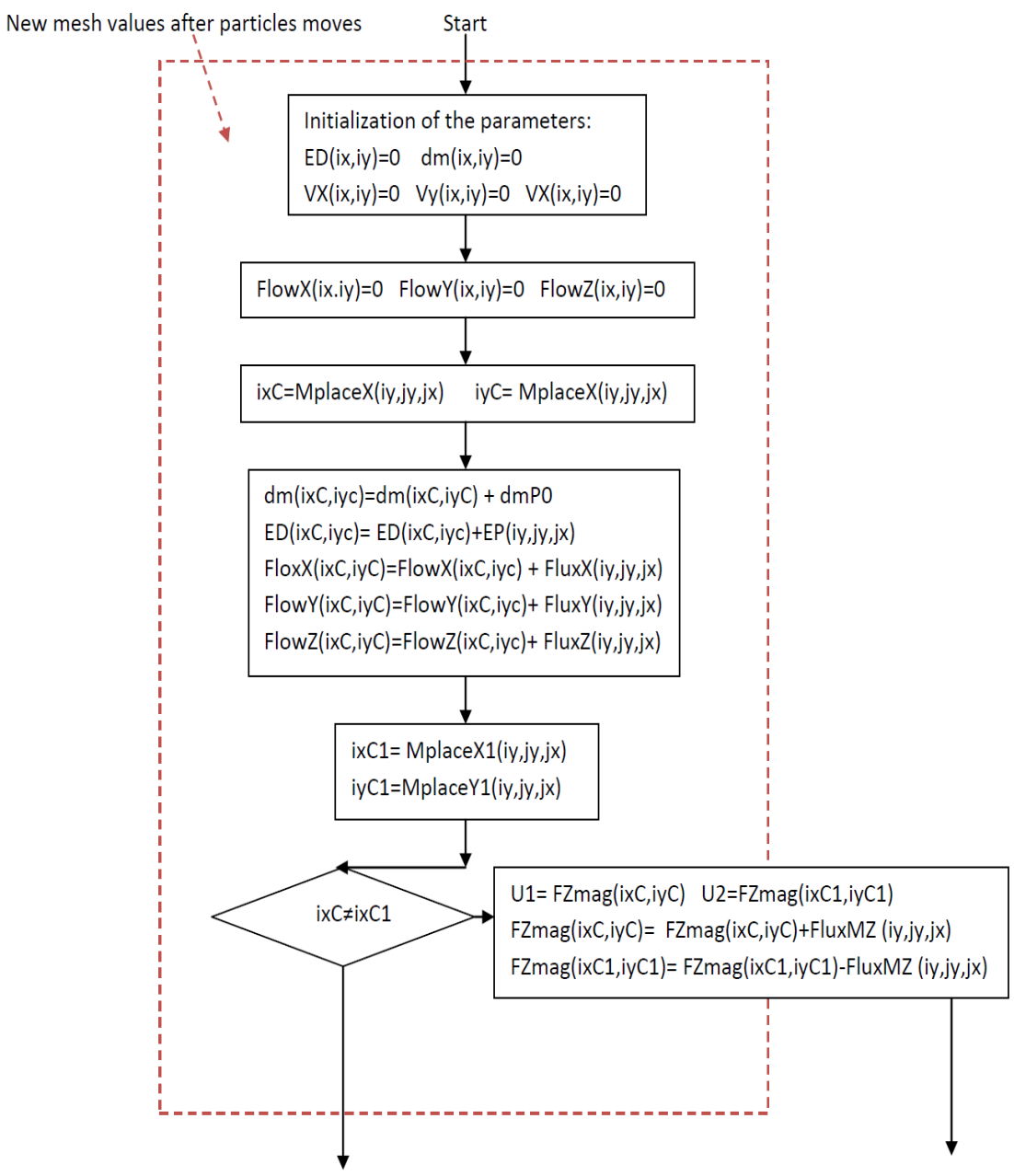


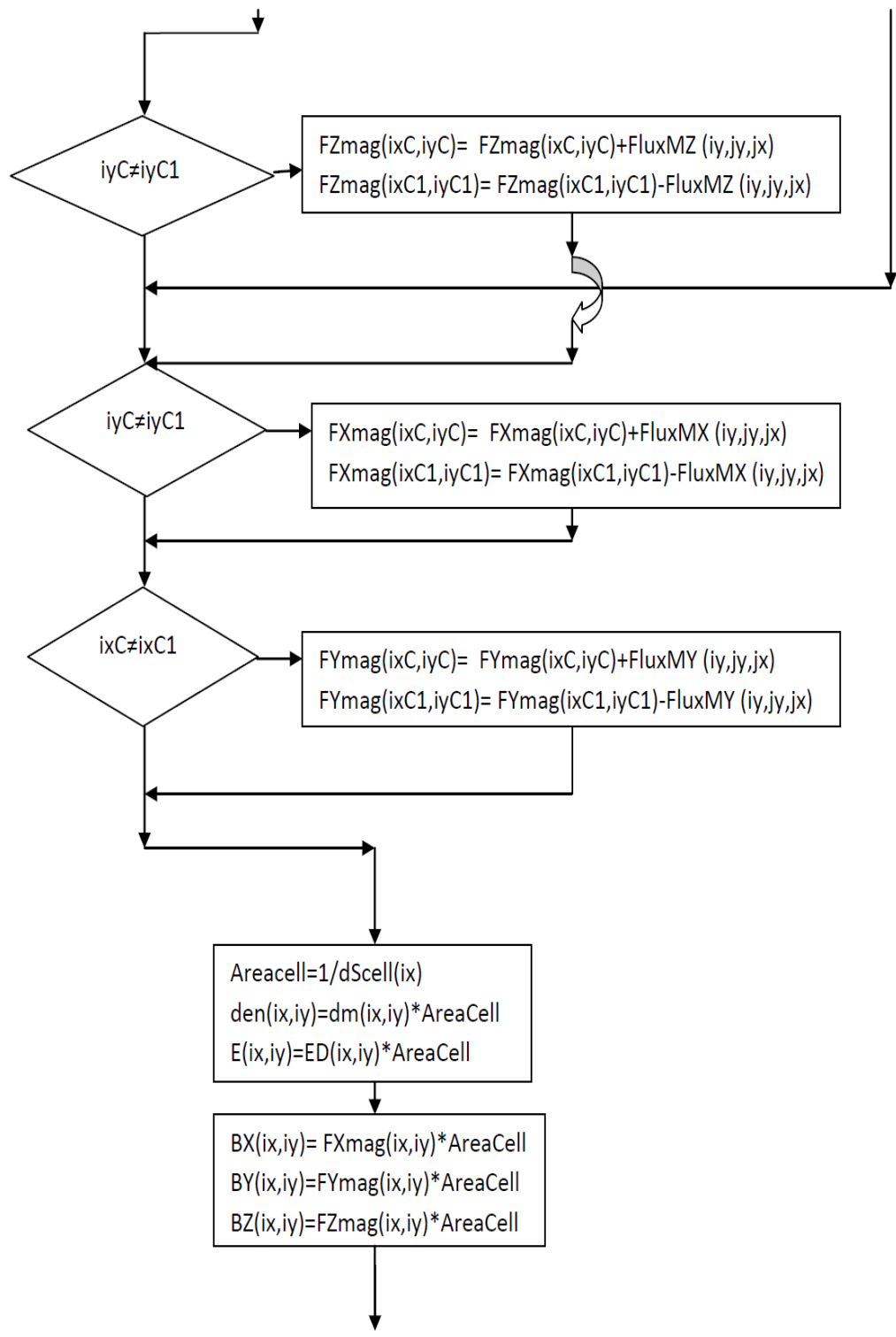
### A9) Subroutine CELL

In this subroutine new mesh values after particles move on new net are calculated. Initially all values of interest are initialized to zero. Then using the data relative the positions of the particles calculated into subroutine MoveonXY, the updated values for the mass, energy and fluxes can be found. Also the updated values for the magnetic force can be calculated. With these values, the new values for the B field components can be calculated as the new values for the velocities  $V_x$ ,  $V_y$  and  $V_z$ . At the same time also the

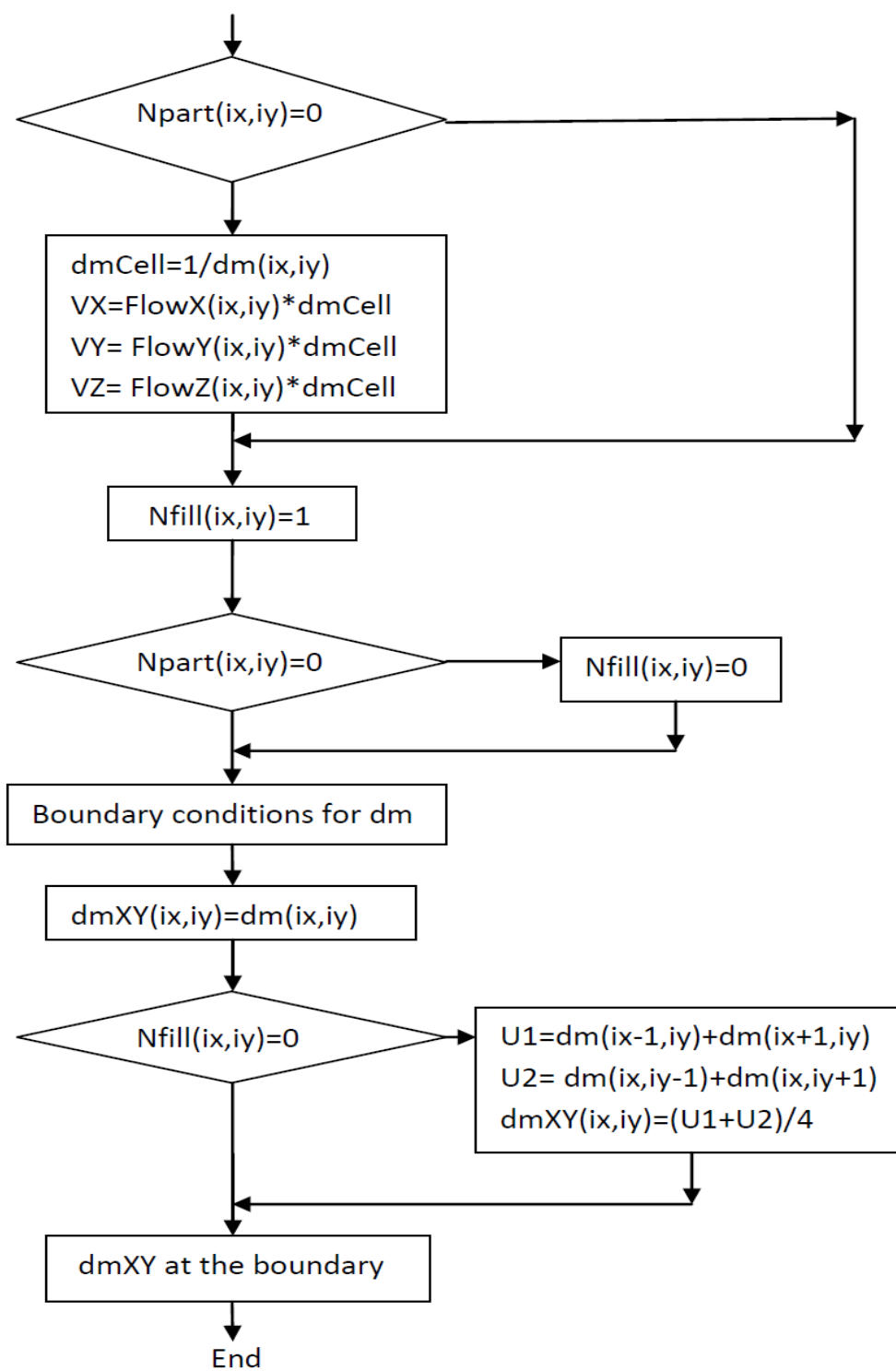
values for the boundary cells are calculated. The flowchart for the subroutine follows here.

### FLOW CHART SUBROUTINE CELL





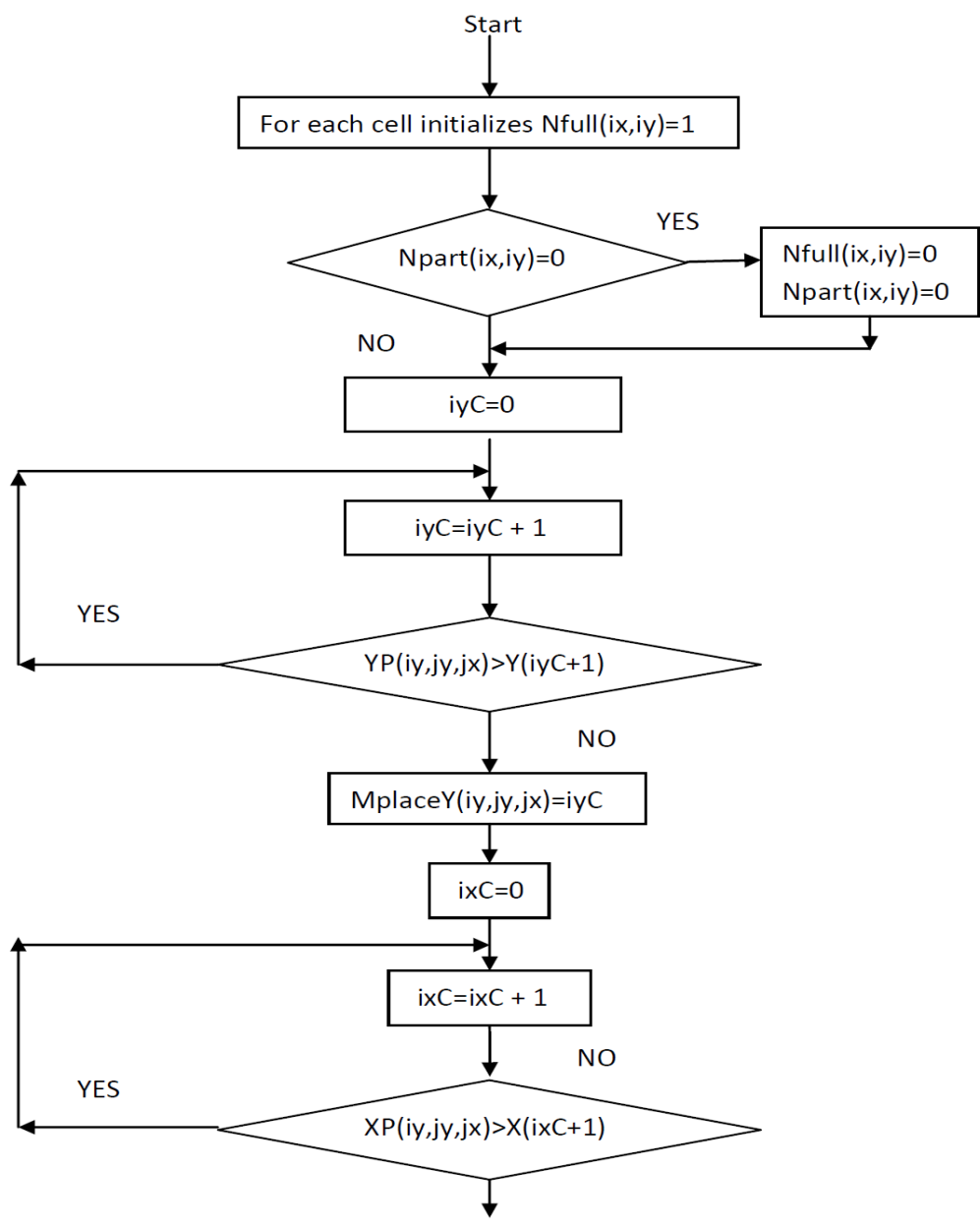


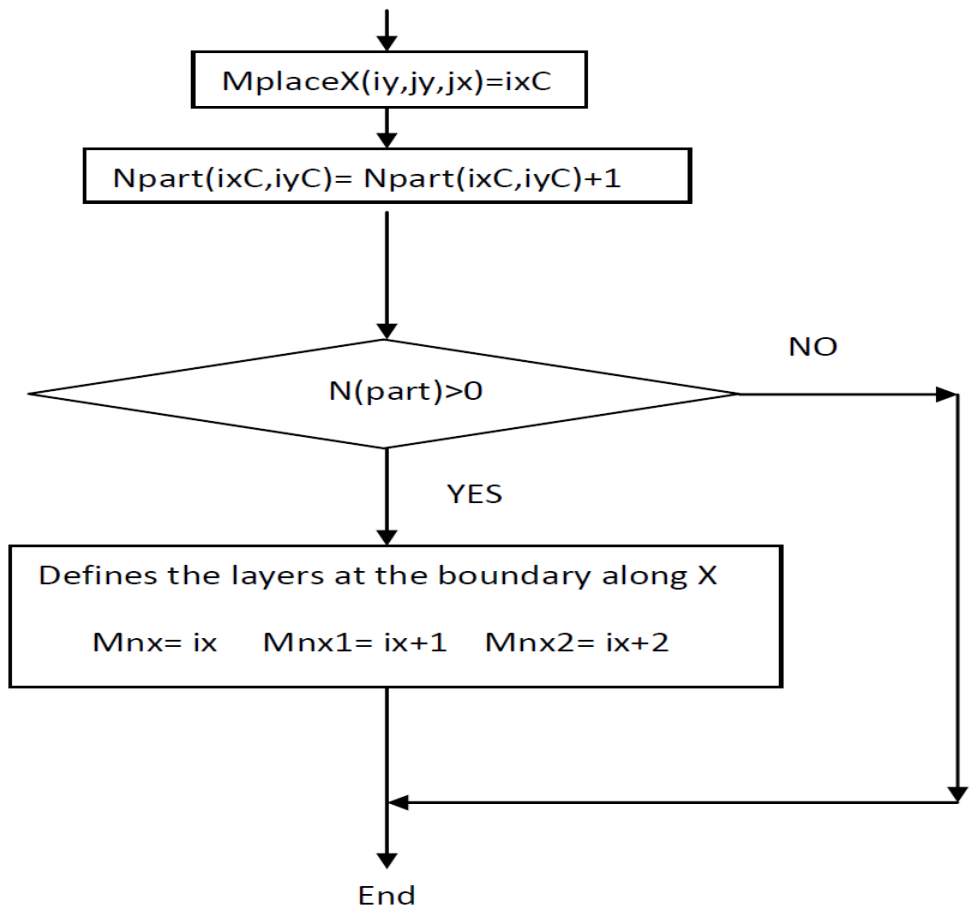


**A10) Subroutine ORDER**

This subroutine is particularly important because contains the particle mover. If there is no super particle into the cell, it does not perform any update.

**FLOW CHART SUBROUTINE ORDER**





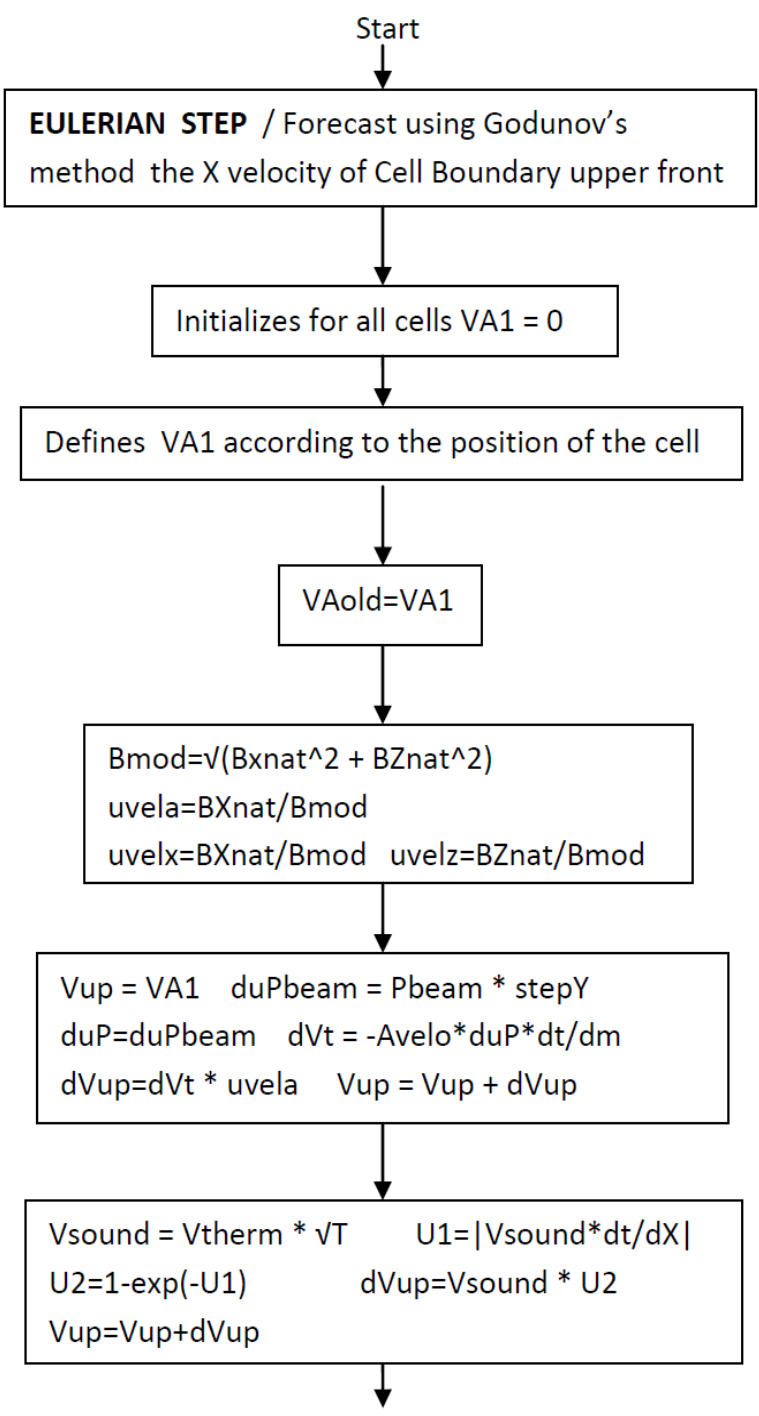
Otherwise using the information regarding the carbon plasma front, it examines one by one each cell comparing both along the axis X and the axis Y the position at that time. If the front has advanced and overcome the physical boundary of the cell, than the position along the grid is updated. At the same time also the vectors MplaceX and MplaceY are updated and will be particularly useful when calculating the new momentum and energy distribution. This scheme of particle mover is adopted with one significant difference between ELM and LASER/MK200 experiments. In fact, in the latters the use of a Gaussian shape implies that the particles directions of movements and velocities

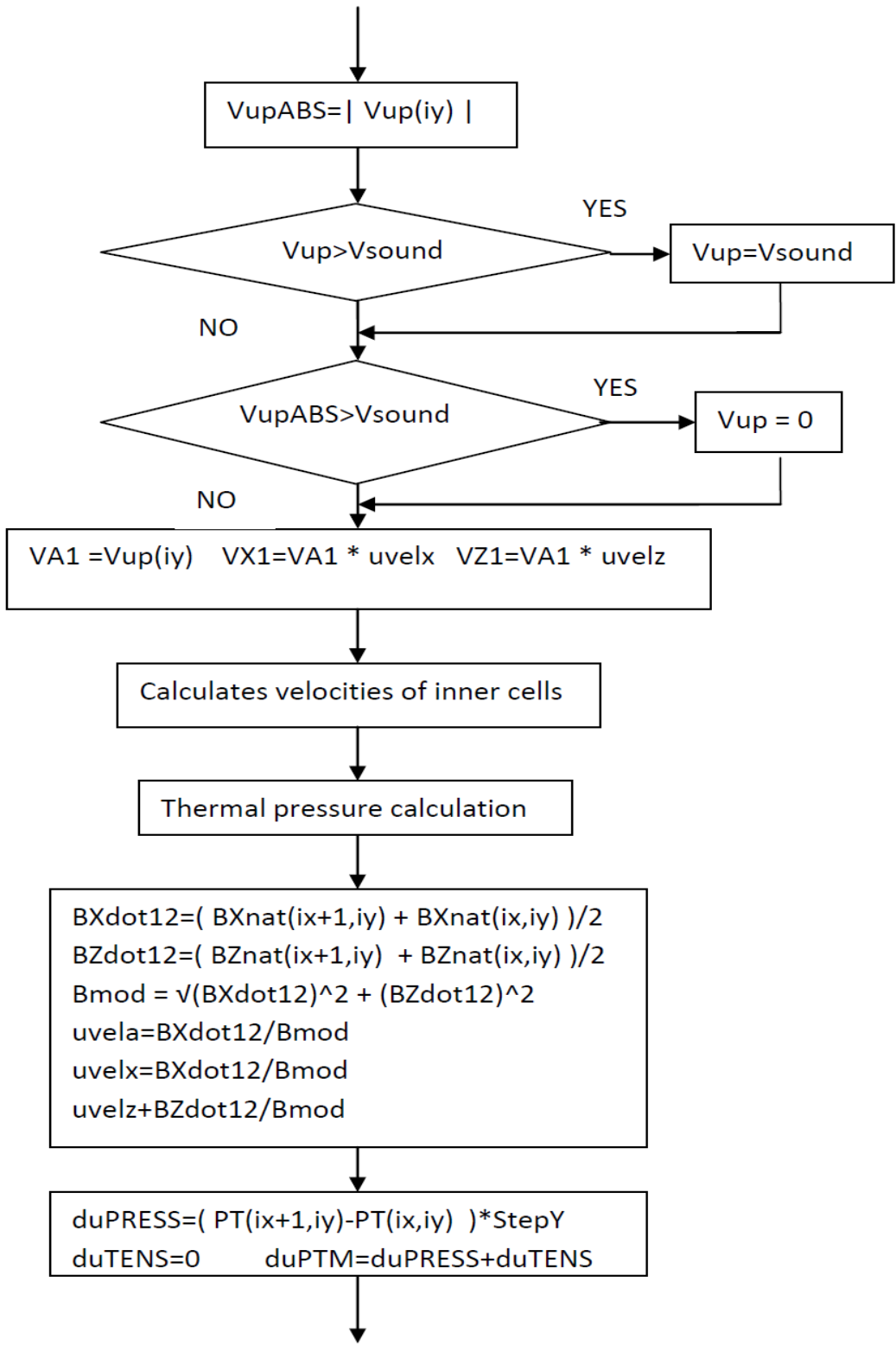
associated will have different signs. This is taken into account creating a perfectly symmetrical beam.

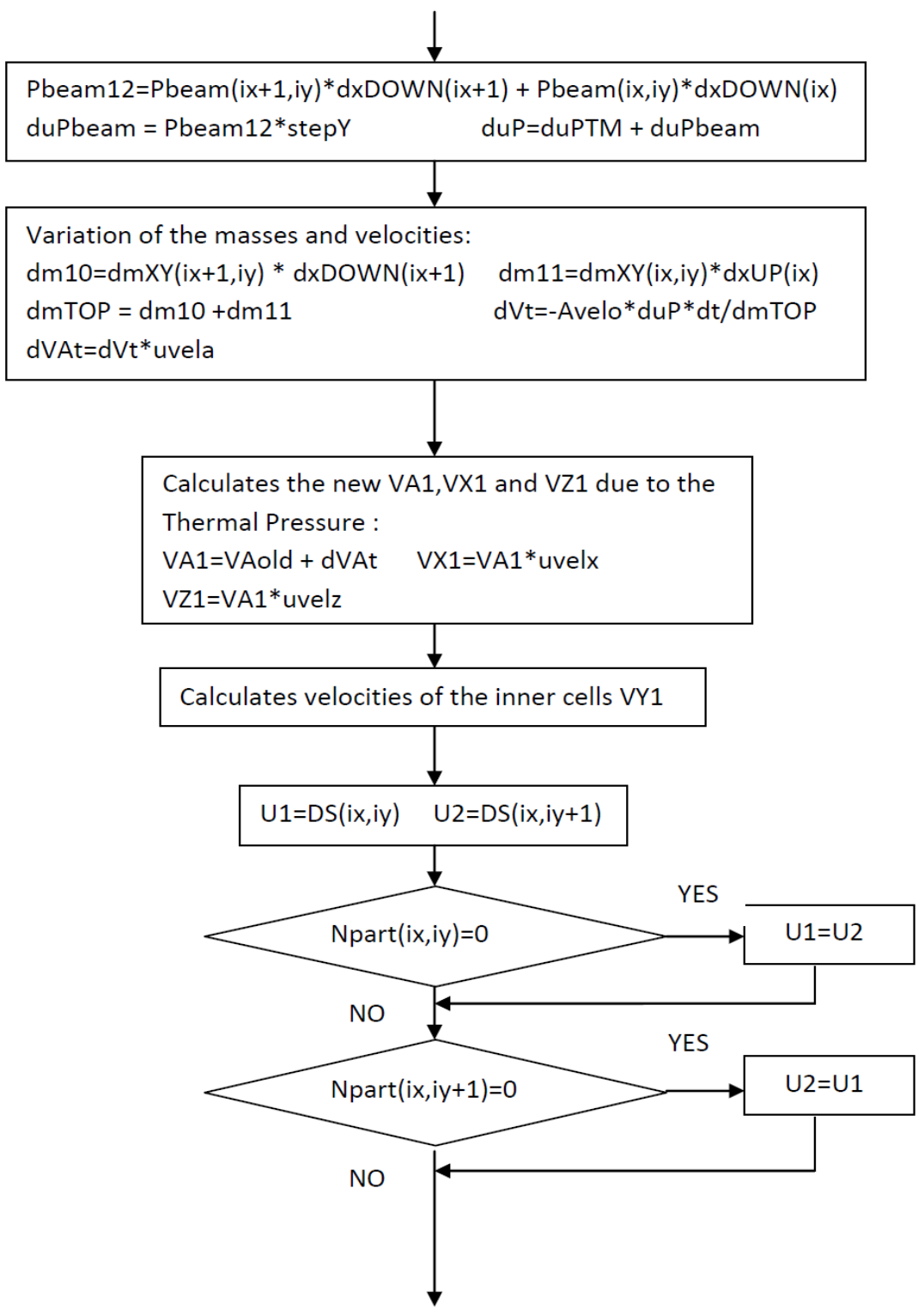
#### **A11) Subroutine VBOUNDARY**

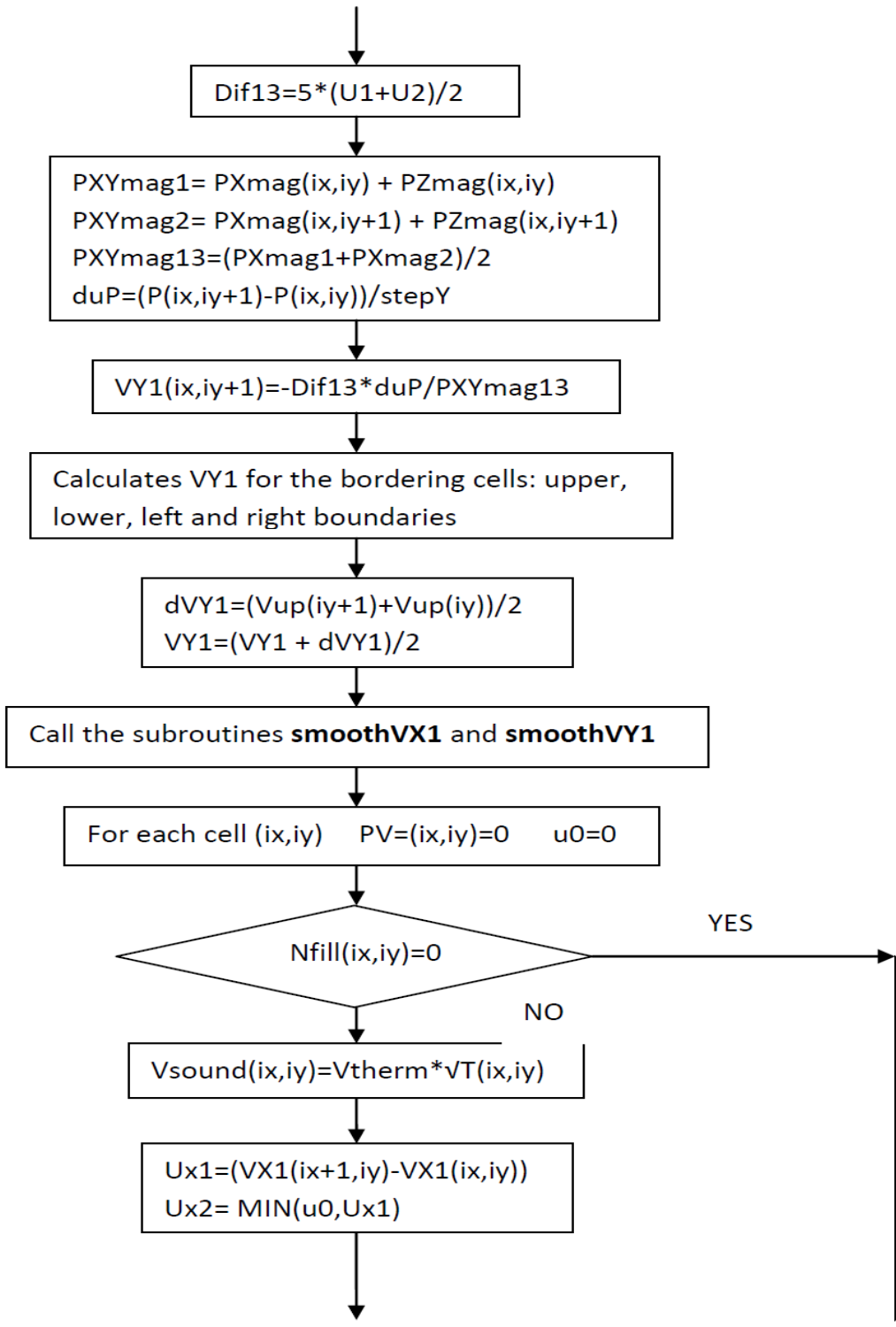
This subroutine is developed into the Eulerian step and is used to forecast the velocities  $VX1$  of the cell boundary and the velocity of the Plasma vapor cloud upper front. The influence of the magnetic field is taken into account as well as the comparison with the rarefaction wave ( $V_{\text{sound}}$ ). Then the velocities of the inner cells are also calculated taking into account the pressure of the beam. All boundaries (up, left bottom and right) are evaluated. At the end the calculation for the thermal pressure and magnetic one is also performed. All quantities are calculated only for those cells which have some super particles. If  $N=0$ , no calculation is performed. The flow chart develops as follows:

## FLOW CHART SUBROUTINE V BOUNDARY

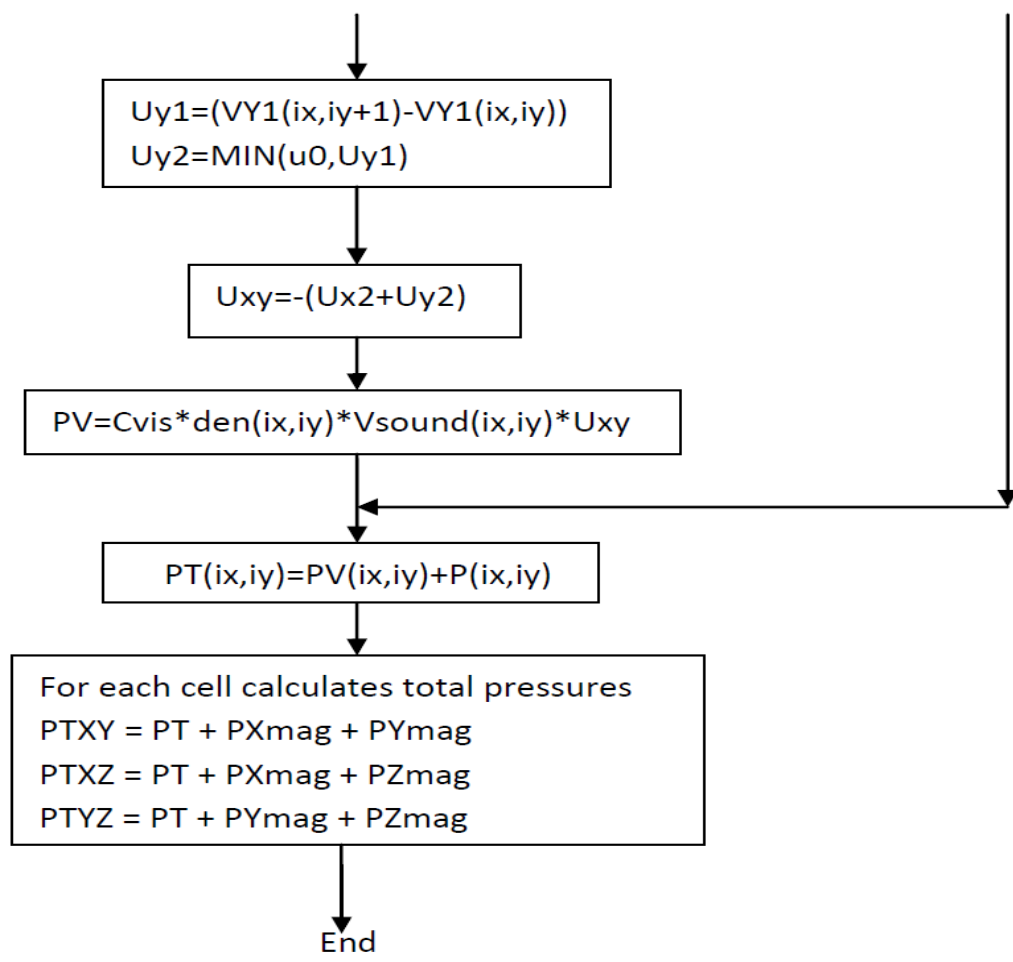








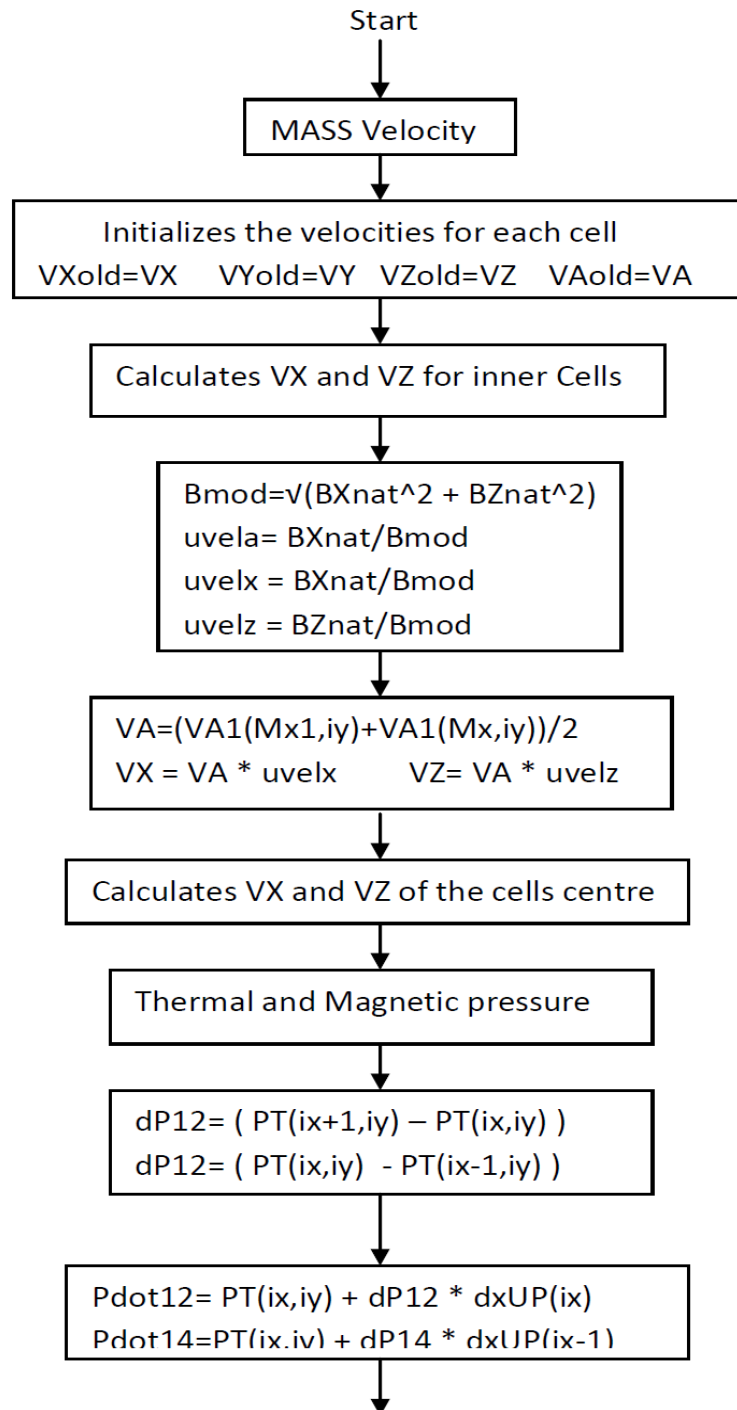


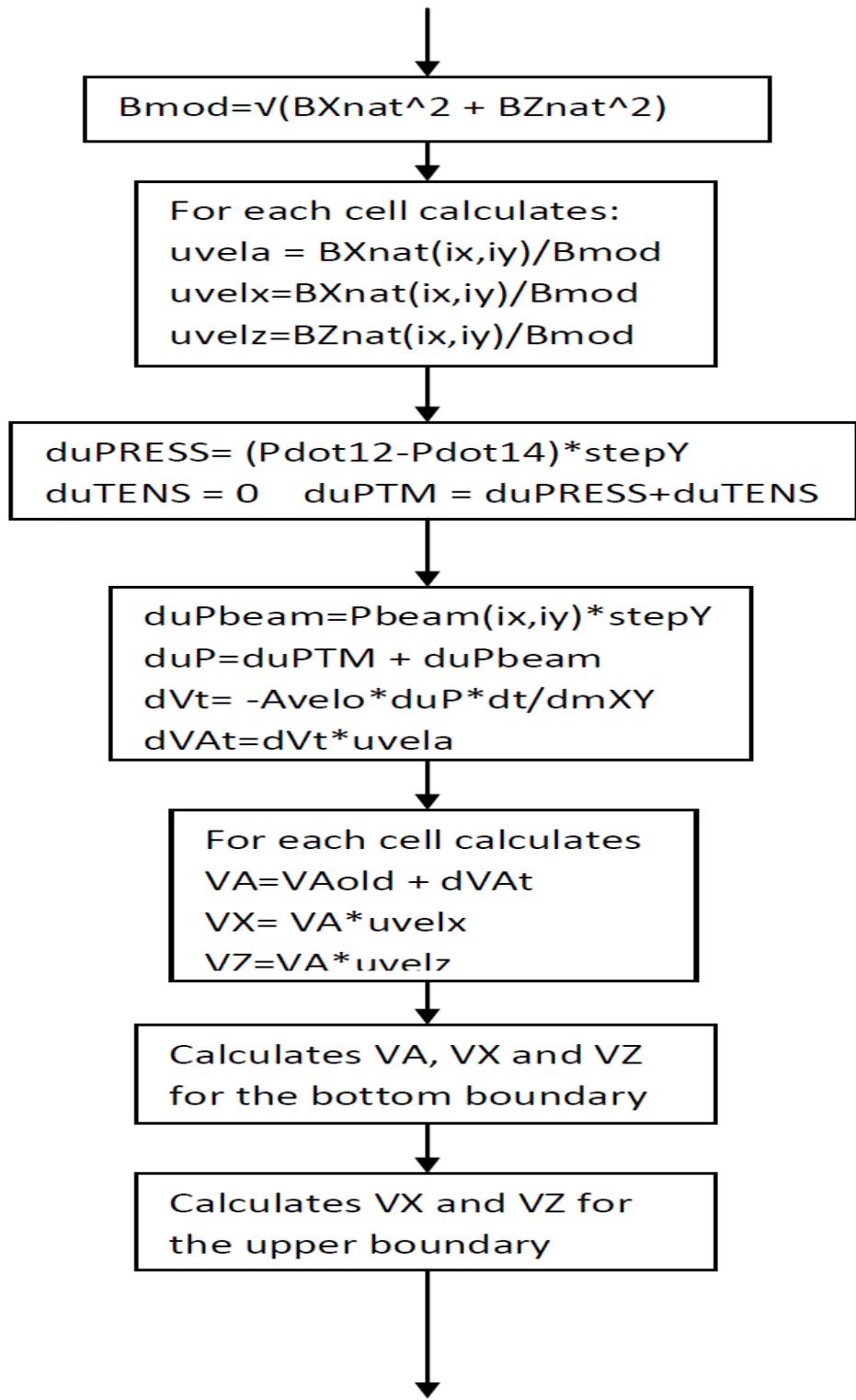


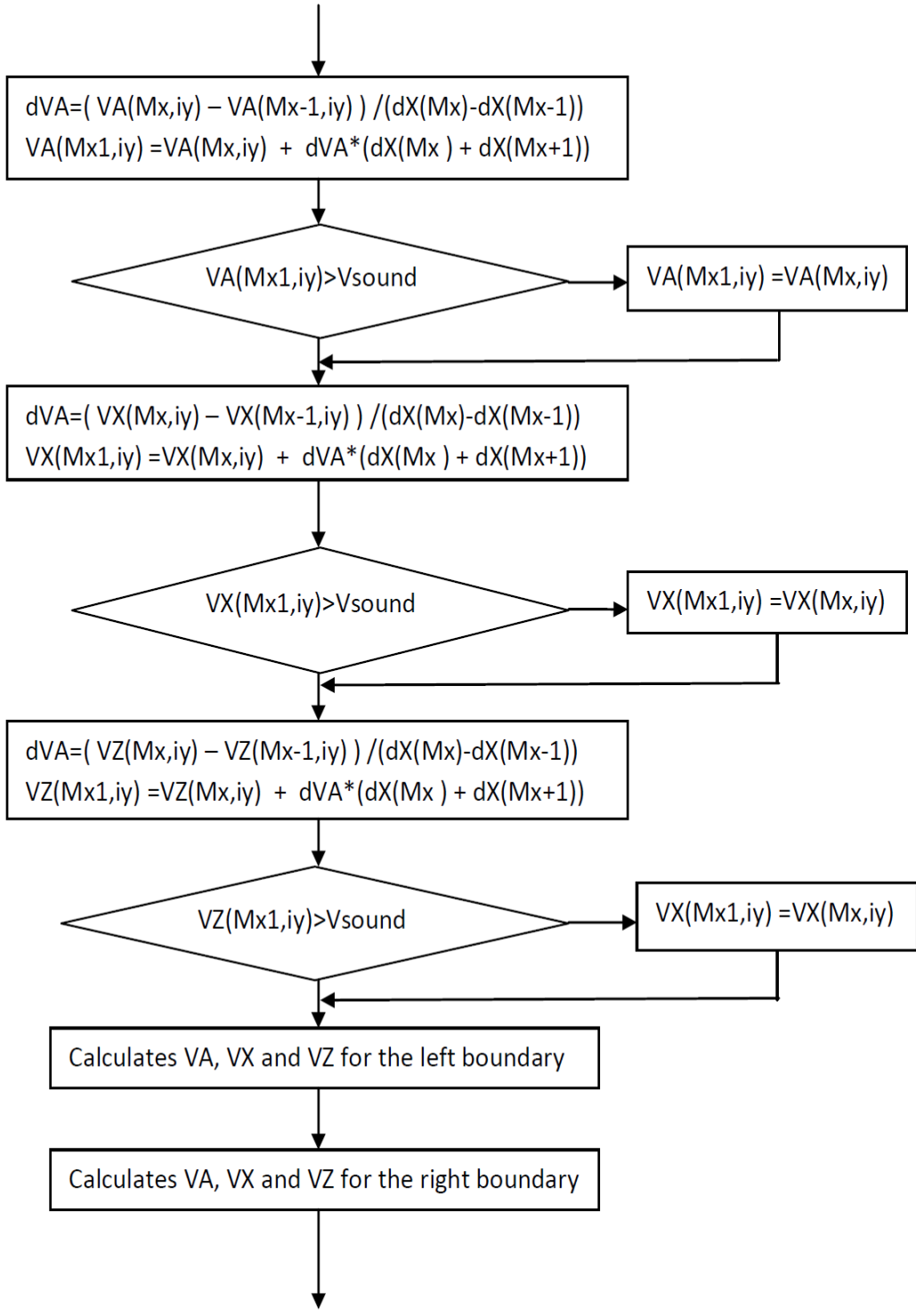
**A12) Subroutine VMASS**

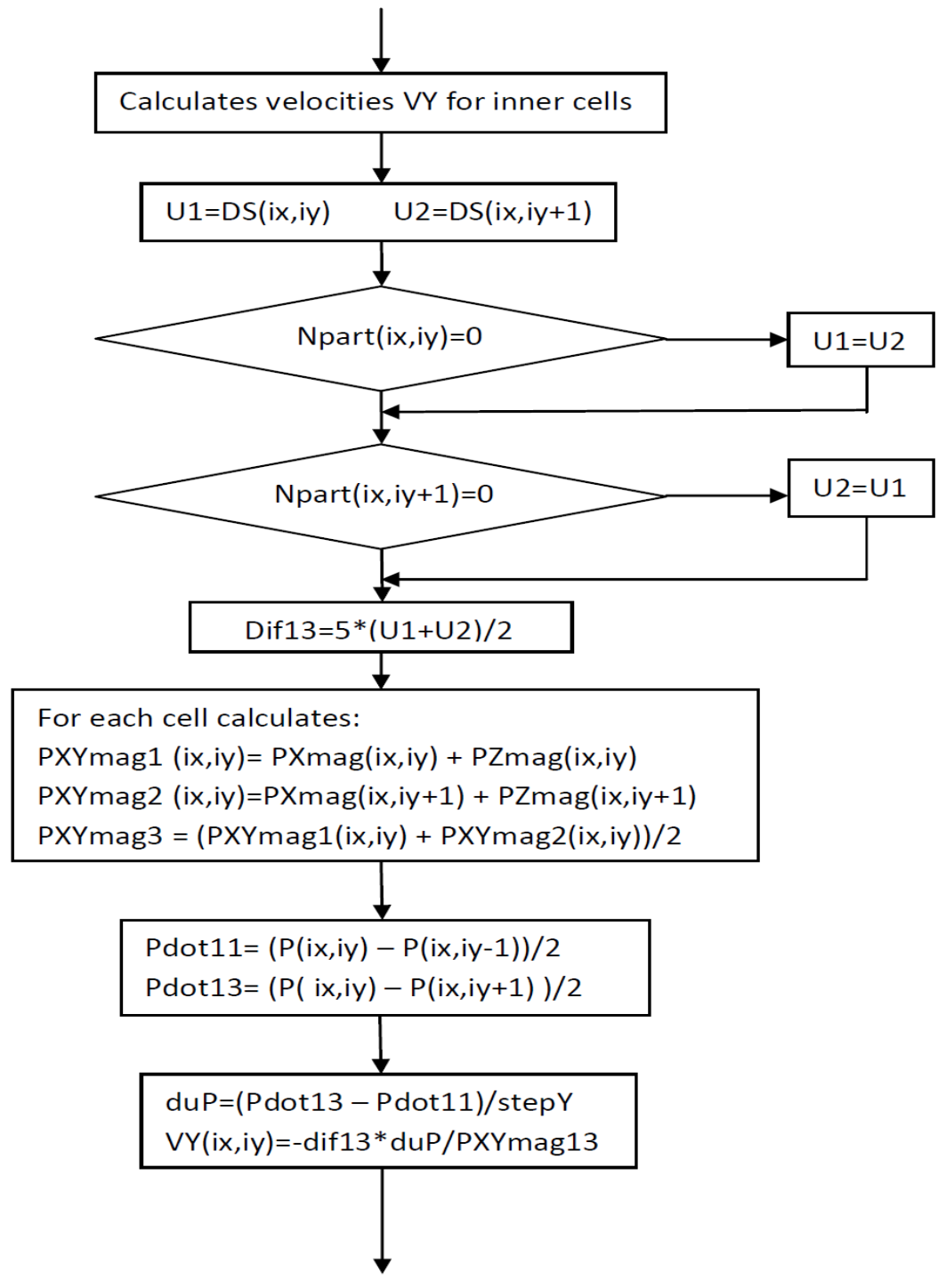
This subroutine is similar to the previous one, but focuses more on the calculation of the velocities of the inner cells. In this case the velocities of the cells centers are evaluated as well as the relative pressures. Also the velocity along Y-axis( plate ) due to diffusion is calculated in this phase using the diffusion coefficients for each cell calculated with the subroutine BDIFFUSION. The flow chart follows.

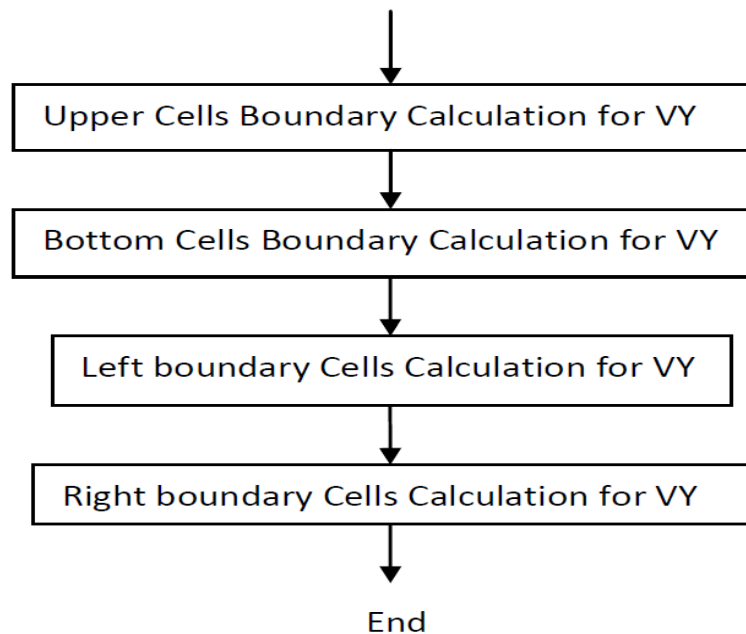
## FLOW CHART SUBROUTINE V MASS









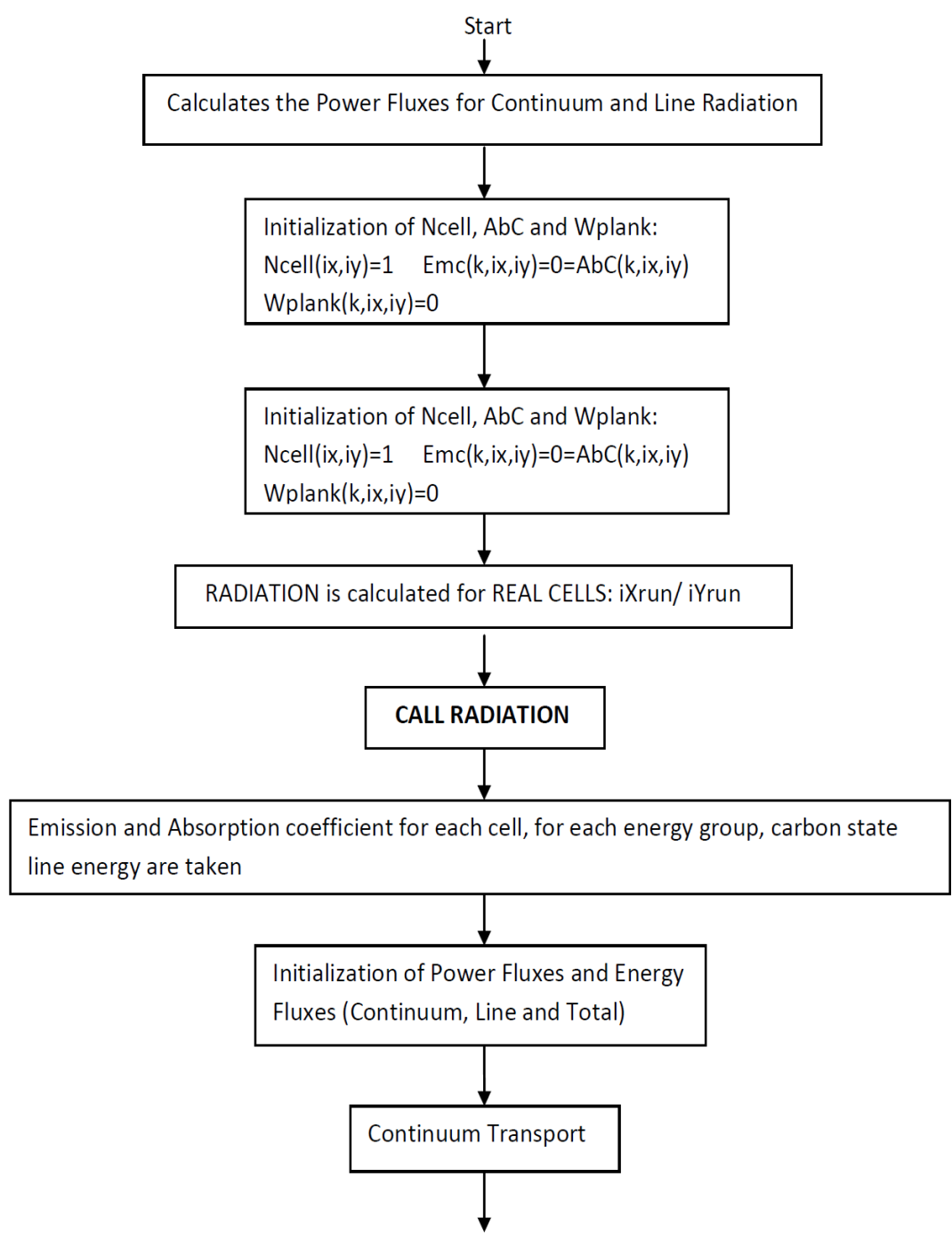


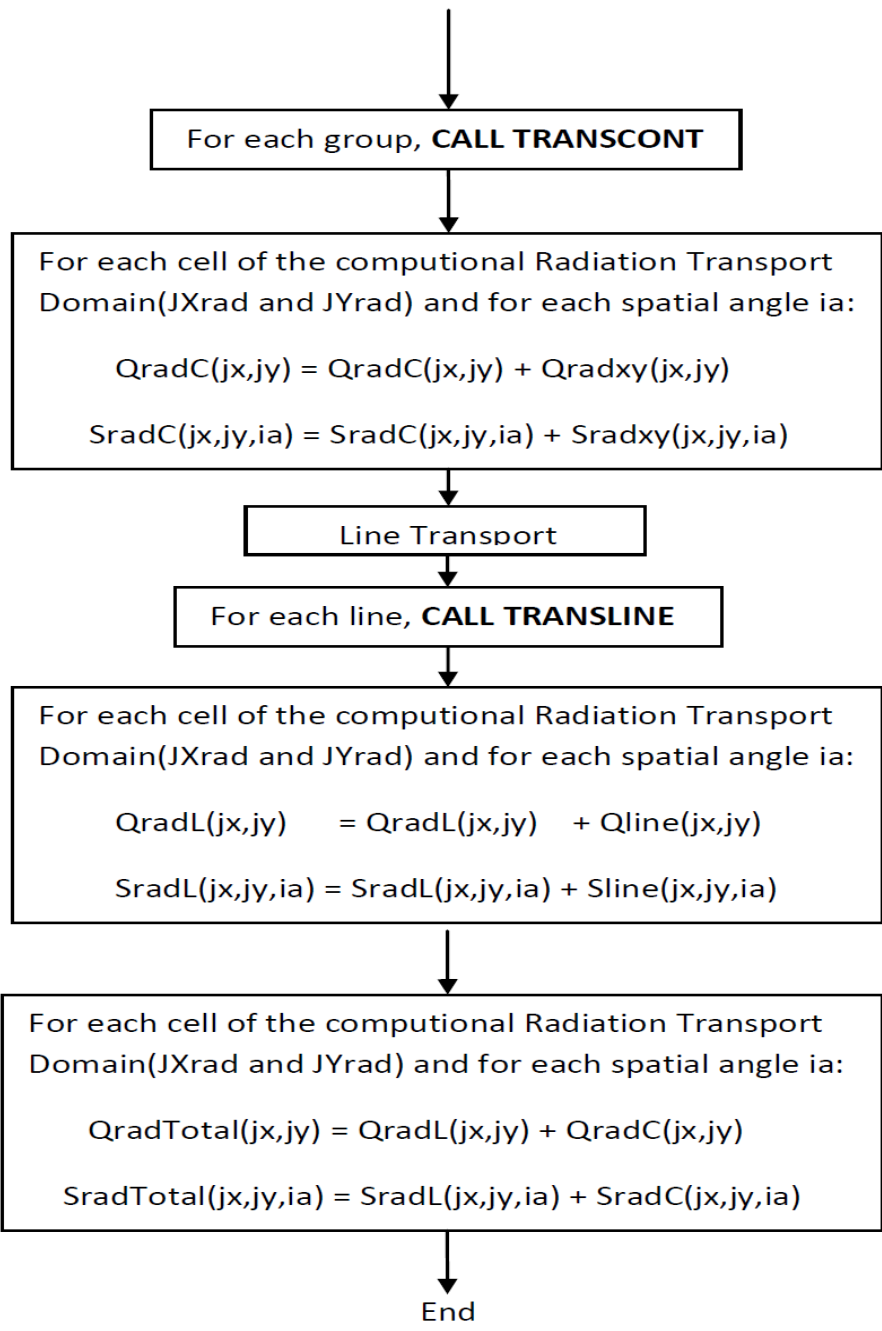
Appendix B Flow Charts of HEIGHTS-PIC/Radiation Transport

**B1) Subroutine RAYTWO**

This subroutine is the heart of the radiation transport calculations. In fact both the radiation flux and energy flux are calculated for each cell for both line radiation and continuum radiation. It uses the subroutine RADIATION, TRANSCONT and TRANSLINE for this purpose evaluating for each cell the Emission and Absorption coefficients for both line and continuum radiation. Inputs (temperature of the cell, density of the cell, ionization rate) are coming directly from the solution of the hydrodynamics presented before.

# FLOW CHART SUBROUTINE RAYTWO







## B2) Subroutine CHARGE

In this subroutine the concentration of ions or Carbon ionization is calculated for each single cell. If the temperature of the cell is less than the Temperature of carbon vaporization the Saha formula is used. If not, then kinetic description is used. The ionization level is calculated as follows:

$$ratio_{DEGENERACY} = r = \frac{G_{LEVEL}}{G_{GROUND}}$$

$$u_{k1} = \left( \frac{1}{2} e^{-\frac{IonizationPotential}{T}} \rho \right)^2$$

$$C_{IONS} = \sqrt{e^{-\frac{IonizationPotential}{T}} \cdot \rho \cdot r + \left( \frac{1}{2} e^{-\frac{IonizationPotential}{T}} \rho \cdot r \right)^2} - \left( \frac{1}{2} e^{-\frac{IonizationPotential}{T}} \rho \cdot r \right)$$

$$C_{IONS\_GROUND} = 1 - C_{IONS}$$

$$\rho_{ELECTRONS} = \rho \cdot C_{IONS}$$

$$Z_{AVERAGE} = C_{IONS}$$

If instead the temperature relative to the cell is higher than T of vaporization, then a different approach is required. First of all the subroutine RATE is called again to provide the frequencies of all physical processes. Then for all interested energy levels, we want to know the total frequency of recombination which is produced by the combined effect of photon recombination, electron recombination and three-body recombination:

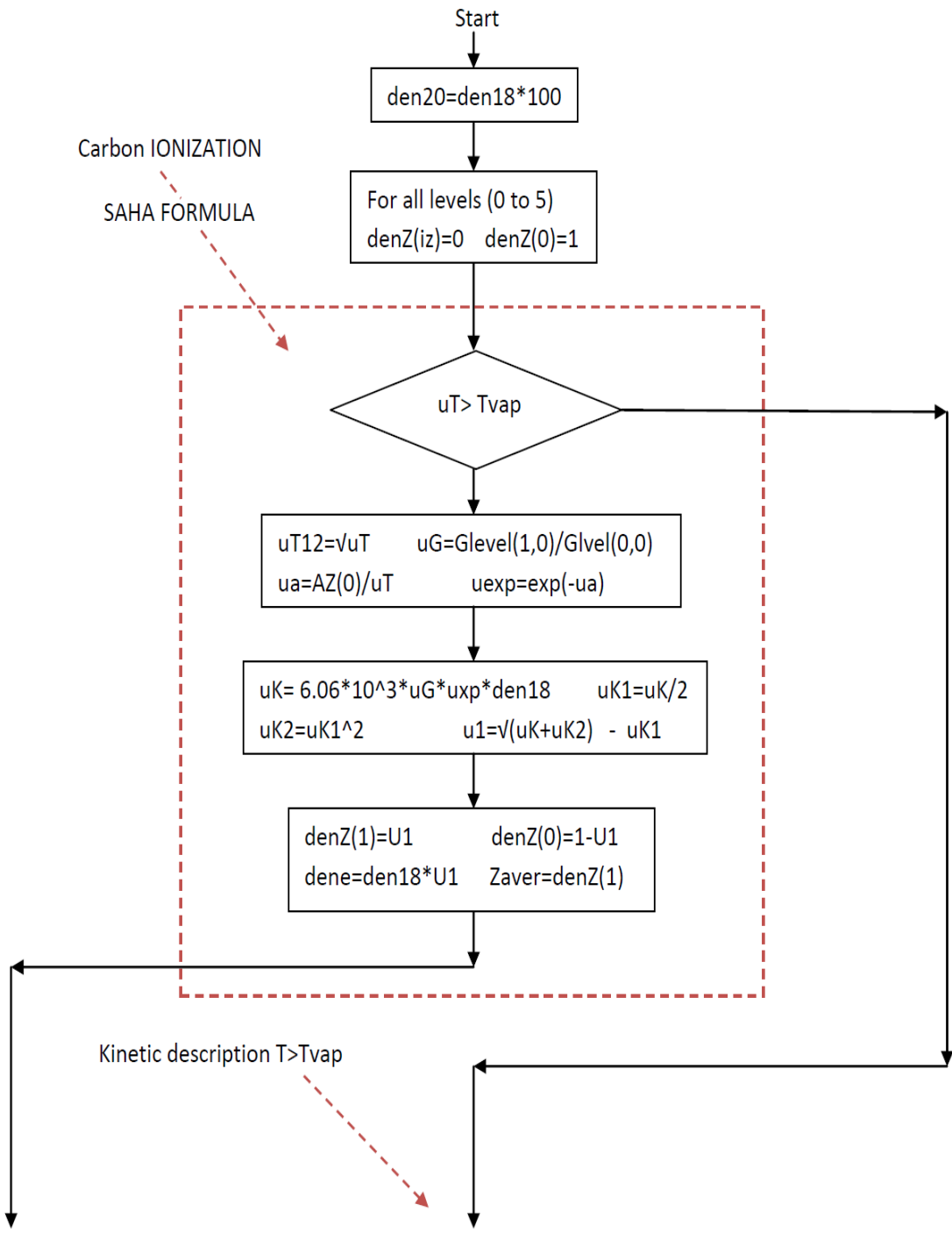
$$f_{RECOMBINATION} = f_{Photon\ Recombination} \cdot \rho_{Electrons} + (f_{Electron\ Recombination} + f_{3\ Body\ Recombination}) \cdot \rho_{Electrons}^2$$

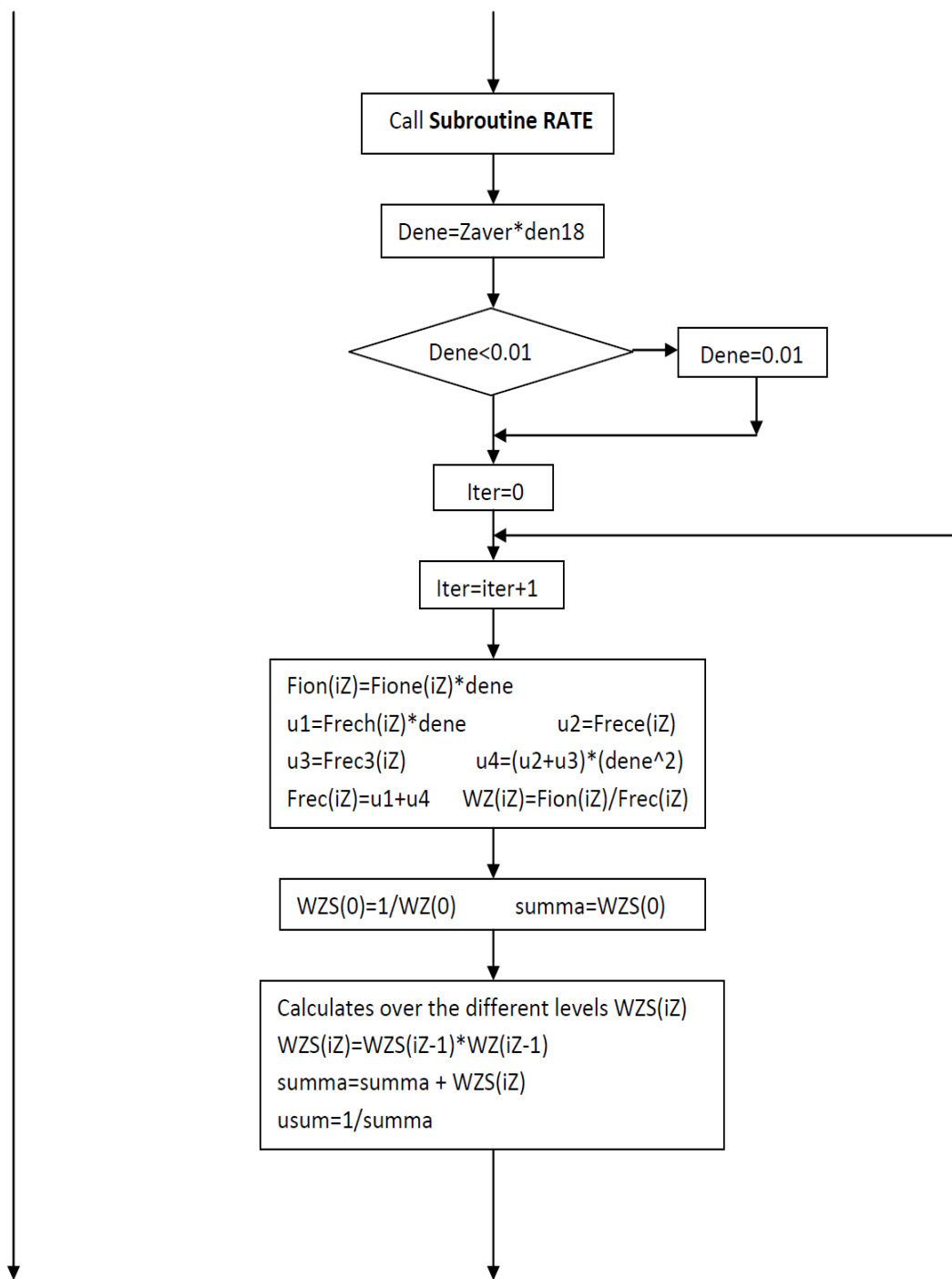
To evaluate the electron density the general formula is used:

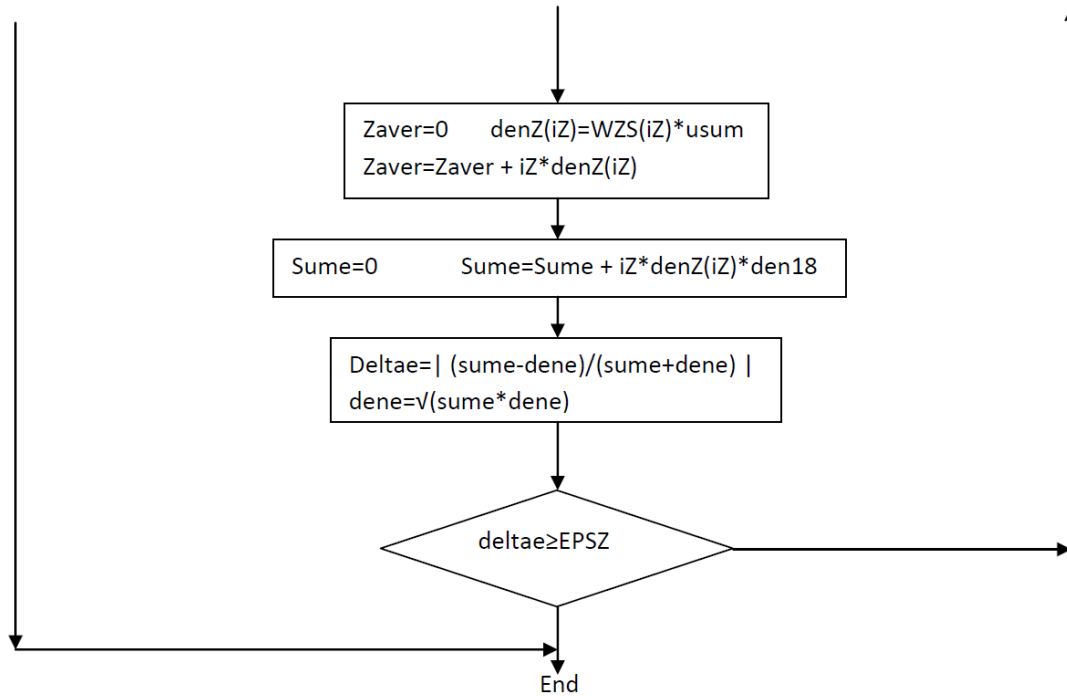
$$den_E = Z \cdot den$$

At this point the frequencies as indicated above are calculated providing also an evaluation of the average ionization state. The flow chart of the subroutine develops as follows:

### FLOW CHART SUBROUTINE CHARGE







### B3) Subroutine RADIATION

This subroutine inside the solution for the radiation transport equation is critical: absorption and emission coefficient are calculated following the CRE model for each cell, while input is plasma density. Both cases for optically thin or thick plasma are examined. Initially through the use of the subroutines CHARGE and NZ, calculates Planck radiation for each single energy group:

$$W_{PLANCK}(T) = \frac{2h \nu^3}{c^2} \left( \frac{1}{e^{\frac{h\nu}{k_B T}} - 1} \right)$$

Then continuum radiation is calculated using the laws for free-free absorption and Kramer's law for opacity of a medium for each k group:

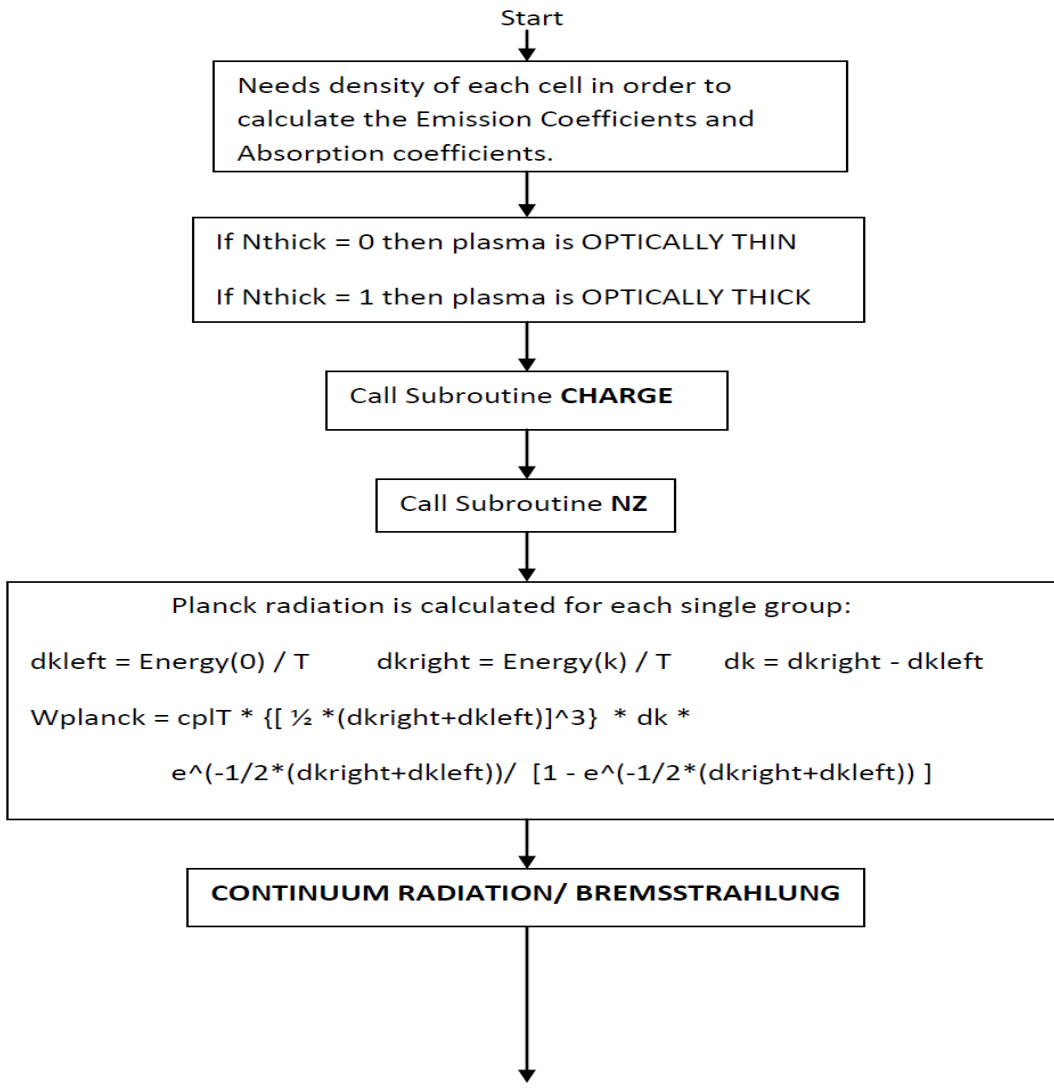
$$K_{absorption} = \rho T^{-7/2} \cdot Gaunt\ factor \cdot Z_{Average}^2 \cdot F(E)$$

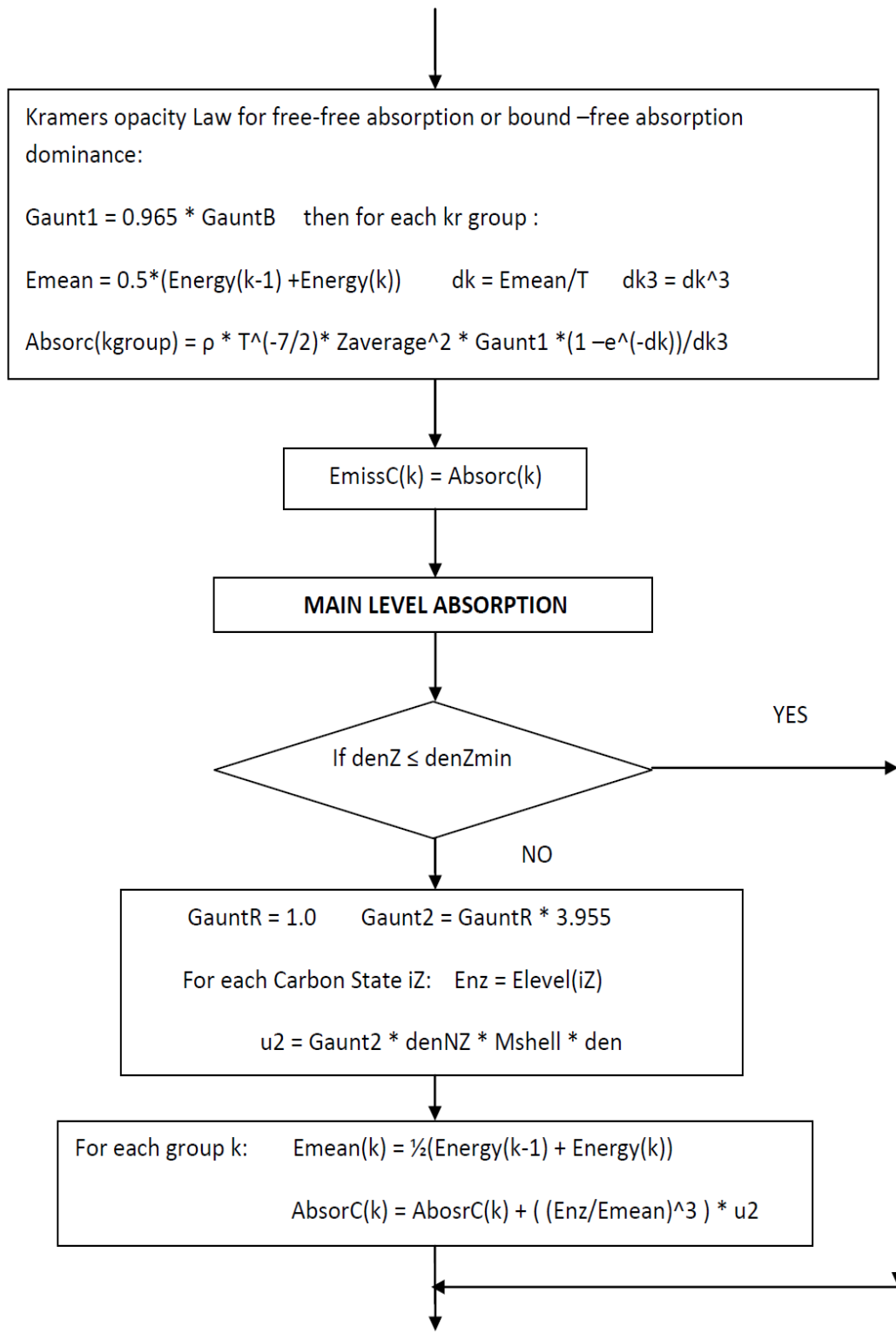
$$F(E) = \left( 1 - e^{(-Emean/T)} \right) / (Emean / T)^3$$

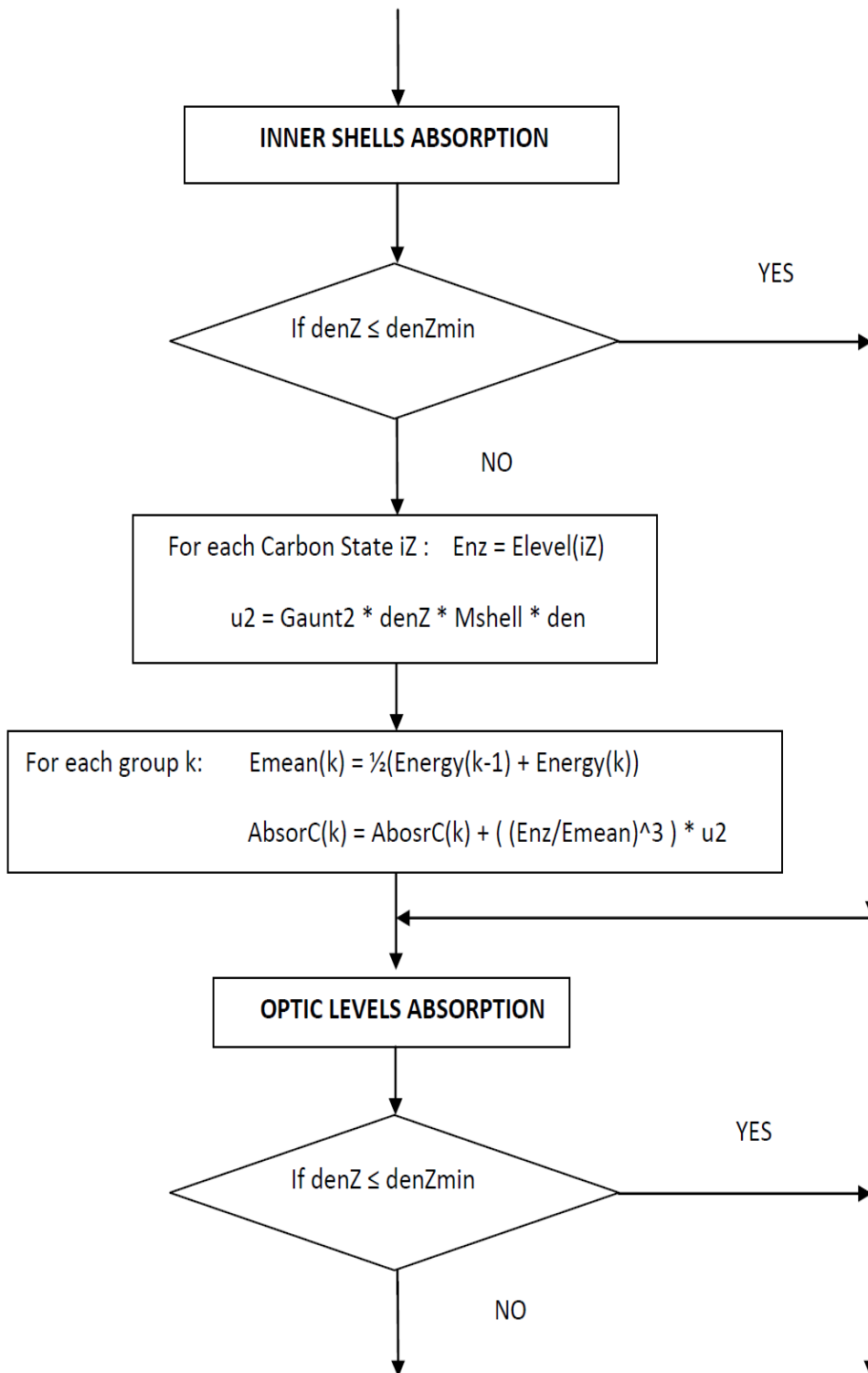
$$Emean = \frac{1}{2} (E(k) + E(k-1))$$

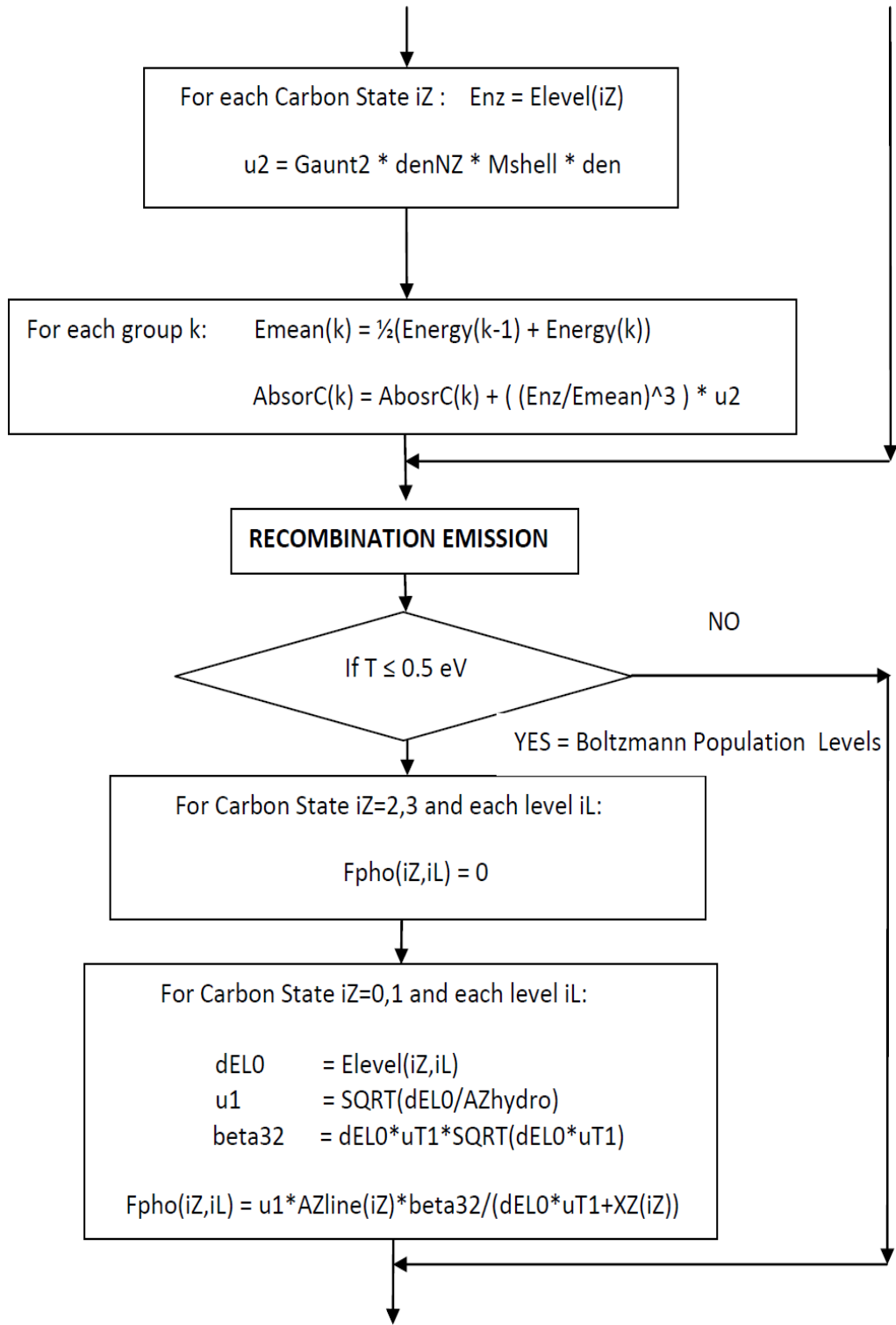
The emission coefficient is here supposed to be equal to the absorption coefficient. Three levels of absorption are then considered: main level absorption, inner shells and optic level absorption. Finally recombination emission is also evaluated. The Last part of the subroutine deals with the LINE radiation which is calculated for each carbon state. The flow chart follows as:

### FLOW CHART SUBROUTINE RADIATION









For each Carbon State iZ :  $E_{nz} = E_{level}(iZ)$   
 $u_2 = Gaunt2 * den_{NZ} * M_{shell} * den$

For each group k:  $E_{mean}(k) = \frac{1}{2}(Energy(k-1) + Energy(k))$   
 $AbsorC(k) = AbsorC(k) + ((Enz/E_{mean})^3) * u_2$

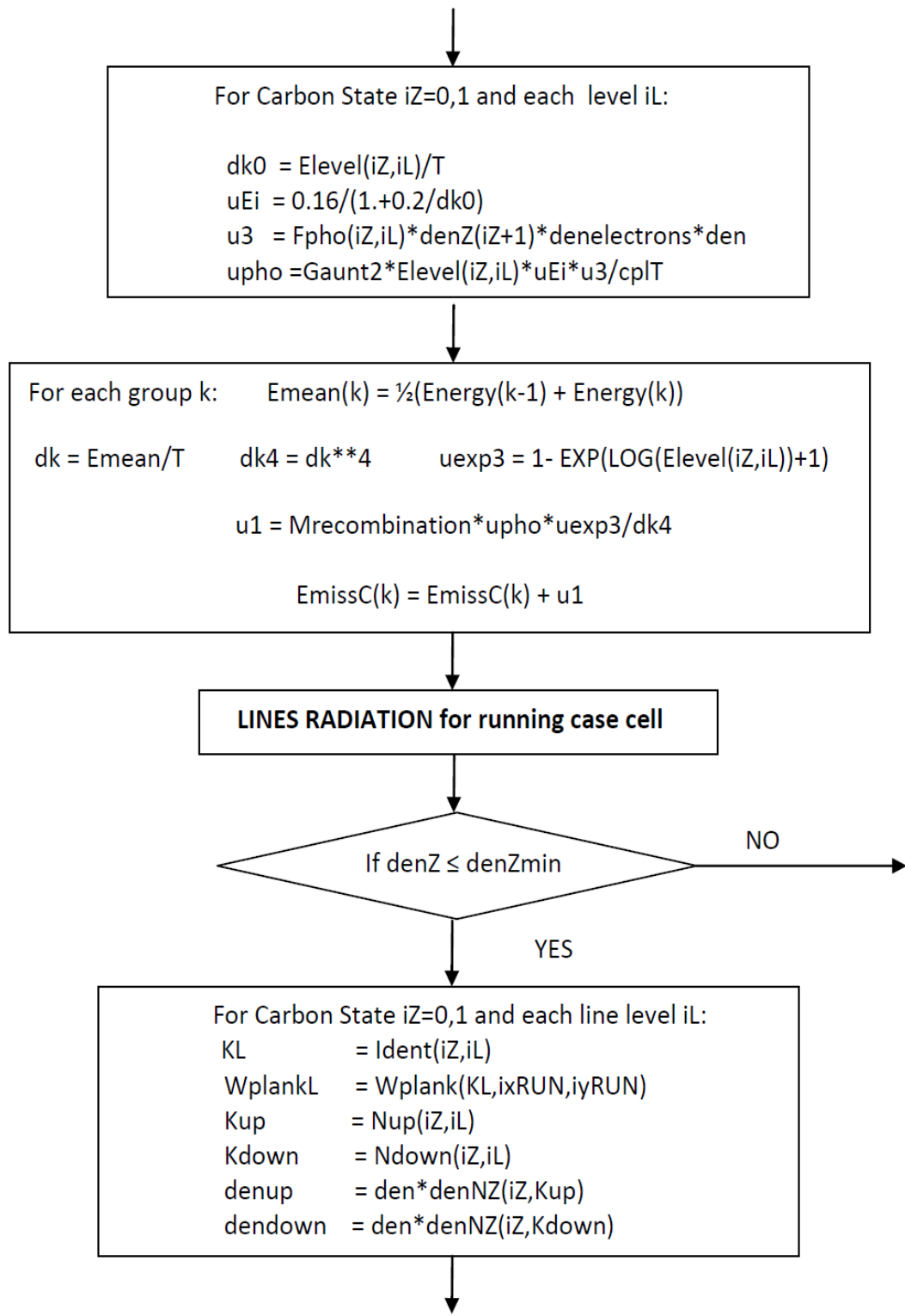
**RECOMBINATION EMISSION**

If  $T \leq 0.5 \text{ eV}$

For Carbon State  $iZ=2,3$  and each level  $iL$ :  
 $F_{pho}(iZ,iL) = 0$

For Carbon State  $iZ=0,1$  and each level  $iL$ :  
 $dELO = E_{level}(iZ,iL)$   
 $u_1 = \text{SQRT}(dELO/AZ_{hydro})$   
 $\beta_{32} = dELO * u_{T1} * \text{SQRT}(dELO * u_{T1})$   
 $F_{pho}(iZ,iL) = u_1 * AZ_{line}(iZ) * \beta_{32} / (dELO * u_{T1} + XZ(iZ))$





For Carbon State  $iZ=0,1$  and each level  $iL$ :

$$dk0 = E_{level}(iZ,iL)/T$$

$$u_{Ei} = 0.16/(1.+0.2/dk0)$$

$$u3 = F_{pho}(iZ,iL)*denZ(iZ+1)*denelectrons*den$$

$$upho = Gaunt2 * E_{level}(iZ,iL) * u_{Ei} * u3 / cplT$$

For each group  $k$ :  $E_{mean}(k) = \frac{1}{2}(Energy(k-1) + Energy(k))$

$$dk = E_{mean}/T \quad dk4 = dk^{**}4 \quad u_{exp3} = 1 - \text{EXP}(\text{LOG}(E_{level}(iZ,iL))+1)$$

$$u1 = M_{recombination} * upho * u_{exp3} / dk4$$

$$E_{missC}(k) = E_{missC}(k) + u1$$

**LINES RADIATION for running case cell**

If  $denZ \leq denZ_{min}$  NO →

YES ↓

For Carbon State  $iZ=0,1$  and each line level  $iL$ :

$$KL = Ident(iZ,iL)$$

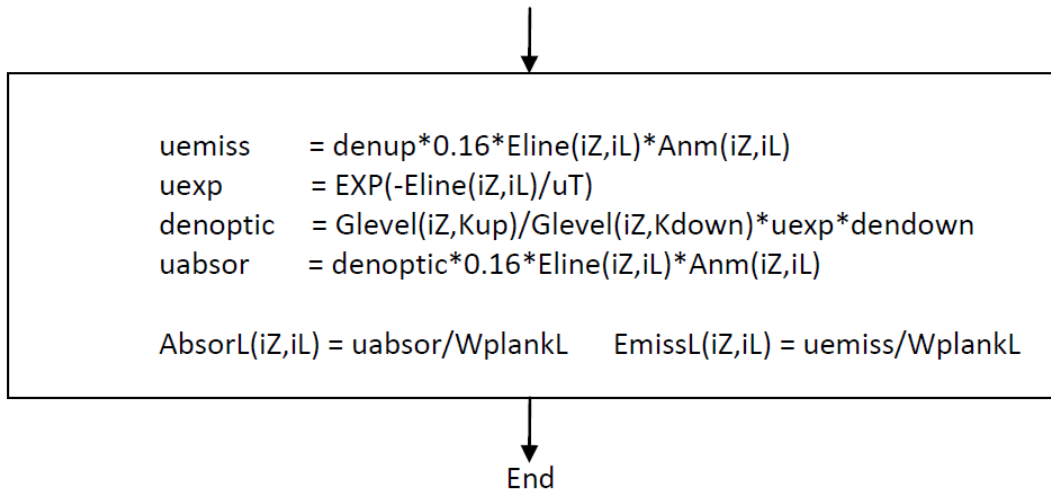
$$W_{plankL} = W_{plank}(KL,ixRUN,iyRUN)$$

$$K_{up} = N_{up}(iZ,iL)$$

$$K_{down} = N_{down}(iZ,iL)$$

$$den_{up} = den * denNZ(iZ,K_{up})$$

$$den_{down} = den * denNZ(iZ,K_{down})$$



VITA

## VITA

Filippo Genco  
Graduate School, Purdue University

Education

B.S & MS. (Italian Laurea), Mechanical Engineering, 2002, Politecnico di Bari, Bari, Italy

M.S., Aeronautics & Astronautics Engineering, 2005, Purdue University, West Lafayette, Indiana

M.S., Nuclear Engineering, 2012, Purdue University, West Lafayette, Indiana

Ph.D., Nuclear Engineering, 2013, Purdue University, West Lafayette, Indiana

Research Interests

Plasma Material Interactions.

Magnetic Fusion Applications.

Radiation damage in materials

Advanced numerical methods

Power generation and heat exchangers

Nuclear and electric propulsion

Direct energy conversion systems and applications

Teaching Experience

Teaching Assistant/Lecturer, Foreign Language Department, Purdue University, 2004-2008.

Tutor, Foreign Language Department, Purdue University, 2005-2010.

Teaching Assistant, School of Nuclear Engineering, Purdue University, 2006-2011.

Research Experience

Research Assistant/IMASS Project, School of Nuclear Engineering, Purdue University, 2007-2008.

Research Assistant CMUXE Center/IMPACT Laboratory, School of Nuclear Engineering, Purdue University, 2008-2009.

Research Assistant CMUXE Center/HEIGHTS Simulations, School of Nuclear Engineering, Purdue University, 2009-2013.

Professional Affiliations

AIAA, American Institute of Aeronautics and Astronautics.

ASME, American Society of Mechanical Engineers.

ANS, American Nuclear Society.

Professional Engineer (Ing.) in Italy.

Honors & Awards

IGCC (Institute of Global Conflict & Cooperation) - UC San Diego Summer fellowship (2008)

Technology of Fusion Energy (TOFE) Student Travel Award (2010)

Purdue University ISS Outstanding Volunteer Award (2011)

Nuclear Engineering Honor Society, Alpha Nu Sigma (since 2012)

Engagement

Member of the Purdue GSAC Graduate Student Advisory Council Committee (2008-2013), representing the School of Nuclear Engineering.

Purdue University SURF (Summer Undergraduate Research Fellowships) Graduate Mentor at the CMUXE Laboratory (Summer 2013)

Contributed to the creation of the Purdue Italian Club.

Purdue International Students and Scholars (ISS) Volunteer 2004-2011

## PUBLICATIONS

## PUBLICATIONS

1. Genco F. and Hassanein A., (2011) Modeling of Damage and Lifetime Analysis of Plasma Facing Components during Plasma Instabilities in Tokamaks  
Fusion Science & Technology 60(1) 339-343 (Chapter 3-4)
2. Genco F. and Hassanein A., (2013) Numerical Simulations of Laser Ablated Plumes Using Particle-in-Cell (PIC) Methods. Submitted to Laser and Particle Beams, Cambridge University Press, Under Review (Chapter 4).
3. Genco F. and Hassanein A., (2013) Particle-in-Cell (PIC) Simulations of damage to Tokamaks Plasma Facing Components during Intense Power Deposition. Submitted to Fusion Engineering and Design, IOP Science, Under Review, (Chapter 4-5).
4. Genco F. and Hassanein A., (2013) Particle-in-Cell (PIC) Methods in predicting materials behavior during high power deposition. Submitted to Laser and Particle Beams, Cambridge University Press, Accepted for Publications (Chapter 2-4).